UNIVERSITÀ DEGLI STUDI DI MILANO

Doctorate School in Chemical Sciences and Technologies

Department of Chemistry

PhD course in Chemical Sciences – XXV cycle

Nanostructured semiconductor films: synthesis, surface functionalization and innovative applications

Settore CHIM/02 Chimica Fisica

PhD Thesis by

DANIELA MERONI

Tutor: Prof. Silvia ARDIZZONE

PhD course Coordinator: Prof. Silvia ARDIZZONE

Academic Year 2011-2012

Once we accept our limits, we go beyond them.

Albert Einstein

Acknowledgements

efforts and passion they put in their work and for being also nice and funny lab-mates. May your thesis be the first step of a career full of achievements and satisfactions!

My thesis period would not have been the same without all the other laboratory-mates: bachelor, master and PhD students in Milan and Jena, who made my workplace a lot funnier!

A special thank goes to my friends in Jena: Markus, Erica, Francesca, Claudia, Gabriele, Keda, Justyna, Esra, and all the others. Thank you for making me feel welcome in Jena and for sharing with me those unforgettable months!

Last but not least, I would like to thank my family and Dario for their invaluable support and for all the love they have given me.

Extended abstract

In recent years, photoactive semiconductors have received ever growing interest, as testified by the remarkable number of related publications,[1] thanks to their promising applications in manifold fields such as environmental remediation and photovoltaics. Among the photoactive semiconductors, titanium dioxide has been by far the most investigated owing to its cheapness, non-toxicity and stability to photocorrosion.[2] Titanium dioxide can be successfully applied to the photocatalytic remediation of air and water pollutants, H_2 production from water splitting, and in solar light harvesting using second generation solar cells; it is a biocompatible material, and it can be employed to obtain self-cleaning surfaces.[3] Although a few commercial applications employing nanometric TiO_2 are already on the market, many issues still remain to be addressed to obtain efficient, reliable and durable materials. The present thesis work focuses onto the synthesis and the study of the physicochemical properties of nanometric TiO_2. My research activity has focused on two main subjects, one more applicative and the other more fundamental.

The first part was devoted to the photocatalytic applications of TiO_2. Photocatalytic oxidation of pollutants is one of the most promising technologies in environmental protection and remediation, especially for the removal of low concentration pollutants in slightly contaminated enclosed atmospheres.[4] Nanometric titania has been successfully applied to the photo-oxidation/reduction of numerous organic and inorganic pollutants, both in gaseous phase and in solution.[1] Several concretes and paintings containing nanometric titania that photo-oxidize pollutants are already on the market, but many disadvantages remain to be overcome in order to obtain commercially successful products. Hence, the first part of my research was directed towards the improvement of the photocatalytic activity of TiO_2 to obtain more efficient photocatalysts for the degradation of environmental pollutants. The photocatalytic activity of titania is strongly affected by its particles' physicochemical features, which, in their turn, are imposed by the synthetic path adopted for the material preparation.[5] Therefore, it is essential to tailor the physicochemical characteristics of titania particles using an appropriate synthetic procedure in order to obtain highly active samples. A considerable part of my PhD project was devoted to the optimization of several synthetic procedures in order to produce TiO_2 powders and films with tailored optical, morphological and electronic features.

One of the main disadvantages of TiO_2 is its large band gap (3.2 eV for anatase, 3.0 eV for rutile), which corresponds to a light absorption in the UV region. Thus, currently TiO_2 based materials require UV irradiation in order to activate the photocatalytic process. As only 5% of solar light is in the UV region,[6] a shift towards visible absorption is required to improve the

photocatalytic activity of TiO_2 under solar irradiation. The introduction of non-metal ions in the TiO_2 lattice represents one of the most promising approaches to induce a bathochromic shift, *i.e.*, a shift of the absorption edge of TiO_2 to longer wavelengths, and consequently increase the photocatalytic response of doped samples into the visible region. Therefore, during my thesis, I synthesized several doped samples with non-metals such as N, in order to assess if a bathochromic shift effectively leads to a higher photocatalytic activity in the visible region and, more important, under solar irradiation. N-doped TiO_2 samples were obtained from different titania precursors ($Ti(Oi-Pr)_4$, $TiCl_3$) and adopting different N-sources (ammonia, triethylamine, tea). All obtained samples were exhaustively characterized, in order to obtain a complete picture of the modifications induced in the titania structure and surface features by the modifications of the synthetic pathway. Samples were characterized from the structural, morphological, electrochemical, optical and compositional point of view. Moreover, other features, such as magnetic properties, were determined and ab initio calculations of the electronic properties of the doped samples were performed. All N-doped samples showed a broad absorption in the visible region which was traced back, on the grounds of first principles calculations, to the formation of localized intragap electronic levels (Figure 1). Sample thin films were tested for their photocatalytic activity, under UV, visible and simulated solar irradiation, towards the degradation of gas phase ethanol and acetaldehyde. The most active N-doped sample, both under UV and solar irradiation, was the oxide showing the largest amount of paramagnetic $N_b^\bullet$ species. Under visible irradiation instead, the sample with the largest activity was the one showing the narrowest apparent band gap and the concomitant presence of anatase and brookite polymorphs, which might hinder charge recombination processes.

The structure of N-doped samples was elucidated not only by ordinary powder diffraction, but also by means of synchrotron radiation, using Extended X-ray Absorption Fine Structure (EXAFS) to understand the position of dopant ions inside the TiO_2 crystal lattice. These data were obtained during a short research stay at the European Synchrotron Radiation Facility (ESRF) in Grenoble. Average Ti nearest neighbors distances were obtained from EXAFS experiments and compared with Density Functional Theory (DFT) calculations, showing that N substitutes oxygen at low levels of doping, whereas oxygen vacancy creation is observed at higher dopant concentrations.
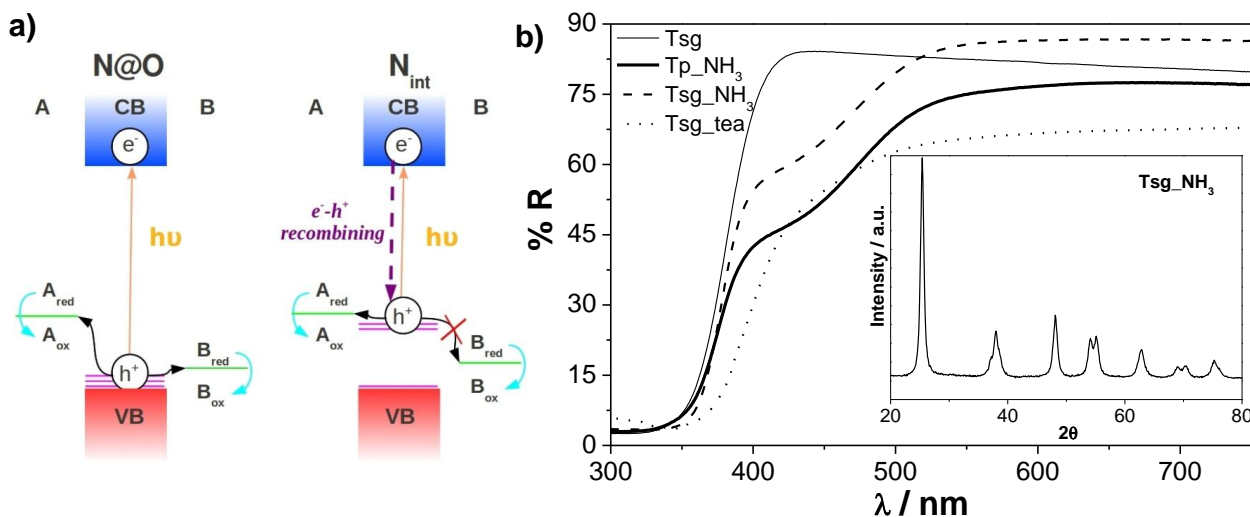
Figure 1 – **a**) Band structure and schematic photocatalytic oxidation mechanism for substitutional (left) and interstitial (right) N-doped titania. **b**) Diffuse Reflectance spectra of pristine (Tsg) and N-doped TiO_2 from several nitrogen sources. Inset: X-ray diffraction spectrum of a N-doped sample.

Another strategy to improve the photocatalytic activity of TiO_2 involves the enhancement of the adsorption and diffusion of pollutants into TiO_2. In this respect, I investigated the effect of the modification of TiO_2 morphology to obtain mesoporosity via different template syntheses. Mesoporous materials have been consistently proposed to produce better performing catalysts in many fields of catalysis. Here, the morphologic features of titania particles were tailored by using soft templates, in order to obtain materials with a high degree of porosity in the mesoporosity range. Two classes of soft templates were investigated: alkylpyridinium surfactants and block copolymers of the Pluronic family. As for the first class, both monomeric (dodecylpyridinium chloride, DPC) and dimeric gemini-like surfactants (gemini spacer 3, GS3) were employed. Mesoporous TiO_2 samples were synthesized by a classical sol-gel route followed by an hydrothermal growth in the presence of one of the structure directed agents. The surfactant/oxide interactions at the solid/liquid interface were evaluated by adsorption isotherms, showing marked differences between the two surfactants (Figure 2a,b). While DPC exhibited weak adsorbate/adsorbent interactions and weak self-aggregation tendency, resulting in the formation of very small, globular micelles, GS3 instead showed strong interactions with the TiO_2 surface and the formation of elongated rods and further hexagonal arrangements could be proposed. Such different behaviors lead to significant diversities in the porous structure of the TiO_2 samples. The small pores generated by the DPC micelle tend to collapse because of the heat of combustion generated during the surfactant removal step at 600 °C. On the contrary, GS3 leads to a significant fraction of pores in the mesoporosity range (Figure 2c).
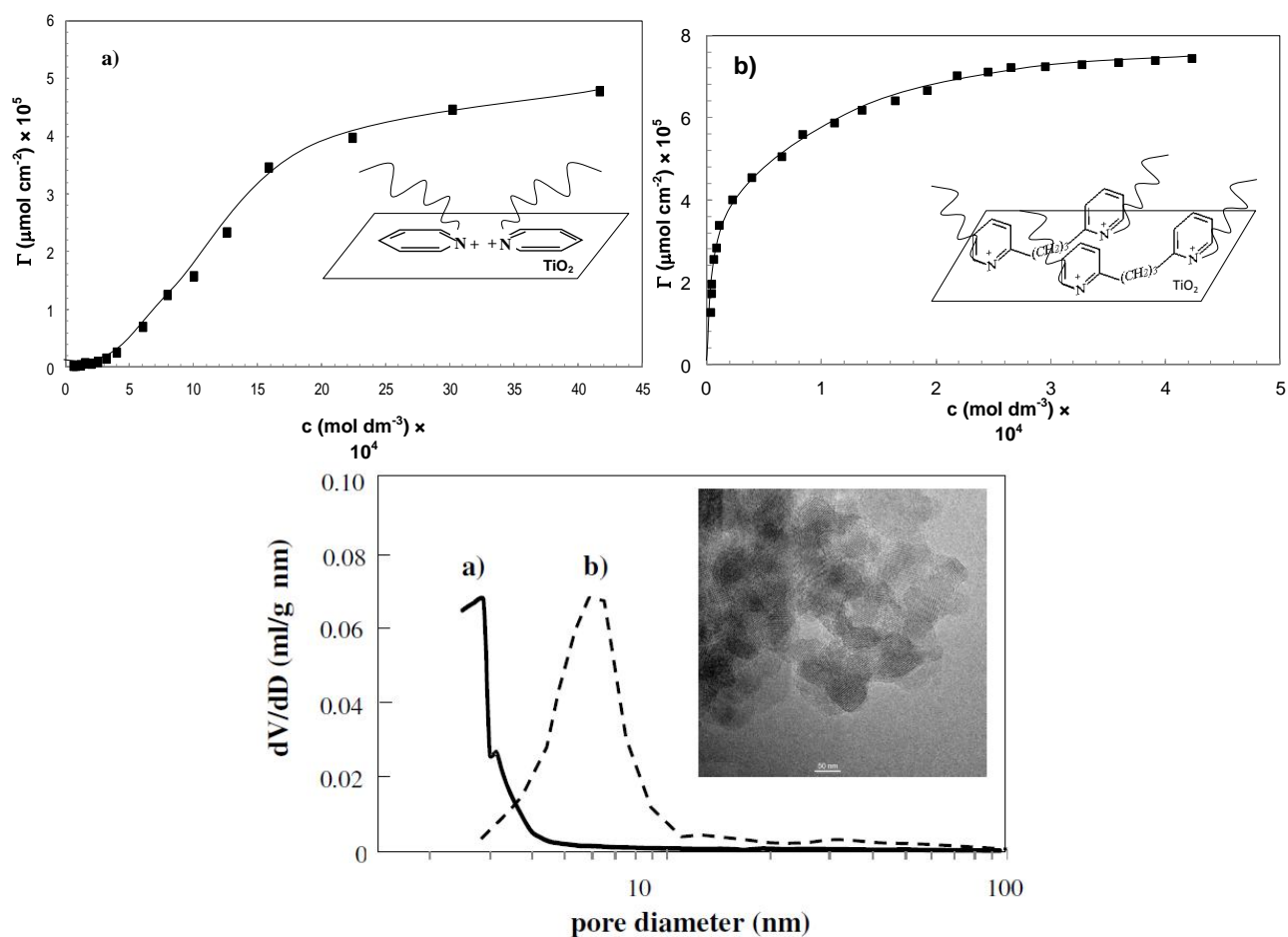
Figure 2 – Adsorption isotherms (surface excess Γ vs. equilibrium concentrations) in aqueous solutions of different solutes at the TiO_2/solution interface of **a**) monomeric DPC and **b**) dimeric GS3 surfactants. Inset: sketches of possible disposition/orientations of the adsorbed surfactant at the titania surface. **c**) Pore size distribution curve of TiO_2 bare particles (solid line) and treated with GS3 (dashed line). Inset: HRTEM image of GS3 sample.

However, the use of cationic surfactants has an intrinsic limitation: high calcination temperatures are required to remove entirely the template. Such harsh conditions markedly reduce the surface area of the oxide due to particle sintering and crystal growth. Non-ionic structure directing agents, such as amphiphilic block copolymers, can be instead completely removed at much lower temperatures. Three block copolymers of the Pluronic family, characterized by different micelle size in water as determined by light scattering analysis, were employed to induce mesoporosity in nano-TiO_2. The surfactants were removed by combining UV and thermal treatments in order to avoid pore collapse while obtaining a good oxide crystallinity. Obtained samples presented a high surface area and significant fraction of pores in the mesoporosity range. A good correlation was observed between the sequence of average pore size in mesoporous TiO_2 and the micelle size of the used copolymer (Figure 3a,b). A fine modulation of pore size and total volume was obtained by changing polymer type and concentration (Figure3c), effectively

enhancing the photocatalytic properties of the oxide towards the degradation of methylene blue (Figure 3d). The mesoporous oxides were also used as scaffolds to obtain Bi-promoted TiO_2, resulting in a further increase of the photocatalytic performance (see below).
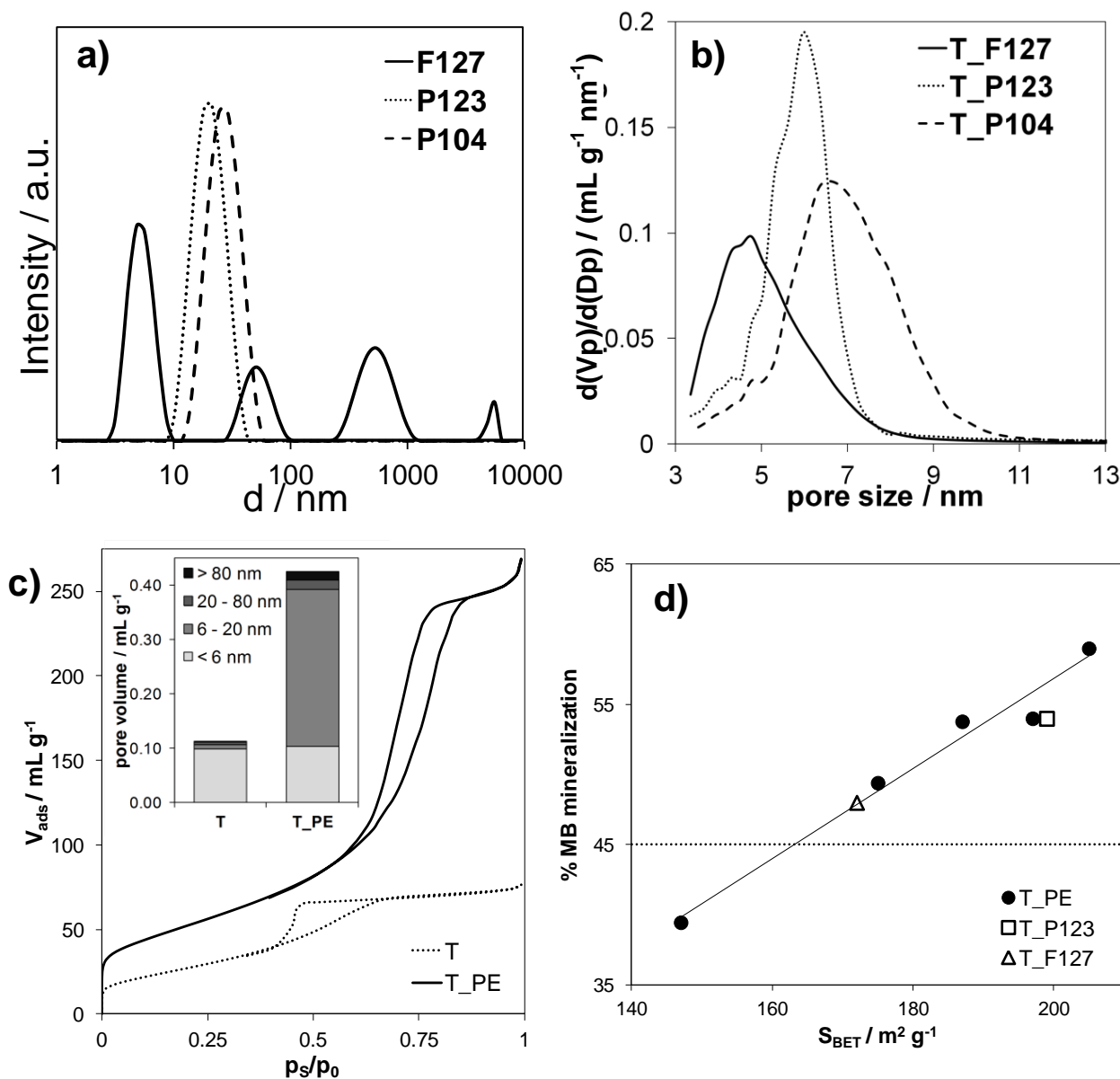
Figure 3 – **a**) Micelle size distribution by DLS for the three used block copolymers; **b**) Pore size distribution of the TiO_2 samples obtained using the three different templates; **c**) N_2 adsorption–desorption isotherms at subcritical temperatures of TiO_2 from a traditional sol-gel (T) and template-assisted synthesis (T_PE). Inset: Relative pore volume distribution of the two samples. **d**) Photocatalytic degradation of methylene blue by mesoporous samples: Mineralization degree is shown as a function of the surface area of the TiO_2 samples. The dotted line represents the mineralization degree obtained by reference sol-gel titania.

Another limitation of TiO_2 as photocatalyst is its low quantum yield. Among the factors that concur to reduce the titania photocatalytic efficiency, the recombination of photogenerated electrons

9

and holes plays a leading role by competing with the transfer of photogenerated charges to species adsorbed at the photocatalyst surface. Quantum yields could thus be improved by slowing down such recombination processes. The use of metal particles or mixed oxides with a suitable band structure has been proposed to slow down the recombination process. In fact, if the metal/second oxide has an available electronic level just below the conduction band of TiO_2, electrons photogenerated on TiO_2 are prompted to migrate to the metal/second oxide, thus enhancing the charge separation and slowing down the recombination process. Noble metals, such as Pt, have been extensively studied in the literature for this purpose and they have proven to be highly effective in enhancing the TiO_2 photocatalytic activity. In my work, Bi_2O_3 was investigated as a cheaper alternative to noble metals to enhance the photocatalytic performances of TiO_2. Bi_2O_3 is non-toxic and environmentally friendly material which, thanks to its band structure,[7] could trap photo-generated electrons, and thus improve the overall quantum efficiency of the material. Theoretical calculations have shown that the specific band structure of Bi_2O_3-TiO_2 could significantly improve the oxide photocatalytic efficiency.[8] In my study, Bi_2O_3 was allowed to form into the mesoporous network of TiO_2 samples obtained by surfactant template synthesis. The obtained materials were characterized by X-ray diffraction (XRD), N_2 adsorption at subcritical temperatures (BET), high resolution transmission microscopy (HRTEM), Fourier transform infrared (FTIR) spectroscopy, and zeta potential determinations, providing an insight into the composite structure and into the specificity of the Bi_2O_3-TiO_2 composites with respect to traditional sol-gel TiO_2 nanomaterials. All samples were tested for the photocatalytic degradation of methylene blue stains and of formic acid under dry and wet conditions, respectively. The presence of Bi promotes the photocatalytic activity of the final samples in both tested reactions. Photocurrent measurements of Bi_2O_3-TiO_2 composites were performed in order to assess any effect of the Bi addition on the fate of the photogenerated electron-hole pair (Figure 4a). The obtained results agree with the observed marked enhancement in photocatalytic activity of the Bi_2O_3-TiO_2 samples, showing an increased recombination time of photogenerated charges in Bi_2O_3-TiO_2 composites. This effect may be related to the finely dispersed nature of Bi_2O_3 within the mesoporous network of the TiO_2 scaffold (Figure 4b,c).
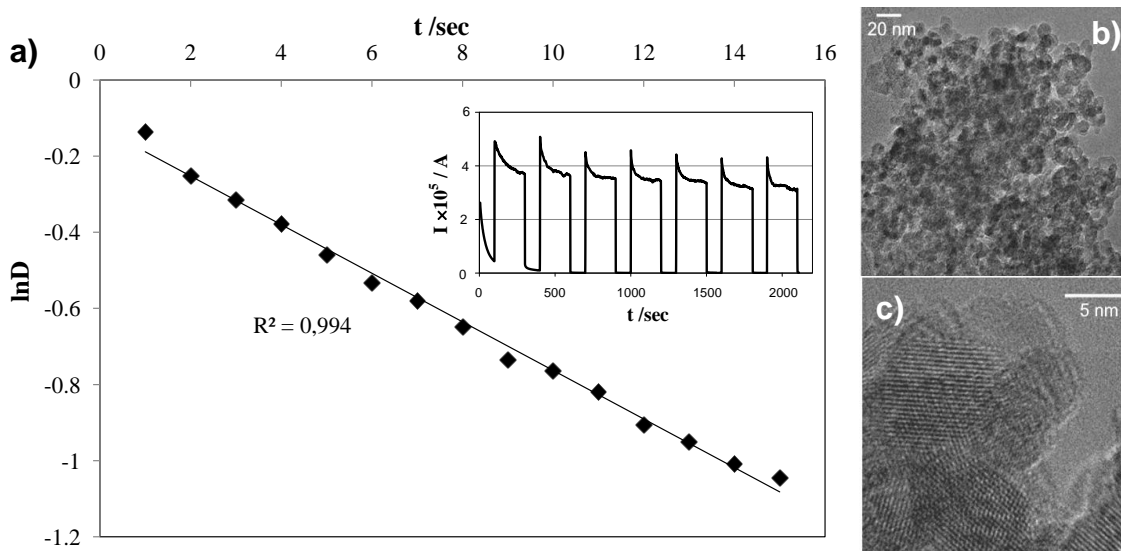
Figure 4 – **a**) lnD versus time plot ($D = \dfrac{I(t) - I(st)}{I(in) - I(st)}$) and photocurrent kinetic curve (inset) of Bi_2O_3-TiO_2 composites. **b,c**) HRTEM micrographs of Bi-promoted titania powders.

A crucial aspect that needs to be addressed for the commercial application of TiO_2 materials is their reusability, which is strictly connected to their efficiency in removing recalcitrant compounds. Real life effluents often contain a mixture of pollutants, some of which can be highly recalcitrant compounds. It has been observed that such recalcitrant pollutants or their degradation intermediates can strongly adsorb onto the TiO_2 surface, irreversibly poisoning the photocatalyst.[9] The deposition of titania particles in a thin layer is essential for the material applications because it simplifies the separation of the photocatalyst from the effluents and optimizes photon absorption. However, by reducing the available surface area, the deposition in films markedly increases the poisoning effects. A possible strategy to tackle this issue is the combination of photocatalysis with other oxidation techniques, in particular advanced oxidation techniques. In this thesis work, a combination of photocatalysis by TiO_2 films and ozonation treatments was studied to achieve the complete oxidation of highly recalcitrant pollutants such as bisphenol A and cumylphenol. A specific deposition procedure of the TiO_2 film onto a rough Al support was developed in order to obtain photocatalytic films with high surface area and good mechanical stability (Figure 5). Photocatalytic ozonation was compared to the separate photolytic, photocatalytic, and ozonation techniques to investigate the synergistic processes taking place in the combined treatment. The combination of the two treatments leads to synergistic effects that dramatically enhance the final mineralization of the pollutants. Moreover, the degradation pathway taking place during the photocatalytic ozonation of bisphenol A and 4-cumylphenol was studied by combining HPLC–MS determinations and FTIR analyses of the used catalyst.

11
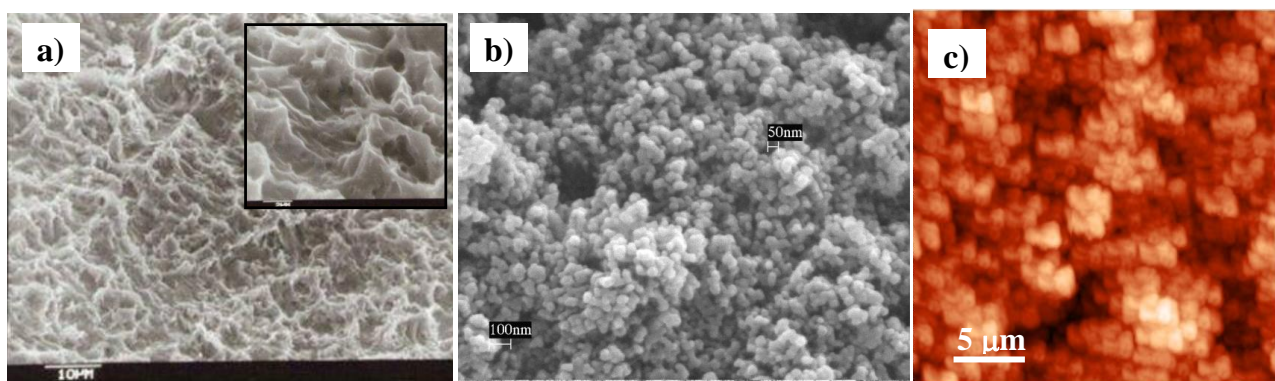
Figure 5 – SEM images of **a)** the roughened bare aluminium lamina and of **b)** the final TiO$_2$ layer. **c)** AFM image of the TiO$_2$ film.

The knowhow gained in the field of oxide synthesis and photocatalysis was then exploited in the development of oxide-based materials with tailored surface properties by means of surface functionalization with siloxanes. In recent years, hydrophobic modification of oxide surfaces has attracted growing attention[10,11] because of its vast technological relevance.[12-14] Siloxanes, compounds with the general formula R-(CH$_2$)$_n$-Si-(OR')$_3$, are among the functionalizing agents employed to modulate the surface energy, wettability and adhesion properties of oxides, thanks to their ability to form durable bonds with inorganic compounds, upon hydrolysis of labile –OR' groups. Furthermore, siloxanes may serve as robust coupling agents between organic materials and the oxide for the preparation of a new class of hybrid nanocomposites showing interesting photophysical properties and applications.[15]
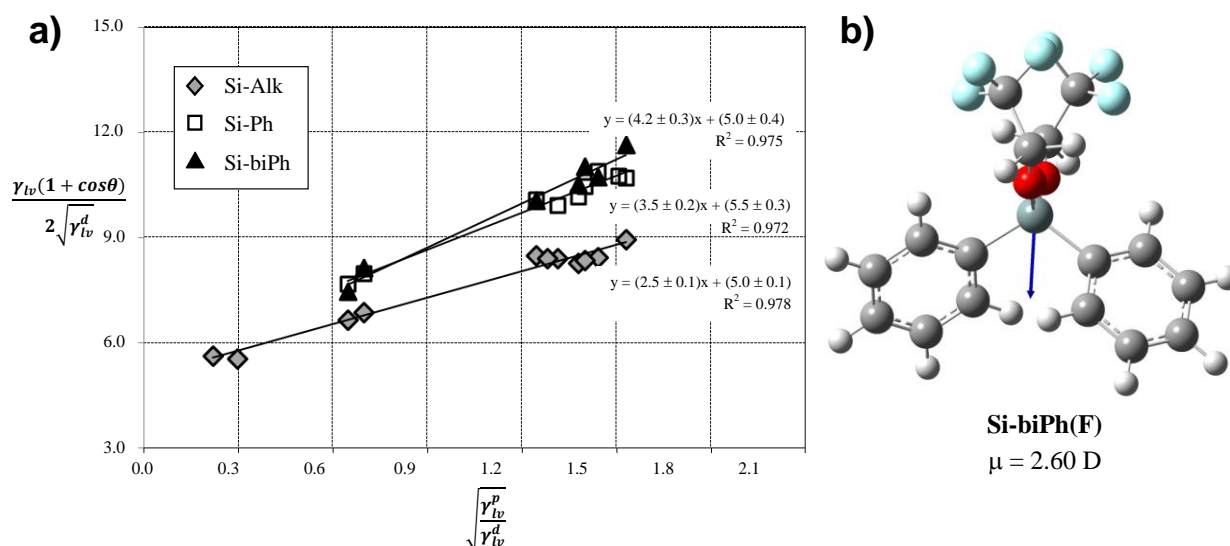
Figure 6 – **a**) Determination of surface energy components by Owens-Wendt-Rabel-Kaelbe method for different siloxane molecules; **b**) calculated dipole moment for diphenylbis-(trifluoroethoxy)silane.

Firstly, the role played by the structure of the siloxane molecule onto the wetting features of a smooth surface was investigated. The surface energy of different hydrophobing molecules, both

fluorinated and unfluorinated, deposited in smooth layers over an inert substrate, was determined by analyzing contact angle values with literature models (Figure 6a). The obtained values were compared with dipole moments determined by theoretical calculations employing semiempirical Hamiltonians (Figure 6b), finding a close correlation between the calculated dipole moments and the polar components of the surface energy.

Siloxanes were then employed to functionalize TiO_2 nanoparticles, in order to obtain rough composite films. The functionalization of nanometric TiO_2 with siloxanes is even more promising as it has lead to a series of applications uniquely related to the peculiar features of this oxide.[1] For instance, the photocatalytic activity of TiO_2 can be exploited to create hydrophobic/hydrophilic patterns by irradiating a siloxane-TiO_2 film with UV light through a suitable photomask, a procedure known as photocatalytic lithography.[16] The siloxane is photocatalytically degraded in the areas exposed to UV light, while the siloxane monolayer remains intact in the areas covered by the photomask. The resulting hydrophobic/hydrophilic pattern can be exploited in numerous applicative fields, for example to promote the site selective condensation of water from the gas phase or the site specific adsorption of hydrophilic/hydrophobic molecules. In this study, the TiO_2 surfaces functionalized by different siloxanes were tested in self-cleaning experiments (Figure 7a-d). Further, patterned structures with tunable hydrophobic and oleophobic patches were obtained by exploiting the photocatalytic activity of TiO_2 films. The resulting wetting contrast was exploited to obtain a site selective adsorption of a dye molecule (Figure 7e), with a procedure that can be adapted to the site selective deposition or growth of a large variety materials, such as semiconductor quantum dots, polymers or biological molecules.
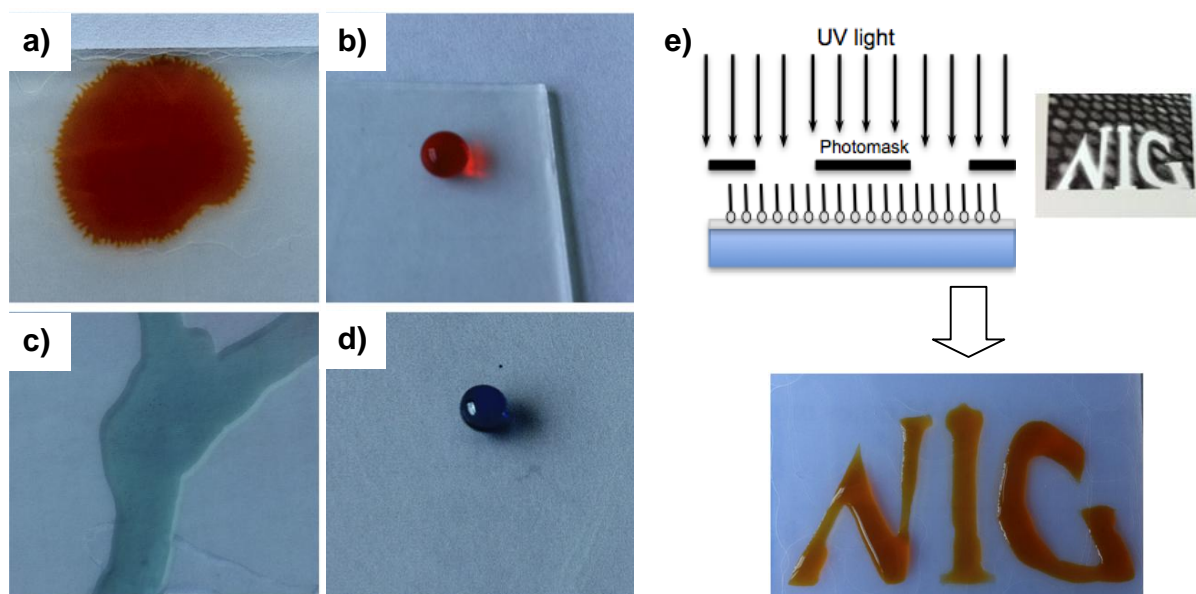

Figure 7 - Self-cleaning tests on (**a, c**) pristine TiO_2, and (**c, d**) TiO_2 coated with perfluorooctyl-triethoxysilane with respect to dye stains either dissolved in water (methyl orange) or non-aqueous solvent (methylene blue in CH_2I_2). **e**) Schematic representation of the

photocalatlytic lithography process: the logo of the group I belong to (NIG, Nanomaterials and Interfaces Group), was photocatalitically lithographed and revealed with an aqueous dye solution.

Notwithstanding the great interest and the manifold applications of these composite materials, the attachment of hydrophobizing molecules at TiO_2 surfaces still remains poorly understood at the molecular level and hardly discussed in the literature. My research activity was aimed at filling the gap by investigating the fundamental features of bonding and structure of the siloxane layers onto TiO_2 nanoparticle films. The influence of the siloxane amounts on the wettability (Figure 8a,b) and self-cleaning properties of TiO_2 was studied, together with the role played by the hydrophobing molecule structure (aliphatic vs. aromatic side-chain, linear vs. branched, length of the side-chain, fluorinated vs. un-fluorinated molecules). The studied siloxanes were both commercial and laboratory-made, the latter synthesized by the research group of Prof. Benaglia (Dipartimento di Chimica, Università di Milano). The modes of attachment of siloxane molecules at the TiO_2 surface were investigated by combining data of CP/MAS NMR with ATR-FTIR and XPS analyses, giving a detailed picture of the siloxane layer structure and interaction with the oxide (Figure 8c). It appears that the attachment modes of silicon, besides changing with the siloxane content of the surface, are markedly affected by the siloxane structure. For instance, alkyl trifunctional siloxanes give rise, starting for low oxide coverage (9 % w/w), to continuous functionalized layers in which silicon atoms are progressively bound by one, two, or three groups, these being either $-$ O–Ti or –O–Si (Figure 8c). These films are uniform and highly hydrophobic showing excellent self-cleaning properties at low contents; they present a Cassie-Baxter wetting behavior in which water drops float over a composite solid-gas carpet (Figure 8d). The substitution of the alkyl chain with aromatic end groups favors localization versus spreading for the siloxanes, due to π-π stacking interactions. In these cases, the films, which are locally ordered, are less uniform on the whole. The bifunctional biaryl compound gives rise to layers which are initially, i.e., at low coverage, hydrophilic and end up to be hydrophobic at higher coverage. These are characterized by patch-wise localizations producing a wettability in which the water drops spread following the surface rough profile (Figure 8e). Therefore, the structure of the siloxane appears to be a key parameter tuning the features of wettability of the surface by water.
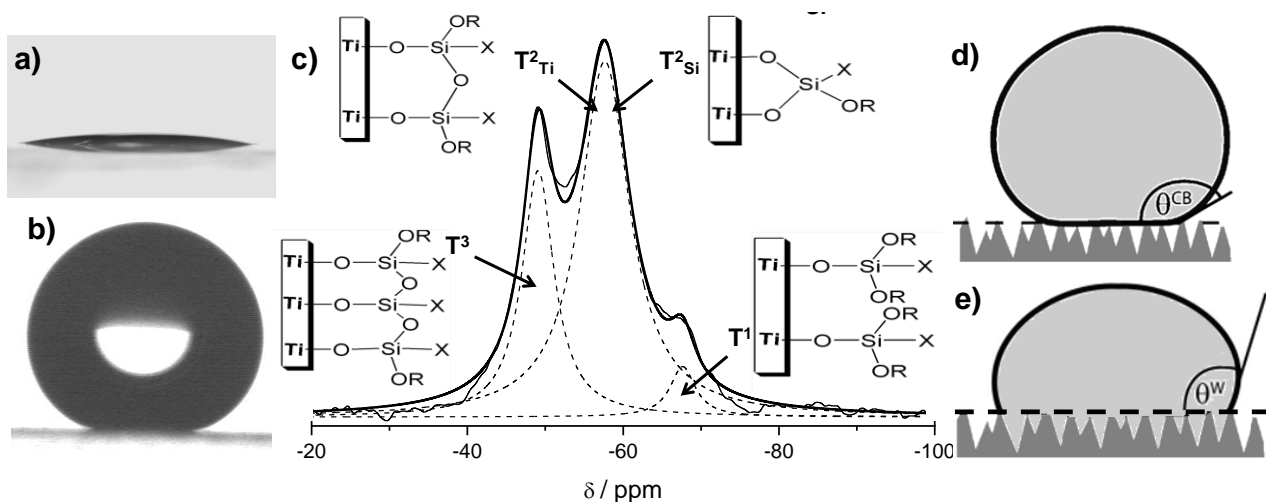
Figure 8 – Water contact angles of **a**) hydrophilic pristine TiO_2 film and **b**) superhydrophobic TiO_2 functionalized with siloxanes. **c**) ^{29}Si CP/MAS NMR of TiO_2 functionalized with octyltriethoxysilane, and the proposed attribution of the peak components with various attachment modes of siloxane molecules at the TiO_2 surface. **d,e**) The models describing wetting over rough surfaces: Cassie-Baxter (**d**) and Wenzel (**e**) models.

Siloxanes are employed not only to modulate the wettability of oxides, but they can be exploited as linkers to attach new functionalities, such as dyes, biological molecules, and nanoparticles, to the oxide surface.[17] By patterning the siloxane monolayer, a site-selective functionalization of the oxide surface can be obtained. Among the available patterning techniques, probe-based electro-oxidative lithography offers one of the best lateral resolution available (line width as narrow as 30 nm).[18] So far, this technique has been applied almost exclusively to Si substrates. In order to fully exploit this technique, its application to other technologically relevant substrates is required. In the present thesis, probe-based electrooxidative lithography of octadecyltrichlorosilane (OTS) monolayers adsorbed on TiO_2 and indium tin oxide (ITO) are reported for the first time. The conductivity of the layer and the environmental humidity are critical parameters, affecting the stability of the water meniscus between the probe and the substrate and thus the electro-oxidation process. The resulting surface functionalization was exploited to obtain the site selective growth of metal nanoparticles (Figure 9a,b). The electro-oxidation mechanism was studied by advanced characterization techniques such as Scanning Kelvin Probe Microscopy (SKPM) (Figure 9c,d), and the oxidation processes taking place on Si, ITO and TiO_2 were compared. For instance, in the case of OTS-ITO, a local overoxidation of the ITO substrate occurs simultaneously to the monolayer oxidation, whereas in OTS-TiO_2, no overoxidation of the oxide substrate takes place.
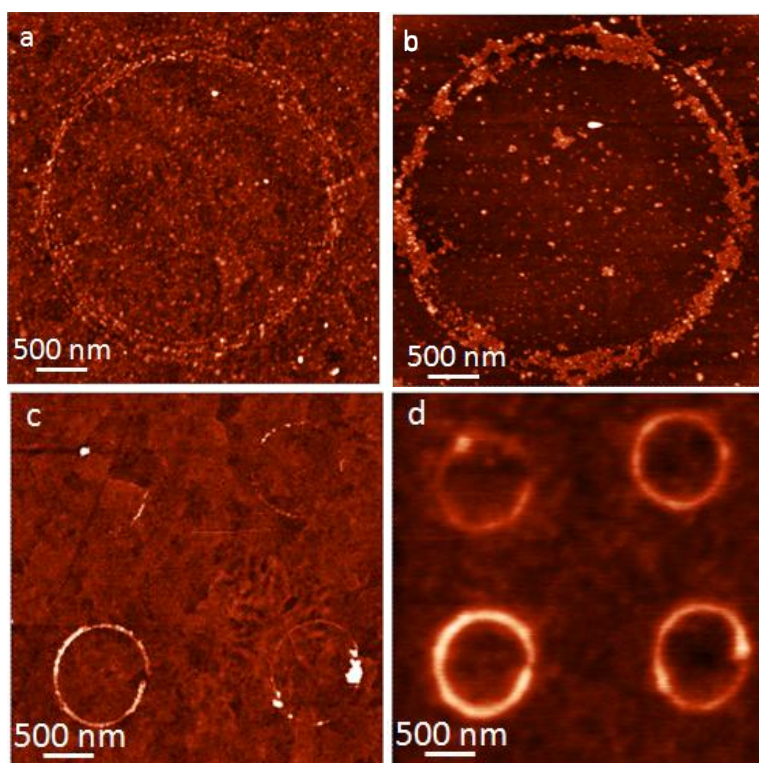
Figure 9 – AFM images for lithographed OTS-ITO before (**a**) and after (**c**) the site-selctive growth of Ag nanoparticles. **c**) AFM height and **d**) SPKM images of lithographed OTS-ITO.

This latter part of the work was carried out as collaboration between the group I belong to (Prof. Ardizzone's group of the Università degli Studi di Milano) and the group of Prof. Schubert of the Friedrich-Schiller Universität, Jena (Germany), where I spent a 5-month research period followed by several short stays.

References

1. Fujishima A., Zhang X., Tryk D.A. (2008) TiO$_2$ photocatalysis and related surface phenomena. Surface Science Reports 63:515-582.

2. Nakata K., Fujishima A. (2012) TiO$_2$ photocatalysis: Design and applications. Journal of Photochemistry and Photobiology C: Photochemistry Reviews 13:169–189.

3. Chen X., Mao S.S. (2007) Titanium Dioxide Nanomaterials: Synthesis, Properties, Modifications, and Applications. Chemical Reviews 107:2891-2959.

4. Carp O., Huisman C.L., Reller A. (2004) Photoinduced reactivity of titanium dioxide. Progress in Solid State Chemistry 32:33-177.

5. Ardizzone S., Bianchi C.L., Cappelletti G., Gialanella S., Pirola C., Ragaini V. (2007) Tailored Anatase/Brookite Nanocrystalline TiO_2. The Optimal Particle Features for Liquid and Gas-Phase Photocatalytic Reactions. Journal of Physical Chemistry C 111:13222-13231.

6. Ohtani B. (2008) Preparing Articles on Photocatalysis—Beyond the Illusions, Misconceptions, and Speculation. Chemistry Letters 37:217-229.

7. Bian Z.F., Zhu J., Wang S.H., Cao Y., Qian X.F., Li H.X. (2008) Self-assembly of active Bi_2O_3/TiO_2 visible photocatalyst with ordered mesoporous structure and highly crystallized anatase. Journal of Physical Chemistry C 112:6285-6262.

8. Long R., English N.J. (2009) Synergistic Effects of Bi/S Codoping on Visible Light-Activated Anatase TiO_2 Photocatalysts from First Principles. Journal of Physical Chemistry C 113:8373–8377.

9. Piera E., Ayllón J.A., Doménech X., Peral J. (2002) TiO_2 deactivation during gas-phase photocatalytic oxidation of ethanol. Catalysis Today 76:259–270.

10. Zhang X., Jin M., Liu Z., Nishimoto S., Murakami T., Fujishima A. (2007) Superhydrophobic TiO2 Surfaces. Preparation, Photocatalytic Wettablility Conversion and Superhydrophobic-Superhydrophilic Patterning. Journal of Physical Chemistry C 111:14521-14529.

11. Xu Q.F., Wang J.N., Sanderson K.D. (2010) OrganicInorganic Composite Nanocoatings with Superhydrophobicity, Good Transparency, and Thermal Stability. ACS Nano 4: 2201–2209

12. Manoudis P.N., Karapanagiotis I., Tsakalof A., Zuburtikudis I., Kolinkeovà B., Panayiotou C. (2009) Superhydrophobic films for the protection of outdoor cultural heritage assets. Applied Physics A 97:351-360.

13. Manoudis P.N., Karapanagiotis I., Tsakalof A., Zuburtikudis I., Panayiotou C. (2008) Superhydrophobic Composite Films Produced on Various Substrates. Langmuir 24:11225-11232.

14. Liaw W.-C., Chen K.-P. (2007) Preparation and characterization of poly(imide siloxane) (PIS)/titania(TiO_2) hybrid nanocomposites by sol–gel processes. European Polymer Journal 43: 2265-2278.

15. Haensch C., Hoeppener S., Schubert U.S. (2010) Chemical modification of self-assembled silane based monolayers by surface reactions. Chemical Society Reviews 39:2323–2334.

16. Paz Y. (2011) Self-assembled monolayers and titanium dioxide: From surface patterning to potential applications. Beilstein Journal of Nanotechnology 2:845–861.

17. Herzer N, Hoeppener S., Schubert U.S. (2010) Fabrication of patterned silane based self-assembled monolayers by photolithography and surface reactions on silicon-oxide substrates. Chemical Communications 46:5634–5652.

18. Wouters D., Hoeppener S., Schubert U.S. (2009) Local Probe Oxidation of Self-Assembled Monolayers: Templates for the Assembly of Functional Nanostructures. Angewandte Chemie International Edition 48:1732-1739.

Table of contents

1. Introduction

In recent years, photoactive semiconductors have received ever growing interest, as testified by the remarkable number of related publications [Fujishima2008], thanks to their promising applications in manifold fields such as environmental remediation and photovoltaics. Among the photoactive semiconductors, titanium dioxide has been by far the most investigated owing to its cheapness, non-toxicity and stability to photocorrosion [Nakata2012]. Titanium dioxide has been successfully applied to the photocatalytic remediation of air and water pollutants, H_2 production from water splitting, and in solar light harvesting using second generation solar cells; it is a biocompatible material, and it can be employed to obtain self-cleaning surfaces [Chen2007, Fujishima2008]. Although a few commercial applications employing nanometric TiO_2 are already on the market, many issues still remain to be addressed to obtain efficient, reliable and durable materials. Therefore, the present thesis work focuses onto the synthesis, characterization and post-synthetic functionalization of TiO_2 to improve the material properties for applications in photocatalysis and self-cleaning materials.

Photocatalytic oxidation of pollutants is one of the most promising technologies in environmental protection and remediation, especially for the removal of low concentration pollutants in slightly contaminated enclosed atmospheres [Carp2004]. Nanometric titania has been successfully applied to the photo-oxidation/reduction of numerous organic and inorganic pollutants, both in gaseous phase and in solution [Chen2007]. Several concretes and paintings containing nanometric titania that photo-oxidize pollutants are already on the market, but many disadvantages remain to be overcome in order to obtain commercially successful products. Hence, the first part of my research was directed towards the improvement of the photocatalytic activity of TiO_2 to obtain more efficient photocatalysts for the degradation of environmental pollutants. The photocatalytic activity of titania is strongly affected by its particles' physicochemical features, which, in their turn, are imposed by the synthetic path adopted for the material preparation [Ardizzone2007]. Therefore, it is essential to tailor the physicochemical characteristics of titania particles using an appropriate synthetic procedure in order to obtain highly active samples. A considerable part of my PhD project was devoted to the optimization of several synthetic procedures in order to produce TiO_2 powders and films with tailored optical, morphological and electronic features.

One of the main disadvantages of TiO_2 is its large band gap (3.2 eV for anatase, 3.0 eV for rutile), which corresponds to a light absorption in the UV region. Thus, currently TiO_2 based materials require UV irradiation in order to activate the photocatalytic process. As only 5% of solar light is in the UV region [Onthani2008], a shift towards visible absorption is required to improve

the photocatalytic activity of TiO_2 under solar irradiation. The introduction of non-metal ions in the TiO_2 lattice represents one of the most promising approaches to induce a bathochromic shift, *i.e.*, a shift of the absorption edge of TiO_2 to longer wavelengths, and consequently increase the photocatalytic response of doped samples into the visible region. Therefore, during my thesis, I synthesized several doped samples with non-metals such as N, in order to assess if a bathochromic shift effectively leads to a higher photocatalytic activity in the visible region and, more important, under solar irradiation. All the obtained samples were exhaustively characterized, in order to obtain a complete picture of the modifications induced in the titania structure and surface features by the modifications of the synthetic pathway. Samples were characterized under the structural, morphological, electrochemical, optical and compositional point of view. Moreover, other features, such as magnetic properties, were determined. The sample structure was elucidated not only by ordinary powder diffraction, but also by means of synchrotron radiation, using EXAFS to understand the position of dopant ions inside the TiO_2 crystal lattice.

Another limitation of TiO_2 as photocatalyst is that its quantum yields in photocatalytic oxidation are generally quite low (under UV irradiation, they range from 1% to over unity [Fujishima2008]). Among the factors that concur to reduce the titania photocatalytic efficiency, the recombination of photogenerated electrons and holes plays a leading role by competing with the transfer of photogenerated charges to species adsorbed at the photocatalyst surface. Quantum yields could thus be improved by slowing down such recombination processes. The use of mixed oxides or metal particles with a suitable band structure has been proposed to slow down the recombination process. In fact, if the metal/second oxide has a band just below the conduction band of TiO_2, electrons photogenerated on TiO_2 are prompted to migrate to the metal/second oxide, thus enhancing the charge separation and slowing down the recombination process. Noble metals, such as Pt, have been extensively studied in the literature for this purpose and they have proven to be highly effective in enhancing the TiO_2 photocatalytic activity. In my work, Bi_2O_3 is investigated as a cheaper alternative to noble metals to enhance the photocatalytic performances of TiO_2. Bi_2O_3 is non-toxic and environmentally friendly material which, thanks to its band structure [Bian2008], could trap photo-generated electrons, and thus improve the overall quantum efficiency of the material. Theoretical calculations have shown that the specific band structure of Bi_2O_3-TiO_2 [Long2009] could significantly improve the oxide photocatalytic efficiency. In my study, photocurrent measurements of Bi_2O_3-TiO_2 composites were performed in order to assess any effect of the Bi addition on the fate of the photogenerated electron-hole pair. The obtained results agree with the observed marked enhancement in photocatalytic activity of the Bi_2O_3-TiO_2 samples.

Another strategy to improve the photocatalytic activity of TiO_2 involves the enhancement of the adsorption and diffusion of pollutants onto TiO_2. In this respect, I investigated the effect of the modification of TiO_2 morphology to obtain mesoporosity via a template synthesis. Mesoporous materials have been consistently proposed to produce better performing catalysts in many fields of catalysis. Here, the morphologic features of titania particles were tailored by using soft templates, in order to obtain materials with a high degree of porosity in the mesoporosity range. A marked effect of the titania morphology on the photocatalytic activity was observed and significant improvements over commercial samples could be obtained.

A crucial aspect that needs to be addressed for titania commercial applications is the reusability of TiO_2 materials, which is strictly connected to their efficiency in removing recalcitrant compounds. Real life effluents often contain a mixture of pollutants, some of which can be highly recalcitrant compounds. It has been observed that such recalcitrant pollutants or their degradation intermediates can strongly adsorb onto the TiO_2 surface, irreversibly poisoning the photocatalyst [Piera2002]. The deposition of titania particles in a thin layer is essential for the material applications because it simplifies the separation of the photocatalyst from the effluents and optimizes photon absorption. However, by reducing the available surface area, the deposition in films markedly increases the poisoning effects. A possible strategy to tackle this issue is the combination of photocatalysis with other oxidation techniques, in particular advanced oxidation techniques. In this thesis work, a combination of photocatalysis and ozonation treatments was studied to achieve the complete oxidation of highly recalcitrant pollutants such as bisphenol A and cumylphenol. The combination of the two treatments leads to synergistic effects that dramatically enhance the final mineralization of the pollutants.

The knowhow gained in the field of oxide synthesis and photocatalysis was then exploited in the development of oxide-based materials with tailored surface properties by means of surface functionalization with siloxanes. In recent years, hydrophobic modification of oxide surfaces has attracted growing attention [Zhang2007, Xu2010] because of the fundamental role played by wetting phenomena in technological applications such as self-cleaning processes, the prevention of clotting in artificial blood vessels, or the protection of outdoor cultural heritage [Manoudis2009, Manoudis2008, Liaw2007]. Siloxanes, compounds with the general formula $R\text{-}(CH_2)_n\text{-}Si\text{-}(OR')_3$, are among the functionalizing agents employed to modulate the surface energy, wettability and self-lubricity of oxides, thanks to their ability to form durable bonds with inorganic compounds, upon hydrolysis of labile –OR' groups. Furthermore, siloxanes may serve as robust coupling agents between organic materials and the oxide for the preparation of a new class of hybrid nanocomposites showing interesting photophysical properties and applications [Herzer2010].

The functionalization of nanometric TiO_2 with siloxanes is even more promising as it has lead to a series of applications uniquely related to the peculiar features of this oxide [Nakata2012]. For instance, in the field of dye sensitized solar cells, functionalization of TiO_2 thin films with siloxane adsorbates has shown to be useful as a surface passivation technique that hinders recombination processes and improves the overall efficiency of light to electricity conversion [Lin2006]. The functionalization of mesoporous nanocrystalline TiO_2 with siloxane groups results in smaller dark currents and higher open circuit photovoltages [Morris2008]. Moreover, the photocatalytic activity of TiO_2 can be exploited to create hydrophobic/hydrophilic patterns by irradiating a siloxane-TiO_2 film with UV light through a suitable photomask, a procedure known as photocatalytic lithography [Paz2011]. The siloxane is photocatalytically degraded in the areas exposed to UV light, while the siloxane monolayer remains intact in the areas covered by the photomask. The resulting hydrophobic/hydrophilic pattern can be exploited in numerous applicative fields, for example to promote the site selective condensation of water from the gas phase or the site specific adsorption of hydrophilic/hydrophobic molecules.

Notwithstanding the great interest and the manifold applications of these composite materials, the attachment of hydrophobizing molecules at TiO_2 surfaces still remains poorly understood at the molecular level and hardly discussed in the literature. My research activity tried to fill the gap by investigating the fundamental features of bonding and structure of the siloxane layers onto TiO_2 nanoparticle films. The influence of the siloxane amounts on the wettability and self-cleaning properties of TiO_2 was studied, together with the role played by the hydrophobing molecule structure (aliphatic vs. aromatic side-chain, linear vs. branched, length of the side-chain, fluorinated vs. un-fluorinated molecules). The studied siloxanes were both commercial and laboratory-made, the latter synthesized by the research group of Prof. Benaglia (Dipartimento di Chimica, Università di Milano). The modes of attachment of siloxane molecules at the TiO_2 surface were investigated by combining data of CP/MAS NMR with ATR-FTIR and XPS analyses, giving a detailed picture of the siloxane layer structure and interaction with the oxide.

Siloxanes are employed not only to modulate the wettability of oxides, but they can be exploited as linkers to attach new functionalities, such as dyes, biological molecules, and nanoparticles, to the oxide surface [Haensch2010]. By patterning the siloxane monolayer, a site-selective functionalization of the oxide surface can be obtained. Among the available patterning techniques, probe-based electro-oxidative lithography offers one of the best lateral resolution available (line width as narrow as 30 nm) [Wouters2009]. So far, this technique has been applied almost exclusively to Si substrates. In order to fully exploit this technique, its application to other technologically relevant substrates is required. In the present thesis, probe-based electrooxidative

lithography of siloxane monolayers adsorbed on TiO_2 and ITO is reported for the first time. The resulting functionalization was exploited to obtain the site selective growth of metal nanoparticles. The electro-oxidation mechanism was studied by advanced characterization techniques such as Scanning Kelvin Probe Microscopy, and the oxidation processes taking place on Si, ITO and TiO_2 were compared. This part of the work was carried out as collaboration between the group I belong to (Nanomaterial and Interfaces Group of the Università degli Studi di Milano) and the group of Prof. Schubert of the Friedrich-Schiller Universität, Jena (Germany), where I spent a 6-month research period.

Photocatalytic applications of TiO$_2$

2.1 Introduction to TiO$_2$ photocatalysis

2.1.1 Structural properties of TiO$_2$

Titanium dioxide occurs in nature in three main polymorphs: anatase, rutile and brookite. Moreover, two additional high-pressure forms have been synthesized starting from rutile: TiO$_2$(II), which has the α-PbO$_2$ structure, and TiO$_2$(H) with the hollandite structure.

Rutile

Rutile is the most common natural TiO$_2$ polymorph: it is present as an accessory mineral in high-pressure and high-temperature metamorphic and igneous rocks. Rutile is the preferred polymorph of TiO$_2$ in such environments because it has the lowest molecular volume among the three polymorphs.

Rutile is a mineral with a very high refractive index (n$_0$ = 2,55 - 2,65; n$_e$ = 2,83 - 2,95 depending on the incident wavelength), thus it is largely used as white pigment. Rutile has a specific weight of 4.3 x 10^3 kg m^{-3}.

Rutile crystallizes in the tetragonal system (*P*4$_2$/*mmm* space group) with cell constants $a = b$ = 4.593 Å and c = 2.959 Å. Its structure is constituted by a distorted hcp lattice of O^{2-} ions, where Ti^{4+} cations occupy only half of the octahedral holes.
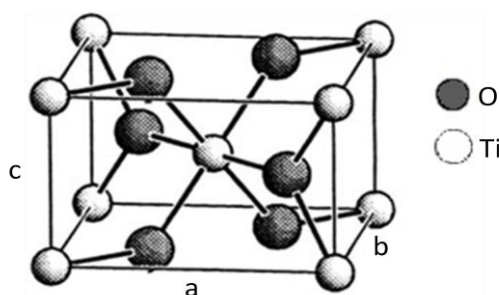
Figure 2.1.1 Rutile unit cell (a = b = 4,593 Å, c = 2,959 Å).

As it can be clearly seen from the image above, every titanium atom is surrounded by a slightly distorted octahedron of O^{2-} ions (Ti^{4+} coordination number = 6, O^{2-} coordination number = 3). The octahedron at the centre of the unit cell is differently oriented from octahedrons at the vertex of the unit cell (turned by 90°).

The rutile structure can be equivalently described in terms of a chain of octahedral units TiO$_6$. Every octahedron shares two opposite edges with neighbors, giving rows of octahedrons parallel to the [001] direction. Rows are connected along [110] directions through the vertex of the octahedron. Channels are created along [001] directions
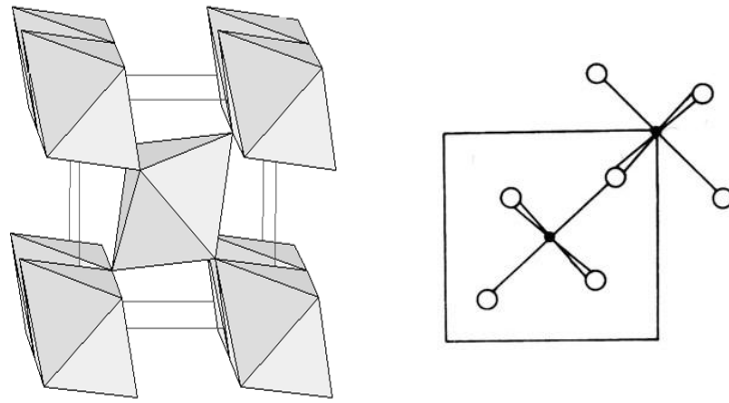
Figure 2.1.2 Rutile structure described in terms of chains of TiO$_6$ octahedrons.

Anatase

Anatase is usually found in nature in very small crystals with a very variable coloration (from blue to yellow), depending on the type of impurities. Its specific weight is 3.85 x 10^3 kg m^{-3}.

Anatase crystallizes in the tetragonal system (I4$_1$/*amd* space group) with cell constants $a = b$ = 3,785 Å, c = 9,514 Å. The unit cell contains 4 formula units instead of 2, which is the case of rutile.
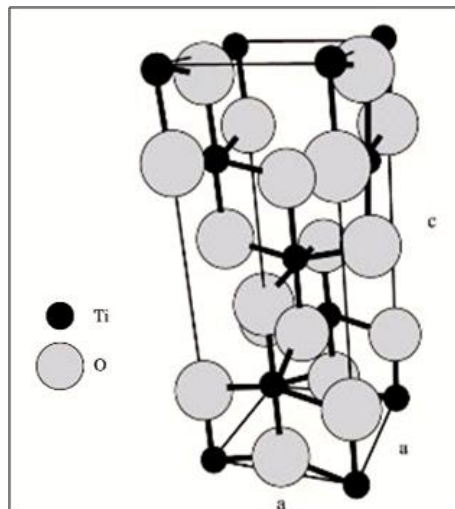
Figure 2.1.3 Anatase unit cell (a = b = 3,785 Å, c = 9,514 Å).

In the anatase structure, TiO$_6$ octahedrons are still present, even if they are much more distorted: every octahedron shares 4 edges and 4 corners with neighbors. This increases Ti-Ti distances and reduces O-O distances with respect to rutile.
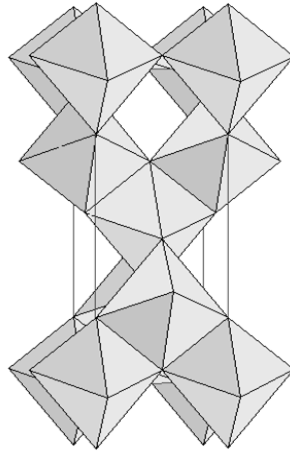
Figure 2.1.4 Anatase structure described in terms of chains of TiO_6 octahedrons.

The anatase structure is rich in channels. These holes are large enough to host either cations or anions that can be included in the structure at the synthesis stage.

Brookite

Brookite forms small tubular to platy crystals, with a color that varies from pink to brown. Its 4.1 x 10^{-3} kg m^{-3}.

Brookite is the TiO_2 polymorph with the greatest structural complexity. It crystallizes in the orthorhombic system (*Pbca* space group), with cell constants: a = 9,184 Å, b = 5,447 Å and, c = 5,145 Å. The unit cell contains 8 formula units.
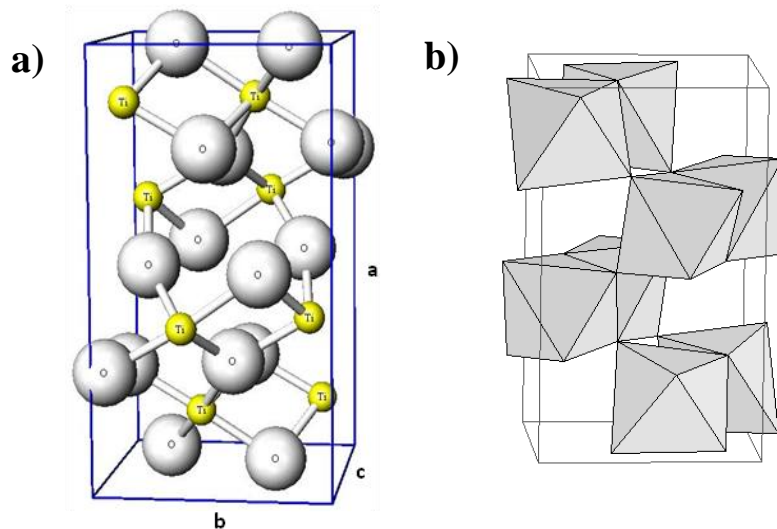
Figure 2.1.5 a) Brookite unit cell (a = 9,184 Å, b = 5,447 Å, c = 5,145 Å); b) Brookite structure described in terms of chains of TiO_6 octahedrons.

The TO_6 octahedrons are remarkably distorted: all distances between the atoms are different. Each TiO_6 octahedron shares three edges with the others. Small ions, for example H and Li, can be guests in the channels formed along the c axis ([001]) direction.

2.1.2 Photocatalytic properties of TiO$_2$

Basic principles of photocatalysis

Photocatalysis is a method to accelerate photochemical reactions by means of a catalyst activated by light irradiation. The light irradiation causes excitation of the system. The initial excitation is followed by an energetic and/or electronic transfer; the system relaxation leads to the chemical reaction [Linsebigler1995].

Semiconductors like TiO$_2$, ZnO, ZrO$_2$, SnO$_2$, CdS, ZnS, are typical heterogeneous photocatalysts. Their photocatalytic activity arises from their band structure, formed by two distinct electronic bands: the valence band (VB), at lower energy, and the conduction band (CB) at higher energy. The energetic gap between the valence and the conduction bands is called band gap E$_g$. In the case of TiO$_2$, the valence band has mainly a 2p–O character whereas the conduction band has mainly a 3d–Ti character [Fox1993].

The probability f that a certain energy level E is occupied at a certain absolute temperature T is given by the Fermi–Dirac distribution:

$$f(E) = \frac{1}{1 + e^{\frac{E - E_g}{k_B T}}}$$

with k$_B$ the Boltzmann constant. Thus, the width of the band gap determines the thermal population of the conduction band and, consequently, the electric conductivity of the semiconductor in its intrinsic (non-doped) state. At room temperature, undoped semiconductors with E$_g$ > 1.5 eV have an almost completely filled VB and an empty CB.

Compound	E$_g$ (eV)
PbS	0.37
Ge	0.67
Si	1.11
CdS	2.42
TiO$_2$	**3.2**
ZnO	3.2
ZnS	3.6

Table 2.1.1 Band gap values of some semiconductors at room temperature.

Electrons can be excited from the VB to the CB by light irradiation with $E \geq E_g$: the band gap determines which wavelength can be absorbed by the semiconductor. TiO_2, having a band gap larger than 3 eV (3.05 eV for rutile, 3.2 eV for anatase), absorbs in the UV region ($\lambda < 400$ nm for rutile, $\lambda < 410$ nm for anatase).

The initial process in photocatalysis is the generation of an electron-hole pair in the semiconductor, caused by the light-induced electron promotion from the VB to the CB (Figure 2.1.6). Unlike metals, semiconductors do not possess a continuum of interband energetic levels that can assist the e^--h^+ recombination. Thus, the e^--h^+ pair has a sufficient lifetime – in the order of nanoseconds – to allow the transfer of the photoexcited electron or hole to a reagent adsorbed at the catalyst surface. The process is called heterogeneous photocatalysis if the semiconductor remains intact and the charge transfer to the adsorbed species is continuous and exothermic.

The charge transfer happens at the surface of the photocatalyst. Therefore, electrons and holes must migrate to the semiconductor surface, where the electron can reduce an acceptor species (generally O_2 in an aerated environment) and the hole can combine with an electron released by the oxidation of a donor species. The interfacial charge transfer is more effective if reagents are pre-adsorbed on the photocatalyst surface. Often photogenerated holes h^+ combine with hydroxyl species adsorbed at the TiO_2 surface, giving rise to hydroxyl radicals, which are active intermediates in the oxidation of other substances.

Reductive processes
- **In aerated environments:**
  $O_2 + e^- \rightarrow {}^\cdot O_2^-$
- **Trapping of e^- at surface Ti:**
  $Ti^{4+} + e^- \rightarrow Ti^{3+}$

Oxidative processes
- **Hydroxyl radical generation:**
  $H_2O + h^+ \rightarrow {}^\cdot OH + H^+$
- **Direct oxidation of adsorbed species**
- **Trapping of h+ at surface hydroxyl group**
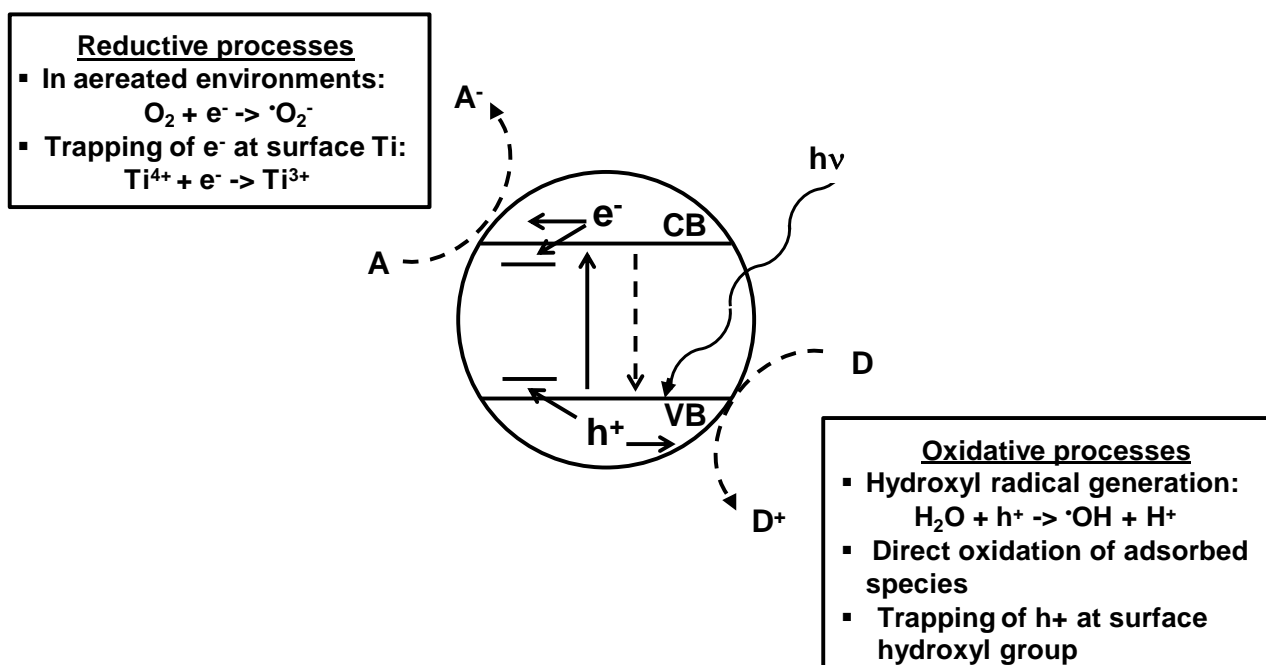
Figure 2.1.6 Scheme of redox reactions occurring during photocatalysis at a TiO_2 surface.

The probability and rate of the transfer process depend on the relative positions of valence and conduction bands with respect to the redox potentials of the adsorbed species. The redox

potential of the acceptor species should be less positive than the CB potential, whereas the redox potential of the donor species should be less negative than the VB potential. In fact, the driving force of the process is the energy difference between the semiconductor bands and the redox potential of the adsorbed species.

In the case of titania, the position of the top of the VB is ca. 3V vs. NHE (at pH 0), thus the potential of photogenerated holes is far more positive than that for oxidation of ordinary organic compounds. This is a characteristic of all metal oxides, i.e. they all have the same oxidation ability since the VBs of metal oxides are mainly composed of the same O 2p atomic orbitals, while the potential of the CB varies depending on the type of metal. However, titania has a much higher activity compared with that of other metal oxides. Ohtani [Ohtani2008] proposed a possible explanation of this phenomenon based on the higher ability of titania to reduce oxygen under photoirradiation. In fact, photocatalytic reactions must proceed with the consumption of the same numbers of photogenerated electrons and holes. Hence, photogenerated holes cannot be used unless photoexcited electrons are consumed. In other words, titania has sufficient ability for electron utilization to drive oxidation by photogenerated holes of high oxidation ability, while other metal oxides possess a low photocatalytic activity because of their low reduction ability even though they have high oxidation ability.

The charge transfer towards the adsorbed species competes with the e^--h^+ recombination process. The latter is a thermal disexcitation path that can happen both in the bulk and at the surface of the semiconductor particle. Thus, the efficiency of photocatalysis depends on the relative rates of the two competing processes and is expressed by the quantum yield. The quantum yield ϕ is the number of reaction events for every absorbed photon and is given by:

$$\phi = \frac{k_{CT}}{k_{CT} + k_R}$$

where k_{CT} is the charge transfer rate;

k_R is the e^--h^+ recombination rate.

(The measurement of the actual amount of absorbed light is very difficult in heterogeneous systems, because of scattering phenomena at the semiconductor surface [Loddo2006]. It is usually assumed that all the light is absorbed – apparent quantum yield.)

As the e^--h^+ recombination reduces the quantum yield, semiconductor surface modifications – such as addition of metals, dopants or combination with other semiconductors – are exploited to slow down the recombination rate. In fact, defects in the semiconductor surface are associated with superficial localized electronic states that can act like a trap for charge carriers. In this way, charge carriers remain blocked at the semiconductor surface, increasing the efficiency of the charge

transfer process. The role of defects in affecting the photocatalytic efficiency is a highly debated topic.

TiO₂ as a photocatalyst

Numerous semiconductors exhibit photocatalytic activity, but several other characteristics are required in order to obtain an efficient photocatalyst: stability under irradiation, high activity and absorbed wavelength compatible with the desired use. The most commonly studied photocatalysts are TiO_2, ZnO and CdS; TiO_2 is by far the most promising.

In fact, it conjugates a high photocatalytic activity to a good resistance to photocorrosion. Its main downside is its large band gap (3.2 eV for anatase and 3.0 eV for rutile) that corresponds to an absorption in the UV (λ < 390 nm for anatase, λ < 410 nm for rutile). This limits TiO_2 photocatalytic activity under solar irradiation, which is composed of UV rays by less than 5% [Ohtani2010].

Nonetheless, TiO_2 has plenty of applications in photocatalysis. Titania has been studied to catalyze several functional group transformations in organic molecules [Carp2004], like isomerizations, substitutions, condensations and polymerizations. However, the most important class of reactions photocatalyzed by TiO_2 is oxidation: virtually every organic functional group bearing a non-bonded lone pair of any π conjugation can be activated towards TiO_2 photocatalyzed oxidative reactivity, either by dehydrogenation, oxygenation or oxidative cleavage. A great advantage of photooxidation compared to catalyzed thermal oxidation is its better selectivity. Photocatalytic reductions are less frequently encountered than oxidations, because the reducing power of a CB electron is significantly lower than the oxidizing power of a VB hole and because most reducible substrates are overruled by O_2 in trapping photogenerated CB electrons. However, photocatalytic reduction by TiO2 has been successfully applied, in the presence of hole scavengers, to the reduction of metal pollutants, such as Cr(VI), in order to reduce their toxicity or their solubility [Cappelletti2008].

An important application exploiting the reduction power of photogenerated electrons is H_2 production by water photosplitting on TiO_2 electrodes. This phenomenon, discovered by Fujishima and Honda in 1972 [Fujishima1972], can be exploited to harvest the solar radiation, producing H_2 that can function as an energetic vector.

Present industrial applications of nanostructured titania are in the field of environmental remediation for both air and water. In fact, TiO_2 can photocatalyze the complete mineralization of several organic pollutants and is also effective in oxidizing inorganic pollutants such as NO_x, SO_2 and CO to less harmful species (NO_3^-, SO_4^{2-}, CO_3^{2-}…). This performance is attributed to either

direct oxidation by photo-generated highly oxidizing holes or mediated oxidation via hydroxyl radicals (HO$^{\bullet}$). The oxidizing potential of this radical is 2.80 V, being exceeded only by fluorine.

TiO_2 can therefore be exploited for pollutant removal from industrial wastewater, where it constitutes a valuable alternative to chemical oxidation because of its cheapness, non-toxicity and capability of extended use without substantial loss of photocatalytic activity. It can be also employed in air purification, because of its broad applicability to common, oxidizable air contaminants. Several TiO_2 based products are already on the market: concrete and paintings containing nanometric titania that photooxidize atmospheric pollutants and have antibacterial and self-cleaning properties.

Parameters that influence the photocatalytic activity of TiO$_2$

The photocatalytic activity of titania is strongly affected by the particles' physicochemical features, with respect to both structural and morphological characteristics: phase composition, degree of crystallinity, surface area, pore volume and pore size distribution, superficial hydration, surface charge, presence of dopants and impurities. These features are imposed by the synthetic path adopted for the material preparation.

One of the most critical parameters is the surface area: a higher surface area generally leads to a more active sample, because there is more available area for the reagent adsorption. A remarkable advantage of nanometric powders is their enormous specific surface, with values that can reach several hundreds of square meters per gram.

Particle size can also affect the electronic properties of materials. In fact, among the unique properties of nanomaterials, quantum confinement governs the movement of electrons and holes in semiconductor nanomaterials, and the size and geometry of the materials largely affect the transport properties related to phonons and photons [Chen2007]. However, in the case of titania, care must be taken in using terms such as quantum-size effect. The quantum-size effect occurs when the radius of a particle becomes smaller than its Bohr radius, causing the bottom of the CB and the top of the VB to shift in negative (higher electronic energy) and positive (lower electronic energy) directions, respectively, and thus in an expansion of the band gap. However, the Bohr radius for anatase particles and rutile particles was calculated to be 2.5 and 0.3 nm, respectively [Ohtani2010]. As crystalline titania particles are generally much larger than those sizes, any observed blue shift of the absorption edge might be related to the amorphous part of titania and not to the quantum-size effect.

Sample crystallinity is another important factor that influences photocatalytic activity. Defects are associated with localized electronic states that can act as traps for charge carriers. A high degree of crystallinity limits the number of localized states, increasing the conductivity of the

TiO$_2$ network and thus promoting its photocatalytic activity. The reduced activity of amorphous samples compared to crystalline ones may be explained on the ground of their decreased charge carrier mobility. On the other hand, surface imperfections increase the charge transfer efficiency by trapping electron and holes at the semiconductor surface, near the adsorbed species. Therefore, the introduction of surface modifications in highly crystalline samples appears desirable in order to improve the activity of titania particles.

Besides the degree of crystallinity, the phase composition plays a key role in determining the sample activity. Anatase polymorph is generally reported to show the highest activity in photocatalytic oxidation compared to brookite or rutile polymorphs. Several explanations are possible: a lower recombination rate of photogenerated electrons and holes [Yanagisawa1999], its slightly higher Fermi level or a higher surface density of hydroxyl groups [Bickley1991; Gerischer1992]. However, the precise reasons for differing activities have not been elucidated in detail [Fujishima2008].

Nonetheless, samples composed by several polymorphs often exhibit a higher activity compared to mono-phase ones. The increased efficiency may be due to a reduced recombination rate and to an extension of the energy range of photoexcitation. In fact, nanometric rutile absorbs in the visible region (which makes rutile look yellow) and combining it with anatase might increase the spectral response of the sample. In addition, the intimate mixing of the two phases might increase the charge separation efficiency because of interfacial charge transfer via the junction between the two phases.

Furthermore, a good surface hydroxylation is necessary to promote the oxide wettability and the interfacial reactivity. In fact, hydroxyl radicals, generated by the reaction between photogenerated holes in the valence band with hydroxyl species adsorbed at the TiO$_2$ surface, are important intermediates involved in photooxidation.

However, the photocatalytic response of TiO$_2$ crystals appears to be the result of a complex balance between the nature of the adsorbing molecule and the relevant particle physicochemical features. A certain physicochemical parameter may have a different importance in affecting the sample activity depending on the nature of the adsorbing molecule [Ardizzone2007].

Current limitations of TiO$_2$ as photocatalyst

As discussed in the introduction, TiO$_2$ photocatalysis has currently several shortcomings that hinder its application. Titania main disadvantage is its large band gap that prevents an efficient exploitation of solar light to activate the photocatalytic process. Another drawback is the low photocatalytic efficiency that is limited by the process of recombination of photogenerated charges.

Another issue for titania application is the reusability of the photocatalyst and its application to real life effluents containing high concentrations of recalcitrant pollutants.

These problems and strategies proposed to their solution are presented in the detail in the following sections.

2.2 Combination of photocatalysis and other advanced oxidation techniques

Conventional water and wastewater treatments have proven inefficient for the substantial removal of several pollutants from industrial and urban effluents. Photocatalysis with TiO_2 powders has emerged as an alternative technique for the degradation of such recalcitrant compounds thanks to the high oxidizing potential of photogenerated holes (ca. 3 V vs. NHE at pH 0 [Ohntani2008]) and hydroxyl radicals generated upon irradiation of the photocatalyst.

The application of photocatalysis to real life effluents requires the immobilization of TiO_2 particles into films. In fact, the use of suspended powders presents several disadvantages. A more powerful light source is required because the cloudiness of the slurry reduces the amount of light effectively absorbed by the photocatalyst [Bai2010]. Furthermore, a lengthy and highly expensive filtration step is needed to separate the photocatalyst from the reacting suspension at the end of the photocatalytic process. However, the deposition of photocatalyst powders in films reduces the surface area available for pollutant adsorption, thus curbing the removal efficiency and increasing the reaction time required to achieve a complete pollutant degradation. This could lead to poisoning effects that can affect the lifetime and reusability of the photocatalyst.

In order to improve the degradation efficiency towards highly recalcitrant pollutants, photocatalysis using TiO_2 films can be combined with other Advanced Oxidation Processes (AOPs). AOPs are a class of techniques based on the in situ generation of extremely oxidant hydroxyl radical species [Agustina2005; Augugliaro2006]. The most commonly investigated AOPs are oxidation by ozone [Gultekin2007], ultrasounds [Bremner2008], and electrochemical methods [Fierro2010], photolysis and photocatalysis [Cappelletti2008], Fenton and photo-Fenton processes [Bremner2009]. Previous studies proved that the combination of different AOPs can synergically enhance the overall degradation of several pollutants [Agustina et al. 2005; Augugliaro et al. 2006]. Thus, the combination of photocatalysis by TiO_2 films and other AOPs represents a promising technique to promote the degradation of highly recalcitrant pollutants while preserving the activity of the photocatalyst.

An important class of highly recalcitrant pollutants is that of Endocrine Disrupting Compounds (EDCs), such as bisphenols, alkylphenols, and phthalates. These compounds possess a high resistance to traditional wastewater treatments and have an almost ubiquitous environmental distribution. Moreover, their health effects have raised growing concerns since several alkylphenols are able to interfere with animal and human endocrine systems [Gultekin2007]. Health concerns are

increased by the fact that alkylphenols, being hydrophobic substances, tend to bioaccumulate in lipids of living organisms [Biggers2004]. Bisphenol A (BPA) and 4-Cumylphenol (4-CP) (Figure 2.2.1) have been recognized as two of the most relevant pollutants of the alkylphenol family, so much so that they are among the EDCs routinely tested in water samples. They are released in the environment from a wide range of anthropogenic sources and possess a very low biodegradability [Gultekin2007, Biggers2004]. As a consequence, their environmental concentrations and distribution are on the rise.
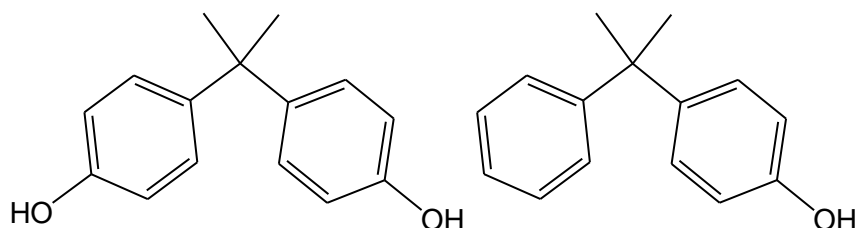
Figure 2.2.1 Chemical structure of bisphenol A (left) and 4-cumylphenol (right).

Conventional wastewater treatments and single AOPs have only a limited efficiency towards EDC removal. For instance, ozonation generally produces a fast degradation of BPA, but a significant mineralization of the pollutant rarely occurs because of the formation of stable by-products [Garoma2009], which exert an endocrine activity even higher than that of the parent compound [Alum2004]. With respect to other AOPs, photocatalysis by TiO_2 leads to a complete BPA mineralization, even if the degradation takes place over long or very long reaction times [Wang2002]. Therefore, the coupling of ozonation and photocatalysis by TiO_2 (photocatalytic ozonation) could represent a promising combined method for a fast and complete mineralization of EDCs. Indeed, the two techniques appear to be highly complementary and their combination has a plant scale feasibility.

So far, the application of combined AOPs to the EDC removal has been scantly investigated [Guo2009; Rivas2009; Torres-Palma2010]. In this study, single (ozonation, photolysis, photocatalysis by TiO_2 films) and combined (photocatalytic ozonation) AOPs were tested for their ability to mineralize BPA and 4-CP. Although the degradation of BPA by single AOPs has been extensively studied, only few studies focus on the application of combined AOPs to BPA mineralization and they generally employ TiO_2 slurries instead of films [Rivas2009; Oyama2009]. Instead, no previous study could be found in the literature concerning the application of AOPs, neither single or combined, to the degradation of 4-CP. In this study, photocatalytic ozonation was compared to the separate photolytic, photocatalytic, and ozonation techniques to investigate the synergistic processes taking place in the combined treatment. Moreover, the degradation pathways

taking place during the photocatalytic ozonation of BPA and 4-CP were studied by combining HPLC–MS determinations and FTIR analyses of the used photocatalyst.

Experimental section

All chemicals were of the highest purity available and were used as received without further purification. Water purified by a Milli-Q apparatus (Millipore) was used to prepare solutions and suspensions.

Film deposition. The support for the film deposition was an aluminium lamina (geometric area: 85 cm^2), previously sand blasted and etched in oxalic acid 10%. The used photocatalyst was a well-known commercial TiO$_2$ powder, Degussa P25 (anatase–rutile composite 75 : 25, specific surface area 50 m^2 g^{-1}). The TiO$_2$ powder (0.2 g) was suspended in a solution of sodium dodecyl sulphate in 2-propanol (10^{-3} mol L^{-1}). The suspension was drop casted onto both sides of the aluminum lamina. After solvent evaporation, the film was calcined in air at 573 K for 2h.

Film characterization. The morphology of the Al lamina and TiO$_2$ films was characterized by Scanning Electron Microscopy (SEM), using a LEO 1430 (Zeiss), equipped with energy-dispersive X-ray spectroscopy (EDX). Moreover, Atomic Force Microscopy (AFM) images of the TiO$_2$ films were acquired by a NT-MDT Solver PRO-M.

Degradation tests. Degradation experiments were performed at 25 °C and at spontaneous pH using the experimental set-up showed in Figure 2.2.2. A 600 mL cylindrical jacketed glass reactor was utilized.
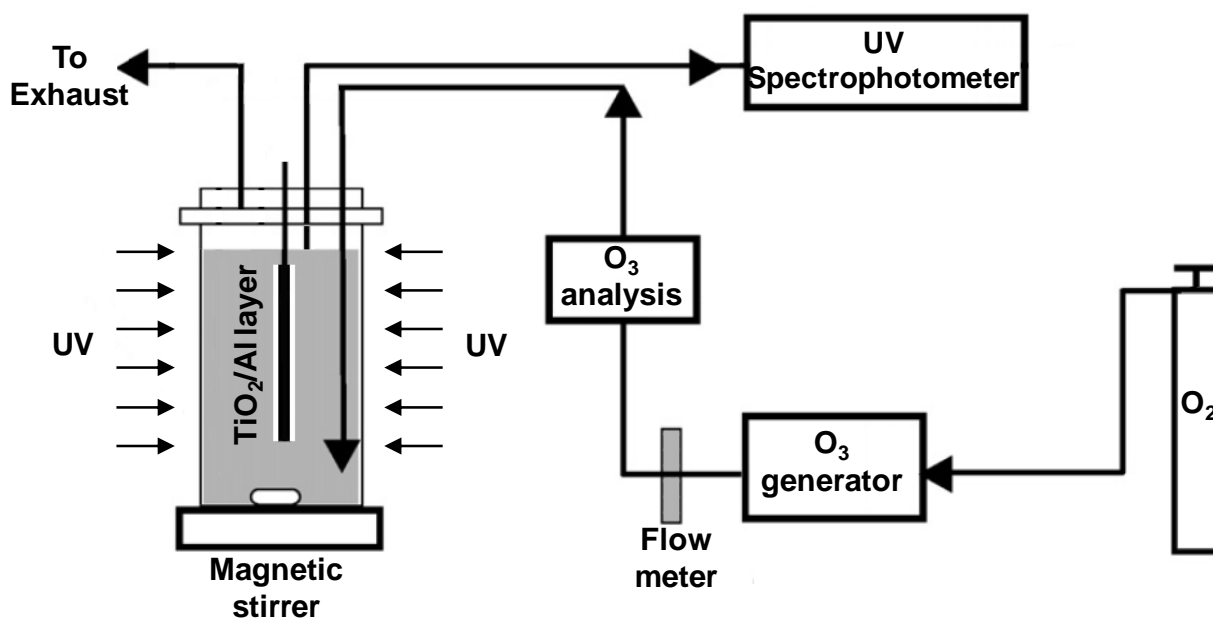
Figure 2.2.2 – Photocatalytic set-up.

The ozone feed required for ozonation and photocatalytic ozonation tests, was produced from pure oxygen by an ozone generator (Ozono Elettronica Internazionale S.r.l.). During

photocatalytic ozonation, the O_3 feed was started 90 min before switching the lamp on to allow a complete ozone solubilization. An ozone flow rate of 30 L h^{-1} was kept during the entire duration of the degradation test to maintain a constant dissolved O_3 concentration of 3 mg L^{-1} (determined by iodometric analyses).

Photolysis, photocatalysis and photocatalytic ozonation tests were performed under UV-A irradiation, provided by two iron halogenide lamps (Jelosil HG 500, wavelength range 315-400 nm). The actual irradiation intensity inside the Pyrex jacketed glass reactor was 27 mW cm^{-2}, measured by Thorlabs S314C.

During photocatalysis and photocatalytic ozonation, the employed photocatalyst was the previously described TiO_2 layer supported on Al.

The target compound was either 4-Cumylphenol (4-CP) or bisphenol A (BPA) (Sigma-Aldrich). The initial pollutant concentration was varied in the range 0.2 - 0.4 mM for 4-CP and 0.1– 1.5 mM for BPA.

The progressive disappearance of the pollutant (either 4-CP or BPA) was monitored by measuring the absorbance at 275 nm using a UV-visible spectrophotometer (Beckman DU 640). In the case of 4-CP, the mineralization degree was determined by means of chemical oxygen demand (COD) analysis kit (Spectroquant Merck), using the following equation:

$$\% \text{ mineralization} = \frac{COD_0 - COD_t}{COD_0}$$

where COD_0 and COD_t are the initial COD value and the COD at time "t", respectively. In the case of BPA, the mineralization degree was monitored by Total Organic Carbon (TOC) analyses, adapting the equation reported for 4-CP.

Blank tests were performed using pure oxygen instead of O_3: No significant improvement was observed with respect to plain photocatalysis.

Determination of the degradation intermediates. The degradation mechanisms of the two pollutants during photocatalytic ozonation were studied by combining High Performance Liquid Chromatography-Mass Spectrometry (HPLC/MS) determinations on solutions sampled at different reaction times and Attenuated Total Reflectance Fourier Transform Infrared Spectroscopy (ATR-FTIR) analyses of the used catalyst at the end of the reaction.

The HPLC/MS analyses were performed using an Agilent 1100 chromatographic system (quaternary pump, autosampler, thermostated column holder) equipped with a diode array detector and a Bruker ion-trap Esquire 3000+. The column was a Supelco Ascentis-Express (50 x 4.6 mm, 2.7 μm). A two phase mixture was used as the mobile phase with a flow-rate of 1 mL min^{-1} in gradient mode. Phase A was Milli-Q water containing 0.05 % (v/v) TFA or 10 mM ammonium

acetate in the case of ESI+ or ESI- respectively; phase B was Acetonitrile (LC-MS grade), containing 0.05 % TFA only in the case of ESI+. The adopted gradient was the following: from 5 % B to 95 % B in 6 min, washing at 100 % B for 1 min, equilibration at 5 % B in the next 3 min. Peak UV detection was carried out at 220 and 254 nm (reference at 500 nm, 40 nm bandwith). Mass spectrometry was performed with an electrospray ionization (ESI) source in either positive or negative mode with the following parameters: detection in the 50-2000 m/z range with alternating MS/MS, capillary voltage $\pm$ 3500 V, drying gas temperature 365 °C, nebulizer pressure 50 psi, drying gas flow 10 L min^{-1}. The other tuning parameters were optimized with the standard tuning mix provided by Bruker for a generic detection in the above mass range.

A FTIR (Jasco 4200) accessorized with an ATR module, was used to study the chemical structure of organic species adsorbed on the used TiO_2 surface.

Results and discussion

Film deposition. The adopted deposition procedure allowed us to obtain photocatalytic films with high surface area and good mechanical robustness.

The employed substrate was an Al lamina, owing to its cheapness and reusability. Moreover, its Al_2O_3 native oxide enhances the adhesion of the titania particles to the metallic support. The surface roughness of the aluminum support was purposely increased by sand blasting and etching in oxalic acid 10%, in order to increase the available surface area.

The adopted photocatalyst was a commercial titania powder, Degussa P25, a benchmark photocatalyst commonly used in the literature. Films were deposited by drop-casting from a titania suspension. The film homogeneity was improved by adding sodium dodecyl sulphate as a stabilizer to the TiO_2 suspension. The film annealing served the double purpose of removing the surfactant and improving the adhesion between the TiO_2 particles and the substrate.

The resulting films exhibit an excellent mechanical robustness: No particle release was ever observed during photocatalytic tests, nor appreciable weight variation of the coated Al laminas was observed after the degradation experiments. Furthermore, the films present a high surface roughness, which in turn increases the available surface area for pollutant adsorption. Figure 2.2.3 reports SEM and AFM images of the bare aluminum support and of the TiO_2 film. The aluminum lamina after the sand abrasion and chemical etching presents high roughness on the micron scale (Figure 2.2.3a). After coating with TiO_2, a homogeneous distribution of spherical aggregates without cracks and cleavages is appreciable (Figure 2.2.3b). AFM images of the coated substrate (Figure 2.2.3c,d) show an average roughness in the range 0–200 nm.
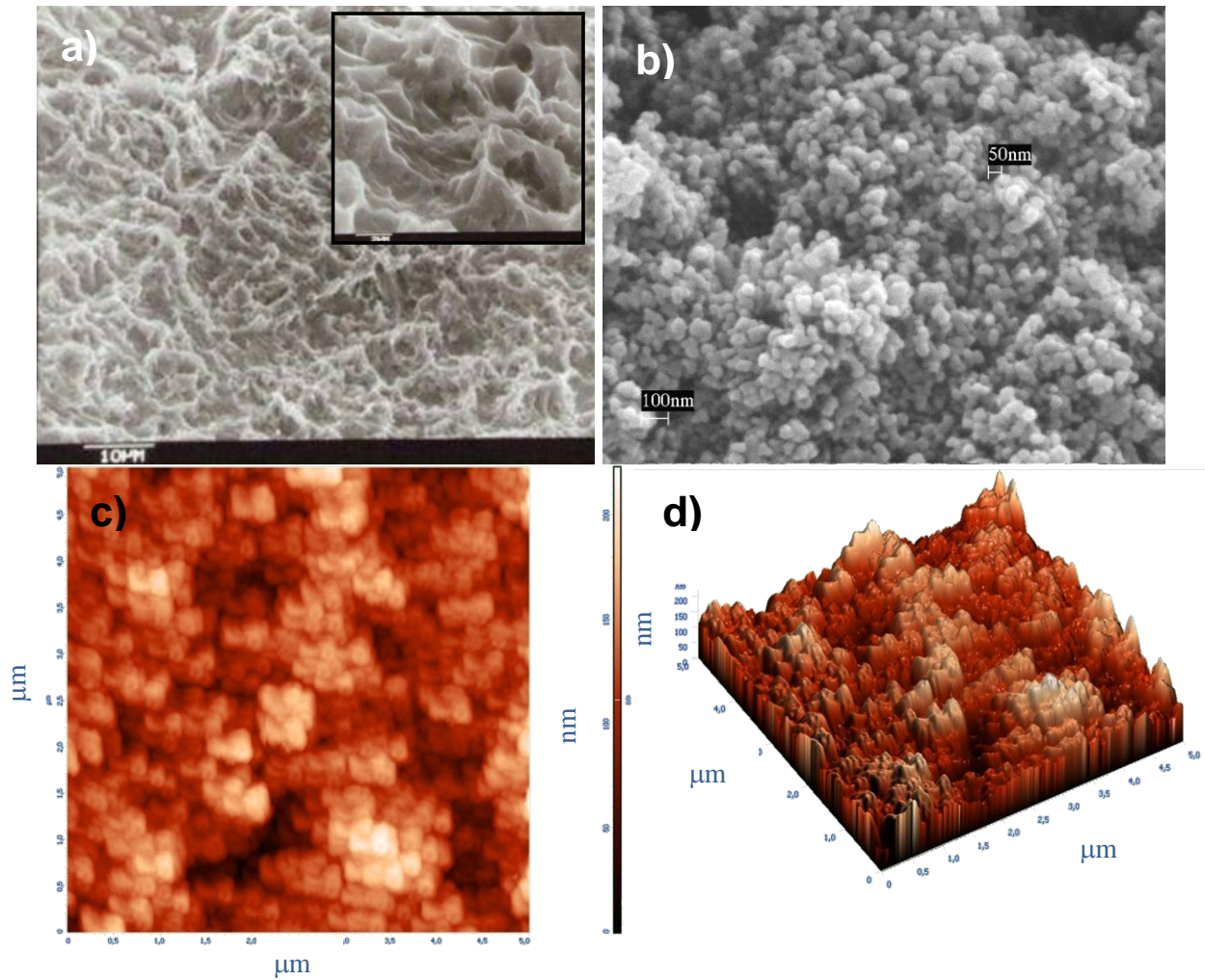
Figure 2.2.3 SEM images of a) the bare aluminum lamina after the surface treatments and of b) the final TiO$_2$ layer. AFM 2D (c) and 3D (d) images of the TiO$_2$ film.

A semi-quantitative elemental analysis of TiO$_2$ films was performed by EDX. EDX spectra (Figure 2.2.4) reveal the presence of low percentages (ca. 1%) of Al in the TiO$_2$ film, which can derive from the thermal diffusion of Al ions from the native Al$_2$O$_3$ layer into the titania film.
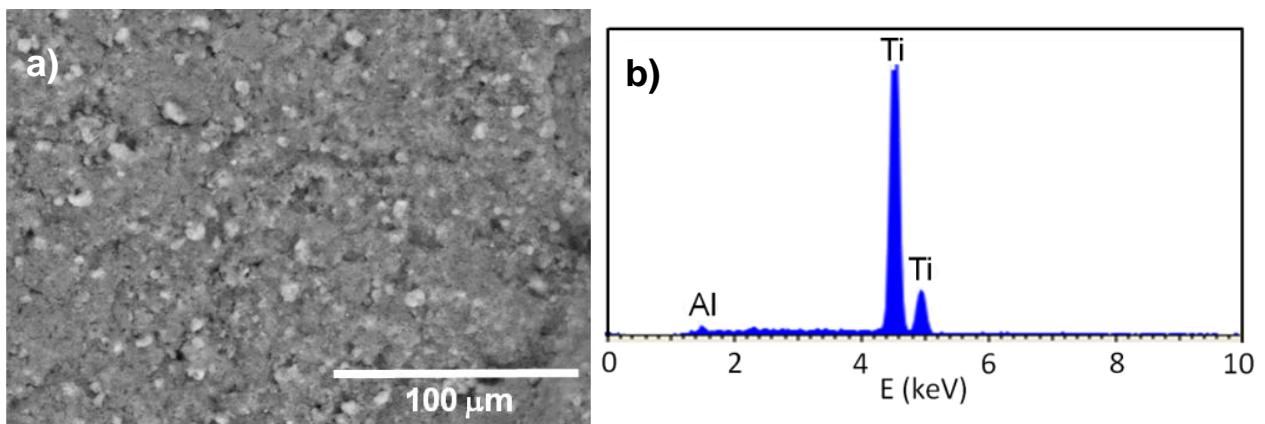
Figure 6.2.4 a) SEM image of the Al-supported TiO$_2$ film and b) the relative EDX spectrum.

Degradation tests. Photolysis (UV), TiO_2 photocatalysis (TiO_2 + UV), and ozonation (O_3) were first tested independently and then in combination to study their efficiency in BPA and 4-CP removal.

Table 2.2.1 reports the mineralization degree obtained at the end of the treatment (t_{fin} = 90 min) by the different separate and combined tests in the case of BPA degradation. Both ozonation and photocatalysis produce little mineralization (about 6%), while UV light irradiation resulted in no appreciable mineralization.

Test		BPA % mineralization	S
Separate AOPs	*photolysis (UV)*	–	–
	photocatalysis (TiO_2 + UV)	6	–
	ozonation (O_3)	6	–
Combined AOPs	O_3 + UV	13	1.2
	O_3 +TiO_2	15	1.5
	O_3 + TiO_2 + UV	55	4.1

Table 2.2.1 Mineralization degree of the separate and combined AOPs for the degradation of BPA. In combined tests, the mineralization percentage due to the O_3 pretreatment has been subtracted. Synergy parameter (S) for combined experiments. $[BPA]_0$ = 0.3 mM, $[O_3]$ = 3 mg L^{-1}, t_{fin} = 90 min.

As for the combined processes, both the addition of the TiO_2 layer to the O_3 treatment in the dark (O_3 +TiO_2) and the concurrence of UV irradiation and O_3 (O_3 + UV) does not significantly enhance BPA mineralization (Table 2.2.1). A previous study by Rivas et al. [Rivas2009] found a synergistic effect of the combined UV light and O_3, but in that study a UV-C irradiation was used. It is in fact known that UV-C (λ < 300 nm) can photolyze O_3 to O (1D) species, which in their turn can form $^{\bullet}$OH radicals, thus increasing the degradation efficiency. Instead, when near UV irradiation is employed, like in this study, ozone photolysis generates the much less reactive H_2O_2 [Augugliaro2006].

Photocatalytic ozonation (O_3 + TiO_2 + UV) is by far the most efficient removal treatment, resulting in a final mineralization of more than 50% for a BPA initial concentration of 0.3 mM.

In order to verify if any synergistic effect was taking place during the combined treatments, a synergy parameter (S) was calculated by adapting the equation proposed by Torres et al. [Torres2008] for a different combined AOP:

$$S = \frac{\% \, min_{combined}}{\sum \% \, min_{independent}} = \frac{\% \, min_{combined}}{\% \, min_{UV} + \% \, min_{ozone} + \% \, min_{photocatal}}$$

where $\% min_{combined}$ corresponds to the mineralization percentage (or removed TOC) at the end of combined treatment, from which the mineralization due to the initial ozonation step (6%) have been subtracted; $\% min_{UV}$, $\% min_{ozone}$, and $\% min_{photocatal}$ represent instead the TOC removed by the independent photolysis, ozonation, and photocatalysis, respectively. If S is equal to 1, only additive effects take place, whereas S values higher or lower than 1 indicate the occurrence of synergistic or antagonistic effects, respectively, among the AOPs.

Table 2.2.1 (4th column) reports the calculated S values for the tested combined processes. The combination of O_3 either with UV irradiation or with TiO_2 in the dark results in S values close to the unity, evidencing the occurrence of mere additive effects. Instead, the combination of ozone and TiO_2 photocatalysis ($O_3 + TiO_2 + UV$) gives a calculated S value of 4.1, which highlights the occurrence of relevant synergistic effects among the involved AOPs. The observed synergistic mineralization can be traced back to the manifold interactions taking place between O_3 and the TiO_2 surface. Indeed, ozone could decompose at the TiO_2 surface leading to the formation of active oxidizing species, such as $^\bullet OH$ and $^\bullet OOH$. Further, O_3 may act as a more efficient electron scavenger for photogenerated electrons than O_2, thus slowing down the recombination between photogenerated charges and increasing the photocatalytic quantum efficiency. In addition, the electron transfer from TiO_2 to O_3 generates one $^\bullet OH$ radical for each transferred electron through the formation of ozonide radicals [Augugliaro2006; Addamo2005].

The most efficient treatment, photocatalytic ozonation, was carried out on several initial BPA concentrations, in the range 0.1–0.8 mM (Figure 2.2.5).
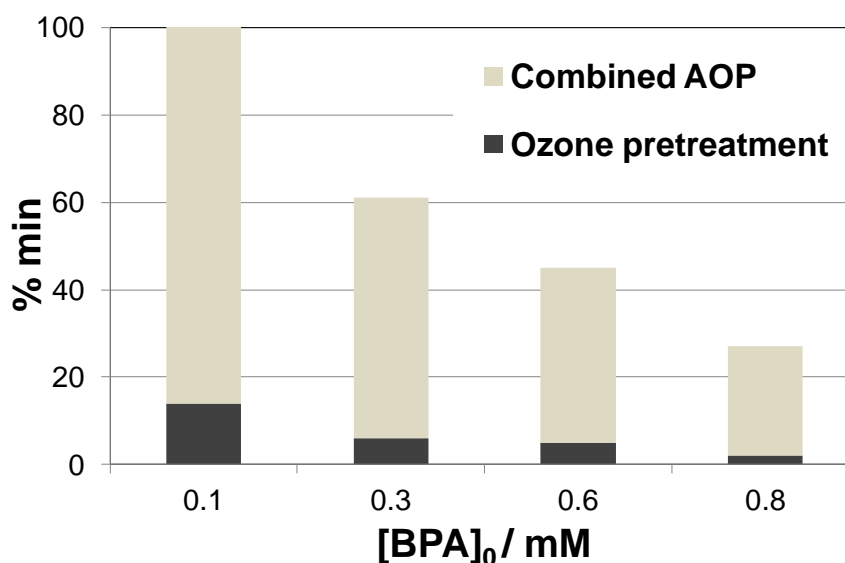
Figure 2.2.5 Mineralization percentages for photocatalytic ozonation at increasing initial BPA concentration. The effects of the initial step of ozone equilibration (O_3 pre-treatment) is shown separately.

In the case of the lowest tested concentration (0.1 mM), a complete mineralization was achieved after only 90 min of combined treatment. Even for the highest tested concentration (0.8 mM), the mineralization is still significant after such a short reaction time.

Comparable results were obtained in the case of 4-CP (Table 2.2.2). Photolysis has a negligible effect on mineralization, while ozonation leads only to a 16% mineralization after 90 min of treatment. Photocatalysis is even less efficient requiring a 2.5 longer time to obtain a comparable mineralization (18% of mineralization after 240 min instead than 90 min). Photocatalytic ozonation results in a much higher mineralization (86% mineralization at the end of the combined test, including 16% during the ozonation pre-treatment and 70% during photocatalytic ozonation). Such an efficient mineralization of 4-CP may result from the synergistic effects taking place between O_3 and the surface of irradiated TiO_2, previously invoked in the case of BPA degradation.

	$[4\text{-CP}]_0$ mM	COD_{in} $mgO_2\ L^{-1}$	COD_{fin} $mgO_2\ L^{-1}$	% mineralization
Ozonation	0.3	151	127	16
Photocatalysis*	0.3	151	123	18
Photocatalytic ozonation	0.2	103	0	100
	0.3	151	21	86
	0.4	186	56	70

Table 2.2.2 Mineralization data of separate and combined test (t_{fin} = 90 min; * t_{fin} = 240 min).

Photocatalytic ozonation was tested on three different initial 4-CP concentrations in the range 0.2-0.4 mM (Table 2.2.2). A significant final mineralization was obtained in all cases, indicating that no accumulation of stable intermediates occurs even at high pollutant concentrations. In the case of the lowest starting concentration, a complete mineralization was achieved after only 90 min of combined treatment. Increasing the initial pollutant concentration leads as expected to a reduction of both the mineralization and the pollutant disappearance rate, but a significant final mineralization is still achieved in a very short reaction time.

Degradation mechanisms. The degradation pathways of BPA and 4-CP during photocatalytic ozonation were investigated by combining HPLC/MS determinations on solutions sampled at different reaction times and ATR-FTIR analyses of the used catalyst at the end of the reaction. No previous data about the intermediates and mechanisms of such processes could be found in the literature.

In the case of BPA degradation, previous studies investigated the mechanism of the separate ozonation or photocatalytic treatment. Ozone has been reported to act either as a direct oxidant [Gultekin2007] or to decompose to $^{\bullet}OH$ radicals, especially in alkaline conditions. Moreover, due to its electrophilic character, ozone can react with aromatic rings by electrophilic substitution or dipolar cycloaddition [Deborde2008]. As for the photocatalytic degradation of BPA by TiO_2, Watanabe et al. [Watanabe2003] proposed a reaction mechanism involving the attack of $^{\bullet}OH$ and $^{\bullet}OOH$ radicals on the two methyl groups of the BPA molecule, followed by the cleavage of the methyl moieties and the generation of aldehydes, acids, and carbon dioxide.

In this work, HPLC–MS analysis was employed to determine the nature of the reaction intermediates (Figure 2.2.6).

Figure 2.2.6 a) HPLC chromatogram and b) relative mass spectra of 1.5 mM BPA solution at the end of the photocatalytic ozonation. The structures of the attributed compounds and corresponding fragmentation peaks are reported in inset.

47

The HPLC chromatogram of a BPA solution (starting concentration: 1.5 mM) at the end of the combined treatment shows an intense peak centered at 4.4 min, which can be attributed to BPA, and several other peaks at different retention times (from 2.6 to 4.0 min). A tentatively attribution of the intermediate peaks was carried out on the grounds of the mass values; the peaks at 4.0 and 2.6 min could be respectively attributed to the compounds labeled as B1 and B2 (Figure 2.2.6 inset).

Additionally, ATR-FTIR analyses were carried out to clarify the nature of intermediate species adsorbed onto the used photocatalyst. Figure 2.2.7 reports the FTIR spectra of TiO_2 samples withdrawn from the reaction mixture at the end of photocatalytic ozonation tests for several BPA starting concentrations. The curve relative to the bare oxide was subtracted. The spectrum of pure BPA is reported for the sake of comparison. In the case of the highest initial concentration (1.5 mM), appreciable amounts of unreacted BPA can be detected, in agreement with HPLC/MS determinations. Adsorbed carbonyl species are observed in the spectral region at about 1,700 cm^{-1}, supporting the occurrence of intermediates with carbonyl moieties, like compound B2.
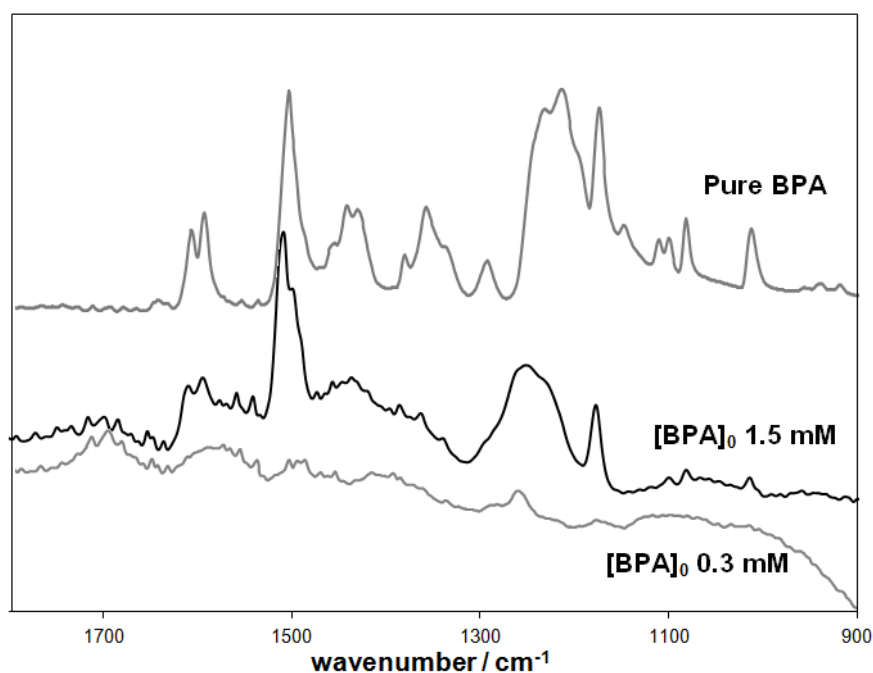
Figure 2.2.7 ATR-FTIR spectra of pure BPA molecule, and of the TiO_2 sampled at the end of photocatalytic ozonation tests in the case of 1.5 mM and 0.3 mM starting BPA concentrations. For the latter curves, the spectrum of the bare TiO_2 was subtracted.

Hence, the following BPA degradation mechanism can be proposed (Figure 2.2.8): The molecule oxidation starts with the direct attack of a $^{\bullet}OH$ radical at the aromatic ring, which forms the compound B2. A further oxidation of B1 could lead to a ring opening (compound B2) and to progressive loss of CO_2 producing aliphatic byproducts and ultimately CO_2.
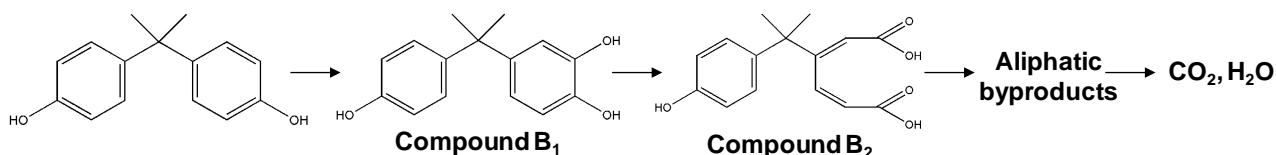
Figure 2.2.8 Proposed degradation mechanism occurring during the photocatalyitic ozonation of BPA.

In the case of 4-CP, the HPLC/MS chromatogram (Figure 2.2.9a) of the solution of the end of the run (starting 4-CP concentration: 0.4 mM), shows a peak at a retention time of 5.6 min, which can be attibuted to 4-CP by comparison with the mass spectrum of pure 4-CP (Figure 2.2.9b). The chromatogram presents also two chromatographic peaks at a retention time of about 4.5 min, which correspond to a mixture of intermediate products. Since the peak separation did not improve even by changing the polarity of the eluent, the attribution of those peaks was carried out using the method of the internal calibration by addition of a known compound (BPA). Thus, the peak at 4.6 min was attributed to bisphenols bearing the second hydroxyl group on the non-phenolic aromatic ring, such as BPA (Figure 2.2.9c). Instead, the peak at 4.4 min was attributed to BPA isomers bearing the second hydroxyl group in ortho or para position with respect to the hydroxyl group of 4-CP. The latter attribution was made on the grounds of spectrophotometric considerations and of the proximity of the peak to the one of BPA-type compounds.
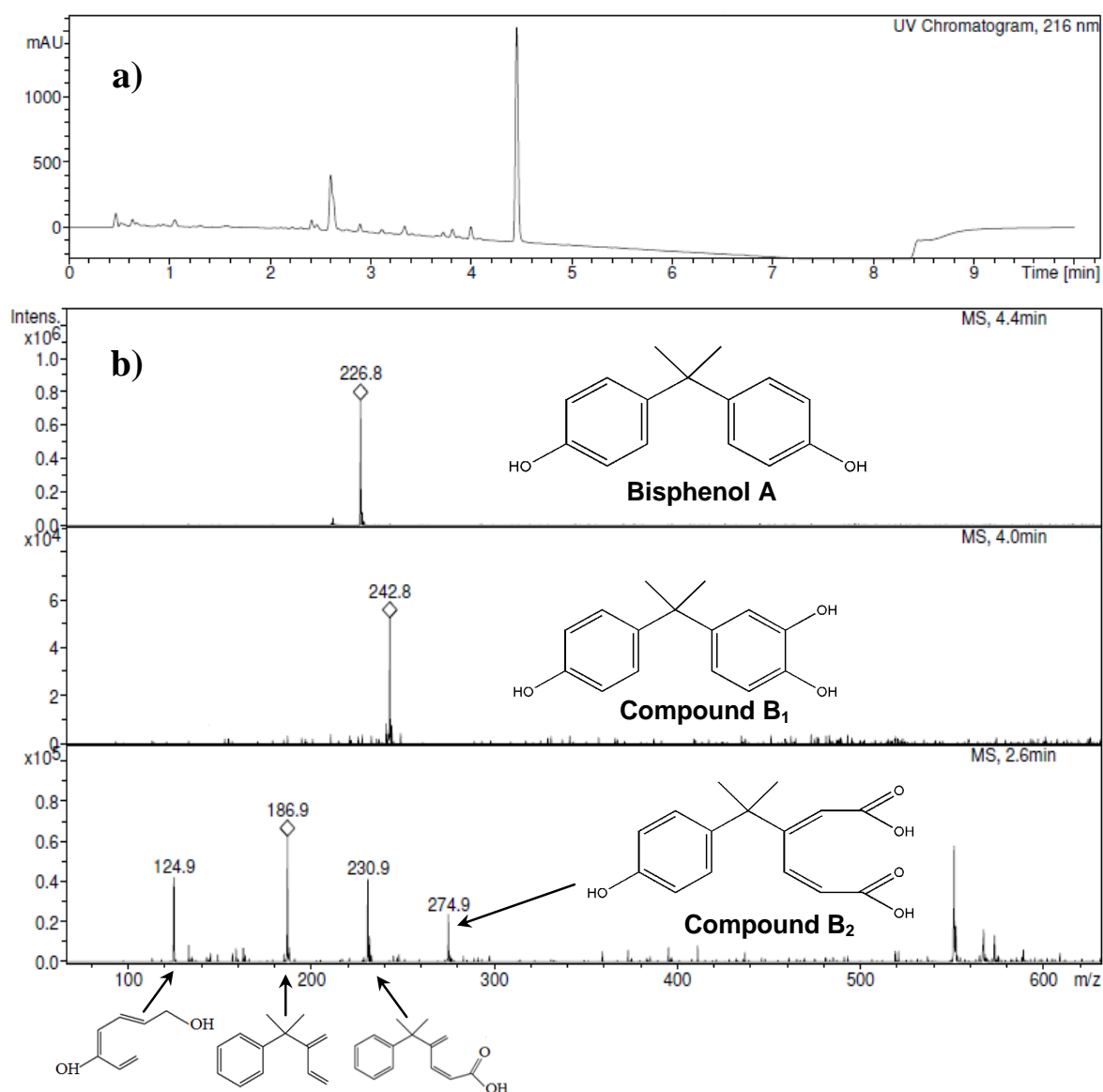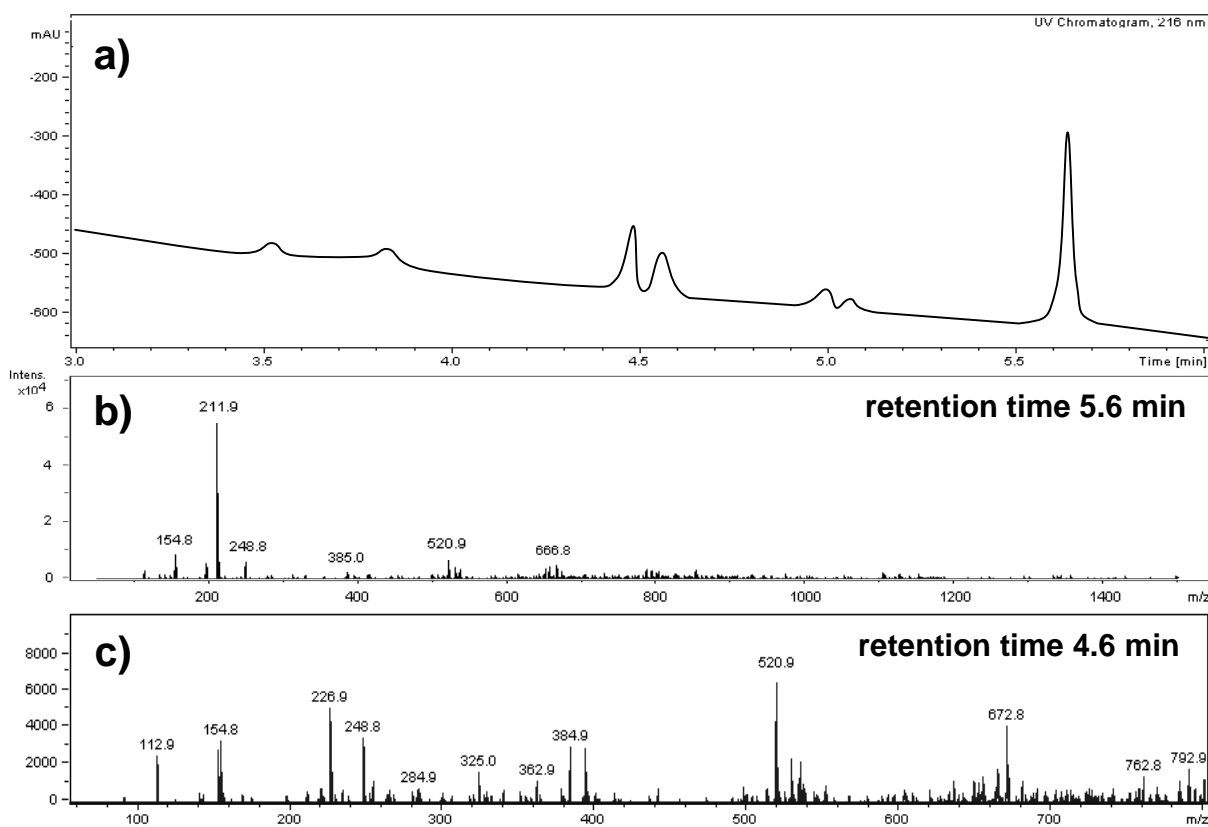

Figure 2.2.9 a) HPLC chromatogram and b,c) relative mass spectra of a 0.4 mM 4-CP solution at the end of the photocatalytic ozonation treatment.

However, a precise chemical structure cannot be attributed to each peak since several isomers may occur. In addition to the previously described peaks, few minor chromatographic peaks were observed at very low retention time. These peaks can be attributed, in agreement with literature studies on other EDCs [Deborde2008], to smaller and more polar molecules such as acids or aldehydes.

Figure 2.2.10 reports the FTIR spectrum of the TiO_2 withdrawn from the reaction mixture at the end of a photocatalytic ozonation run (initial 4-CP concentration 0.3 mM). No trace of the 4-CP characteristic peaks are appreciable. The spectrum shows instead a peak at about 1,700 cm^{-1} that can be attribute to COOH/CHO moieties and a peak centered at 1550 cm^{-1} attributable to double bonds [Addamo2005].
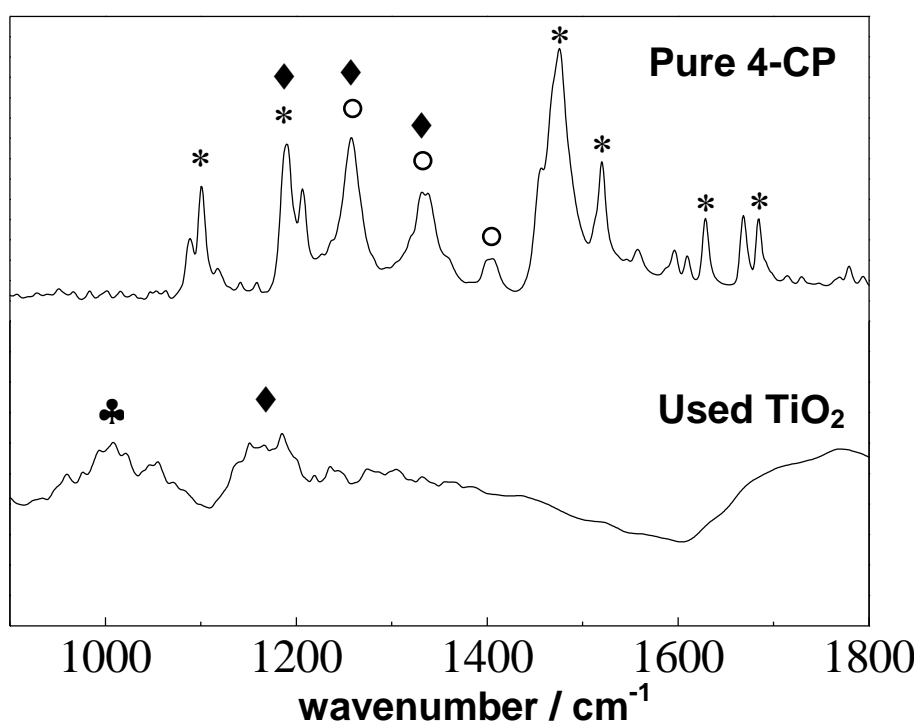
Figure 2.2.10 ATR-FTIR spectra of a) pure 4-CP molecule, b) TiO₂ sampled at the end of photocatalytic ozonation (starting 4-CP concentration: 0.3 mM, the curve of bare TiO₂ was subtracted). Peaks are labeled according to the following attributions: * aromatic ring, ○ C-OH, ♦ alkenes, and ♣ CHO/COOH.

On the grounds of the reaction intermediates identified by HPLC/MS and FTIR analyses, the following degradation mechanism can be proposed for the photocatalytic ozonation of 4-CP (Figure 2.2.11). In analogy with the degradation of BPA, it can be suggested that the oxidation of 4-CP starts with an attack of an hydroxyl radical on one of the aromatic rings. This claim is supported by the occurrence of bispenols as reaction intermediates, as determined by HPLC/MS. However, the attack of the hydroxyl radical might be more favored on the phenolic ring owing to the presence of the former –OH group of the 4-CP molecule. The attack on the phenolic ring would lead to BPA isomers bearing the second hydroxyl group in ortho or para position with respect to the hydroxyl

group of 4-CP. In the case of an ortho attack, the proximity of two –OH groups might lead more easily to ring opening products. Figure 2.2.11 reports two possible structures of open ring intermediates, proposed on the grounds of FTIR and HPLC/MS data.
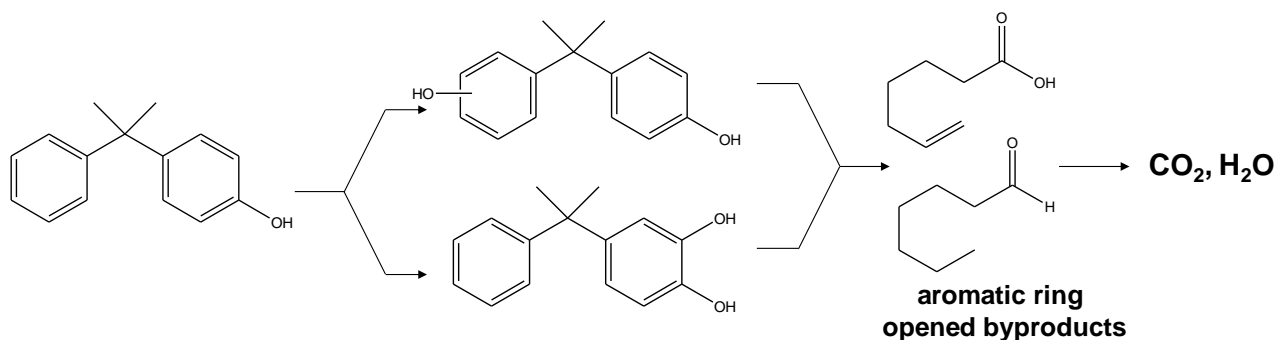
Figure 2.2.11 Proposed degradation route for the photocatalytic ozonation of 4-CP.

Conclusions

The coupling of two AOPs, ozonation and photocatalysis by a TiO_2 film, was successfully applied to the removal of two highly recalcitrant pollutants, BPA and 4-CP. To the author's best knowledge, this was the first study reporting the degradation of 4-CP by AOPs.

Complete mineralization of the pollutants was obtained after very short reaction times, at room temperature, by the photocatalytic ozonation. The complete degradation to CO_2 is of paramount importance as degradation intermediates can be even more toxic than the parent compound; moreover, stable degradation intermediates can irreversibly adsorb at the photocatalyst surface blocking its active sites.

The efficiency of the tested combined treatment was traced back to significant synergistic effects taking place between ozonation and photocatalysis. Such synergy might arise from manifold interactions occurring between O_3 and the irradiated TiO_2 surface.

The degradation pathways occurring during the combined process were also analyzed by combining FTIR and HPLC/MS determinations. For both molecules, the degradation starts with a direct attack of $^\bullet OH$ radicals at an aromatic ring. In the case of 4-CP, two possible reaction pathways are possible depending on the aromatic ring attacked by the hydroxyl radical; the attack of the phenolic ring is suggested as the most favored degradation route. After the initial attack, the degradation of BPA and 4-CP proceeds with ring opening reactions and further oxidation leads to aliphatic polar compounds and finally to CO_2.

The use of nanometric TiO_2 immobilized in a thin film is of pivotal importance for the plant-scale applicability of the process, as it facilitates the separation of the photocatalyst from the treated effluent and improves light absorption, which is fundamental if low intensity irradiation sources, such as solar light, are to be exploited. Moreover, by combining an ozone treatment with

photocatalysis by a TiO$_2$ layer, the reduction of the degradation efficiency usually associated with the photocatalyst surface area loss was overcome by the synergistic effects between O$_3$ and TiO$_2$, also limiting undesired poisoning effects.

The employed TiO$_2$ layer represents a good candidate for plant-scale application as a cheap and reusable substrate was employed. Further, the TiO$_2$ film was mechanically robust and presented a rough surface, thus offering a large number of adsorption sites for both the pollutant and ozone.

The excellent mineralization, the process simplicity and the absence of suspended solids or sludge, make the presented combined AOP a leading candidate for the removal of recalcitrant pollutants, such as EDCs, in water and wastewater treatment plants.

2.3 Modulation of titania morphology: Mesoporous TiO$_2$

The modulation of the morphology of TiO$_2$ represents a promising strategy to improve its photocatalytic efficiency. The tailoring of the material grain size, shape, surface area, and pore network has been extensively studied in order to obtain better performing photocatalysts [Sanchez2008, Bleta2010]. In particular, the use of templates to synthesize materials with high surface area and high degree of mesoporosity has been investigated to enhance the adsorption and diffusion of pollutants onto TiO$_2$. In fact, a material with high surface area offers more adsorption sites per gram for gas/solid interactions and a continuous mesosporous network serves as an efficient pathway for molecular transport. Another promising aspect of mesoporous materials is that they can serve as "host material" for growing metal nanoparticles or a highly dispersed oxide phase, which can slow down the recombination of photogenerated charges.

Saadoun and coauthors [Saadoun2000] reported that increasing the pore size enhanced the photocatalytic activity of titania towards the degradation of formaldehyde under UV light, while Martinez-Ferrero et al. reported an increased activity of mesoporous titania with pore size of 7.5 and 5.5 nm with respect to the decomposition of methylene blue and lauric acid, respectively [Martinez-Ferrero2007].

However, there is no general consensus over the optimal pore size required for photocatalytic reactions, and it is often difficult to discriminate the increase in photocatalytic activity due to the higher surface area from the effect of the pore size [Yu2002]. Moreover, the effect of the crystallinity of the pore walls is also to take into account as it is difficult to change the material porosity without altering the crystallinity and the grain size of the titania crystallites, which have also a drastic impact on the photocatalytic activity [Sanchez2008].

Mesoporous oxides, such as TiO$_2$, can be synthesized using soft templates, like surfactant and amphiphilic block copolymers. Such an approach was developed during the nineties using low molecular weight cationic surfactants as structure directing agents for the synthesis of mesoporous silica and alumino-silicates [Kresge1992; Attard1997]. In time this synthetic strategy has been extended to numerous systems, including TiO$_2$ [Sanchez2008], using various kinds of micellar and lyotropic liquid-crystal phases, including ionic/nonionic surfactants and block copolymers [Ozin2000; Antonietti1998]. By template synthesis, the morphology features of the oxide (pore size, specific surface area, particle size) can be tailored by changing the nature of the adopted template.

Two main mechanisms have been proposed to explain the formation of mesostructures from template synthesis. In the so called liquid crystal templating mechanism, the inorganic phase condenses around a stable surfactant mesophase [Attard1995]. Instead, in the cooperative self-assembly mechanism, surfactant molecules and inorganic species combine to form hybrid intermediate entities, which are composed of oligomeric building blocks that associate with the amphiphilic component [Firouzi1995].

The application of template syntheses to TiO_2 has proved more challenging than in the case of silica. In fact, at the end of a template synthesis, a final thermal treatment is required to remove the structure directing agent from the pore network and to promote the crystallinity of the oxide. However, TiO_2 presents a faster grain growth with respect to SiO_2, which can result in the collapse of the pore structure during the thermal treatment when the crystal size exceeds the pore wall thickness. In order to avoid such pore collapse, low calcination temperatures are often employed resulting in a poor crystallinity of the oxide.

Most literature studies concerning the preparation of mesoporous TiO_2, employ the so called evaporation-induced self-assembly (EISA) method, in which the structure directing agents are introduced in the reaction mixture together with the titania precursor [Brinker1999; Choi2004]. In this approach, the condensation of the metal ions and the self-assembly of the template take place simultaneously. The "nanoparticle route" is a novel strategy in which the structure directing agent is added to the pre-formed TiO_2 nanoparticulate sol, so that only the self-assembly between template and nanoparticles takes place [Bleta2010, Bosc2003]. In comparison with the EISA process, collapse problems associated with template removal and crystallization may be reduced using the nanoparticle route [Sanchez2008]. Although more synthetic steps are required, this novel approach is inherently more flexible as every synthetic step can be tailored to produce the desired effect. Moreover, the use of pre-synthesized nanoparticles allows a fine control of the material properties (e.g., introduction of dopants) [Wang2010b].

In this thesis, monomeric and dimeric alkylpiridinuim surfactants and amphiphilic block copolymers of the Pluronic family, were employed as structure directing agents in multi-step synthetic procedures for the obtainment of TiO_2 samples with tailored morphological features. The role played by the two different template families will be separately presented in the next two chapters.

2.3.1 Alkylpyridinium surfactants as structure directing agents

Cationic surfactants were the first class of structure directing agents employed in the synthesis of mesoporous silica and alumino-silicates. They have also been employed in the preparation of mesoporous titania. For instance, Mohamed and coworkers [Mohamed2007] reported that the use of cationic surfactants (cetyltrimethylammonium bromide and cetylpyridinum bromide) as structure directing agents during a hydrothermal treatment resulted in high surface area (240–418 m^2 g^{-1}), control of the pore size (2.3–4.4 nm) and of the particle morphology (from nano-sized spheres to cotton fibrils). Moreover, they reported an effect of the surfactant addition also on the bulk features of the oxide (crystallite size and phase composition).

In the present thesis work, cationic gemini surfactants were employed as structure directing agents for the synthesis of TiO_2 with controlled morphology. Gemini surfactants, which are composed by two single-tail amphiphilic moieties connected by a spacer group (e.g., polymethylene or short poly(oxyethylene) chains) [Quagliotto2003], are promising candidates as structure directing agents owing to their unusual properties with respect to similar non-gemini surfactants. In general, they present lower critical micelle concentration (CMC) values with respect to their single monomers, and higher adsorption at the air/water and solid/water interfaces. Moreover, they tend to form micelles of different dimensions and shapes (e.g., spherical, vesicles, rod-like), even at low concentration [Hait2002; Menger2000].

In this work, TiO_2 nanoparticles were synthesized using a "gemini-like" alkylpyridinium surfactant (1,1'-dodecyl-2,2'-trimethylendipyridine-dichloride or "gemini spacer 3", GS3). The corresponding monomeric surfactant (dodecylpyridinium chloride, DPC) was also tested as a reference. The comparison between this two surfactants is of particular interest because of their widely different self-aggregation behavior. DPC has been reported to form spherical micelles in water (aggregation number of ca. 20; micellar radius of ~1.9 nm, comparable with the length of a C_{12} chain, 1.67 nm) that do not tend to aggregate in tridimensional structures [Simoncic1998; Fujo1992; Galan2002]. On the other hand, the corresponding gemini surfactant, GS3, owing to its double cationic charge and short spacer (n = 3), may give rise to elongated, rod-like micelles, as previously reported for similar gemini surfactants [Manne1997; Cao2006]. Such rod-like micelles have been reported to assemble at high concentrations or in the presence of an oxide surface, in hexagonal arrangements of cylinders [Manne1997].

The two surfactants (DPC and GS3) were separately employed as structure directing agents for the modulation of the morphological features of TiO_2 nanoparticles. The adopted synthetic procedure involved a hydrothermal growth of pre-synthesized sol-gel nanoparticles in the presence

of a varying amount of the chosen structure directing agent. A final thermal treatment was employed to remove the surfactant. The final samples were investigated from the structural and morphological point of view to determine the effects provoked by the template addition. The obtained results were rationalized on the grounds of the self-aggregation of the surfactants and of their adsorption behavior at the titania surface, as determined by adsorption isotherms on an aqueous suspension of TiO_2.

Experimental section

All the chemicals were of reagent grade purity and doubly-distilled Milli-Q water was used to prepare solutions and suspensions.

Template Synthesis of TiO_2. Titanium dioxide nanoparticles were synthesized by a sol-gel reaction. A solution of $Ti(OC_4H_9)_4$ in 2-propanol was stirred at 300 rpm for 10 min at room temperature. Then, water was added, dropwise, fast, to the alkoxide solution in order to obtain a water/alkoxide molar ratio of 81.7 and a water/2-propanol molar ratio of 8.5. The sol was dried overnight in oven to obtain xerogel powders, that were subsequently purified by centrifugation-resuspension cycles. Then, the powder fractions were aged at 80 °C and at pH 8 (to give rise to attractive electrostatic interactions between the oxide and the cationic surfactants) for 5 h in the presence of different surfactant concentrations: 1–100 mM and 0.1–50 mM for dodecylpyridinium chloride (DPC), and 1,1'-dodecyl-2,2'-trimethylendipyridine-dichloride or "gemini spacer 3" (GS3), respectively (Figure 2.3.1).
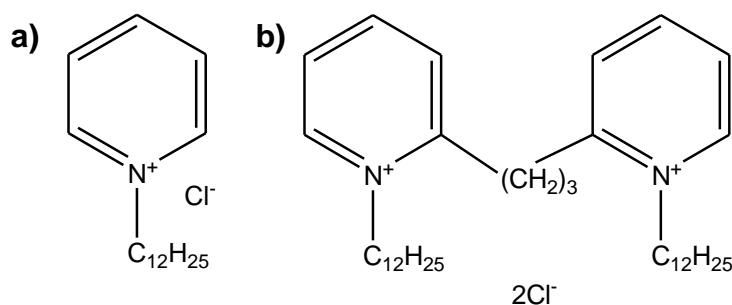
Figure 2.3.1. Chemical structure of a) dodecylpyridinium chloride, DPC and b) gemini spacer 3, GS3.

At the end of the ageing process, the suspensions were dried in oven at 80 °C and finally the powders were calcined at 600 °C for 6 h under O_2 flux (9 L h^{-1}).

Samples Characterization. X-ray powder diffraction (XRPD) patterns were collected at room-temperature between 10 and 80° with a Siemens D500 diffractometer, using the Cu Kα radiation. Rietveld refinement was performed using the GSAS software suite and its graphical interface EXPGUI. The average crystallite diameter, *d*, was estimated from the most intense reflection (101) of the anatase phase using the Scherrer equation.

Specific surface area was determined by the BET method using a Coulter SA3100 instrument. Pore size distribution was determined from desorption isotherms using the Barrett-Joyner-Halenda (BJH) method.

Particles morphology was investigated by scanning electron microscopy (SEM) using a LEO 1430.

The CMC values of the surfactants in water were determined by conductometric determinations as a function of the temperature. On the grounds of these results and of literature data [Koopal1995; Quagliotto2003; Bhat2007; Simoncic1998; Fujo1992; Galan2002], the CMC values at 80 °C were estimated for the two surfactants (18–22 mM, for DPC and 2–4 mM in the case of GS3).

The adsorption isotherm of GS3 at the TiO_2 interface was obtained at 25 °C, in a 2×10^{-3}M KCl solution and pH of 8.0. The determinations were carried out as follows. At the end of the adsorption time (4 h), the supernatant solution was sampled and the residual surfactant concentration was determined by UV-visible spectroscopy at 265 nm. The adsorption isotherm of DPC on TiO_2 was obtained elaborating data from the literature [Koopal1995] (T = 21; pH = 8; equilibration time = 12 h; 1×10^{-3} M NaCl).

Results and discussion

Surfactant Adsorption at TiO₂-Solution Interface. The adsorption isotherms of DPC and GS3 at the TiO_2/solution interface, obtained by plotting the surface excess (Γ) as a function of the final concentration at equilibrium, are reported in Figure 2.3.2.
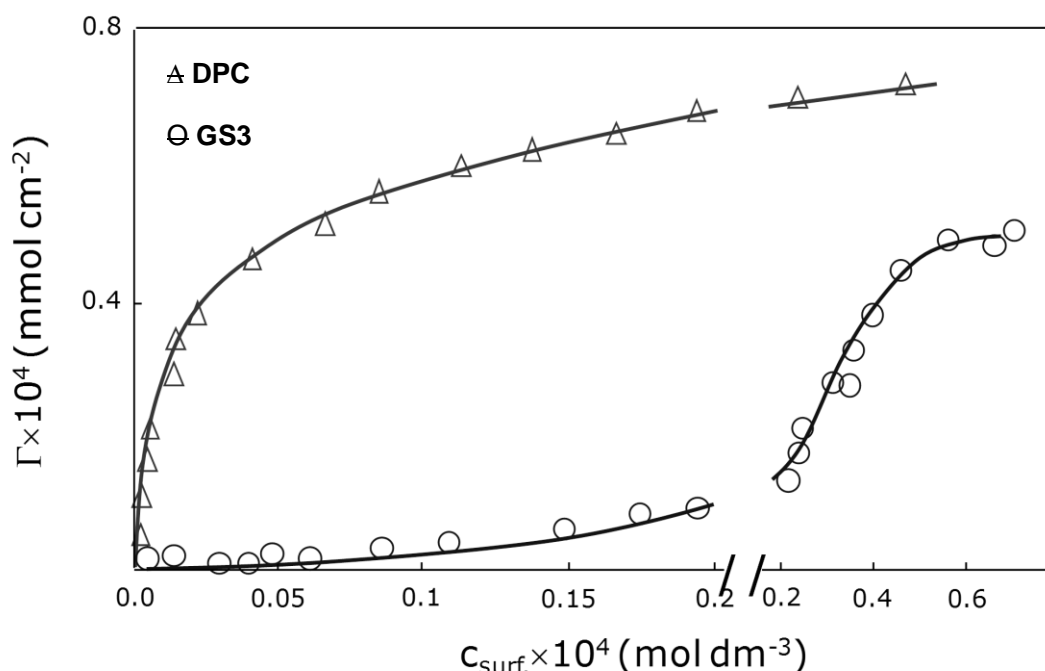
Figure 2.3.2 Adsorption isotherms at the TiO₂/solution interface of DPC and GS3 surfactants.

The two curves exhibit completely different shapes: An S-shaped curve is observed for DPC, while GS3 gives an L-type shape. S-type curves are generally associated in the literature with low adsorbent-adsorbate affinity due to weak interactions between the surfactant and the oxide [Koopal1995]. On the grounds of previous XPS results [Ardizzone2006], it can be proposed that the DPC adsorption leads to the formation of surface ion pairs, in which the negative surface charge of TiO_2 at pH 8 partially compensates the surfactant aromatic charge. As for GS3, its L-type curve is generally attributed to the coverage of the solid surface by a monolayer of adsorbate molecules due to the presence of strong adsorbent-adsorbate interactions. The higher affinity of GS3 for the solid is also testified by the larger adsorbed amount in the quasi-plateau region (Γ_{max}) with respect to that of DPC (7.7×10^{-5} and 4.8×10^{-5} µmol cm^{-2} for GS3 and DPC, respectively). Therefore, the isotherm data relative to DPC and GS3 were elaborated using the Frumkin-Fowler-Guggenheim (FFG) and the Langmuir model equations, respectively. Indeed, the FFG model applies to weak adsorbent-adsorbate interaction in the presence of electrostatic and non-electrostatic lateral interactions [Fowler1965], while the Langmuir model better describes strong adsorbent-adsorbate interaction with no lateral interactions between adsorbate molecules. Table 2.3.1 reports the parameters obtained from the data treatment.

Surfactant	model	R^2	β	ΔG^0 kJ mol^{-1}	a
DPC	FFG	0.97	$(16 \pm 2) \times 10^1$	-5.6 ± 0.2	3.2 ± 0.2
GS3	Langmuir	0.997	$(48 \pm 6) \times 10^3$	-27.1 ± 0.3	—

Table 2.3.1 Adsorption equilibrium constant β, standard adsorption Gibbs energy ΔG^0, and lateral interaction parameter a from the elaboration of GS3 and DPC isotherms.

A good correlation (R^2) is observed in both cases, justifying the adoption of the two models for the analysis of the two different isotherms. Higher values of the adsorption equilibrium constants, β, and of the relative standard adsorption Gibbs energy, ΔG^0, are determined for GS3, supporting a stronger adsorption of the gemini surfactant at the TiO_2 surface with respect to DPC. The DPC isotherm shows instead a positive lateral interaction parameter, a, deriving from the electrostatic repulsive interactions between the positive charges of the surfactant headgroups. This result is in agreement with literature data about DPC adsorption on clays [Mehrian1993].

The co-areas å calculated from the surface excess at maximum coverage (Γ_{max}) are 350 and 216 Å^2 for DPC and GS3, respectively. Literature data of the DPC co-area obtained by surface tension measurements at the air-water interface [Ottewill1960] are much lower: 110 and 35 Å^2 for a

flat-lying and vertical orientations, respectively. The observed higher co-area supports the formation of a diluted film, where DPC molecules lie flat over the surface and with electrostatic repulsion between the charged pyridinium heads (Figure 2.3.3a). GS3 surfactant exhibits a much lower value of co-area that could derive from a vertical orientation of the gemini molecules (Figire 2.3.3b). Chloride counterions may play a pivotal role in compensating part of the positive charge of the pyridinic headgroups, thus reducing possible lateral repulsive interactions, as suggested by literature data about gemini surfactants [Ardizzone2002].
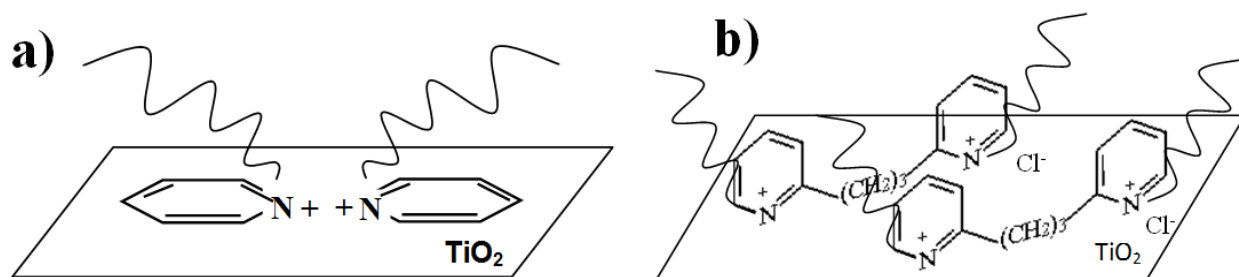
Figure 2.3.3 Sketches of possible orientations of the adsorbed surfactant at the TiO$_2$ surface.

Log-log plots of the isotherms are reported in Figure 2.3.3 to enable a better interpretation of the region at low surface excess values.
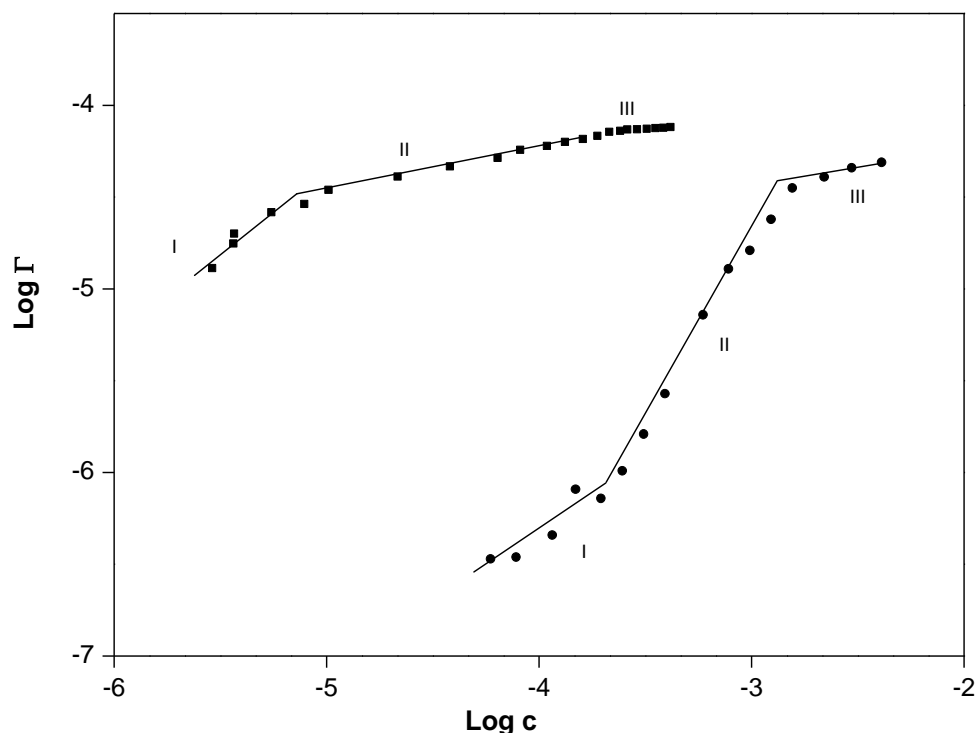
Figure 2.3.4 Log-log plot of the surface excess Γ as a function of the equilibrium concentration for DPC (full circles) and GS3 surfactants (full squares).

The log-log plot of the two surfactants show different regions (Figure 2.3.3) that can be interpreted on the grounds of the four-region model proposed by Somasundaran et al. [Somasundaran1966; Fan1997]. The four regions are attributed to the surface adsorption of

monomers by electrostatic interactions (region I), to the formation of surface aggregates (hemi-micelles) up to the substratum charge compensation (region II), to the head-out insertion of adsorbate molecules by chain-chain interactions (region III), and to the formation of a complete bilayer (region IV). A further increase in the solution concentration of the surfactant does not lead to any further increases in Γ. In the case of DPC and GS3, only three regions are appreciable; the isotherms are thus limited to a monolayer coverage (as the maximum concentration must be lower than the surfactant CMC) and the complete formation of a bilayer does not take place.

The formation of hemi-micelles at the TiO$_2$ surface occurs at 1.8×10^{-4} M and 8.0×10^{-6} M, for DPC and GS3, respectively. The bulk micellization occurs at much larger concentrations: CMC values at 25 °C obtained by conductimetric/tensiometric determinations are 1.6×10^{-2} M and 1.5×10^{-3} M for DPC and GS3, respectively [Bath2007; Fujo1992; Koopal1995; Galan2002; Quagliotto2003]. This observation is in agreement with the criterion reported by Fuerstenau [Fuerstenau1991] that hemi-micelle formation can occur at about 1/100th of the CMC.

The observed shift along the x-axis of the DPC isotherm with respect to the GS3 one, the variation of the slope in the different regions and the distribution of surface excesses can be rationalized on the grounds of the presence of a second pyridinic ring in GS3. For both surfactants, the slope of the plot in the Region I (the Henry region) is almost equal to unity, in agreement with the ideal situation (ΔG^0 constant) [Koopal1995]. The isotherms differ instead in Region II. In fact, in the case of DPC, Region II is steeper than Region I, as typical for S-shaped isotherms, indicating that in this region the adsorption is increased by the formation of surface aggregates [Koopal1995]. On the contrary, in the case of the GS3 the slope of Region II, where hemimicelles form, is decreased, possibly due to steric hindrance.

Surfactant-Assisted Synthesis of TiO$_2$ Samples. Titania samples were prepared employing either DPC or GS3, at different concentrations, both lower and higher than the surfactant CMC.

The structural and morphological features of the resulting materials are reported in Table 2.3.2. The phase composition is largely affected by the amount of surfactant utilized during the hydrothermal growth treatment. Interestingly, when the surfactant concentration is lower than the CMC, *i.e.* for non-aggregated surfactant units, the anatase polymorph is prevalent and crystallite sizes are comparable to those of surfactant-free synthesis. For surfactant concentrations larger than the CMC, the rutile polymorph content and the crystallite sizes are promoted. It has been often reported that anatase transformation into rutile takes place when anatase grains have reached a certain threshold size, of about 30–40 nm [Wang1999].

Also the sample specific surface area seems to follow a similar trend: It remains almost constant for surfactant concentration below the CMC, then for higher concentrations it decreases

significantly. Comparing the two surfactants, it appear that GS3 better preserves the surface area at high surfactant concentrations with respect to the DPC.

	Sample	% anatase	% rutile	d^a_{101} nm	d^r_{110} nm	S_{BET} $m^2 g^{-1}$
	no SURF	90	10	28	—	18
DPC	*1 mM*	92	8	20	—	19
	10 mM	91	9	22	—	19
	25 mM (~CMC)	93	7	24	—	16
	50 mM	69	31	32	86	8
	100 mM	43	57	41	> 100	5
GS3	*0.1 mM*	87	13	23	—	20
	2.5 mM	80	20	30	54	16
	5 mM (~CMC)	68	32	37	63	13
	10 mM	58	42	44	73	14
	30 mM	42	58	43	76	11

Table 2.3.2 Phase content, average crystallite sizes for anatase, d^a_{101}, and rutile, d^r_{110}, polymorphs, and specific surface area, S_{BET}, of TiO$_2$ samples synthesized with DPC and GS3.

These considerations are in full agreement with the particles' morphological features revealed by SEM images (Figure 2.3.5).
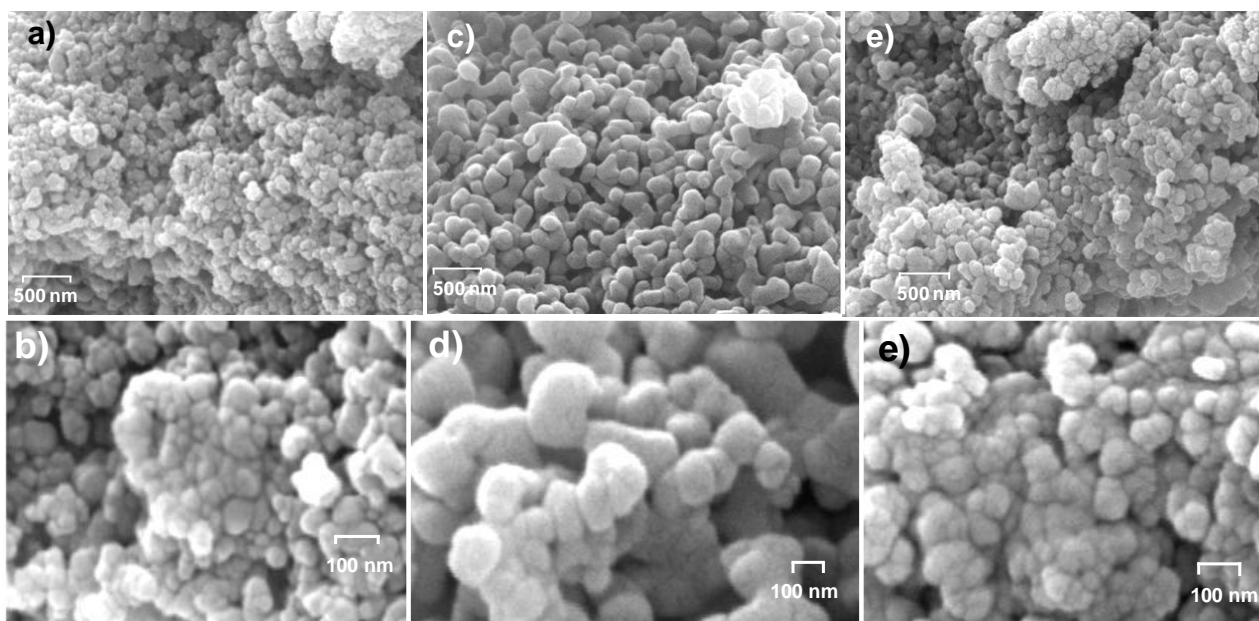
Figure 2.3.5 SEM micrographs of TiO$_2$ samples prepared without surfactants (a,b) and with 100 mM DPC (c,d) or 30 mM GS3 (d,e).

61

The reference titania sample (Figure 2.3.5a,b) presents spheroidal particles of average size ~30 nm, grouped in raspberry-like aggregates. The sample synthesized with high DPC concentration (Figure 2.3.5c,d) exhibits much larger particles (100-330 nm) with a smooth surface. Such effects are probably related to surface annealing and sintering phenomena taking place because of the heat of combustion of the surfactant. The sample synthesized with high GS3 concentration presents an intermediate situation: Particles maintain a spheroidal shape and have a size of about 60–70 nm.

The trend observed in the structural and morphological features of the oxide at increasing surfactant concentrations could tentatively be attributed to the adsorption of surfactant molecules at the surface of the growing particles, which could have resulted in lower crystal growth, and to the heat of combustion of the surfactant, which increases with the surfactant concentration.
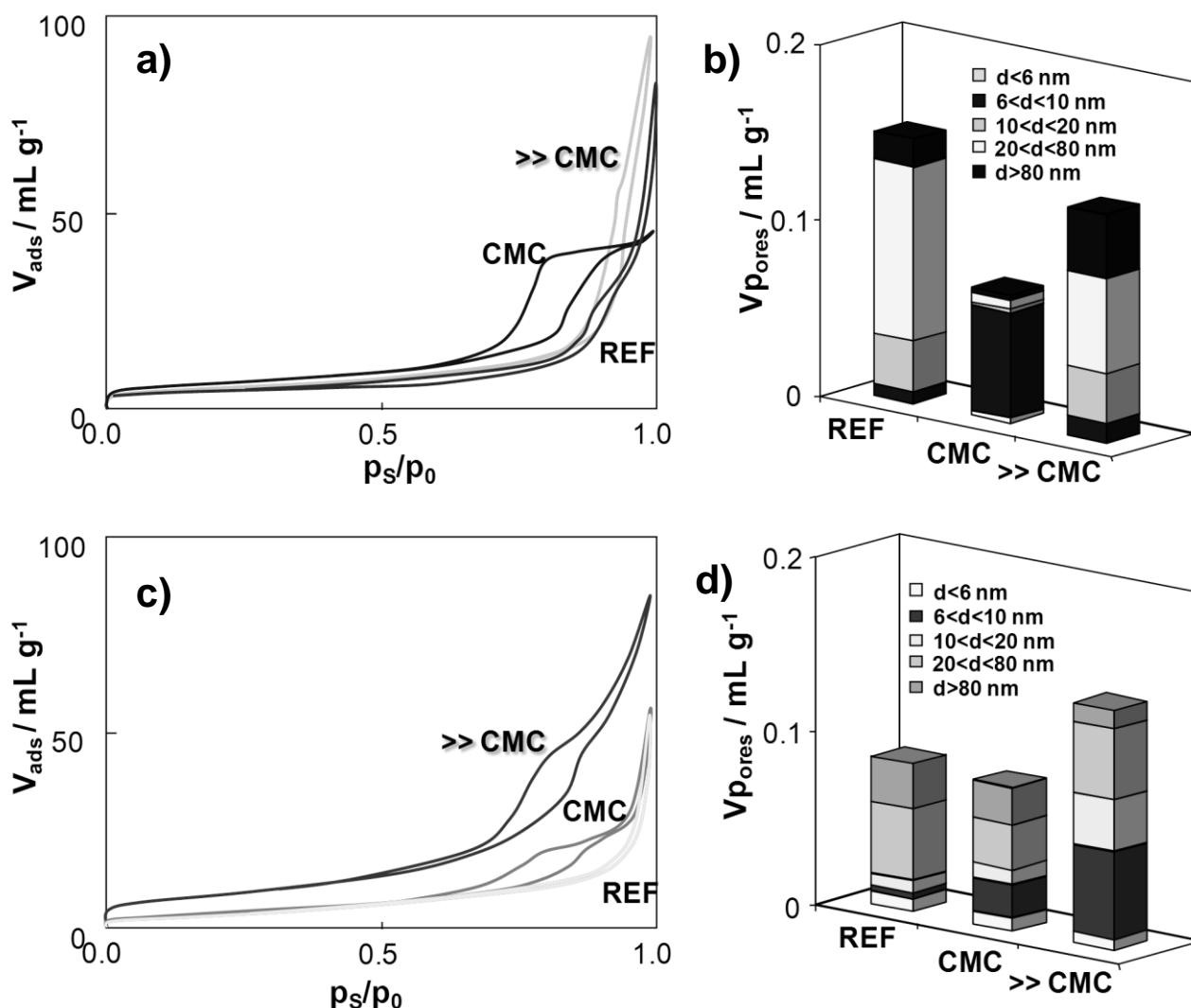
Figure 2.3.6 N$_2$ adsorption–desorption isotherms at subcritical conditions and pore volume distribution as a function of surfactant concentration, of TiO$_2$ samples prepared with a,b) DPC and c,d) GS3.

The differences in the morphological features of DPC- and GS3-treated titania can be better appreciated in Figure 2.3.6. Comparing the N$_2$ adorption-desorption isotherms at subcritical

temperature of DPC-treated samples, a striking difference emerges between the sample prepared with surfactant concentration close to the CMC and the one with concentration much larger than the CMC (Figure 2.3.6a). The former exhibit a hysteresis loop characteristic of bottle-neck-shaped pores [Barrett1951; de Boer1966; Rouquerol1999], and presents porosity mainly in the range 6-10 nm (Figure 2.3.6b), which is comparable with the average diameter of the globular DPC micelles (~4 nm) [Manne1997]. Instead, when c_{DPC} > CMC, the hysteresis loop becomes similar to the reference sample and, even if the total pore volume increases, mesopores are almost absent.

The gemini surfactant exhibits an opposite behavior. For both tested concentrations, the shape of the hysteresis loop is similar and can be related to open-ended slit-shaped pores (Figure 2.3.6c) and the total pore volume increases at increasing surfactant concentration (Figure 2.3.6d). More significantly, the fraction of mesopores with diameter in the range 6-20 nm increases with the surfactant content. By plotting the pore volume distribution with respect to pore size (Figure 2.3.7a) a fairly narrow size distribution can be observed and a marked increase in the mesoporosity is appreciable with respect to the reference TiO_2, prepared without surfactants. Figure 2.3.7b reports an HRTEM image of a GS3-treated sample, where part of its mesoporous structure can be appreciated.
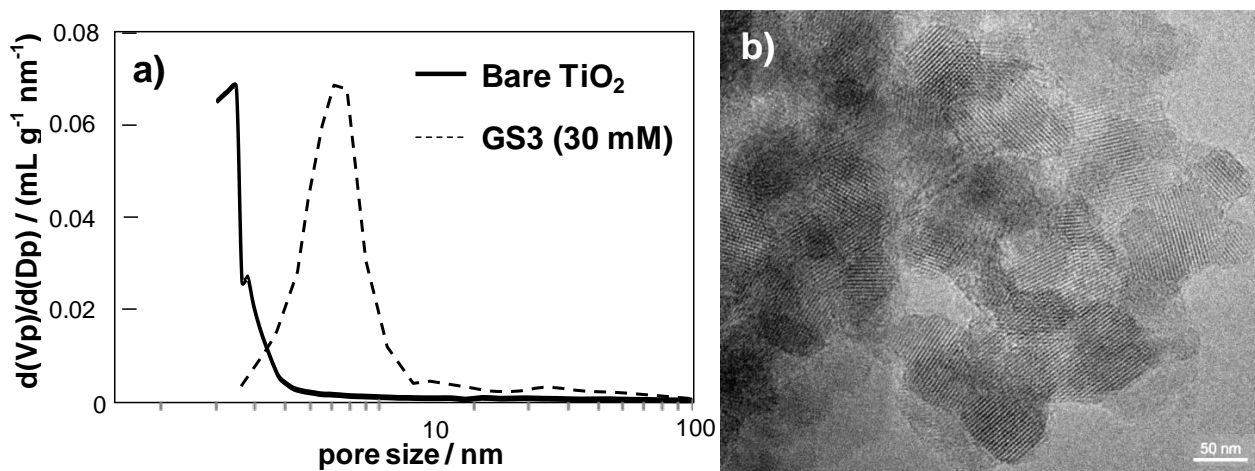
Figure 2.3.7 a) Pore size distribution curve of TiO$_2$ bare particles and treated with GS3 (30 mM); b) HRTEM image of TiO$_2$ treated with GS3.

On the grounds of the reported results, it can be proposed that the local heat of combustion of the surfactant during calcination leads to the collapse of the porous structure of DPC, especially at high surfactant concentrations, because of the unstructured and small spherical shape of the DPC micelles. On the other hand, the GS3 porous structure, possibly due to ordered hexagonal arrangement of elongated micelles, better resists the calcination step, resulting in higher final mesoporosity.

Conclusions

Monomeric (DPC) and gemini (GS3) alkylpyridinium surfactants were employed in a template synthesis of TiO_2 for the obtainment of controlled porosity. The two molecules present largely different self-aggregation behavior. DPC forms small, globular micelles and no long range ordered mesostructures, whereas the gemini molecule presumably forms elongated rods and further hexagonal arrangements. Such elongated structures are fully consistent with the observed vertical orientation of the GS3 molecules suggested by adsorption data.

The two surfactants show also markedly different adsorption behavior at the TiO_2 surface, as shown by adsorption isotherms at the water/oxide interface. In particular, the monomeric surfactant forms very diluted surface film, because of weak adsorbate/adsorbent interactions and the presence of repulsive lateral interactions. On the contrary, the gemini surfactant forms strong interactions with the oxide surface, occurring in the absence of lateral interactions.

The different aggregation features and interaction with the TiO_2 surface give rise to largely different oxide samples. In the case of DPC, the local heat of combustion may cause, during the final calcination treatment, the collapse of the pore structure formed by small spherical micelles, resulting in low mesoporosity and particle sintering. On the other hand, the gemini surfactant gives rise to TiO_2 with far better morphological features, which could be traced back to the higher self-aggregation tendency of GS3.

2.3.2 Pluronic block copolymers as structure directing agents

One of the main disadvantages of cationic structure directing agents, such as alkylpyridinium based surfactants, is that their complete removal requires high temperature treatments, which give rise to sintering processes and consequently, to a decrease in specific surface area and total porosity. To this respect, amphiphilic block copolymers have been recently proposed as an alternative to ionic surfactants [Wu2011; Bleta2010].

Block copolymers are composed by two or more chemically distinct polymer blocks, which are covalently bound together [Alexandridis1995; Taylor2007]. If the blocks are thermodynamically incompatible with each other, micro-phase separation takes place on the molecular scale producing complex nanostructures, whose morphology depends on the relative volume fraction of one block with respect to the other [Tadros2009].

In this thesis work, triblock copolymers of the Pluronic family were employed to produce highly mesoporous and crystalline TiO_2 samples by a nanoparticle route. Three different copolymers were studied: Their self-aggregation behavior in water is compared to the mesoporosity obtained in the resulting oxides. The role of the copolymer concentration is also discussed. The obtained samples were tested for their photocatalytic activity towards the degradation of methylene blue stains. The role played by the morphological properties on the sample photocatalytic performance is investigated.

Experimental section

All of the chemicals were of reagent grade purity and were used without further purification; doubly distilled water passed through a Milli-Q apparatus was used to prepare solutions and suspensions. The used Pluronic block copolymers (P104, F127 or P123) were obtained by courtesy of BASF Company (USA).

Synthesis of Mesoporous Titania. Mesoporous TiO_2 nanoparticles were synthesized by mixing the chosen Pluronic block copolymer with a titania sol. Three different block copolymers were adopted (Table 2.3.3).

Pluronic copolymer	MM (g mol^{-1})	EO$_x$PO$_y$EO$_x$	HLB
P104	5900	x = 25, y = 56	8
P123	5750	x = 20, y = 70	7 – 12
F127	12600	x = 106, y = 70	18 – 23

Table 2.3.3 Properties of Pluronic P104, P123, and F127 copolymers: Average molecular weight, average composition (EO and PO stand for ethylene oxide and propylene oxide units, respectively), hydrophilic-lipophilic balance (HLB) [Taylor2007].

The synthesis was carried out as follows. A solution of titanium isopropoxide (0.1 mol) in 2-propanol (38 mL) was stirred at 25 °C. Then, water (180 mL) was added dropwise to the alkoxide solution. The final water/alkoxide molar ratio was 100, while the water/2-propanol molar ratio was 20. The obtained sol was stirred for 90 min to complete the hydrolysis. Then, the sol was treated with 2 mL of HCl 37% to peptize the hydroxide precipitate and kept under reflux at 80 °C for 5 h until an homogeneous milky suspension was obtained. Preliminary studies showed that a separate HCl addition followed by a hydrothermal treatment allows to maximize the final sample surface area and porosity. The sol was then treated with a suitable amount of the chosen Pluronic triblock copolymer, after being liquefied in 2-propanol. The ratio between the number of ethoxy units and the Ti moles (EO/Ti) was varied in the range 0-1.6. The mixture was stirred for 3 h at 50 °C. Then, the sol was dried in a vacuum oven at 40 °C and 40 mbar. The resulting xerogels were calcined at 350 °C in static air for 5 h using a heating ramp of 3 °C min^{-1}. Finally the TiO_2 powders were irradiated with UV light (iron halogenide lamp Jelosil HG500, 315-400 nm, irradiation intensity reaching the sample: 30 mW cm^{-2}) for 5 h in order to remove eventual organic traces.

Samples are identified according to the following notation: T_copolymer_(EO/Ti). For instance, T_P123_1.0 indicates the use of the P123 copolymer and of an EO/Ti ratio of 1.0.

Sample Characterization. X-ray powder diffraction (XRPD) patterns were collected at room-temperature between 10 and 80° with a Siemens D500 diffractometer, using the Cu Kα radiation. Rietveld refinement was performed using the GSAS software suite and its graphical interface EXPGUI. The average crystallite diameter, *d*, was estimated from the most intense reflection (101) of the anatase phase using the Scherrer equation.

Specific surface area was determined by the BET method using a Coulter SA3100. Pore size distribution was determined from desorption isotherms using the Barrett-Joyner-Halenda (BJH) method.

The critical micelle concentrations (CMCs) of the used block copolymers in water were determined at room temperature by surface tension measurement using the DuNouy method (Gibertini TSD).

The micelle size distributions of the adopted block copolymers in water were determined at the polymer concentrations used in the synthesis, by dynamic light scattering (DLS) using a Malvern Nano Zetasizer (ZEN 1600).

Thermogravimetric analyses (TGA) were carried out using a Perkin Elmer TGA7 to determine the temperature of complete decomposition of the organic species present in the TiO_2 xerogels.

Particles were analyzed also by high resolution transmission electron microscopy (HR-TEM), using a 300 kV JEOL JEM 3010UHR microscope fitted with a LaB_6 single crystal filament and an energy dispersive X-ray (EDX) detector (Oxford INCA Energy TEM 200). All samples were dry deposited on Cu "holey" carbon grids (200 mesh).

The sample photocatalytic activity was tested towards the mineralization of methylene blue in dry conditions using the following procedure. A TiO_2 film (100 mg, total surface area 100 cm^2) was stained with an isopropanol solution of methylene blue (5 mmol). The stain was allowed to dry, then the film was irradiated for 7 h under UV-A irradiation. The photon sources was an iron halogenide lamps (Jelosil HG500) emitting in the 315-400 nm wavelength range (effective total power 85 mW). The final mineralization of methylene blue was determined by chemical oxygen demand (COD) measurements using a Merck Spectroquant apparatus.

Results and Discussion

The optimization of the synthetic parameters and the role of the polymer content will be firstly discussed. In this first part of the work, only the P104 copolymer was employed. Then, the role of the structure of the block copolymer adopted as structure directing agent will be presented, comparing three different Pluronic block copolymers.

Optimization of the synthetic parameters. The most critical parameter in the synthesis of mesoporous TiO_2 is the final calcination step, which serves the double purpose of removing the template and promoting the oxide crystallitnity. To this purpose, mild calcination treatments (350 °C) are generally adopted in the literature [Bleta2004; Shamaila2010] in order to prevent pore collapse ensuing the template removal.

Figure 2.3.8 reports the TG analyses of uncalcined TiO_2 xerogels: After an initial mass loss at about 150 °C, which can be attributed to the loss of physisorbed water, the larger mass loss, due to the polymer decomposition, takes place between approx. 200 and 270 °C. Most of the copolymer is removed between 200 and 300 °C, however, a smaller but significant weight loss occurs at ca. 350 °C. The degradation process is entirely completed at around 400 °C. TGA results demonstrate that the copolymer is not completely decomposed at 350 °C. Therefore, in the present work, the complete removal of the template was carried out by a mild heat treatment (350 °C, slow heating rate, static air) followed by UV irradiation. In this way the complete template removal is achieved by means of the photocatalytic activity TiO_2, which promotes the mineralization of organic residues, avoiding high temperature treatments that could induce crystallite growth and consequent pore collapse. The time of irradiation was optimized by monitoring the increase of the sample

specific surface area as a function of the irradiation time: The measured surface area and pore volume increase till 5 h of irradiation, then they reach a plateau value.
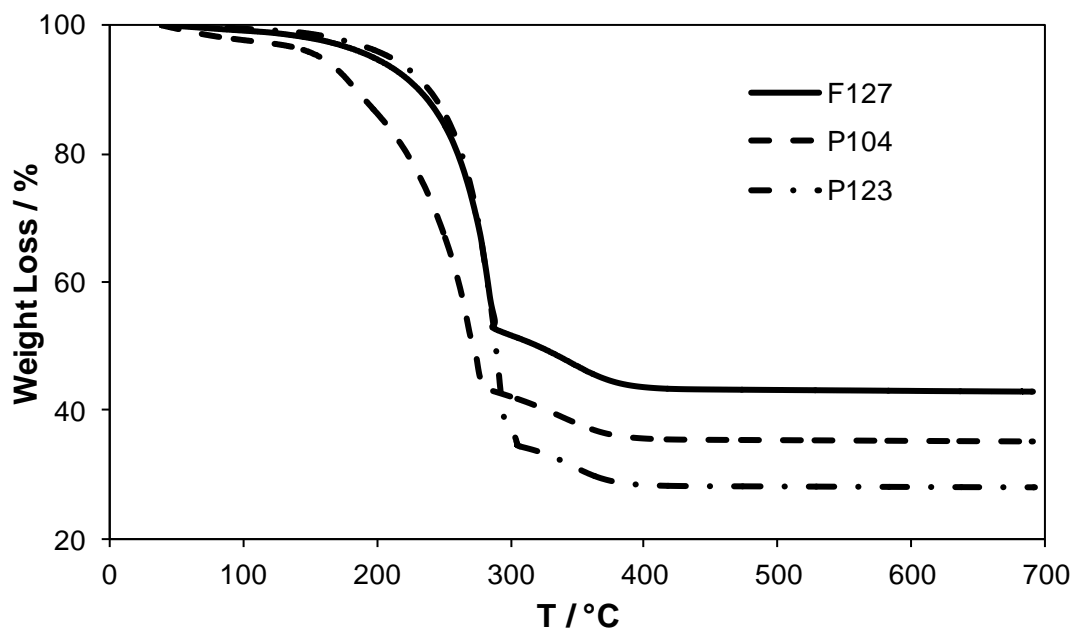
Figure 2.3.8 TG analyses under N_2 atmosphere of uncalcined T_P104_1.2, T_P123_1.2, and T_F127_1.2.

The adopted slow calcination treatment under static air results also in a good sample crystallinity, as appreciable from the high incidence of fringe patterns in HRTEM images (Figure 2.3.9). Mesoporous TiO_2 samples are characterized by a small crystallite size (5-8 nm) and show smooth edges and high transparency to the electron beam. The analysis of the lattice spacings reveals that the main termination is the (101) crystal plane of anatase (JCPDS file n. 21-1272), while the (111) crystal plane of brookite (JCPDS file n. 2-514) is less frequent.
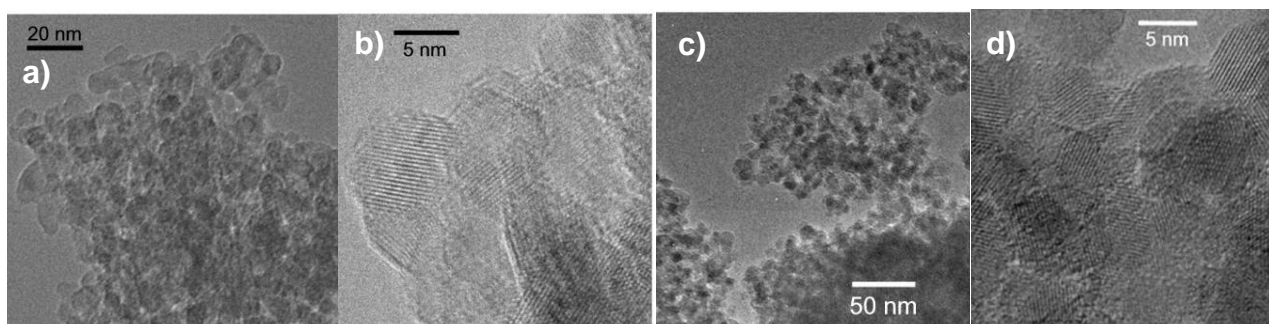
Figure 2.3.9 HRTEM micrographs of a,b) TiO_2 from a traditional sol-gel synthesis and c,d) TP104_1.2.

The morphologic features of the obtained TiO_2 samples were investigated by BET analysis, showing a completely different behavior for samples synthesized with and without copolymer. The reference sample T, peptized in HCl without the addition of the copolymer and calcined under the same conditions, shows an N_2 adsorption-desorption isotherm with an H2 type hysteresis loop (Figure 2.3.10a) characteristic of bottle-neck pores. The addition of the copolymer, instead, gives rise to type IV isotherms characteristic of mesoporous materials (Figure 2.3.10a), with an H1 type

hysteresis loop typical of spherical agglomerates with homogenous size and cylindrical pores opened at both ends [Barrett1951; de Boer1966; Rouquerol1999]. The pore total volume remarkably increases as a consequence of copolymer addition (Figure 2.3.10b), resulting in a significant increase in the sample specific surface area (92 and 187 m^2 g^{-1} for T and T_P104_1.2, respectively). The pore fraction in the mesoporosity region, almost absent in the reference sample, becomes predominant (Figure 2.3.10b).
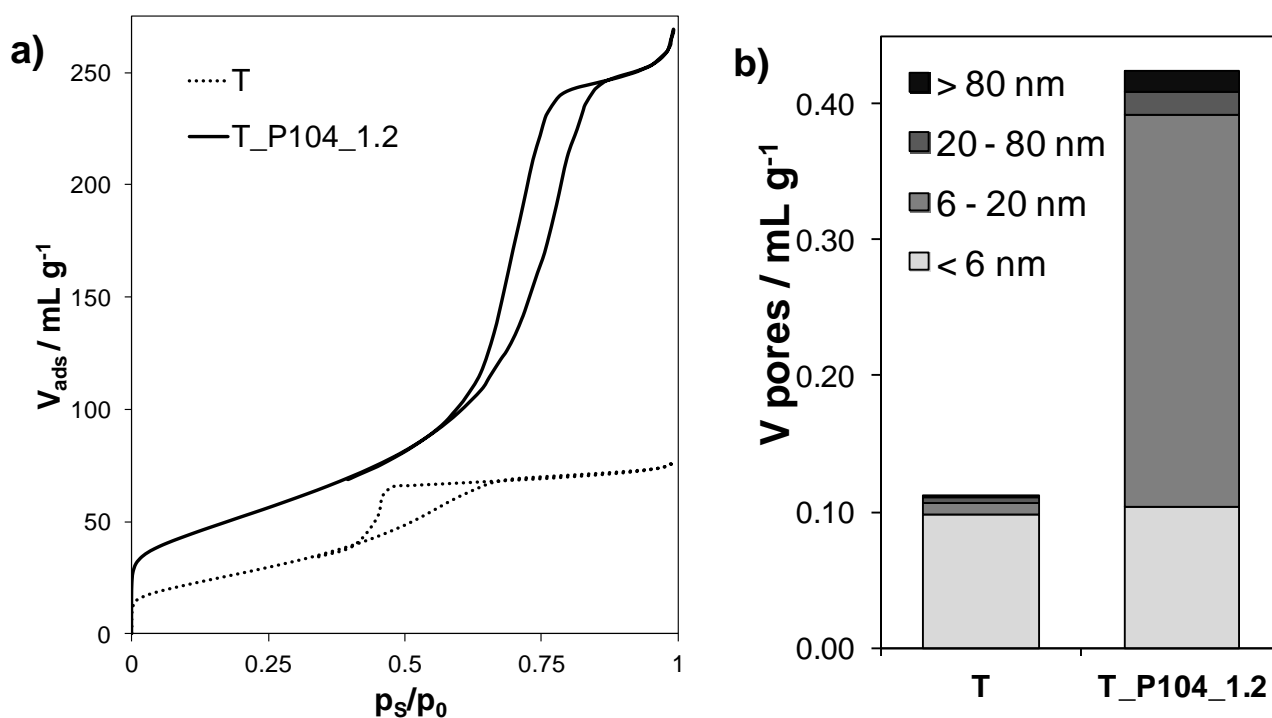
Figure 2.3.10 a) N$_2$ adsorption–desorption isotherms at subcritical temperatures and b) pore volume distribution of T and T_P104_1.2 samples.

Effect of the copolymer content. The role played by the amount of copolymer was investigated varying the concentration of P104 in the synthesis (expressed as the ratio between the number of ethoxy units and the number of Ti atoms, EO/Ti).

Varying the EO/Ti ratio results in slight changes in the structural features of the final oxide (Table 2.3.4). The obtained samples are composed by anatase and brookite polymorphs, and their average crystallite sizes are comparable to those observed by HRTEM analysis. The absence of rutile is expected from the adopted low calcination temperatures. Increasing the EO/Ti ratio causes a slight decrease in the average crystallite diameter and an increase in the brookite content, in agreement with the literature reporting the concurrent formation of the brookite and anatase polymorphs for crystallites of small size [Boiadjieva2004].

69

EO/Ti	% Anatase	% Brookite	d^a_{101} nm	S_{BET} $m^2\,g^{-1}$	V_{pores} $mL\,g^{-1}$
0	73	27	8	92	0.119
0.5	62	38	8	147	0.352
0.8	61	39	7	175	0.395
1.0	74	26	7	178	0.398
1.2	61	39	6	187	0.425
1.4	61	39	6	205	0.429
1.6	70	30	6	197	0.515

Table 2.3.4 Phase content, anatase crystallite sizes d^a_{101}, specific surface area S_{BET} and total pore volume V_{pores} of TiO$_2$ samples synthesized with P104 block copolymer as a function polymer content (EO/Ti).

The copolymer content has a more significant effect on the morphological characteristics of the oxide. The sample specific surface area and total pore volume steadily increase with increasing EO/Ti ratios (Table 2.3.4). On the contrary, the average pore size remains unchanged (ca. 7 nm) for all tested polymer concentrations (Figure 2.3.11), and all samples exhibit a narrow pore size distribution (65 - 70% pores within the 6-10 nm range).
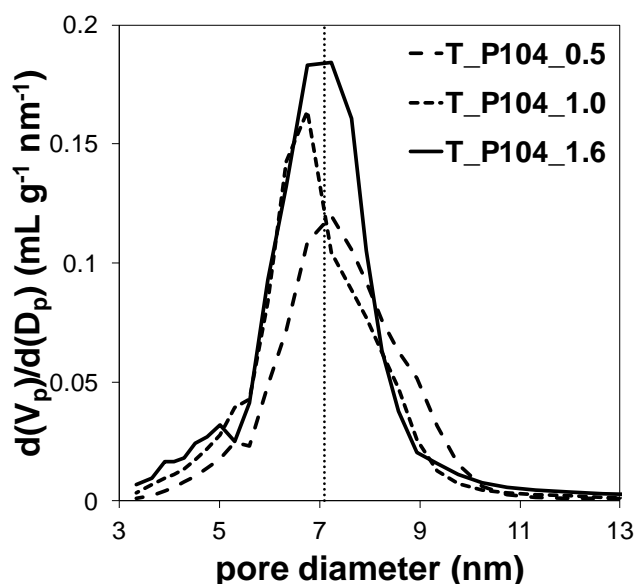
Figure 2.3.11 Pore size distribution curve of TiO$_2$ samples prepared by changing the P104 concentration.

Although the sample specific surface area and porosity increase steadily with the polymer concentration, at the highest tested concentrations the copolymer removal becomes more demanding, requiring progressively longer UV irradiation times. Thus, an EO/Ti ratio of 1.2 was adopted for testing the other two copolymers as this concentration guarantees both the obtainment of a high surface area and mesoporosity and a fast and complete removal of the copolymer.

Role of the copolymer structure. The effect of the copolymer structure on the oxide final features was investigated by employing three Pluronic copolymers, with different average molecular weight and HLB values.

The comparison was made keeping constant the adopted EO/Ti ratio (1.2). For all polymers, the adopted concentration was in any case at least two orders of magnitude higher than the relative critical micelle concentration (4.0, 3.1, 18.0 x 10^{-6} mol L^{-1} for P104, P123 and F127, respectively), whose values were determined by surface tension measurements.

Changing the copolymer type causes a marked effect on the morphology of the resulting oxide, as shown by the N_2 adsorption-desorption isotherms of samples obtained from different templating agents (Figure 2.3.12). A different shape of the hysteresis loop is appreciable as well as largely different total pore volumes and slight differences in the specific surface areas (Figure 2.3.12 inset).

Sample	S_{BET} m^2 g^{-1}	V_{pores} mL g^{-1}
T_P104_1.2	187	0.425
T_P123_1.2	199	0.391
T_F127_1.2	172	0.262
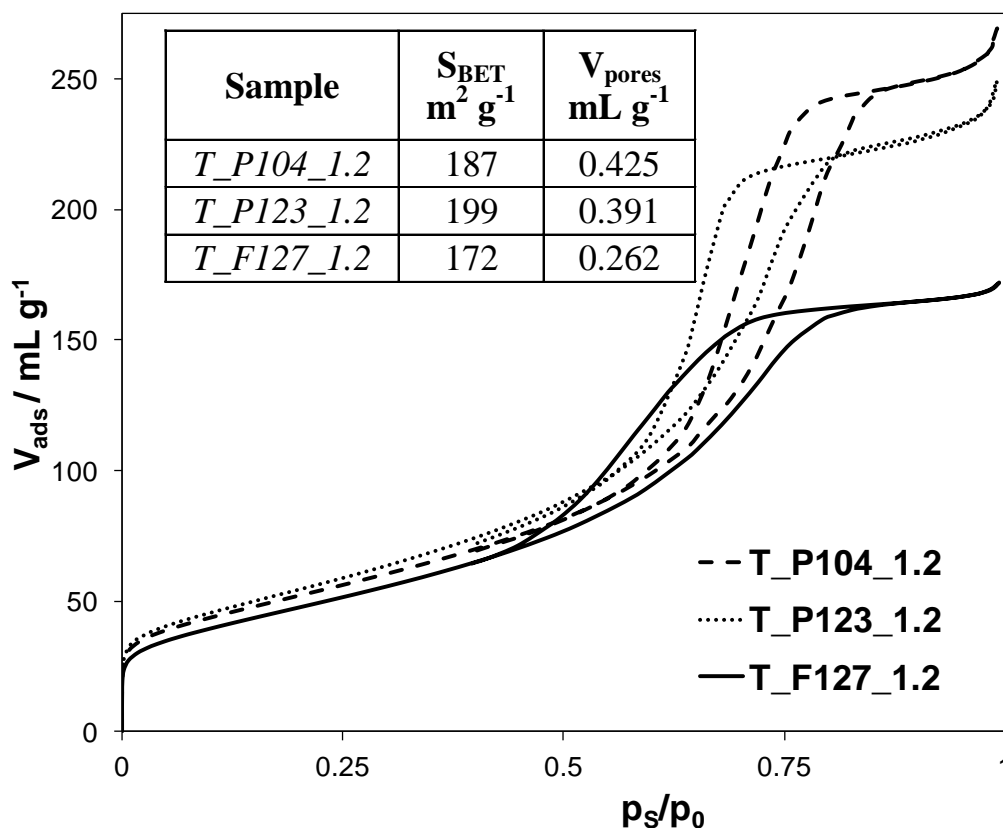
Figure 2.3.12 N_2 **adsorption-desorption hysteresis loops for samples obtained using the same EO/Ti ratio (1.2) but different templating agents. Inset: relative specific surface area, S_{BET}, and total pore volume, V_{pores}.**

Such differences may be related to the different aggregation behavior of the adopted copolymers. Since the relatively rapid solvent evaporation adopted in this study does not allow the formation of ordered mesostructures, the pore features are probably determined only by the micelle characteristics. Figure 2.3.13a shows the micelle size distributions of the adopted copolymers, determined by DLS. While both P104 and P123 exhibit a single size population centered at ca. 10-15 nm, in good agreement with the literature [Alexandridis1995b; Lee2011], F127 shows a multimodal distribution, with the main population centered around 4 nm. Indeed, the sequence of the main populations of micelle size reflects the sequence of the average pore size in the

mesoporous oxides (Figure 2.3.13b). T_F127_1.2 shows only one pore size component, possibly because the larger micelles lead to pores out of the mesoporosity range.
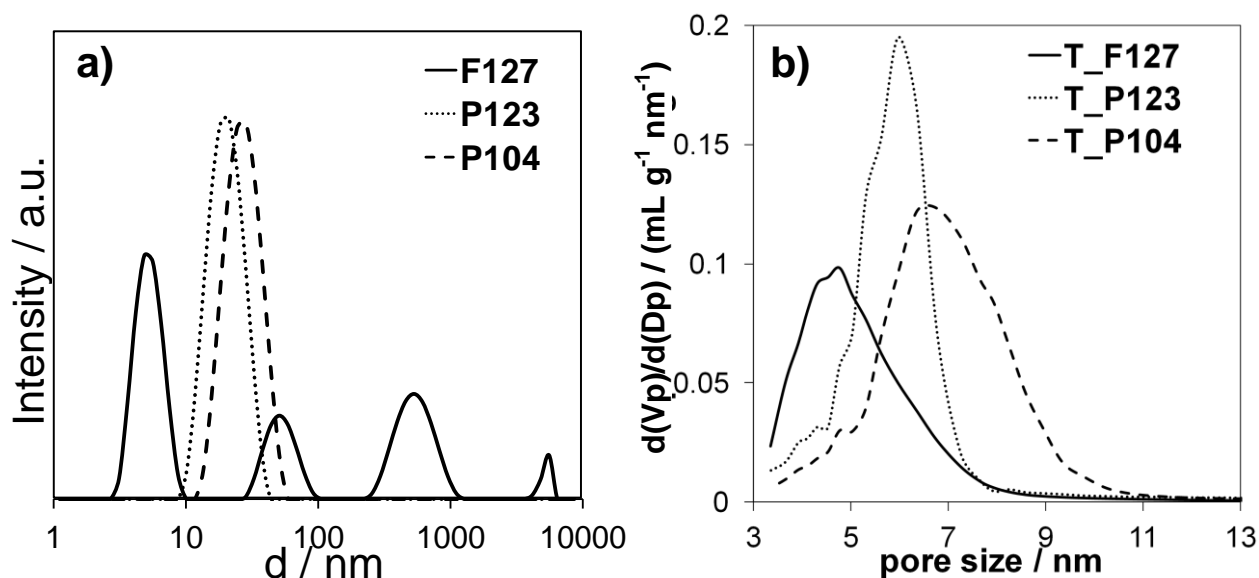
Figure 2.3.13 a) Micelle size distribution of the three Pluronic copolymers determined by DLS; b) pore size distribution of the relative TiO$_2$ samples.

Photocatalytic activity of mesoporous TiO$_2$. The photocatalytic activity of the obtained samples was tested towards the degradation of methylene blue stains under UV irradiation (Figure 2.3.14a,b). The final mineralization degree was considered, since it is well recognized that MB discoloration is not a reliable indicator of the molecule oxidation as the reduced form of MB (leuco MB) is colorless [Yogi2009].

All the mesoporous samples, excepted the one from the lowest tested EO/Ti ratio, exhibit mineralization degrees far higher than those of the reference sample T (45%) and of the traditional benchmark photocatalyst, Degussa P25 (38%) (Figure 2.3.14c). Figure 2.3.14c shows also the good linear correlation between mineralization degree and sample specific surface areas, which is irrespective of the copolymer type, *i.e.* of the sample average pore size. This observation can be rationalized considering that in tests of self-cleaning of dry surfaces, like the present experiment, the extension of the surface area determines the amount of pollutant directly adsorbed at the TiO$_2$ surface. Since in these cases, the degradation probably occurs via a direct oxidation at the photocatalyst surface, a larger surface area should lead to a faster oxidation while the pollutant diffusion into the photocatalyst pore network should play a minor effect.

Conclusions

Highly mesoporous and crystalline TiO$_2$ samples were produced by a template synthesis based on the nanoparticle route approach, using block copolymers of the Pluronic family (P123,

F127, P104) as structure directing agents. The latter (P104) was used for the first time in the synthesis of nano-TiO$_2$.

Synthetic parameters such as the template concentration and the template removal conditions, were carefully tailored to obtain high surface area and high porosity in the mesoporosity range as well as good crystallinity. The role played by the structure of the adopted copolymer was investigated, finding that the sequence of the mesopore size reflects the sequence of relative micelle size in water, as determined by DLS. Moreover, it was found that P104 and P123, copolymers exhibiting a relatively low molecular weight (ca. 6000) and intermediate HLB values, induce larger specific surface areas and pore volumes with respect to F127, possessing a twice as large molar weight and higher hydrophilic component.

As for the effect of the polymer amount, an almost linear correlation between the polymer content and the resulting specific surface area and total pore volume was observed. Such increase in the sample surface area and porosity is highly beneficial for the TiO$_2$ photocatalytic activity. In particular, the extent of the sample surface area plays a crucial role in the tested self-cleaning of a methylene blue stain over a dry surface.

2.4 Modulation of titania electronic and optical properties: doping and mixed oxides

Among the main limitations of TiO_2 are its large band gap, which limits the light absorption to the UV region, and its low quantum yield, which severely reduces the efficiency of phtocatalysis. A promising approach to solve these problems involves the modulation of the electronic properties of TiO_2, by either doping with metal or non-metal ions or by the addition of metal nanoparticles or mixed oxide phases. Indeed, doping with non-metals, such as nitrogen, is currently considered the most promising approach to TiO_2 visible-sensitization [Zhang2010]. On the other hand, noble metal nanoparticles have been consistently proposed to enhance quantum efficiency by promoting the separation of photogenerated charges [Sakthivel2004]. However, the high cost of noble metals has prompted search for alternatives, such as mixed oxides.

In the present thesis work, N-doping and the use of Bi_2O_3-TiO_2 composites have been investigated as effective and convenient routes to promote visible-light activity of TiO_2 and to boost its photocatalytic efficiency.

2.4.1 N-doped TiO$_2$

Titania doping with various transition metal and non-metal ions is one of the strategies more extensively investigated to enhance light absorption in the visible region. Dopants can substitute lattice ions or occupy an interstitial position, or can form mixed oxides or a mixture of oxides.

The effect of doping on titania photocatalytic activity is a complex problem, as the dopant addition may produce numerous effects, modifying, e.g.:

- ✓ the number of charge carriers;
- ✓ the catalyst spectral absorption;
- ✓ the adsorption capacity of the gas phase molecules at the catalyst surface (dopant ions can occupy surface sites modifying important surface properties, such as the point of zero charge, consequently altering the adsorption properties of the catalyst);
- ✓ the interfacial charge transfer rate (dopant ions can act as trapping sites for charge carriers, enhancing the electron-hole recombination rate).

The main aim of doping is to induce a bathochromic shift, i.e., a shift of the absorption edge of TiO_2 to longer wavelengths. One of the first strategies that has been explored to enhance titania

visible absorption was doping with metal ions. Substitution of Ti^{4+} by d^n metallic ions in the TiO_2 lattice creates allowed energy states in the band gap of TiO_2: They may induce photoactive transitions in the visible light, due to an excitation of an electron from this energy level into the TiO_2 conduction band. However, the doped materials suffer from thermal instability and increase of the charge carrier recombination rates. In fact, p-type dopants (i.e. heterocations of valencies lower than that of Ti^{4+}, like Al^{3+}, Cr^{3+} or Ga^{3+}) act as acceptor centers, which trap photoelectrons and, once negatively charged, attract holes, thus forming recombination centers. On the opposite, n-type dopants (heterocations of valencies higher than +4 , like Nb^{5+}, Ta^{5+}, Sb^{5+}) act as donor centers.

Thus, anion non-metal species such as C, S, B, F and N, have been considered to improve the photocatalytic efficiency of TiO_2 under visible light. Among the anion dopants, nitrogen has revealed itself to be one of the most promising. However, the mechanism of the visible light response in N-doped TiO_2 has not yet been clarified. One of the main debated questions concerns the electronic structure of these systems, i.e. whether the enhanced visible-light absorbance is due to a narrowed band gap or mainly to the introduction of localized impurity states in the band gap (intra-gap states). Further questions regard the actual localization of N species in the TiO_2 lattice either interstitial or substitutional and their interactions with oxygen vacancies.

Asahi et al. [Asahi2001] proposed that the substitutional doping of nitrogen into the TiO_2 lattice causes a significant red-shift of the absorption edge of TiO_2 by narrowing the titania band gap: their calculation predicted that N 2p states contribute to the band gap narrowing through mixing with O 2p states in the valence band. The same authors investigated interstitial doping of N and a combination of substitutional and interstitial doping of N, which might correspond to the introduction of molecular NO or N_2. Such molecularly existing dopants give rise to bonding states below the O 2p valence band and antibonding states deep in the band gap: both are well screened and not interacting with the band states of TiO_2, thus they are unlikely to be active for photocatalysis.

Irie et al. [Irie2003] proposed that an isolated narrow band formed above the valence band in N-doped titania is responsible for the visible light response. In addition, they found that an increase in the nitrogen concentration lowered the quantum yield under UV irradiation, indicating that the doping sites could also work as recombination centers. Lindgren et al. [Lindgren2003] used photoelectrochemical measurements to confirm that the nitrogen created states were located close to the valence band edge and that the conduction band edge remains unchanged by nitrogen doping.

Ihara and coworkers [Ihara2003] synthesized N-doped TiO_2 with oxygen deficient stoichiometry active in the visible; they proposed that oxygen deficient sites formed in the grain boundaries were responsible for the visible light response, while the presence of nitrogen only

improved the stabilization of these oxygen vacancies by preventing re-oxidation during heat treatments. Serpone [Serpone2006] argued that the visible light activation of the anion doped TiO_2 was the result of the formation of color centers associated with the oxygen vacancies created during the doping.

Reported experimental results also show considerable diversity. Several different methods have been presented in literature to incorporate nitrogen in titanium dioxide, and different sources of N have been adopted (NH_3/NH_4^+, amines, nitrides, etc) [Emeline2008]. Characterization analyses proved that the predominant type of N dopant species depends on the experimental synthetic conditions. Di Valentin's calculations [Di Valentin2005] suggested that substitutional N-doping can be stabilized by the presence of oxygen vacancies under oxygen-poor experimental conditions, whereas under oxygen-rich conditions interstitial N species become favored.

Absorption spectra of N-doped samples invariably exhibit a shift to the visible region, regardless of the preparative method employed and of the nature of the dopant. Nevertheless, visible-light photoactivity of N-doped TiO_2 appears to be highly sensitive to the preparative routes: although these materials absorb visible light, they are nonetheless frequently inactive in photooxidation, probably because of charge recombination effects [Emeline2008].

In the present thesis, N-doped TiO_2 prepared by different preparation methods and N-sources are compared with respect to their photocatalytic activity under UV, simulated solar and visible light (section 2.4.1.1). Moreover, the debated topic of the actual location of N-species into the TiO_2 lattice is investigated by combining EXAFS analysis and ab initio calculations (section 2.4.1.2).

2.4.1.1 Photocatalytic activity of N-doped TiO₂ under visible light

Nitrogen doping can be achieved by manifold synthetic procedures. Literature studies report both physical and wet-chemical synthetic procedures, such as sol-gel synthesis, precipitation methods, titanium nitride oxidation, N-ion bombardments at high energies, sputtering with Ar-N_2 gas, chemical vapor deposition, molecular beam epitaxial growth, spray pyrolysis, and post-treatment by NH_3 gas at high temperatures [Serpone2008]. Materials produced by so widely different preparation techniques possess largely different properties and conflicting photocatalytic results are often reported. Hence, direct comparisons between literature studies are often difficult to make and unifying conclusions about the photocatalytic properties of N-doped materials cannot be drawn.

In the present thesis, N-doped TiO_2 films were synthesized by different preparative routes (sol-gel and precipitation method) and different N-sources (ammonia and triethylamine). The

resulting materials are extensively characterized and tested for their photocatalytic activity towards the oxidation of both ethanol and acetaldehyde. The sequences of photoactivity of the N-doped samples under UV, simulated solar and visible light irradiation are discussed and related to the materials' surface/bulk properties, light absorption features, nature and amount of paramagnetic species.

Experimental section

All chemicals were of reagent grade purity and were used without further purification. Doubly distilled water passed through a Milli-Q apparatus was used to prepare solutions and suspensions.

TiO$_2$ preparation. A sol-gel synthesis from an alkoxide precursor and a precipitation synthesis from a TiCl$_3$ precursor were adopted to produce N-doped TiO$_2$ samples. In the case of sol-gel samples, either an inorganic (NH$_3$) or an organic (triethylamine, tea) nitrogen sources was employed.

In the sol-gel synthesis, 0.063 mol of Ti(OC$_3$H$_7$)$_4$ were dissolved in 24 mL of 2-propanol under stirring at 300 rpm. An aqueous basic solution (114 ml) was added dropwise to the alcoxide solution. In the case of the undoped TiO$_2$ sample (**Tsg**) and of the tea-doped sample (**Tsg_tea**), KOH was adopted as base. For the Tsg_tea synthesis, the N-source (tea, N/Ti initial molar ratio = 0.1) was also added to the base solution. In the case of the NH$_3$-doped sample (**Tsg_NH$_3$**), the base adopted was instead a buffer solution containing NH$_3$ and (NH$_4$)$_2$CO$_3$ (N/Ti initial molar ratio = 0.7). The final water/alkoxide molar ratio was 100, the water/2-propanol molar ratio was 20 and the calculated pH was 9. The suspension was stirred for 90 min at 25 °C, then dried in oven overnight. Dry powders were washed with milli-Q water by centrifugation and suspension cycles, till the washing solution conductivity was < 1 mS. Subsequently, the powders were calcined at 400 °C for 6 h under O$_2$ stream (9 NL/h).

The sample prepared by the precipitation route TiCl$_3$ (**Tp_NH$_3$**) was synthesized according to Bianchi et al. [Bianchi2009], adopting a final pH value of 9 and an N/Ti initial molar ratio of 7.0.

Although the starting N/Ti ratios are much different, the actual ratios, as determined by XPS analysis, are very close (in the range 0.015-0.022). Apparently an appreciable loss of N-species takes place during the annealing step.

Sample Characterization. X-ray powder diffraction (XRPD) patterns were collected at room-temperature between 10 and 80° with a Siemens D500 diffractometer, using the Cu Kα radiation. Rietveld refinement was performed using the GSAS software suite and its graphical

interface EXPGUI. The average crystallite diameter, d, was estimated from the most intense reflection (101) of the anatase phase using the Scherrer equation [].

Specific surface area was determined by the BET method using a Coulter SA3100. Pore size distribution was determined from desorption isotherms using the Barrett-Joyner-Halenda (BJH) method.

Particles morphology was investigated by scanning electron microscopy (SEM) using a FEI Quanta 200F FEG in high vacuum mode.

Diffuse reflectance spectra in the UV/vis region were acquired using a Cary 5G spectrophotometer, equipped with a diffuse reflectance accessory.

The presence of paramagnetic species was investigated by electron paramagnetic resonance (EPR). Spectra were collected on doped samples 24 h after the calcination, at room temperature, using a Bruker Elexsys X-band spectrometer at a working frequency of about 9.4 GHz. The spectral simulations were obtained by the Bruker SimFonia program.

The particle size distributions of the sample powders in aqueous solution were analyzed by a Beckman Coulter N4 analyzer.

The effect of N-doping on the TiO_2 electronic structure was modeled by periodic three-dimensional Density Functional Theory (DFT) calculations, performed using the VASP 4.6 code [Kresse1996] with the projector augmented wave (PAW) method [Kresse1999]. The generalized gradient approximation (GGA) by Perdew et al. [Perdew1996] was employed and the plane wave basis set cutoff was 400 eV. Geometry optimization with the conjugated gradient scheme was stopped when the forces on the atoms were less than 0.05 eV/Å. The Density of electronic States (DOS) for a 3x3x3 supercell model was calculated both at the Γ point of the Brillouin zone and using a 2x2x2 Monkhorst-Pack set of k-points to check basis set convergence.

Photocatalytic Tests. The photocatalytic activity of the samples was tested towards the degradation of two gas-phase pollutants (ethanol and acetaldehyde), using two different experimental set ups.

Photocatalytic oxidation of ethanol was carried out at 313 K under UV light in a custom-made batch reactor (Figure 2.4.1). An ethanol initial concentration of 275 ppm was adopted. TiO_2 samples were deposited in thin films (area 9.3 cm^2) by spin coating. The ethanol and CO_2 concentrations were monitored in time using mass spectrometry (peaks at 45 and 44 amu, respectively). The initial reaction rate (r_{init}) was determined from the slope of the first linear data points of ethanol disappearance, using the method of initial decay. No appreciable ethanol adsorption onto the TiO_2 layer was observed during dark experiments.
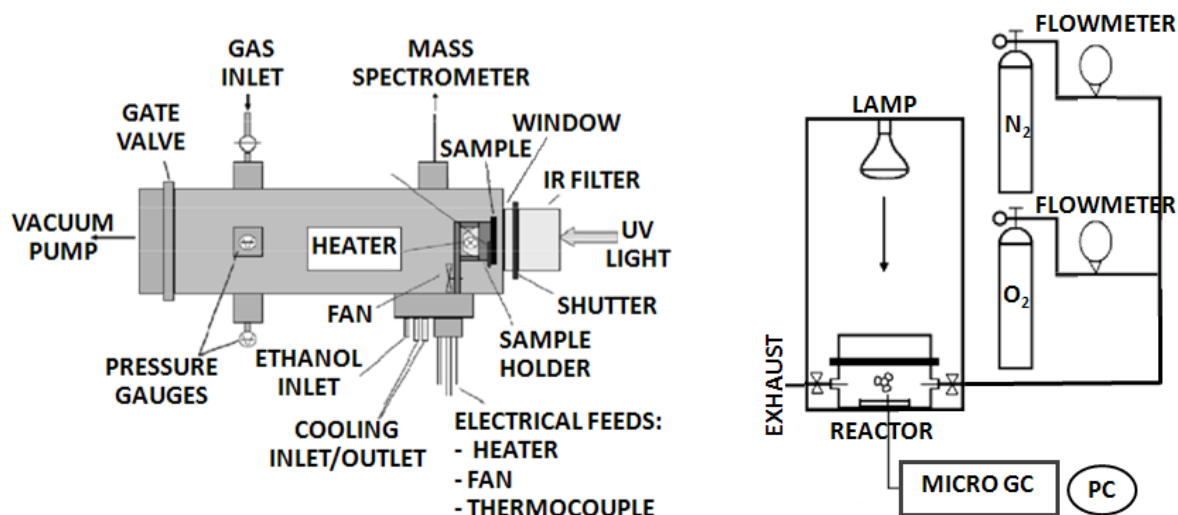
Figure 2.4.1 Photocatalytic set ups adopted for the degradation of ethanol (left) and acetaldehyde (right).

The photocatalytic tests of acetaldehyde degradation were carried out at 308 K in a Pyrex glass cylindrical reactor (Figure 2.4.1). TiO_2 samples were deposited in thin films by drop casting (area 66.4 cm^2). Acetaldehyde initial concentration was 300 ppm. The acetaldehyde disappearance and CO_2 formation were monitored using a micro-GC (3000A Agilent Technologies, equipped with RT PLOT Q and OV-1 columns and TCD detectors). An equilibration time of 15 min was adopted in order to evaluate the pollutant adsorption at the photocatalyst surface (from 25 to 50 ppm, depending on the sample adsorption properties). UV irradiation was provided by an iron halogenide lamp (Jelosil HG 500, photon flux 2.4 · 10^{-5} E dm^{-3} s^{-1}, emitting in the 315-400 nm range) and by a solar lamp (Radium Sanolux HRC 300-280, photon flux 1.2 · 10^{-5} E dm^{-3} s^{-1}, emitting in the 315-800 nm range). Visible tests were performed by cutting the UV portion of the solar lamp using a 400 nm cut-off filter (Edmund optics). Dark experiments revealed that acetaldehyde adsorption onto the TiO_2 layer accounts for the disappearance of 5-10% of acetaldehyde after 3 h, depending on the sample adsorption features.

Photolysis tests (irradiation without photocatalyst) were performed for both pollutants: No appreciable degradation was observed.

Fourier transform infrared (FTIR) spectroscopy was also employed to determine the chemical structure of the organic compounds at the surface of the used photocatalysts (Jasco 4200 spectrometer equipped with an attenuated total reflectance (ATR) module). The curves of the as prepared samples were subtracted from the spectra of the used photocatalyst.

Results and discussion

Structural and morphological properties. The structural features of the doped samples are remarkably influenced by nitrogen addition (Table 2.4.1). Anatase phase is promoted in N-doped

TiO$_2$, even though each N-sources has a different impact. While the undoped TiO$_2$ sample is a composite of anatase and brookite, Tsg_tea shows an increase in anatase content and the NH$_3$-doped samples are composed by pure anatase. The increased anatase content is accompanied as expected by an increase in the crystallite size with respect to the undoped Tsg (Table 2.4.1).

Sample	% Anatase	% Brookite	d_a^{101} nm
Tsg	71	29	7
Tsg_NH$_3$	100	-	15
Tsg_tea	77	23	9
Tp_NH$_3$	100	-	17

Table 2.4.1 Phase composition and average crystallite size of the pure and N-doped TiO$_2$ samples.

The sample morphology is as well affected by N-addition. N-doping results in marked aggregation phenomena, as appreciable from SEM images (Figure 2.4.2). SEM images are in agreement with the values of average particle size obtained by granulometric measurements (ca. 300 nm for Tsg vs. ca. 700 nm for Tsg_NH$_3$).
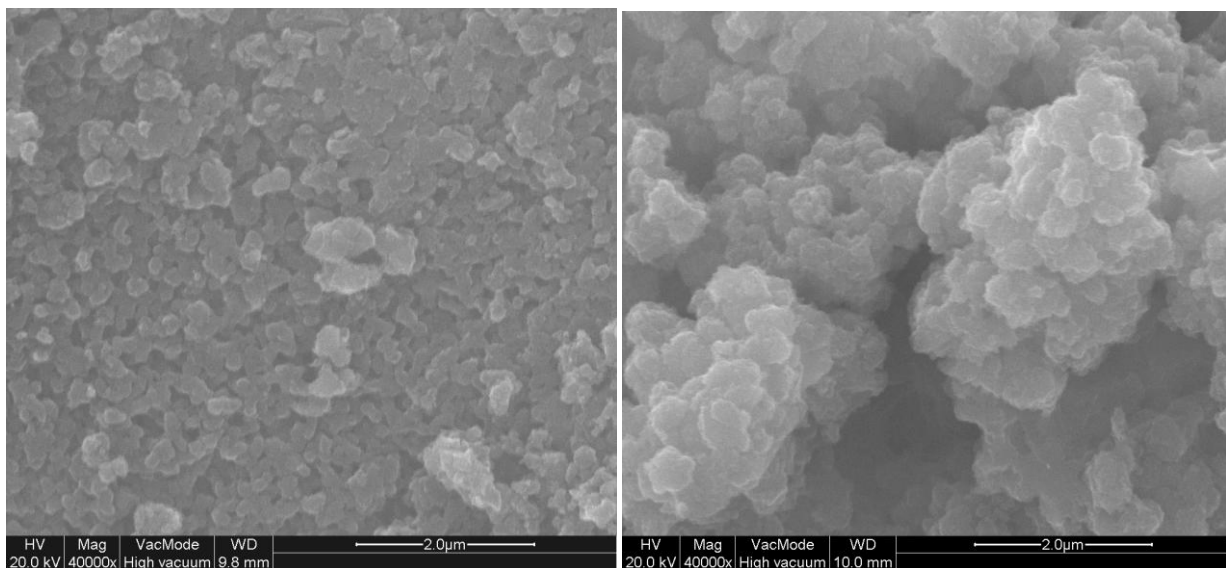
Figure 2.4.2 SEM images of a) Tsg and b) Tsg_NH$_3$.

The observed crystallite growth and sintering phenomena lead to a marked decrease of the specific surface areas of N-doped samples with respect to undoped TiO$_2$ (Figure 2.4.3 Inset). Sample porosity is also markedly influenced by the adopted synthetic route (Figure 2.4.3). Sol-gel samples present N$_2$ adsorption isotherms with relative hysteresis loops characteristic of bottleneck pores and a greater percentages of small pores (d < 6 nm). On the other hand, slit-shaped pores of larger dimensions are predominant in the precipitation method.

sample	S_{BET} $m^2 g^{-1}$	Vpores $mL\ g^{-1}$
Tsg	173	0.478
Tsg_NH$_3$	104	0.223
Tsg_tea	120	0.101
Tp_NH$_3$	98	0.468
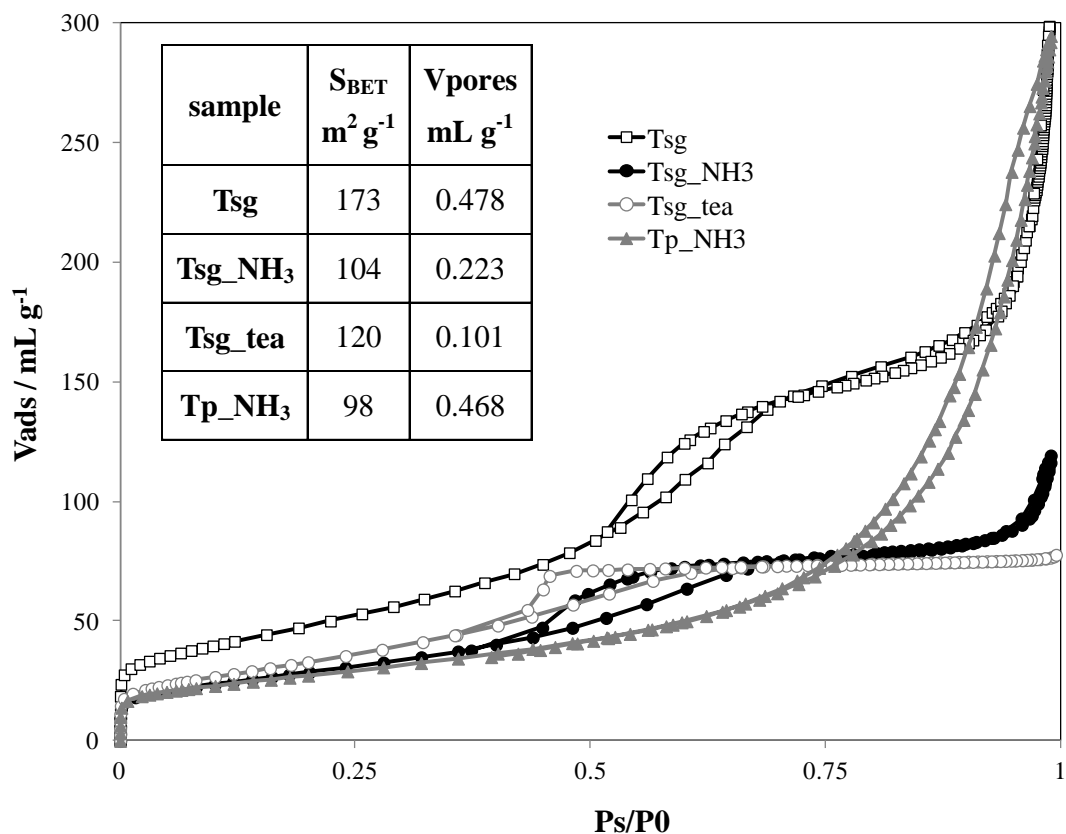
Figure 2.4.3 N$_2$ adsorption isotherms with relative hysteresis loops of pure and N-doped TiO$_2$ samples. Inset: Specific surface area (S$_{BET}$) and total pore volume.

Optical, electronic and magnetic properties. Diffuse reflectance spectra of the bare TiO$_2$ and the N-doped samples are reported in Figure 2.4.4. For all N-doped samples, an increased absorption in the visible region is observed. The sample Tsg_tea shows the largest visible absorption.

DFT calculations were performed in order to rationalize the optical properties of N-doped TiO$_2$ samples on the grounds of their electronic structure. Figure 2.4.4 (inset) shows the calculated electronic structure of N-doped TiO$_2$ both in the case of substitutional and interstitial N species. Both types of N-species generate intragap localized states. The observed bathochromic shift of the light absorption may thus be attributed to electronic transitions from these intragap localized levels to the conduction band, in agreement with the literature [Emeline2008, Zhang2010].
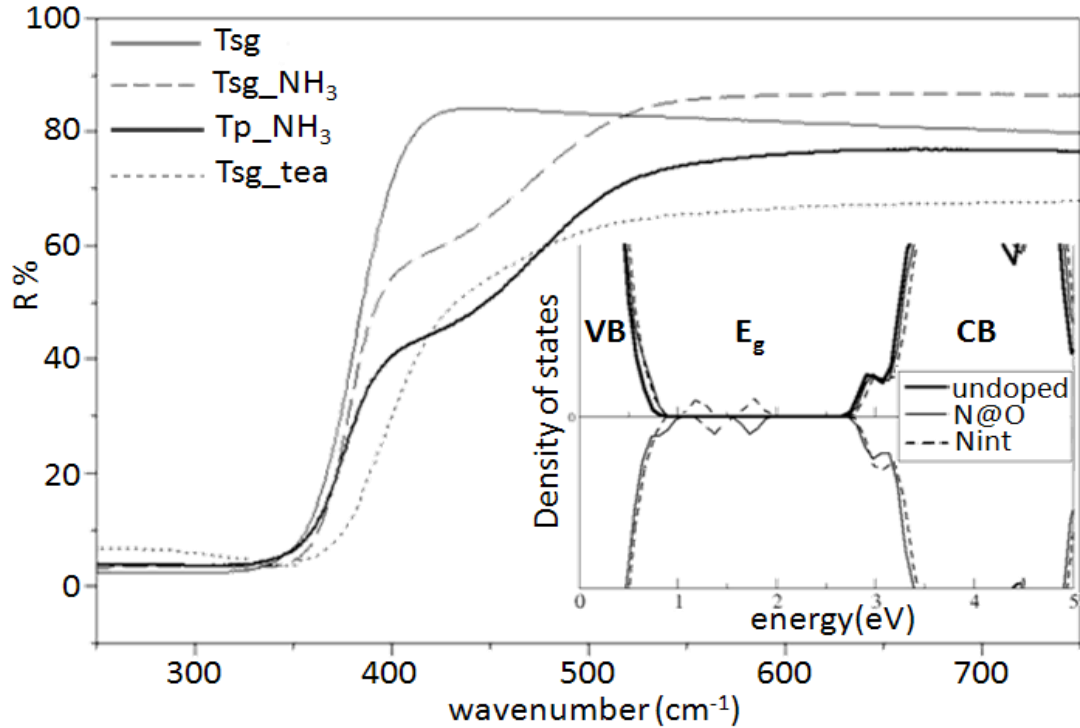
Figure 2.4.4 DRS spectra of pure and N-doped TiO$_2$ samples. Inset: Calculated Spin polarized Density of Electronic States (DOS) for undoped, substitutional and interstitial N-doping at a N/Ti stoichiometric ratio of 0.0185. Upper and lower panels for different spins.

The magnetic properties of N-doped samples were investigated by EPR spectroscopy (Figure 2.4.5). N-doping generates paramagnetic species that give rise to EPR signals. In the case of Tsg_NH$_3$ and Tsg_tea, similar EPR patterns are observed, which can be attributed to a N-paramagnetic defect located in the bulk of the TiO$_2$ nanocrystals ($N_b{}^\bullet$). These patterns were in fact simulated by hypothesizing an unpaired electron with Zeeman energy parameters $g_x = 2.0066$; $g_y = 2.0054$; $g_z = 2.0040$ and interacting with a nuclear magnetic moment $I = 1$ through the hyperfine coupling parameters $A_x \approx A_y \approx 3G$ and $A_z \approx 32.2G$. Tsg_NH$_3$ and Tsg_tea differ for the spectral intensities of the $N_b{}^\bullet$ patterns: Tsg_NH$_3$ shows a signal 1.46 more intense than that of Tsg_tea.

The precipitation sample Tp_NH$_3$ shows a completely different EPR pattern, showing an intense and broad peak. In this case, the signal attribution is more complex due to the low resolution of the pattern. However, a trace of the $N_b{}^\bullet$ signal was observed in this pattern by subtracting from it the EPR spectrum of a sample prepared by an identical synthetic procedure but with lower dopant amount.
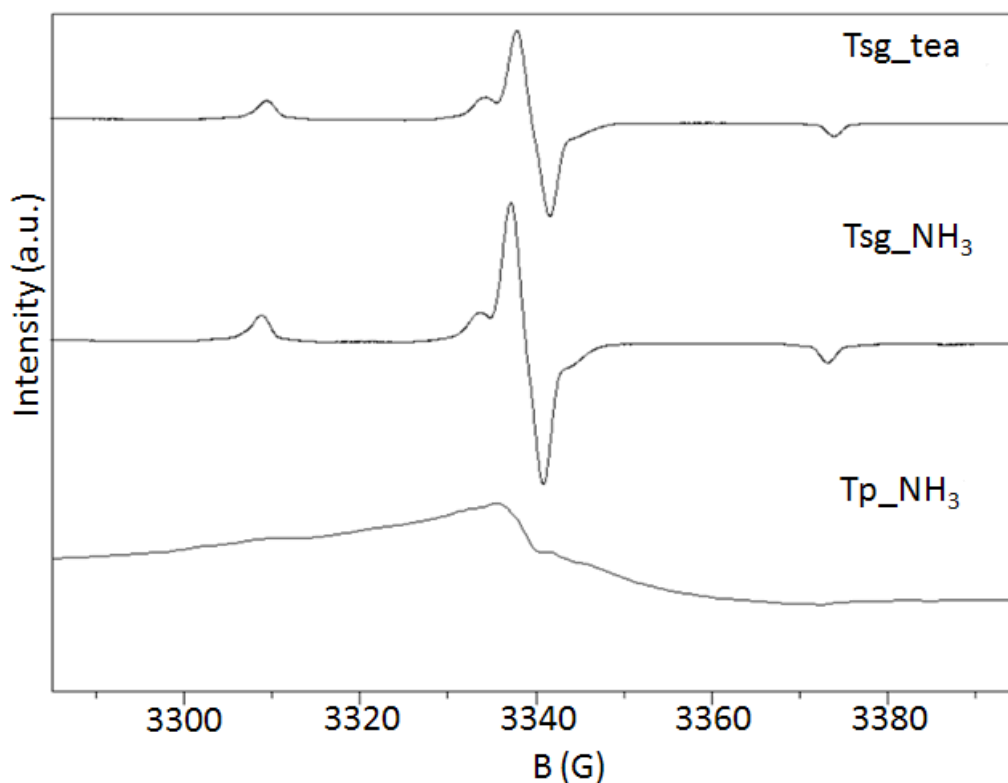
Figure 2.4.5 EPR spectra of N-doped samples.

Photocatalytic activity. The photocatalytic activities of the undoped and N-doped samples were investigated with respect to:

a. the oxidation of two different pollutants (ethanol and acetaldehyde) under the same kind of light irradiation (UV);

b. the degradation of the same pollutant (acetaldehyde) under UV, simulated solar and visible light irradiation.

Initial rates of pollutant photodegradation ($r_{init}^{pollutant}$) were obtained from the tangent of the initial part of the pollutant curve (the slope of the straight line interpolating the first 100 points).

Under UV light, degradation reactions of ethanol and acetaldehyde always reached completion in less than 140 min, as testified by the plateau value reaches by the CO_2 peaks. ATR-FTIR analysis of the used TiO_2 films confirmed the complete mineralization of the pollutants. FTIR spectra showed only peaks attributable to H_2O_{ad} ($\delta(OH)$ at 1635 cm^{-1}) and to CO_3^{2-} ($\nu_s(COO)$ at 1400 cm^{-1}). The degradation reactions proceeded instead more slowly under simulated solar irradiation, while an almost negligible mineralization was detected under visible irradiation.

Figure 2.4.6 reports the initial rates of pollutant degradation for all samples in the different photocatalytic tests.
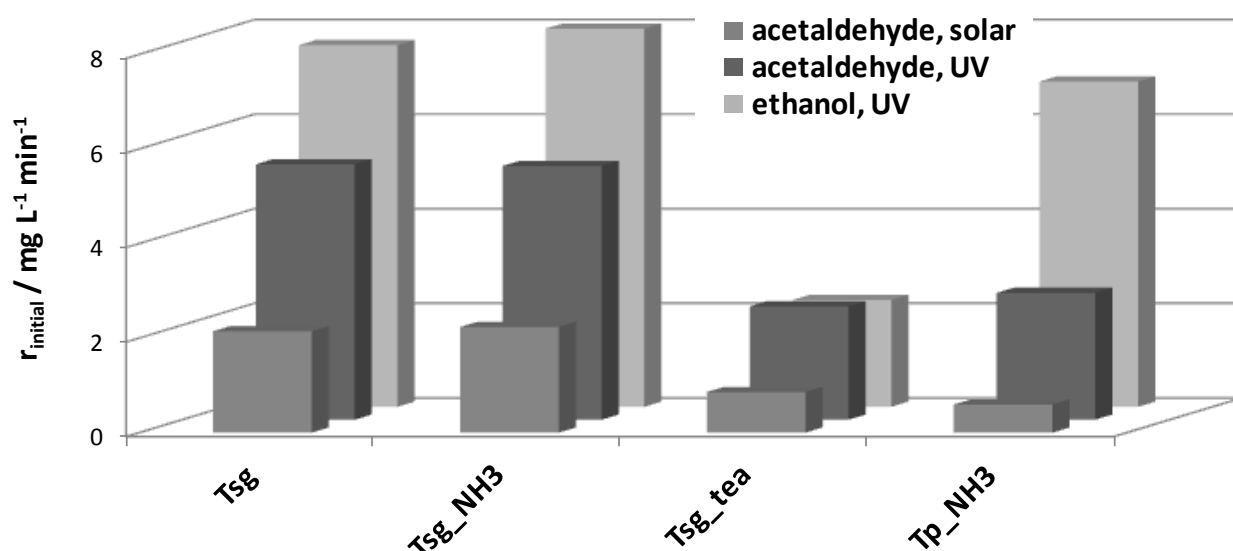
Figure 2.4.6 Initial rates of pollutant removal for ethanol and acetaldehyde photocatalytic degradation.

Concerning experiments under UV irradiation, the same sequence of photocatalytic activity was determined with respect to the two pollutants. The most active sample is Tsg_NH_3, which shows initial rates of photodegradation slightly higher than those of Tsg. The improved activity of Tsg_NH_3 is more striking if specific degradation percentages are considered, *i.e.* normalized with respect to the actual surface area (Table 2.4.2). A much lower activity is shown by the other N-doped samples, with Tsg_tea being the less active, especially for ethanol degradation.

Sample	Ethanol UV	Acetaldehyde UV	Acetaldehyde SOLAR
Tsg	32	12	10
Tsg_NH₃	57	21	17
Tsg_tea	14	8	6
Tp_NH₃	51	11	5

Table 2.4.2 Pollutant degradation percentages after a fixed time (30 min for UV, 60 min for solar) normalized with respect to the actual surface area of each sample.

The sequence of photocatalytic activity is strictly the same for ethanol and acetaldehyde degradation. Acetaldehyde is in fact the main intermediate in ethanol photocatalytic oxidation, and the fact that the same sequence is observed suggests that acetaldehyde degradation may be the rate determining step of ethanol oxidation. Since the activity sequence of the different samples was the same for the two pollutants, the role played by the irradiation source was investigated only in the case of acetaldehyde.

Also under solar irradiation, the sequence of sample activity observed under UV irradiation is maintained (Figure 2.4.6; Table 2.4.2). The presence of a small fraction of UV irradiation in the

simulated solar spectrum might mask any enhancement of sample activity in the visible region of N-doped samples. However, a relative photocatalytic improvement for the Tsg_tea sample with respect to Tp_NH₃was observed under simulated solar irradiation. To better investigate the visible activity (λ > 400 nm), photocatalytic tests were performed cutting off the UV region of solar irradiation with a suitable filter. Most of the samples did not show any significant photocatalytic activity under visible irradiation. The only active sample was Tsg_tea, although with a very low reaction rate.

Conclusions

Different synthetic procedures and N-sources were compared for the obtainment of N-doped TiO$_2$ samples with visible activity. All the synthesized samples showed a broad absorption in the visible region, which could be related to the formation of localized intragap electronic levels, as supported by first principles calculations. The photocatalytic activity of the samples was tested towards the degradation of two pollutants, ethanol and acetaldehyde, and under different irradiation sources. The same sequence of sample activity was observed under UV and solar irradiation for the two pollutants, indicating that the adsorption/degradation of acetaldehyde might be the rate determining step of the process. The most active sample under UV and solar irradiation was the oxide presenting the largest amount of paramagnetic $N_b^\bullet$ species (Tsg_NH₃). However, under visible irradiation the only sample presenting a detectable activity was Tsg_tea. This sample shows the largest visible absorption among the tested samples, and is a composite of anatase and brookite polymorphs, whose concomitant presence might hinder charge recombination processes.

2.4.1.2 Location of N-species in the TiO$_2$ lattice

Another debated aspect of N-doped TiO$_2$ concerns the location of the nitrogen anion in the TiO$_2$ lattice, generically labeled as N$_b$ (where b stands for bulk) [Othani2010]. So far experimental characterization techniques have failed in determining whether N species are located in interstitial or oxygen-substitutional position. Moreover, the presence of other chemical species such as NO$_x$ or NH$_x$ in the bulk of N-doped TiO$_2$ is still a debated topic.

The question of the location of N-species in the titania lattice is of pivotal importance because of the very different electronic structure of the resulting materials, which in turn affects the material photocatalytic properties [Di Valentin2007]. A substitutional or interstitial doping results in a different oxidative potential of the photogenerated hole and in a higher/lower recombination rate due to the different position of the localized intragap states (Figure 2.4.7).
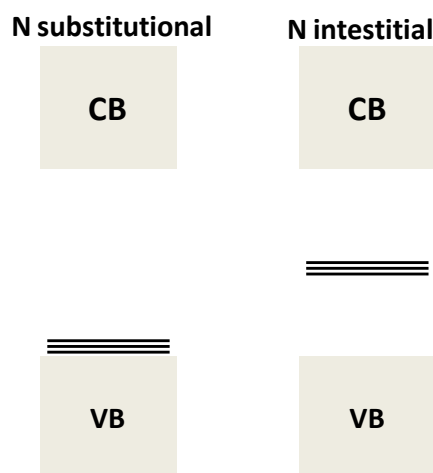
Figure 2.4.7 Scheme representing the electronic structure of substitutional (left) and interstitial (right) N-doped TiO$_2$.

Although ab initio calculations suggested a preferential interstitial location of N-species [Di Valentin2005], a conclusive experimental characterization of their lattice location has so far proved elusive. Among the most commonly employed techniques, X-ray photoelectron spectroscopy (XPS) of N1s provides noisy peaks, due to the low dopant concentration, which are representative only of the surface layers of the material. Other techniques, such as EPR, cannot discriminate between interstitial and substitutional doping [Oropeza2010].

In the present thesis work, the localization of N-species in doped TiO$_2$ was investigated by an innovative approach combining extended X-ray absorption fine structure (EXAFS) and Density Functional Theory (DFT) calculations. EXAFS represents a promising technique to study the localization of N species since it provides information on the local site symmetry and average bond lengths. Being sensible to short-range distortions, EXAFS can be conveniently exploited to study the dopant location in nanostructure materials [Fernandez-Garcia2004]. Here, DFT calculations at

different levels of theory are combined with Ti K-edge EXAFS to provide a detailed picture of the chemical environment surrounding the Ti atoms in N-doped TiO_2 samples. Several N-doped samples with different starting N/Ti ratio, prepared using triethylamine (tea) as N-source, were studied. In fact, a similar sample (Tsg_tea) proved to be the most photoactive N-doped sample under visible irradiation – see section 2.4.1.1.

Experimental section

N-doped TiO_2 synthesis. Pure (T) and doped titania samples (TN_x) were prepared by sol-gel synthesis using tea as N-source, adopting the procedure reported in section 2.4.1.1. The initial N/Ti molar ratio x was varied in the range 0.05-0.50.

EXAFS analysis. X-ray absorption curves were collected around Ti K-edge in transmission mode at room temperature at the BM01B beamline of the European Synchrotron Radiation Facility (ESRF). Sample tablets were prepared by diluting the material in $CaCO_3$ to avoid thickness effects. Pure TiO_2 and N-doped TiO_2 were analyzed in the 4.9-5.4 and 4.9-5.8 keV energy ranges, respectively, by employing a Si (111)-monochromated beam. Data processing and fitting were performed using the Horae suite of programs [Ravel2005] based on the IFEFFIT library [Newville2001]. As our samples contained a non-negligible fraction of brookite, backscattering paths belonging to both anatase and brookite crystal structures were considered. In the case of anatase phase, three Δr parameters were independently refined, corresponding to the Ti-O first-shell equatorial, Ti-O first-shell axial, and Ti-outer shell distances. Backscattering paths involving bulk N atoms were never considered explicitly in order to maintain the total number of parameters below the upper limit set by the Nyquist theorem ($N_{free} = 2\Delta k\Delta r/\pi + 1$). The effect of dopant N atoms was instead derived from the distortion of the average axial and equatorial Ti-O bond distances in the Ti first coordination shell.

Plane Wave Computational Setup. All calculations were spin-polarized and performed using the projector augmented wave (PAW) pseudopotentials to treat the valence-core interactions [Kresse1996]. The Perdew-Burke-Ernzerhof parametrization [Perdew1996] of the generalized gradient approximation [Perdew1992] was adopted for the exchange-correlation potential. The cutoff energy of the plane wave basis was 400 eV. Forces calculated through the Hellmann-Feyman theorem included the Harris-Foulkes corrections [Foulkes1989], and optimizations were performed using the conjugate-gradient scheme [Teter1989]. Iterative relaxation of atomic positions was stopped when the change in total energy between successive steps was less than 0.001 eV and residual forces were below 0.01 eV/Å. As far as the DFT+U approach is concerned [Dudarev1998]. This introduces an on-site correction in order to describe systems with localized d electrons. The

effective on-site Coulombic interactions U (U = U'- J) for Ti 3d were also used, where U' and J represent the energy cost of adding an extra electron at a particular site and the screened exchange energy, respectively. The U value was set at 5 eV since it has been reported to properly account for the electronic structure of the Ti 3d states [Stausholm-Moeller2010]. In order to reproduce the whole N/Ti molar range of the experimental samples, realistic supercell arrangements from 48 up to 162 atoms were employed. For the $Ti_{54}O_{108}$ supercell, reciprocal space sampling was restricted to the Γ-point, which is justified due to the rather large size of the used simulation supercells. For the $Ti_{16}O_{32}$ one, instead, a 5 x 5 x 5 Monkhorst-Pack [Monkhorst1976] k-point mesh was adopted.

Atom centered Gaussian DFT (all-electron) Computational Setup. Periodic optimizations of both pure and defective TiO_2 anatase were performed by solid-state calculations based on the atom-centered linear combination of Gaussian-type functions (LCGTF). The CRYSTAL06 code was employed, adopting a triple-ζ basis sets previously optimized for calculations of inorganic solids[1] and both spin-polarized B3-LYP [Dovesi2006] and PBE0 [Adamo1999] Hamiltonians. To speed up convergence, the frozen-core Stuttgart-Dresden ECP10MDF pseudopotential[2] was applied to Ti atoms in all the N_{int} interstitial solid state optimizations. The starting electron populations on Ti, O, and N were always chosen so that the crystal cell was always electrically neutral.

Results and discussion

EXAFS. Figure 2.4.8 reports the normalized Ti K-edge absorption curve in the relevant edge and post-edge regions of an N-doped TiO_2 sample.
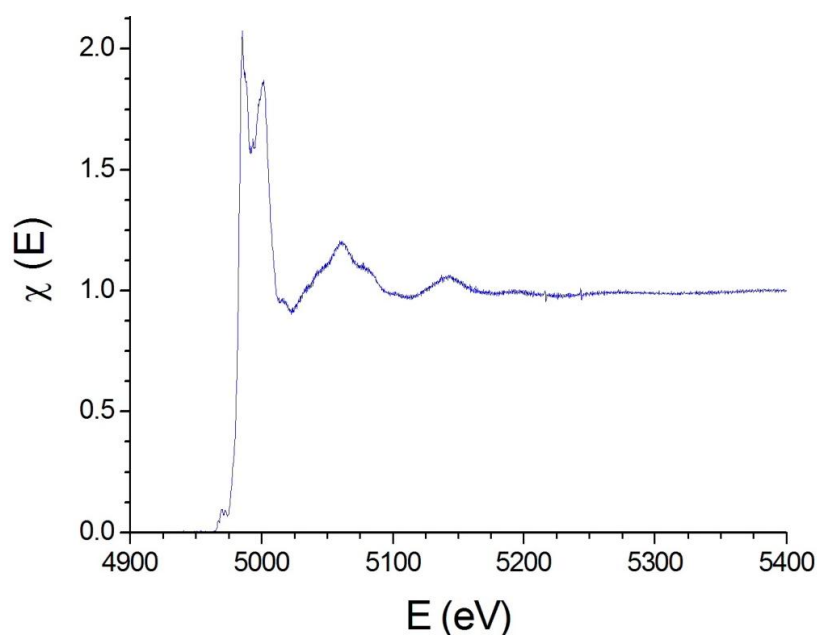
Figure 2.4.8 Normalized Ti K-edge XAS spectrum of TN_0.10.

---

[1] Towler, M. CRYSTAL Resources Page. http://www.tcm.phy.cam.ac.uk/ ~mdt26/crystal.html.

[2] Anderung, L. Pseudopotentials, ECPs http://www.theochem.unistuttgart.de/pseudopotentials/index.en.html.

The average Ti-O distances obtained by the fitting EXAFS data are reported in Figure 2.4.9. Since the scatterer (Ti) is at the centre of an octahedron of O first neighbors, the Ti-O distances can be divided in axial and equatorial Ti-O bonds of the Ti-centered octahedron.
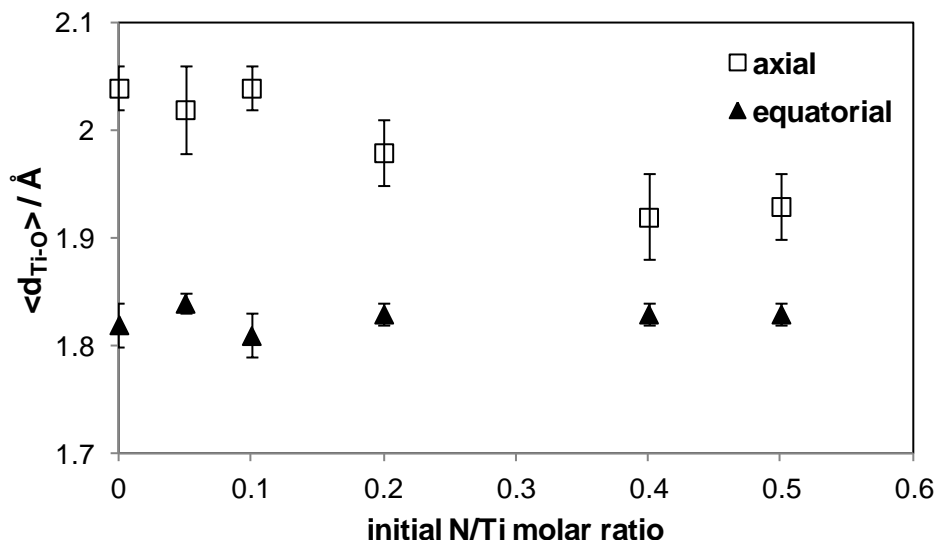
Figure 2.4.9 Average axial and equatorial Ti-O distances within the first coordination shell of Ti as a function of the initial N/Ti ratio.

Figure 2.4.9 shows that the equatorial distances remains basically constant throughout the whole doping range, while the axial distances undergo a reduction (~0.1 Å) when N/Ti molar ratio exceed 0.1, then they remain constant up to the maximum dopant starting concentration.

DFT Modeling. DFT calculations were employed to estimate the average Ti-O axial and equatorial distances in both pure and N-doped TiO_2, either substitutional or interstitial.

Bond		Bare TiO_2	N substitutional equatorial	axial	N interstitial equatorial	axial
Axial	**Ti-O1**	2.00/2.00/1.98	2.01/2.04/2.02	2.03/2.03/2.00	2.00/2.04/2.02	1.89/1.85/1.85
	Ti-O2	2.00/2.00/1.98	2.01/2.01/1.99	-	1.97/1.96/1.94	2.37/2.38/2.35
Equatorial	**Ti-O3**	1.94/1.95/1.94	-	1.93/1.94/1.93	1.90/1.91/1.90	1.94/1.96/1.95
	Ti-O4	1.94/1.95/1.94	1.94/1.94/1.92	1.93/1.94/1.93	2.12/2.13/2.11	1.94/1.96/1.94
	Ti-O5	1.94/1.95/1.94	1.93/1.94/1.93	1.94/1.95/1.94	1.98/2.04/2.02	1.94/1.95/1.94
	Ti-O6	1.94/1.95/1.94	1.93/1.94/1.93	1.95/1.95/1.94	1.99/1.99/1.98	1.94/1.95/1.94
Ti-N		-	1.96/1.98/1.96	2.08/2.10/2.09	2.08/2.06/2.04	2.33/2.48/2.42
NO		-	-	-	1.34/1.37/1.36	1.34/1.37/1.36

Table 2.4.3 Ti nearest neighbors distances (in Å) calculated by PAW with PBE, LCGTF with B3-LYP hamiltonian and LCGTF with PBE0 hamiltonian, respectively.

In the case of pure anatase TiO_2, the axial Ti-O bonds are 2.00 Å long, while all the equatorial ones are 1.94 Å, as reported in Table 2.4.3. The different DFT approaches (PAW with PBE and LCGTF with B3-LYP and PBE0 hamiltonians) show a good agreement (within three digits), so in the following only PAW-DFT data will be presented and commented.

In the case of N-doped TiO_2, both substitutional and interstitial doping give rise to a change of the octahedron shape. The octahedron geometries for substitutional and interstitial N-doping are reported in Figure 2.4.10.
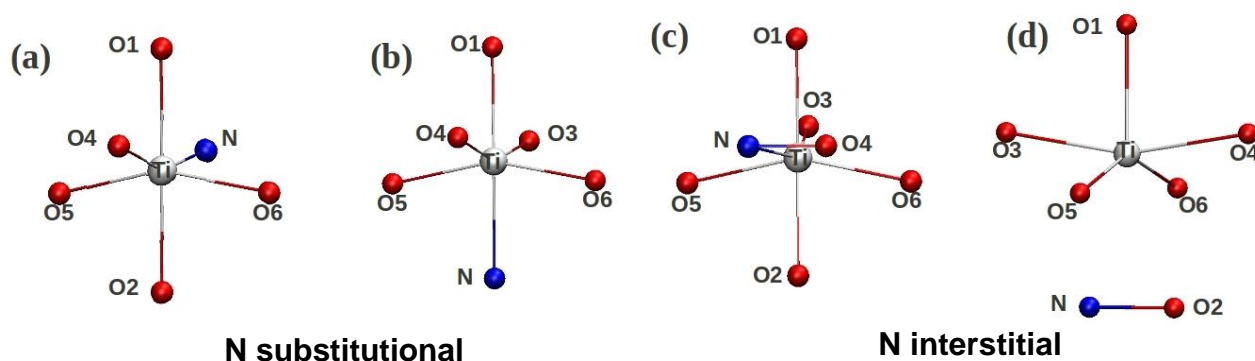
Figure 2.4.10 Structures of substitutional (a,b) and interstitial (c,d) N-doping in axial and equatorial positions.

Substitutional doping preserves the octahedral symmetry and the bond distances of the original anatase phase (Figure 2.4.10a,b), whereas in the case of interstitial doping, the octahedral symmetry is broken, and the distances vary significantly (Figure 2.4.10c,d),. Such dissimilarities can be better appreciated by comparing the Ti-first neighbors distances reported in Table 2.4.3. In the case of substitutional doping, the axial and equatorial average distances are almost unchanged with respect to undoped TiO_2 (2.03 and 1.94 Å, respectively). Concerning interstitial N-species, an equatorial doping results in a marked increase of all Ti-O distances, except the O atom trans-equatorial from the interstitial nitrogen. In the case of axial interstitial doping, instead, axial distances are very much elongated, while equatorial ones are left almost unchanged. However, even if the axial and equatorial geometries for the same kind of doping (substitutional or interstitial) look different when a single octahedron is considered, they are actually equivalent (a equivalent to b and c equivalent to d) in the lattice periodic framework, *i.e.* when the neighboring Ti atom is taken as the octahedron center. So, both structures (c and d) are present in the case of interstitial N-doping and the octahedron can be considered as broken for both geometries.

The DFT calculations of the Ti-O equatorial and axial distances were repeated taking into account the effect of the presence of oxygen vacancies in the local geometrical arrangement, in order to provide a more realistic modeling of N-doped TiO_2. Figure 2.4.11 reports the equilibrium octahedron geometries for undoped TiO_2 in the presence of O-vacancy.
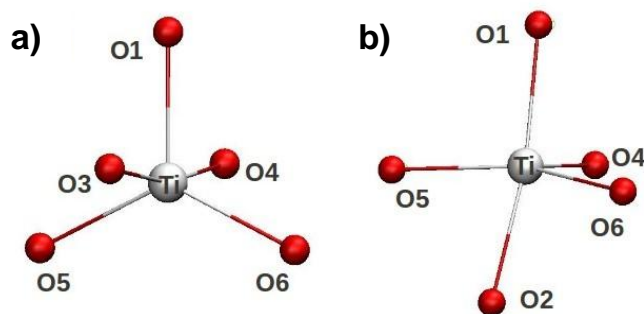
Figure 2.4.11 Nearest Ti neighbors in undoped TiO$_2$ in the presence of axial (a) and equatorial (b) O vacancies.

As a results of the vacancy introduction, the axial distances are reduced and become similar to the unaltered equatorial ones (Table 2.4.4). As a consequence, a single set of distances would be observed in this case by EXAFS analysis.

Bond		Undoped TiO$_2$		N substitutional		N interstitial	
		equatorial	axial	equatorial	axial	equatorial	axial
Axial	**Ti-O1**	1.92	vacancy	vacancy	2.03	2.03	1.88
	Ti-O2	1.96	1.86	1.88	-	vacancy	vacancy
Equatorial	**Ti-O3**	vacancy	1.93	-	1.93	1.93	1.93
	Ti-O4	1.81	1.92	1.9	1.93	1.93	1.93
	Ti-O5	1.92	1.9	1.94	1.81	1.81	1.94
	Ti-O6	1.91	1.9	1.94	vacancy	1.81	1.94
Ti-N		-	-	1.9	1.9	1.9	2.24
NO		-	-	-	-	1.46	1.46

Table 2.4.4 Ti nearest neighbors distances (in Å) calculated by PAW-DFT for oxygen defective octahedral.

The equilibrium geometries calculated for the concomitant occurrence of N-doping and O-vacancy around the same Ti ion are instead reported in Figure 2.4.12.
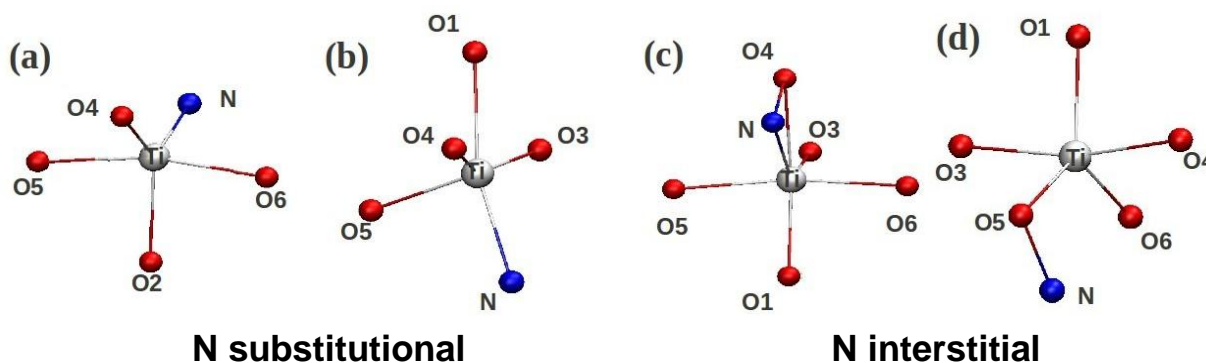
Figure 2.4.12 Ti octahedron geometries of substitutional (a,b) and interstitial (c,d) N-doping in the presence of axial and equatorial oxygen vacancies, respectively.

In substitutional doping, the introduction of an axial vacancy does not alter the original octahedral shape, whereas equatorial vacancies cause the Ti-N axis to tilt with respect to the original octahedron axis. In the case of interstitial doping, the introduction of a vacancy in both the equatorial and axial positions results in the migration of the NO moiety to compensate the O-vacancy by placing the oxygen next to the vacancy. The variation of the Ti-O distances can be better appreciated from Table 2.4.4.

The average equatorial and axial distances calculated using PAW-DFT are summarized in Table 2.4.5.

Ti-O	Undoped	N substitutional	N interstitial	Undoped + O-vacancy	N substitutional + O-vacancy	N interstitial + O-vacancy
equatorial	1.94	1.94	1.98	1.90	1.91	1.90
axial	2.00	2.03	2.11	1.91	1.94	2.05

Table 2.4.5 Average equatorial and axial Ti-O(N) distances (in Å) calculated by PAW-DFT.

To summarize, substitutional doping does not significantly modify the original octahedral distances, whereas interstitial doping results in elongated axial distances. The creation of O-vacancies strongly affects the Ti-O distances of undoped TiO_2 since axial and equatorial distances become almost degenerate. The less frequent scenario in which doping occurs within the same octahedron containing an O-vacancy, was also considered. In such situation, substitutional doping does not significantly alter the equatorial and axial distances with respect to non-defective N-substitutional doping. Instead, when interstitial N shares the same Ti center with an O-vacancy, axial distances are elongated and equatorial ones shortened. The latter two situations may become significant for highly defective TiO_2.

By comparing EXAFS results with data presented in Table 2.4.5, conclusions can be drawn about the preferential location of N-species in the investigated range of N/Ti ratio. Since the original anatase axial and equatorial distances are preserved for initial N/Ti molar ratios below or equal to 0.1, in this range the N-doping seems to occur either superficially or substitutionally. Instead, at higher dopant concentration axial distances observed by EXAFS are reduced. This phenomenon can be rationalized assuming the formation of O-vacancies as an indirect effect of N doping. The formation of O-vacancies at high N doping has been reported to be favored because the O-vacancy extra electrons may be partially accommodated by empty midgap N electronic states [Yang2010; Kuznetsov2009]. At high N/Ti level, it cannot be distinguished if the N-content is either substitutional or interstitial since EXAFS gives an average picture of the sample and the effect of oxygen vacancies is predominant.

The presence of O-vacancies at high N/Ti ratios is confirmed by XPS analysis in the Ti 2p region (Figure 2.4.13), which shows the presence of Ti^{3+} as a shoulder of the Ti^{4+} main component for TN_0.5.
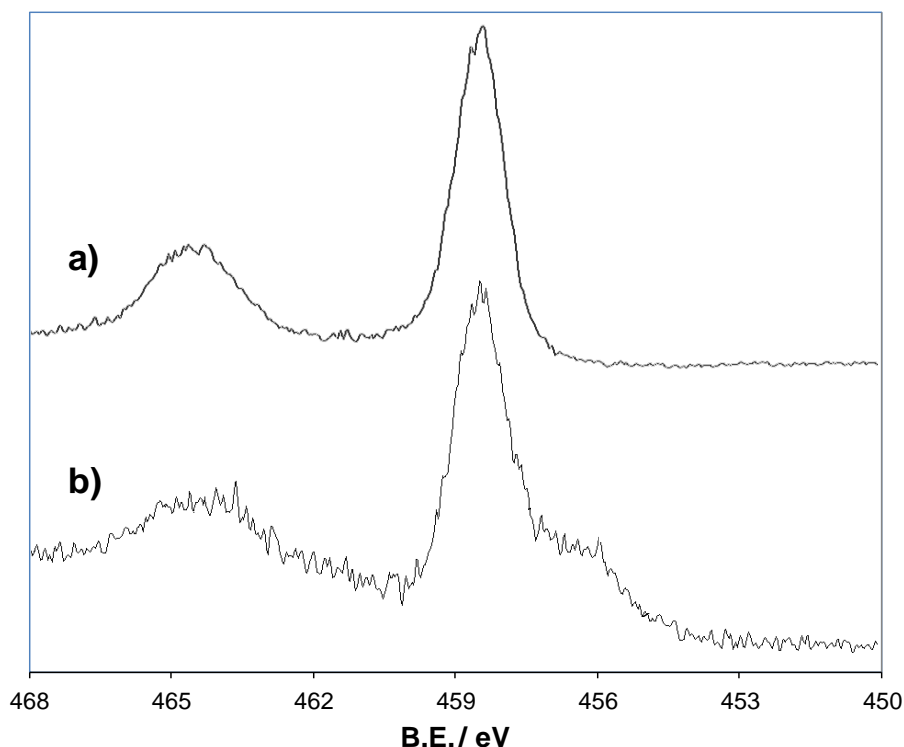
Figure 2.4.13 Ti 2p XPS spectra of a) TN_0.10 and b) TN_0.50.

Conclusions

A combined experimental and theoretical approach was employed to clarify the lattice location of N-species in N-doped materials, an aspect lively debated in the literature and of both fundamental and applicative interest. EXAFS determinations and DFT calculations were used to investigate the average Ti nearest neighbors distances in a series of N-doped TiO_2 samples. By comparing experimental and theoretical average Ti-O distances, two different regions of N-doping were observed. At low initial N/Ti molar ratios (≤ 0.10), substitutional doping seems prevalent, while at higher molar ratios the formation of oxygen vacancies is appreciable. Interestingly, the TN_0.1 sample, which showed photocatalytic activity towards the photocatalytic degradation of acetaldehyde under visible light (section 2.4.1.1), presents the highest concentration of substitutional doping without significant presence of oxygen vacancies.

2.4.2 Bi_2O_3-TiO_2 nanocomposites

The surface modification of TiO_2 nanomaterials with metal nanoparticles or other semiconductors has been reported to alter the charge-transfer properties between TiO_2 and the surrounding environment, resulting in enhanced photocatalytic activity of TiO_2-based material [Chen2007]. Among metal nanoparticles, noble metals are known to significantly improve the TiO_2 photocatalytic activity by promoting the separation of charge carriers at TiO_2-metal nanoheterojunctions [Sakthivel2004]. Surface modification with other semiconductors represents a convenient alternative to metals. Among oxide semiconductors, Bi_2O_3 has attracted growing interest in fields such as photocatalysis, photovoltaics, and hydrogen production [Jing2009; Shamaila2010]. Bi_2O_3 is a non-toxic and environmentally friendly semiconductor that represents a promising material for surface modification of TiO_2. In fact, theoretical calculations [Long 2009] have shown that Bi_2O_3, thanks to its band structure, could trap photo-generated electrons at the TiO_2 surface and thus significantly improve the material photocatalytic efficiency [Bian2008]. Photoluminescence experiments [Shamaila2010] have indeed shown a reduced radiative recombination process of photogenerated charges in Bi_2O_3-TiO_2 composites, although no direct evidence of the actual reduced recombination rate has so far been reported in the literature.

In the present thesis, Bi_2O_3-TiO_2 composites were synthesized and tested for their photocatalytic activity towards the degradation of different pollutants. Moreover, photocurrent measurements were performed to allow a direct evaluation of the effect of Bi addition on the rate of recombination of photogenerated electron-hole pair.

Further, mesoporous TiO_2 (obtained by template synthesis, see section 2.3.2) was employed as host for Bi_2O_3 precipitation. Indeed, the use of mesoporous networks as scaffolds for metal nanoparticles has been reported to give rise to more active and durable photocatalysts [Wu2005; Kitamura2004]. In a metal-mesoporous TiO_2 composite, the metal is better dispersed and forms numerous semiconductor-metal nanoheterojunctions, where electrons can migrate from the semiconductor surface to the metal, thus efficiently suppressing electron-hole recombination. In addition, the robust pore channels of the mesoporous TiO_2 films encapsulate the metal nanoparticles, enhancing their mechanical and thermal stability [Sanchez2008]. Composites of mixed oxide onto a mesoporous scaffold have also been proposed as efficient photocatalysts. They show improved mechanical robustness, thermal stability, and higher surface area with respect to composites with traditional sol-gel TiO_2 [Bosc2006].

Although very promising, composite materials of Bi_2O_3 and mesoporous titania are scantly investigated in the literature [Shamaila2010]. In the present work, highly dispersed Bi_2O_3-

mesoporous TiO_2 composites are synthesized and their photocatalytic activity is compared to that of Bi_2O_3-TiO_2 composites, in which the titanium oxide is obtained by a traditional sol-gel reaction, in order to highlight possible effects introduced by the mesoporous structure of the host oxide.

Experimental section

All of the chemicals were of reagent grade purity and were used without further purification; doubly distilled water passed through a Milli-Q apparatus was used to prepare solutions and suspensions.

Synthesis of Bi$_2$O$_3$-TiO$_2$ composites. Bi_2O_3-TiO_2 materials were synthesized by direct impregnation [Di Paola2002; Shamaila2010] of the calcined TiO_2 powders (a classical sol-gel sample, Tsg, and the mesoporous sample T_P104_1.2, see section 2.3.2) with a 0.1 M acidic solution of $Bi(NO_3)_3$. A starting Bi/Ti molar ratio of 0.02 was adopted on the grounds of literature results [Shamaila2010]. The powders were dried at 90° and then calcined at 350 °C in static air for 5 h using a heating ramp of 3 °C min^{-1}.

Samples Characterization. X-ray powder diffraction (XRPD) patterns were collected at room-temperature between 10 and 80° with a Siemens D500 diffractometer, using the Cu Kα radiation. Rietveld refinement was performed using the GSAS software suite and its graphical interface EXPGUI. The average crystallite diameter, d, was estimated from the most intense reflection (101) of the anatase phase using the Scherrer equation.

Specific surface area was determined by the BET method using a Coulter SA3100. Pore size distribution was determined from desorption isotherms using the Barrett-Joyner-Halenda (BJH) method.

Particles morphology was investigated by high resolution transmission electron microscopy (HR-TEM), using a 300 kV JEOL JEM 3010UHR microscope fitted with a LaB_6 single crystal filament and an energy dispersive X-ray (EDX) detector (Oxford INCA Energy TEM 200). All samples were dry deposited on Cu "holey" carbon grids (200 mesh).

The Bi content in the composite samples was estimated by energy-dispersive X-ray spectroscopy (EDX) using an HITACHI TM-1000 Scanning Electron Microscope (SEM) equipped with EDX probe (Hitachi ED3000).

The electrophoretic mobility and zeta potential of the composite powders dispersed in a 10^{-2} M KNO_3 basic solution (pH 8) were determined using a Coulter DELSA apparatus.

Fourier Transform Infrared (FTIR) spectra of the composite powders were recorded on a Bruker IFS 113v spectrometer equipped with MCT detector. Samples were first activated in high vacuum ($<10^{-4}$ Torr) either at IR beam temperature (RT, ca. 30 °C higher than room temperature) or

at 250° (to get rid of physisorbed and weakly adsorbed surface species). The, samples were pressed into self-supporting pellets (approx 10-15 mg cm^{-2}) and placed in a quartz cell equipped with KBr windows.

The sample photocatalytic activity was tested towards the mineralization of both methylene blue in dry conditions and of formic acid in aqueous solution. For the methylene blue tests, a TiO$_2$ film (100 mg, total surface area 100 cm^2) was stained with an isopropanol solution of methylene blue (5 mmol). The stain was allowed to dry, then the film was irradiated for 7 h under UV-A irradiation. The photon sources was an iron halogenide lamps (Jelosil HG500) emitting in the 315-400 nm wavelength range (effective total power 85 mW). The final mineralization of methylene blue was determined by chemical oxygen demand (COD) measurements using a Merck Spectroquant apparatus. The degradation of formic acid in aqueous solution under UV irradiation was performed according to the procedure reported by Paoli and coauthors [Paoli2010].

Photocurrent transient measurements were performed, according to the literature [Hagfeldt1995], in a electrochemical cell with two platinum counter-electrodes placed in line, the working electrode in the middle and the saturated calomel reference electrode orthogonally with a Luggin capillary (to minimize the ohmic drop). The TiO$_2$ working electrodes were prepared by spin coating an homogenous layer of titania sample on an indium tin oxide glass slide (Aldrich), which was then sintered at 400°C in air for 1 h. A 0.5 M aqueous NaCl solution at spontaneous pH was employed. Before the measurement, the cell was deaerated with N$_2$ and kept in the dark for an equilibration time of 60 s. Then, the working electrode was alternatively exposed to UV light (100 s) and dark (200 s), for at least 6 times, in order to obtain reproducible transient patterns. A Micro III Autolab potentiostat/galvanostat (EcoChemie, The Netherlands) was employed to measure at a constant potential the photocurrent and the photocurrent transient.

Results and Discussion

Structural and morphological properties. The structural properties of bare and Bi-promoted TiO$_2$ were investigated with XRPD (Table 2.4.6). All XRD spectra show the presence of anatase and brookite polymorphs. The brookite phase is slightly promoted by Bi addition. Similar crystallite sizes were determined for all samples.In all Bi-promoted oxides, no peaks relative to separate Bi$_2$O$_3$ phases are appreciable in XRD patterns. The presence of Bi species can instead be observed by EDX: The detected Bi/Ti atomic ratios are comparable with those adopted in the synthesis (1.5% and 2.0% for T_Bi and T_P104_1.2_Bi, respectively).

Sample	% Anatase	% Brookite	d_{101}^a (nm)
Tsg	70	30	7
T_Bi	57	43	7
T_P104_1.2	61	39	6
T_P104_1.2_Bi	53	47	7

Table 2.4.6 Phase composition and average crystallite size for bare and Bi-promoted TiO$_2$ samples.

The morphologic features of the composites show significant differences depending on the synthetic route adopted for the TiO$_2$ precursor (Figure 2.4.14).

Sample	S_{BET} (mL g^{-1})	V_{pores} (ml g^{-1})
Tsg	150	0.338
T_Bi	161	0.420
T_P104_1.2	187	0.425
T_P104_1.2_Bi	148	0.375
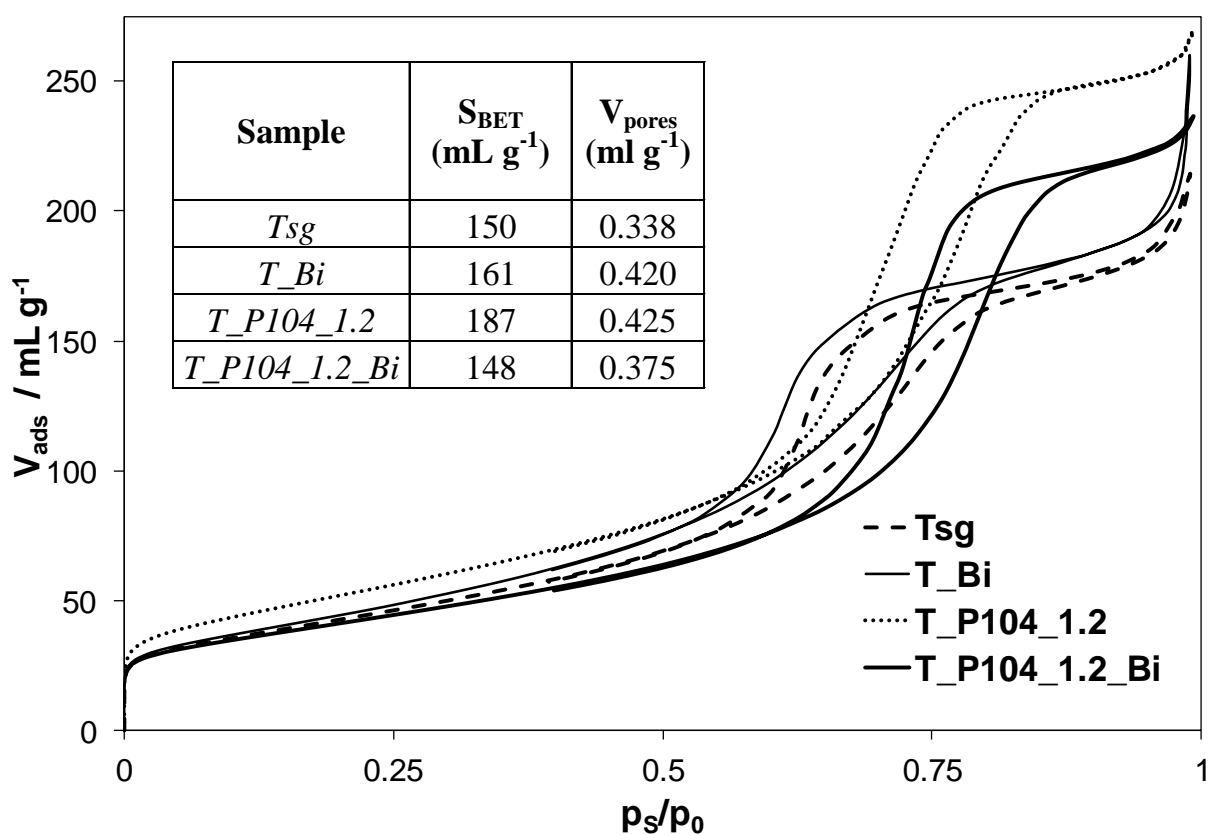
Figure 2.4. 14 N$_2$ adsorption–desorption isotherms of bare and Bi-promoted TiO$_2$ samples. Inset: Specific surface area S$_{BET}$ and total pore volume V$_{pores}$.

For both the bare and Bi-promoted sol-gel samples, the N$_2$ adsorption-desorption isotherms show H2 shaped hysteresis loops, characteristic of bottle-neck pores. The addition of Bi determines a slight increase in the specific surface area and an significant increase in the total pore volume (Figure 2.4.14 inset). The shape of the isotherm hysteresis loop changes drastically from sol-gel to mesoporous samples. In the latter, H1 type hysteresis loops, typical of cylindrical pores, are appreciable. Moreover, in the case of mesoporous samples, both the specific surface area and the total pore volume decrease significantly as a consequence of Bi addition (Figure 2.4.14 inset). The

fact that Bi addition does not alter the shape of the isotherm loop but shifts the curve to lower volumes, may be attributed to a partial filling of the mesopores by Bi_2O_3.

The structure and morphology of the composite powders were also investigated by HRTEM (Figure 2.4.15). HRTEM images show that all samples have a small crystallite size (5-8 nm), in good agreement with the XRD values. Samples exhibit smooth edges and high transparency to the electron beam. Moreover, the high incidence of fringe patterns, generated by crystalline planes exhibiting low hkl indexes, indicates that all the observed samples are highly crystalline. A detailed inspection of the lattice spacings was carried out to investigate the type of crystal planes present in the various samples. The most abundant termination is for all samples the (101) crystal plane of anatase (JCPDS file n. 21-1272). The (111) crystal plane of brookite (JCPDS file n. 2-514) is also observed. Bi-promoted samples show, with respect to bare TiO_2 samples, a general underestimation of the lattice distances ascribable to the (111) crystal plane of the brookite phase. Such a phenomenon, which is more frequently observed in the promoted mesoporous sample, can be traced back to the presence of a highly nanodispersed oxidic phase containing Bi species.

Figure 2.4.15 HRTEM images of a,b) T_Bi and c,d) T_P104_1.2_Bi.

Surface features. FTIR spectroscopy was employed to characterize the surface terminations of the nanoparticles of bare and Bi-promoted TiO_2 samples (Figure 2.4.16).
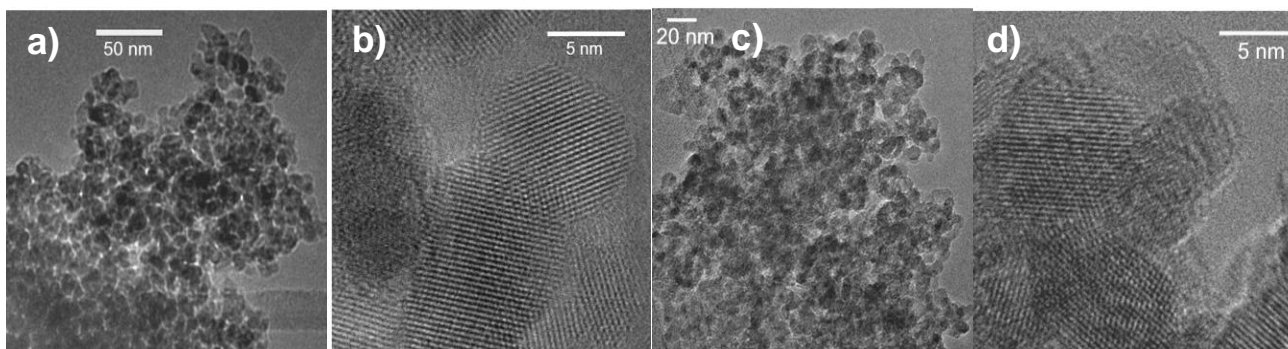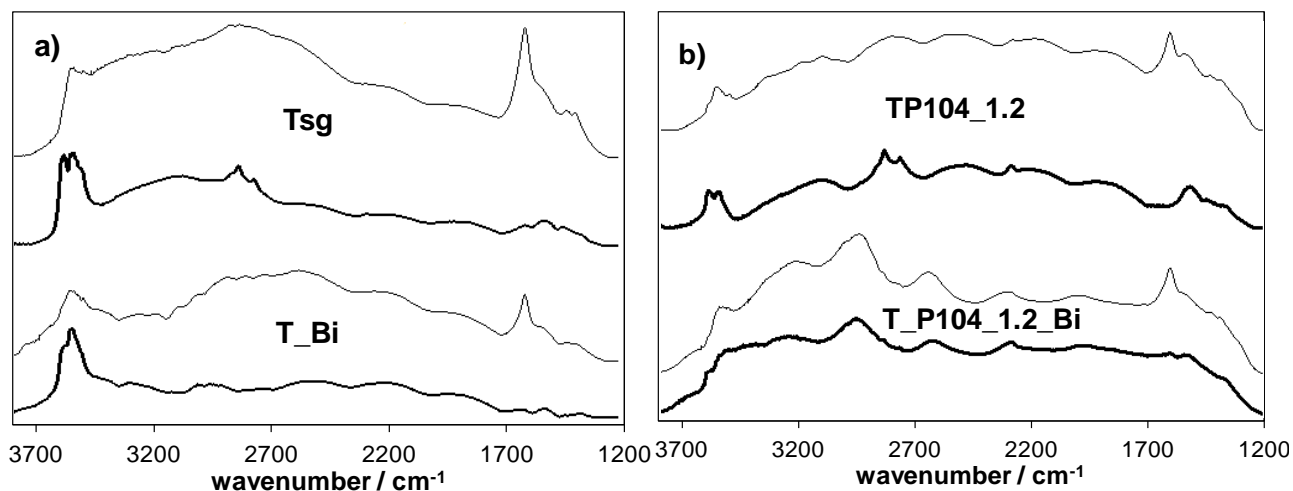

Figure 2.4.16 FTIR spectra of bare and Bi-promoted sol-gel (a) and mesoporous (b) titania samples. Full lines: activation in vacuum at RT, bold lines: activation in vacuum at 250°C.

A broad envelope in the 2500-3500 cm^{-1} range is appreciable in all spectra evacuated at RT. This can be attributed to the ν_{OH} mode of all OH species interacting by H bonding present at the TiO$_2$ surface [Little1966]. The bending vibration of the same species (δ_{HOH}) is also appreciable as a band located at $\sim$ 1620 cm^{-1}. After activation at 250 °C, the above described spectral components are drastically reduced as the thermal treatment has led to a medium degree of dehydration of the oxide surface.

Another prominent feature of all spectra is a broad envelope of singled out components, centered around 3700 cm^{-1}. Its components, ascribable to the ν_{OH} modes of OH species free from H-bonding interaction [Morterra1989], are better observable after activation at 250 °C (Figure 2.4.17).
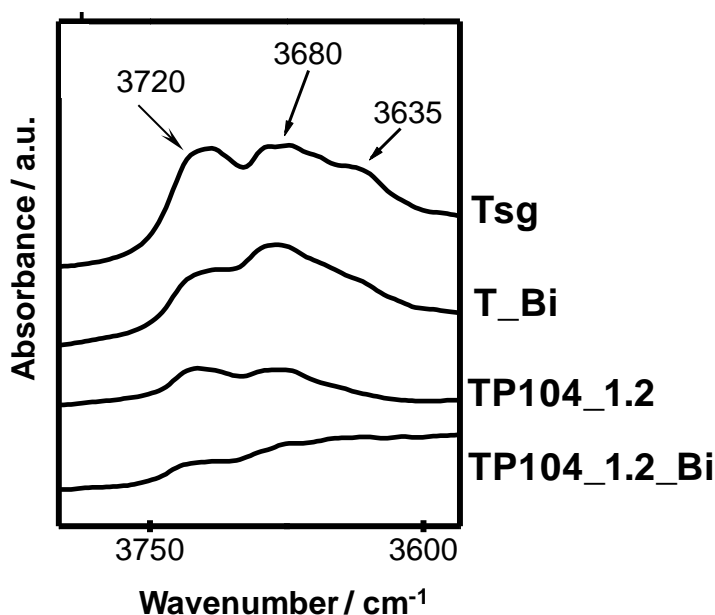
Figure 2.4.17 FTIR region of the ν_{OH} modes of bare and Bi-promoted sol-gel and mesoporous titania samples.

Remarkable differences among the studied samples are observed in this region (Figure 2.4.17). The bare sol-gel TiO$_2$ sample shows at least three different components, which are also observed after Bi addition, even if with a different intensity ratio. In the case of samples with mesoporous scaffold, the spectra present a lower quality, much more marked for TP104_1.2_Bi. In the latter sample, only the highest component can be observed and its intensity is much reduced. The presence of Bi species seems thus related to the covering and/or or disappearance of some specific band ascribable to OH species. Therefore, it can be proposed that the grafting of Bi species occurs with the "consumption" of surface OH species in the TiO$_2$ matrix.

Both sol-gel and mesoporous TiO$_2$ bare oxides show an absorption in the 3000-2750 cm^{-1} range. This band can be ascribed to the ν_{CH} of chemisorbed hydrocarbon species deriving from the synthetic route and/or to the exposure to the atmosphere after the calcination treatment [Magnacca2003].

Zeta potential measurements in aqueous suspensions were resorted to investigate the interfacial electrification features of the oxides. The zeta potential values measured for Bi composites at pH 8, are less negative than those of un-doped TiO_2 samples (-30 for Tsg vs. -10 for Tsg_Bi, -35 for T_P104_1.2 vs. -23 for T_P104_1.2_Bi). The isoelectric point (i.e.p.) of Bi-promoted TiO_2 is thus shifted in the alkaline direction with respect to the i.e.p. of bare TiO_2 (pH ≈ 6). Since the i.e.p. of pure Bi_2O_3 is located at pH 9 [Kosmulski2009], the observed shift of i.e.p. is consistent with the surface presence of Bi_2O_3 in Bi-promoted TiO_2 samples.

Photocatalytic tests. Table 2.4.7 reports the results of the photocatalytic tests towards the degradation of MB and of formic acid. For MB photocatalytic oxidation, the final degree of mineralization is reported (Table 2.4.7, second column). In the case of formic acid degradation, all samples gave rise to a mineralization degree larger than 80% at 3 h reaction time. Table 2.4.7 reports the rate of conductivity decrease due to the progressive disappearance of formic acid (Table 2.4.7, third column).

Sample	% min_{MB}	$(d\chi/dt)_{HCOOH}$ mS min^{-1}
Tsg	46 ± 1	0.51 ± 0.02
Tsg_Bi	68 ± 1	0.58 ± 0.01
T_P104_1.2	54 ± 1	0.48 ± 0.02
T_P104_1.2_Bi	78 ± 1	0.76 ± 0.01

Table 2.4.7 Photocatalytic activity of bare and Bi-promoted TiO_2 samples with respect to MB and formic acid mineralization.

Comparing the photocatalytic activity of the bare TiO_2 samples, the mesoporous sample exhibits a larger final mineralization of MB with respect to the sol-gel sample. This can be traced back to its higher specific surface area, as reported in section 2.3.2. In the case of formic acid degradation, instead, the photocatalytic activities of the two bare TiO_2 samples are comparable.

On the other hand, both degradation tests show a much higher photocatalytic activity for Bi-promoted TiO_2 samples with respect to the bare titania. The most active sample is T_P104_1.2_Bi, which notably presents the lowest specific surface area among the tested oxides.

The enhanced photocatalytic activity of Bi_2O_3-TiO_2 composites may be traced back to their peculiar electronic structure which could allow a better separation of photogenerated electron and holes between the two oxide phase domains. In order to investigate any effect of Bi addition on the recombination rate of photogenerated charges, photocurrent measurements were carried out.

An example of photocurrent kinetics curve is reported in Figure 2.4.18a.
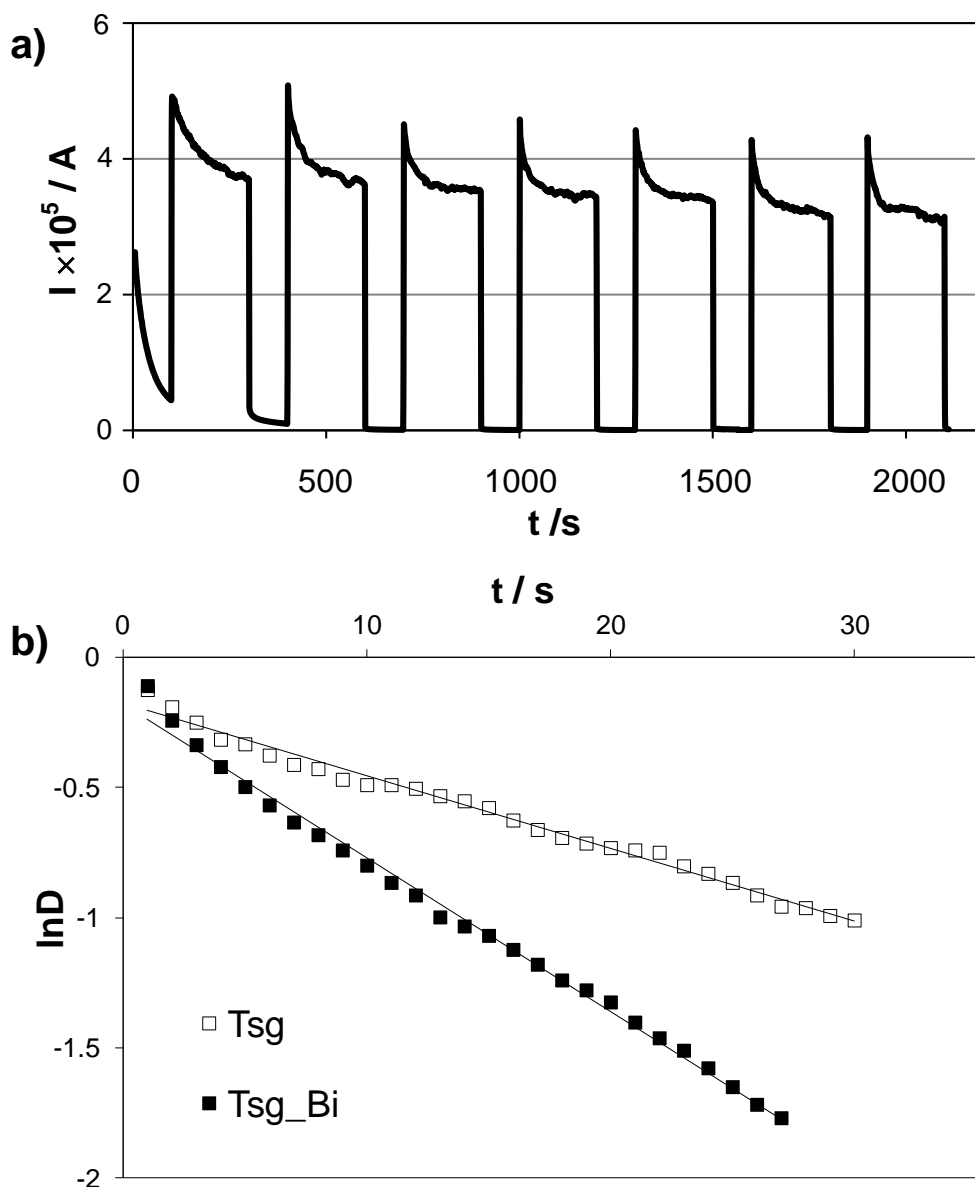
Figure 2.4.18 a) Photocurrent kinetic curve relative to Tsg_Bi; b) lnD vs. time plot of Tsg and Tsg_Bi.

As shown in Figure 2.4.18a, the current intensity rapidly decreases when the UV light is switched off, due to the recombination of photogenerated electron-hole pairs. The rate of the recombination process can be evaluated by the photocurrent transient time constant, τ:

$$\ln(D) = -t/\tau,$$

where $D = \dfrac{I(t) - I(st)}{I(in) - I(st)}$; $I(t)$ is the current at time t; $I(st)$ is the stationary current, and $I(in)$ is the current at $t = 0$. The value of τ can be determined by $\ln(D)$ *vs*. time plots (Figure 2.4.18b). All tested materials exhibit a linear $\ln(D)$ *vs*. time behavior, which indicates that surface recombination dominates the decay mechanism leading to a first-order kinetics in electrons surface concentration [Dholam2010; Tafalla1990].

Table 2.4.8 reports the τ values obtained for the various bare and Bi-promoted samples.

101

Sample	τ s
Tsg	15
Tsg_Bi	16
T_P104_1.2	15
T_P104_1.2_Bi	19

Table 2.4.8 Transient time constant (τ) derived from photocurent measurements.

The obtained values are comparable with literature results for both pure and doped nano-titania photocatalysts [Dholam2010]. Bare TiO_2 samples exhibit similar τ values, while Bi-promoted samples show larger τ values, indicative of a slower recombination rate. Notably, T_P104_1.2_Bi shows an even longer recombination time, supporting a better charge separation efficiency that could be related to the high dispersion of bismuth oxide in the TiO_2 mesopores.

The observed enhancement of the photocatalytic activity of Bi-promoted samples can thus be attributed to an effective reduction of recombinative processes.

Conclusions

Bi-promoted TiO_2 samples were synthesized by using as scaffolds both traditional sol-gel and mesoporous TiO_2. All characterization techniques support the formation of a highly dispersed Bi_2O_3 phase in the Bi-promoted TiO_2 samples. On the grounds of FTIR and zeta potential measurements, Bi_2O_3 appears to be preferentially located at the TiO_2 surface. Further, in mesoporous samples, a decrease in surface area and pore volume suggests the desired formation of Bi_2O_3 in the oxide mesopores.

The obtained Bi_2O_3-TiO_2 composites show a promoted photocatalytic activity towards the degradation of diverse pollutants in two largely different experimental set-ups. In both tests, the Bi_2O_3-mesoporous TiO_2 was the top performing photocatalyst. Such an enhanced photocatalytic activity could be directly related to a larger recombination time of photogenerated electron-hole pairs, as determined by photocurrent measurements. The Bi_2O_3-mesoporous TiO_2 sample presents a promoted photocatalytic efficiency that could thus be traced back to the peculiar band structure of Bi_2O_3, which allows the migration of photogenerated electrons from TiO_2, thus enhancing charge separation. Moreover, the fine dispersion of Bi_2O_3 in the TiO_2 mesopores may promote the formation of nano-junction between TiO_2 and Bi_2O_3 nanocrystals and thus increase the interfacial electron transfer.

Surface functionalization of TiO$_2$ with siloxanes

In recent years, the surface modification of oxide materials has attracted growing attention owing to its enormous technological relevance [Zhang2007; Xu2010; Manoudis2009; Manoudis2008; Liaw2007]. The most commonly employed functionalizing agents are siloxanes, compounds with the general formula $R\text{-}(CH_2)_n\text{-}Si\text{-}(OR')_3$, that are able to modulate the oxide wettability, surface energy, and adhesion properties by forming covalent bonds with the oxide surface upon hydrolysis of labile –OR' groups.

The surface functionalization of nanometric TiO_2 by siloxanes gives rise to hybrid materials with tailored wetting features. The hydrophobic and superhydrophobic behavior of these materials bears relevance to several application fields, such as biomaterials (*e.g.*, in the surface modification of stents for the prevention of clotting in blood vessels), or the protection of outdoor cultural heritage [Manoudis2008; Manoudis2009].

Other applications of siloxane-nano-TiO_2 hybrids are related to the semiconductor features of the oxide, such as in new generation solar cells. The use of siloxane-TiO_2 hybrid films as active layers in dye sensitized solar cells has been reported to result in smaller dark currents and higher open circuit photovoltages [Morris2008]. The higher efficiencies were related to the covalent bond between the chromophores and the titania network which enhances the electron transfer within the network and also between the network and the conducting substrate, thus hindering the recombination processes and improving the overall efficiency of light to electricity conversion[Morris2008; Lin2006].

Another relevant application exploits the photocatalytic activity of TiO_2 under UV irradiation for the site-selective degradation of the siloxane layer, a procedure known as photocatalytic lithography [Nakata2012]. In this way, patterned surfaces with localized superhydrophobic/superhydrophilic patches can be obtained for applications such as water collection from the gas phase, liquid transportation, off-set printing, and smart microfluidics devices [Yao2011; Nakata2012].

Furthermore, siloxanes may serve as robust linkers to attach diverse functionalities, such as nanoparticles, polymers, and bio-molecules, to the oxide surface [Haensch2010; Wouters2009]. By combining surface patterning techniques and surface modification procedures, complex hierarchical structures with tailored properties can be developed for innovative applications.

Despite the great applicative interest, the fundamental issues of the structure of the siloxane layer at the TiO_2 surface and of the influence of the siloxane nature and content on the material final properties, remain poorly understood at the molecular level and hardly discussed in the literature [Paz2011].

The present thesis aims at filling the gap by taking into account both the fundamental aspects of the interaction of siloxane molecules with the TiO_2 surface, and applicative aspects related to the development of highly innovative materials. In the following chapters, the surface properties of bare siloxane materials will be firstly investigated by combining experimental surface free energy determinations and theoretical calculations. Then, the fundamental aspects of the siloxane-TiO_2 interaction in functionalized nanometric TiO_2 materials will be studied by combining a series of advanced spectroscopic characterization and wettability determinations. Finally, such hybrid films will be tested for innovative applications, such as self-cleaning materials and site-selective modification of patterned surfaces.

3.1 Surface energy of bare siloxanes

A key parameter to evaluate the physicochemical features of a solid surface is its surface free energy (SFE). Several phenomena taking place at the solid-liquid and solid-gas interfaces, like adsorption behavior and wetting properties, are crucially related to SFE values. Therefore, the determination of the SFE of siloxanes represents a pivotal step in the understanding and prediction of the wetting behavior of siloxane-oxide composites. However, literature data on the SFE of these materials are scanty.

The SFE of a solid surface cannot be determined directly. Several indirect techniques are available, such as inverse gas-chromatography, evaluation of lattice constant variations, cleavage experiments, adhesion and adsorption measurements, and calorimetric methods [Butt1999]. However, the SFE values obtained by different methods are often difficult to compare. The most commonly employed approach involves the elaboration, by empirical and semi-empirical models, of contact angle values measured employing several test liquids [Żenkiewicz2007]. Such an approach has several advantages: The experimental procedure is simple, inexpensive, and more directly related to the modulation of surface wettability. Several models can be adopted for the elaboration of contact angle data: the models by Zisman [Fox1952a; Fox1952b], Fowkes [Fowkes1964; Fowkes1968; Fowkes1972], Wu [Wu1971; Wu1973], and Van-Oss-Chaudhury-Good [van Oss1986; van Oss1988], the Neumann's equation of state (EOS) [Neumann1974; Li1990], and the Owens-Wendt-Rabel-Kaelble (OWRK) method [Owens1969; Kaelble1970]).

In the present thesis work, the SFE values of both commercial and laboratory-made siloxane layers were evaluated by elaborating experimental contact angle data with several empirical models (Zisman, EOS, OWRK). Such experimental data were compared to dipole moment values obtained by theoretical calculations (semi-empirical Hamiltonians and force-field potential). Such a combined approach was employed to better understand and predict the wetting properties of both fluorinated and unfluorinated siloxane molecules.

Experimental Section

Materials. The studied siloxanes were both commercial and laboratory-made. Literature results on other silanes were also taken into account to get a more accurate picture of the effect of the silane structure on its surface free energy. The adopted silanes are listed in Table 3.1.1.

	Silane molecules	Acronym	Source	Structure
unfluorinated	octadecyl trichlorosilane	**OTS**	literature [Janssen2006]	
	isooctyl triethoxysilane	**Si-Alk**	commercial (Wacker)	
	triethoxy(phenyl) silane	**Si-Ph**	commercial (Aldrich)	
	diethoxy(diphenyl) silane	**Si-biPh**	laboratory-made	
	11-(triethoxysylil) undecanal	**TESU**	literature [Janssen2006]	
fluorinated	1H,1H,2H,2H-perfluorodecyl trichlorosilane	**FDTS**[*]	literature [Janssen2006]	
	phenyltris (trifluoroethoxy)silane	**Si-Ph(F)**	laboratory-made	
	diphenylbis-(trifluoroethoxy)silane	**Si-biPh(F)**	laboratory-made	
	n-perfluoroeicosane	**Alk(F)**[*]	literature [Takashi1999]	

Table 3.1.1 Studied silanes.

[1]H- and ^{13}C nuclear magnetic resonance (NMR) spectra of the laboratory-made compounds were used to confirm the assigned structure. Spectra were acquired on a Bruker Avance 500 spectrometer, operating at 500.130 MHz (^{1}H) and at 125.00 MHz (^{13}C). For the [13]C {[1]H} spectra, a Waltz decoupling was employed and spectra were exponentially multiplied to give 0.8 Hz line broadening before Fourier transformation.

Diethoxy(diphenyl)silane (Si-biPh) was synthesized as follows. A solution of diphenyl-dichlorosilane (100 mmol) in ethanol was stirred at 25°C for 24 hours. The solvent was then

removed by rotary evaporation, resulting in a pale yellow oil that was subsequently purified by fractional distillation at reduced pressure (89% yield). NMR data are in agreement with the literature: ^{1}H-NMR (500 MHz, CDCl$_3$): δ 7.74 (d, 4H, J = 7.5 Hz), 7.49 (t, 2H, J = 7.5 Hz), 7.45 (t, 4H, J = 7.5 Hz), 3.95 (q, 4H, J = 7.0 Hz), 1.33 (t, 6H, J = 7.0 Hz). ^{13}C-NMR (125 MHz, CDCl$_3$): δ 18.1, 58.8, 128.7, 130.0, 133.0, 135.0.

Phenyltris(trifluoroethoxy)silane (Si-Ph(F)) and diphenylbis-(trifluoroethoxy)silane (Si-biPh(F)) were prepared according to the following procedure. A solution of the relative phenylchlorosilane derivative (19 mmol) in trifluoroethanol (137 mmol) was stirred at 25°C for 18 h. Then, the solvent was removed by rotary evaporation, producing a pale yellow or lightly brown oil, which did not require further purification (80 and 91% yield for Si-Ph(F) and Si-biPh(F), respectively). NMR data are in agreement with the literature.

Si-Ph(F): ^{1}H-NMR (300 MHz, CDCl$_3$): δ 7.60-7.38 (m, 5H), 4.22-4.04 (m, 6H); ^{19}F NMR (282.1 MHz, CDCl$_3$): δ -77.7 ppm.

Si-biPh(F): ^{1}H-NMR (300 MHz, CDCl$_3$): δ δ 7.60-7.30 (m, 10H), 4.20-4.05 (m, 4H); ^{19}F NMR (282.1 MHz, CDCl$_3$): δ -77.0 ppm.

Siloxane film deposition. The siloxane layers were deposited on glass slides, previously cleaned by extensive sonication in several solvents (acetone, i-propanol, deionized water). The films were spin coated (2000 rpm, 20 s) from a siloxane solution in i-propanol. The remaining traces of organic solvent were removed in vacuum oven at 40 °C and 400 mbar.

Film characterization. The average surface roughness of the films was determined on 50 × 50 μm^2 areas, by atomic force microscopy using an NT-MDT Solver PRO-M working in tapping mode.

The static contact angles (CAs) of several high purity solvents (Table 3.1.2) on siloxane films were measured using a Krüss EasyDrop. For each solvent, a 3 μL drop was gently placed on the surface, then the drop profile was extrapolated using an appropriate fitting function. At least five determinations on different parts of the layer were carried out for each siloxane film, finding an average standard deviation ≤ 3°. Not all solvents were considered for SFE elaboration, mainly on the grounds of chemical compatibility considerations. For instance, some siloxane layers were dissolved by toluene and diethylene glycol drops, whose CAs were consequently not considered.

Computational set-up. The gas phase dipole moments of the adopted siloxanes were calculated at a semi-empirical level using a PM6 Hamiltonian (Gaussian09 package) in the vacuum for the most stable conformation, as located with Molecular Mechanics techniques and MMFFs force field with a stochastic Monte Carlo analysis of the potential energy surface. Vibrational analysis was used to characterize the PM6 minima.

Solvent	γ_{lv} (mN m^{-1})	γ_{lv}^{p} (mN m^{-1})	γ_{lv}^{d} (mN m^{-1})
water	72.8	51.0	21.8
ethylene glycol/H$_2$O (10/90)	69.4	48.1	21.2
ethylene glycol/H$_2$O (20/80)	64.3	43.4	20.9
ethylene glycol/H$_2$O (50/50)	57.9	37.9	20.0
ethylene glycol/H$_2$O (70/30)	53.4	33.8	19.6
ethylene glycol/H$_2$O (90/10)	50.5	31.3	19.1
ethylene glycol	48.2	29.3	18.9
glycerol	62.7	41.5	21.2
formamide	58.0	19.0	39.0
diethylene glycol	44.8	13.2	31.6
diiodomethane	50.8	2.3	48.5
toluene	28.4	2.3	26.1

Table 3.1.2 Solvents adopted for CA measurements. The polar, γ_{lv}^{p}, and disperse, γ_{lv}^{d}, components of the solvents' surface tensions, γ_{lv}, are reported.

Results and discussion

Morphology of the siloxane layers. Siloxane layers were deposited onto glass substrates by spin-coating, giving rise to stable and reproducible coatings, free of cracks, voids and protrusions. Films deposited by this procedure showed a flat surface with average roughness, R$_{rms}$, of 6.9 nm (measured on a 50 x 50 μm^2 area), thus fully comparable to the roughness of the adopted uncoated glass slides. This deposition technique, simple and inexpensive, is often employed for industrial coatings. The siloxane layers deposited by this procedure are expected to be less ordered than self-assembled monolayers, even if the siloxane molecules likely exhibit a preferential orientation of their dipole moments.

Surface Free Energy determinations. The contact angle of a liquid on a solid surface is the result of a balance between the cohesive forces within the liquid drop and the adhesive forces between the liquid molecules and the surface. The classical model describing the wetting behavior of an ideal surface (Figure 3.1.1) is the Young equation [Young1805]:

$$\gamma_{sv} - \gamma_{sl} = \gamma_{lv}cos\theta$$

where θ is the Young contact angle, γ_{sv}, γ_{sl} and γ_{lv} are the surface tensions at solid-vapor, solid-liquid and liquid-vapor interfaces, respectively. γ_{sv} can be approximated to the SFE of the solid in the case of negligible spreading pressure, π_e.
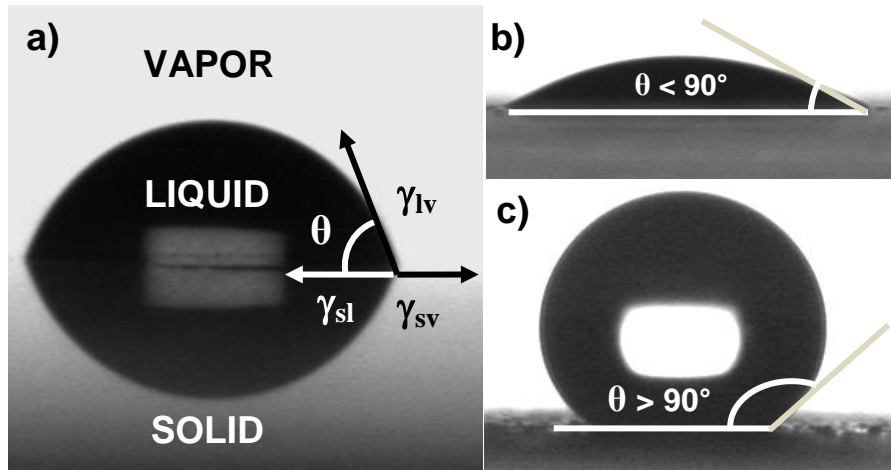
Figure 3.1.1 Classical Young contact angle model (a); water CAs on a hydrophilic (b) and hydrophobic (c) surface.

The surface tensions and the SFE values can be split into two components, one (γ^p) considering only the polar intermolecular interactions (*e.g.*, dipole-dipole, hydrogen and π-bonding) and the other one (γ^d) considering only the dispersion forces:

$$\gamma = \gamma^d + \gamma^p$$

The OWRK model [Owens1969; Kaelble1970] allows the determination of the two components of the SFE of a material from the slope and intercept of the following equation:

$$\frac{\gamma_{lv}(1 + cos\theta)}{2\sqrt{\gamma_{lv}^d}} = \sqrt{\gamma_s^p}\sqrt{\frac{\gamma_{lv}^p}{\gamma_{lv}^d}} + \sqrt{\gamma_s^d}$$

Hence, the SFE of a material, and its polar and disperse components, can be obtained from the CA measurement of at least two solvents with known surface tension components. Such an approach is based on an assumption about the volume of the elements in the two phases: the equation holds only if the wetting liquid molecules present a radius of van der Waals interactions of the same order of the group elements [Fowkes1964].

Another approach, the so called Zisman method [Fox1952a; Fox1952b], approximates the SFE value to the critical surface tension, *i.e.* the theoretical γ_{lv} value at which $cos\theta = 1$. The critical surface tension value can be extrapolated from the linear trend of a $cos\theta$ vs. γ_{lv} plot, the so called Zisman plot. This method, which does not take into account the disperse and polar components of the SFE, fails whenever the relationship between the disperse and polar interactions is different between the solid and the liquid. In general, the model fails when applied to polar surfaces, while it better applies to low-energy surfaces.

The Equation of State (EOS) model [Neumann1974; Li1990] provides a SFE value from a the CA determination of a single liquid (water in the present work). The method is based on the following equation:

$$\cos\theta = -1 + 2\sqrt{\frac{\gamma_s}{\gamma_{lv}}}\,e^{-\beta(\gamma_{lv}-\gamma_s)^2}$$

with $\beta = 0.000125$ $(mJ/m^2)^{-2}$, obtained by Neumann and coauthors by solving the general form of the equation of state, $F(\gamma_s, \gamma_{sl}, \gamma_{lv}) = 0$.

Unfluorinated siloxane layers. Figure 3.1.2 shows the results of the application of the OWKR and Zisman models to the layers of unfluorinated siloxanes. The observed correlation coefficients are quite good ($R^2 > 0.97$).
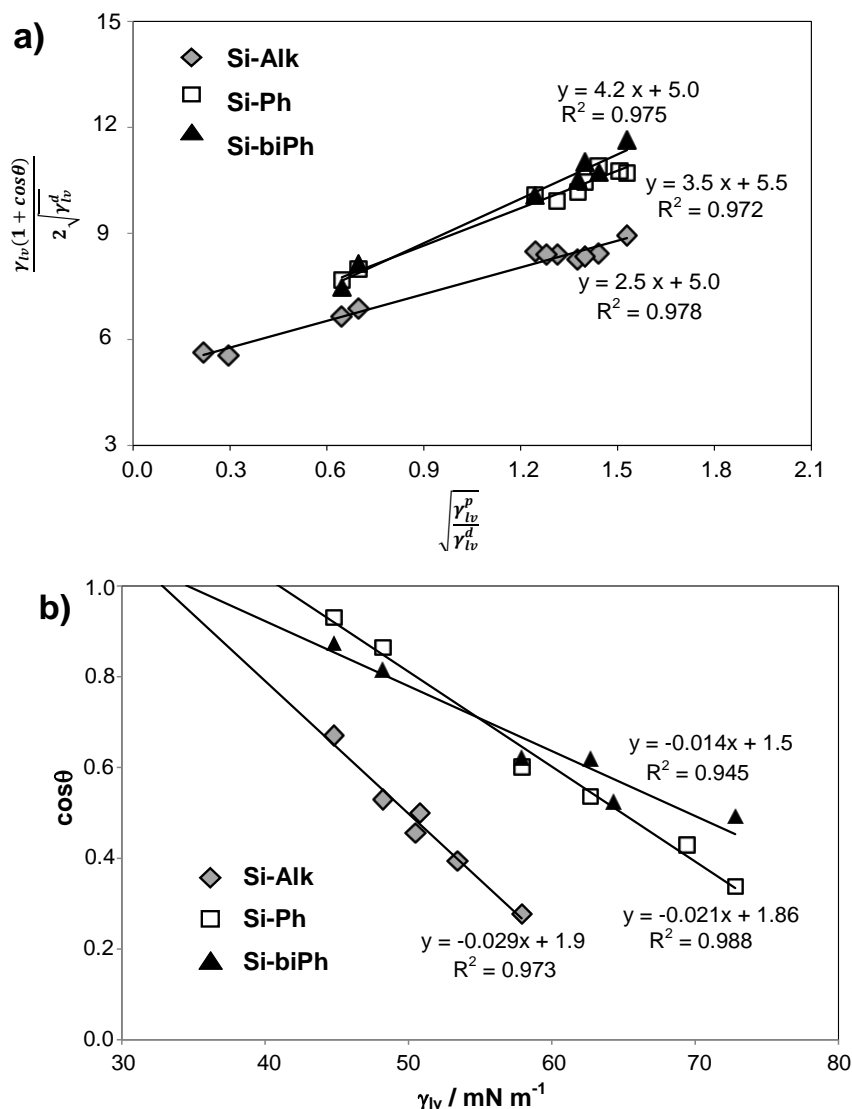

Figure 3.1.2 a) OWRK and b) Zisman plots for Si-Alk, Si-Ph and Si-biPh layers.

The SFE values and relative components obtained by OWRK, Zisman and EOS models are reported in Table 3.1.2. The SFE values of two silanes taken from the literature [Janssen2006]

showing opposite polar and disperse components, are also reported for the sake of comparison. The accuracy of these latter data is higher than that of experimental values. This is expected on the grounds of the different deposition procedures adopted in the two cases: The present films are spin-coated, yielding to layers less ordered than the literature self-assembled monolayers.

Silane	OWRK (mN m^{-1})			Zisman SFE	EOS SFE	μ / D
	SFE	γ^p	γ^d	mN m^{-1}	mN m^{-1}	
OTS*	23.50 ± 0.05	5.43 ± 0.01	18.07 ± 0.05	20.03 ± 0.03	24 ± 1	2.14
Si-Alk	31 ± 2	6 ± 1	25 ± 1	33 ± 5	23 ± 4	2.71
Si-Ph	42 ± 4	12 ± 1	30 ± 3	41 ± 5	33 ± 5	3.82
Si-biPh	42 ± 6	18 ± 3	24 ± 3	35 ± 8	38 ± 3	4.50
TESU*	40.89 ± 0.03	25.12 ± 0.01	15.77 ± 0.03	26.37 ± 0.03	32 ± 2	6.01

Table 3.1.2 SFE values and relative polar and disperse components, obtained by OWRK, Zisman and EOS models, and calculated dipole moments for unfluorinated silanes (* literature data [Janssen2006]).

The OWRK method shows that the disperse components are quite similar for all the studied siloxanes, while the polar components exhibit a larger variation (in increasing γ^p order: OTS < Si-Alk < Si-Ph < Si-biPh < TESU). The polar component of SFE thus increases with the degree of arylation, since the phenyl groups confer increased polarizability. The agreement between the Zisman and the OWRK values is poorer for the molecules with the highest polar components (TESU and Si-biPh), while it is quite good for the other silanes.

These results were compared with the molecule specific geometric and electrostatic properties, in particular with the molecular dipole moments calculated in the gas-phase, *i.e.* a single molecule at a time (Figure 3.1.3).
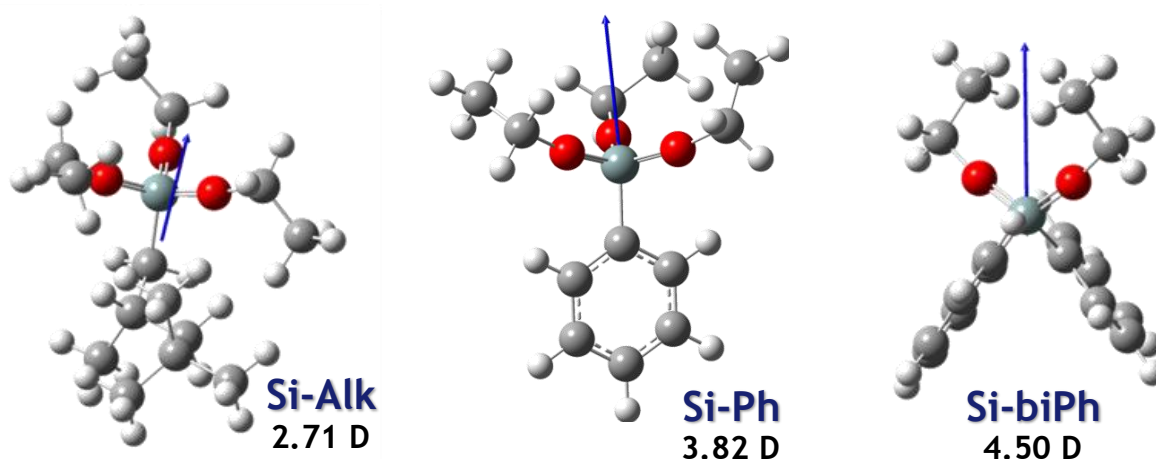

Figure 3.1.3 Calculated dipole moments for Si-Alk, Si-Ph and Si-biPh.

The calculated modules of the dipole moment vectors are reported in Table 3.1.2 (7th column). Interestingly, the calculated dipole moment modules show the same sequence than the experimental polar components.

The obtained polar and disperse components of the SFE can be exploited in a predictive way to determine the wettability of a siloxane layer towards solvents other than water, using the so called wetting envelope (WE) elaborations (Figure 3.1.4). WE plots are obtained by introducing the calculated disperse and polar SFE components into the reversed OWRK equation. Bow-shaped curve are produced by plotting γ_{lv}^{p} vs. γ_{lv}^{d}. If a $\cos\theta = 1$ value was adopted ($\theta = 0°$), all solvents whose surface tension data lie within the WE curve will wet the siloxane film. WE curves for higher contact angles ($\theta = 20\text{-}80°$) can be drawn similarly (by changing the value of $\cos\theta$), providing an indication of the CA of given liquid on a certain film simply from its position in the WE diagram.
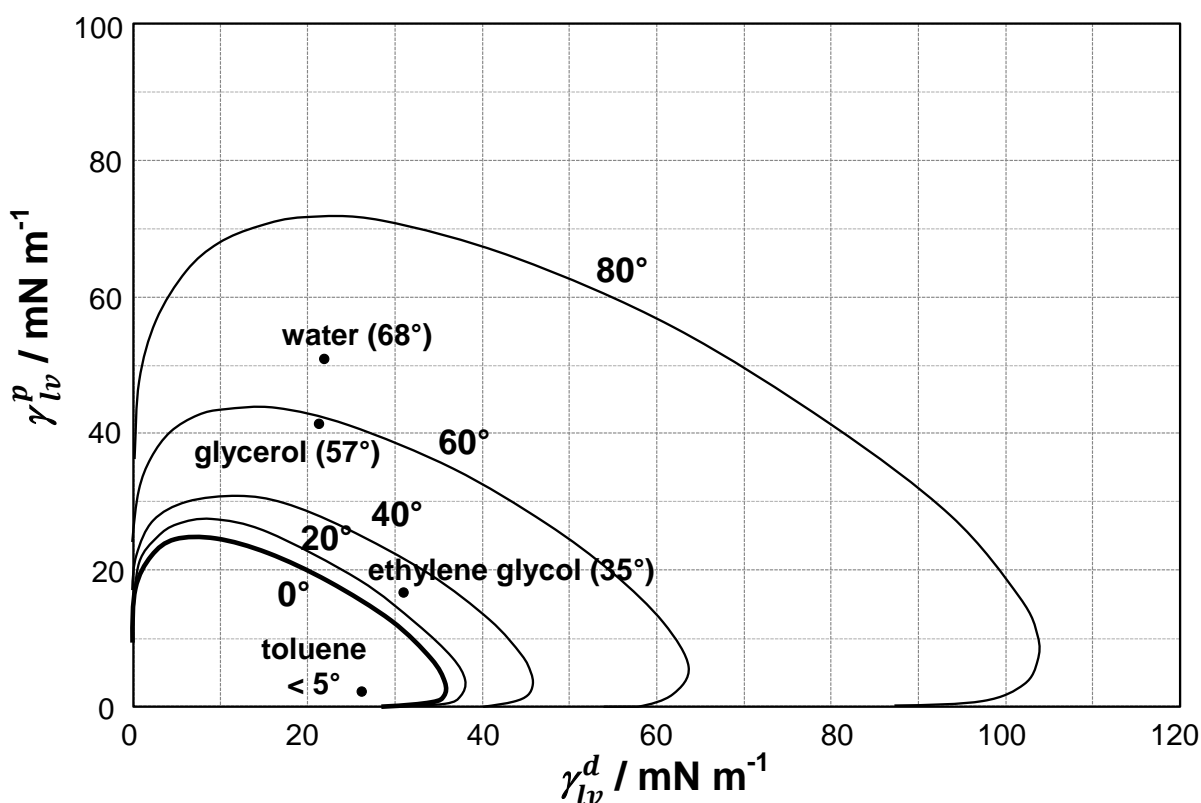
Figure 3.1.4 Wetting envelopes with 0°, 20°, 40°, 60° and 80° contours for Si-Ph.

Figure 3.1.4 shows the good predictive properties of the WE of Si-Ph: The measured CA values for the different solvents are in close agreement with the WE predictions. This consideration is valid for all the investigated unfluorinated silanes, highlighting that the adopted OWRK model well describes the current systems.

Fluorinated siloxane films. In order to analyze the effect of fluorination on the SFE values of siloxane films, fluorinated analogues of the tested siloxanes were synthesized by substituting the methyl end groups with fluorinated ones. Literature data relative to a linear alkyl fluorinated silane,

FDTS [Janssen2006], and a totally fluorinated alkane, Alk(F) [Takashi1999], are also reported for the sake of comparison.

Theoretical dipole moment vectors were calculated in the gas phase for all the fluorinated molecules to better appreciate the effect induced by the fluorination (Figure 3.1.5). The dipole moment modules of Si-Ph(F) and Si-biPh(F) are almost halved with respect to the unfluorinated analogues.

Si-Ph(F)
1.51 D
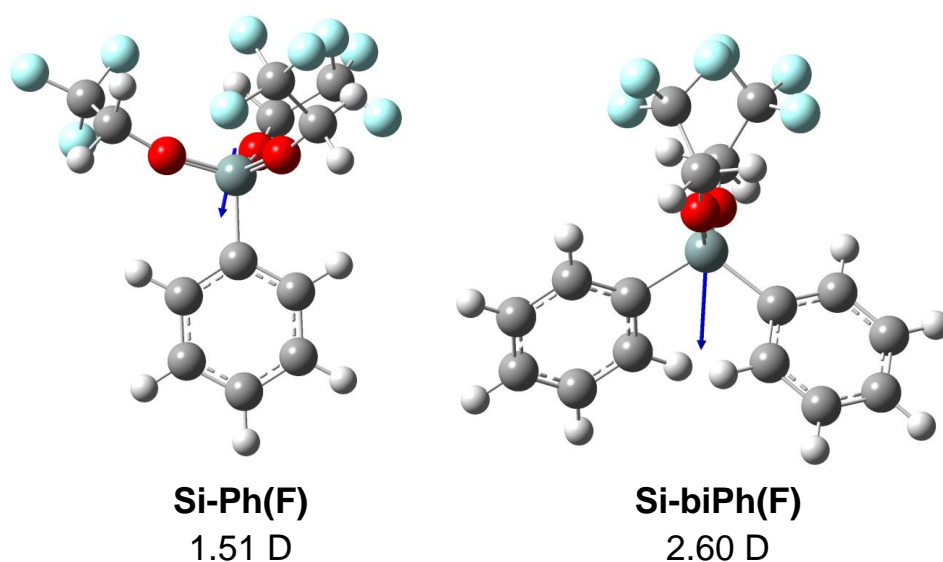
Si-biPh(F)
2.60 D

Figure 3.1.5 Calculated dipole moments for Si-Ph(F) and Si-biPh(F).

Table 3.1.3 reports a comparison between the modules of the calculated dipole moments and the SFE components obtained by the OWRK model for the fluorinated moleculs.

Silane	SFE mN m^{-1}	γ^p mN m^{-1}	γ^d mN m^{-1}	μ D
Si-Ph(F)	28 ± 2	2 ± 1	26 ± 1	1.51
FDTS*	13.5 ± 0.1	2.28 ± 0.07	11.22 ± 0.09	1.79
Si-biPh(F)	33 ± 4	10 ± 2	23 ± 3	2.60
Alk(F)*	6.7	1.2	5.5	0.31

Table 3.1.3 SFE values and relative polar and disperse components, obtained by OWRK model, and calculated dipole moments for fluorinated silanes (* literature data [Janssen2006; Takashi1999]).

Si-Ph(F) and Si-biPh(F) exhibit much lower SFE values with respect to the unfluorinated analogues, mainly related to a marked decrease of the polar SFE component. Also in the case of fluorinated silanes, the sequence of SFE polar components reflects the sequence of gas phase dipole moment modules. However, WE curves show a more complex picture with respect to unfluorinated molecules (Figure 3.1.6). While in the case of Si-Ph and Si-biPh layers, the WE curves are

consistent with the experimental CAs (Figure 3.1.6a), the experimental CAs of FDTS and Alk(F) present a lower agreement with the predictions of the WE elaborations (Figure 3.1.6b).
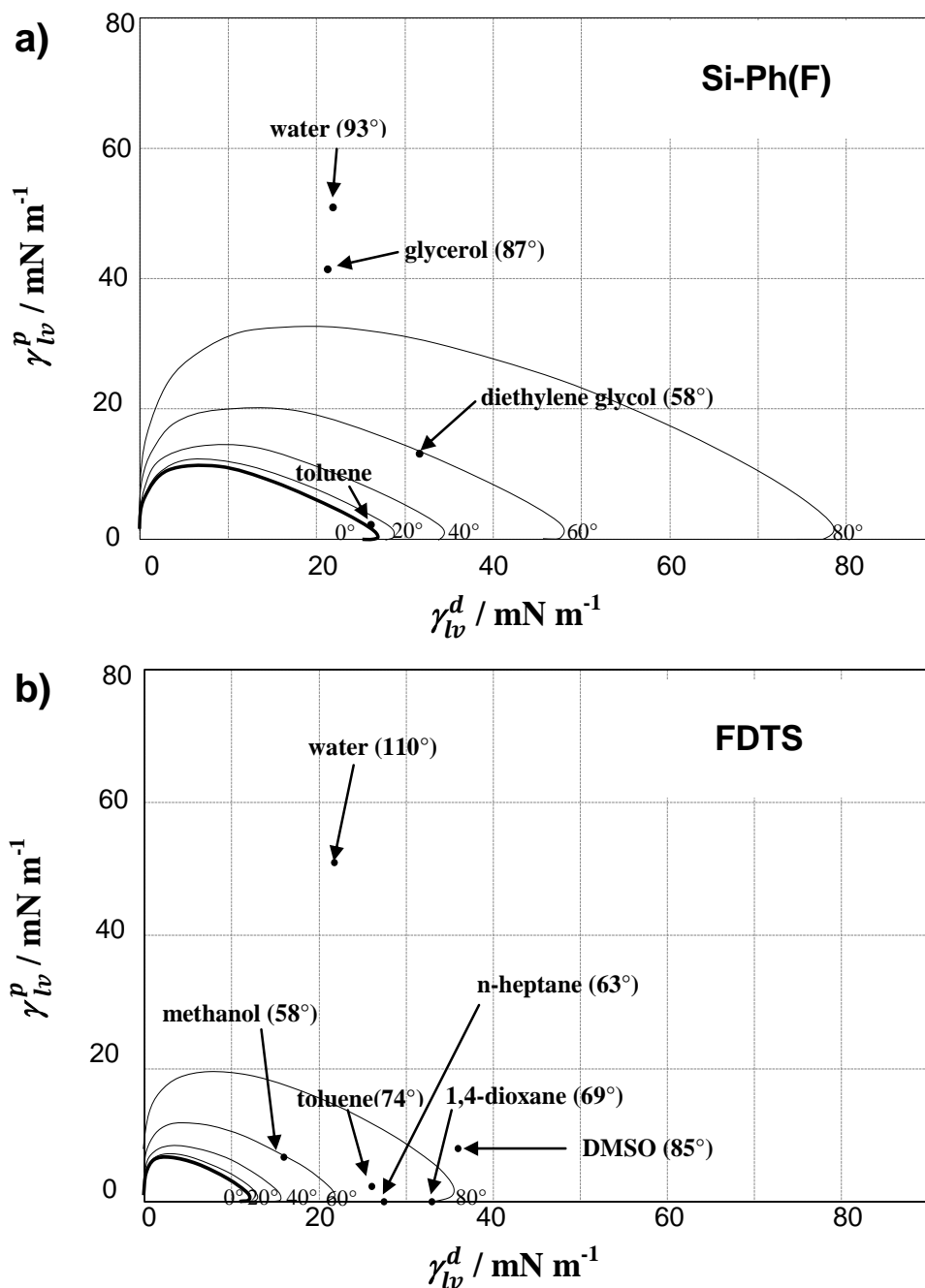
Figure 3.1.6 Wetting envelope plots for a) Si-Ph(F) and b) FDTS.

The discrepancies observed for FDTS and Alk(F) can be traced back from the fact that in these cases the Fowkes' assumptions [Fowkes1964] embedded in the OWRK equation are not fully satisfied. While in alkyl chains the CH_2 volume element (and in the case of aryl compounds, the CH group) has very nearly the same radius as the solvent molecule, the CF_2 group of fluorocarbons is a bit larger and can give rise to an overestimation of the interaction at interfaces [Fowkes1964]. In the case of the Si-Ph(F) and Si-biPh(F), the model holds apparently because the aromatic rings dominate the interaction with the solvents, while the fluorinated ethoxy groups do not appreciably

115

alter the features of the interface zone. It can thus be concluded that the effect of fluorination of CH_3 and/or CH_2 groups strictly depends on the position of the final CF_2/CF_3 groups in the molecule, in particular from whether or not they are oriented towards the surface.

Conclusions

The surface free energy (SFE) values of a series of siloxanes (both alkyl and aryl, unfluorinated and fluorinated compounds) were determined. A close correlation was observed between the calculated dipole moments and the polar components of the SFE (determined by OWRK model).

The considerations drawn from the present experimental data could be extended also to literature data about siloxane molecules deposited by a completely different procedure, proving that the considerations made have a general relevance.

The determined SFE values were adopted in a predictive way to estimate the wettability of the siloxane films. However, such theoretical predictions failed in the case of long fluorinated chains, because of the specific chemical/geometrical features of the interfacial contact.

By changing the structure of the organic tail, a wide range of SFE can be obtained, allowing for a fine modulation of the surface wetting character with respect to the desired application.

3.2 Siloxane-TiO$_2$ composites

The modulation of the wetting properties of oxide surfaces represents a crucial aspect in several fields, from cultural heritage protection to biomaterials, from offset printing to photovoltaics [Nakata2012; Manoudis2009].

In recent years, a great deal of effort has been devoted towards the preparation of superhydrophobic materials [Callies2005; Yao2011], *i.e.* surfaces exhibiting extremely high water contact angels ($\geq$ 150°) and very low contact angle hysteresis. Such surfaces are obtained by the control of both the surface topography and chemical composition [Callies2005]. The interest in superhydrophobic surfaces arises from their numerous applications, such as self-cleaning materials, anti-corrosion and anti-biofouling coatings, anti-freezing and anti-snow surfaces [Xue2010;Yao2011]. However, several applications require predetermined intermediate wetting properties. For instance, proteins adsorption, as well as cell adhesion and growth, take place preferentially on moderate hydrophilic surfaces (water contact angle of ca. 60° [Liang2012]).

While the modulation of the surface wettability by water has been extensively studied, superoleophobic surfaces have been by far less investigated, despite their manifold, economically relevant, potential applications, *e.g.* in fluid power systems, crude oil transfer, antifouling and anticrawling materials.

Only very few recent studies are devoted to the tuning of the wetting features of nano-TiO$_2$ films with respect to both water and non-aqueous solvents [Sawada2012; Yang2011; Zhang2011; Kim2011; Wang2010a]. In these works, complex multi-step synthetic procedures are employed, which are often limited to a special kind of substrate.

In the present thesis work, the wetting properties of TiO$_2$ nanoparticle films were modulated with respect to both water and non-aqueous solvents by functionalization with siloxanes. The obtained hybrid films can be employed to tailor the wetting features of almost every kind of substrate, thanks to the very simple adopted synthetic procedure. Several siloxanes with largely different structures (alkyl or aryl side-chains, fluorinated and unfluorinated, side-chains of different length and branching degree) were employed in order to study the role played by the siloxane structure and content on the final material properties. The morphological features of the hybrid TiO$_2$-siloxane materials were investigated in detail, by combining BET method, atomic force microscopy (AFM), and scanning electron microscopy (SEM). The chemical interactions between the siloxane end-groups and different solvents were also investigated.
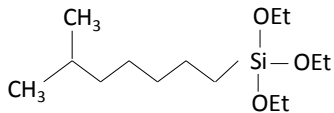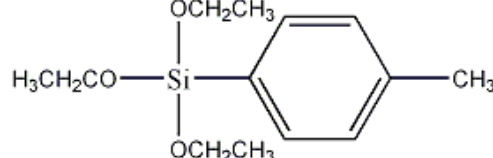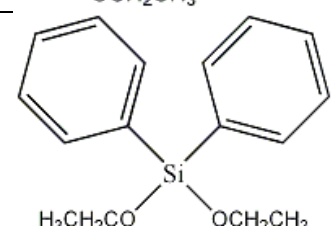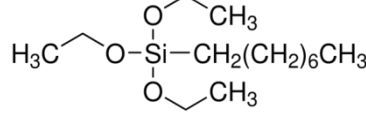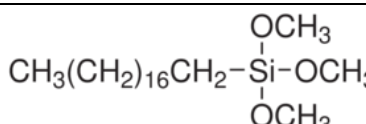
The more fundamental features of bonding and structure of the hydrophobizing layer at oxide surfaces were also studied. Such aspects have so far received limited attention in the

literature, especially in the case of nanoparticle films. Nanoparticles are expected to form less ordered monolayers than flat surfaces because of the high curvature of the nanoparticles and their high content of structural defects, which may limit the packing efficiency of the siloxane molecules. Since AFM, which is generally utilized to investigate the quality of monolayers deposited onto flat surfaces, is not feasible to characterize very rough surfaces like nanoparticle films, a combination of several advanced spectroscopic techniques (solid state NMR, FTIR, XPS, EDX) was here employed to gain deeper insight of the role played by the functionalizing molecule amount and structure. In particular, solid state NMR has recently emerged as an important tool to study organic molecules chemisorbed on oxides surfaces. This technique is here employed to provide information about the functionalization of oxide materials with the organic moieties and about the characteristics of the attachment bonds. Such fine characterization will allow us to gain a deeper insight of the functionalizing layer and draw conclusions about the relationship between the layer structure and the wetting behavior of the film.

Experimental Section

Materials. All the chemicals were of reagent grade purity and were used without further purification; doubly distilled water passed through a Milli-Q apparatus was used to prepare solutions and suspensions.

The adopted siloxanes, listed in Table 3.2. were both commercial and laboratory-made.

Name	Acronym	Source	Formula
Isooctyltriethoxysilane	**Si-Alk**	Commercial (Wacker)	
Triethoxy(p-tolyl)silane	**Si-Tol**	Laboratory-made	
Trimethoxy(diphenyl)silane	**Si-biPh**	Laboratory-made	
Triethoxy(octyl)silane	**Si-8C**	Commercial (Aldrich)	
Trimethoxy(octadecyl)silane	**Si-18C**	Commercial (Aldrich)	
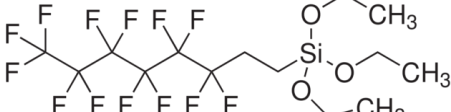
*1H,1H,2H,2H-*perfluorooctyl-triethoxysilane	**Si-8C(F)**	Commercial (Aldrich)	

Table 3.2.1 Studied siloxanes.

Triethoxy(p-tolyl)silane (Si-Tol) was synthesized according to the following procedure. A solution of *n*-BuLi 1.6 M (1.1 eq, 16.5 mmol) was added at -60 °C under N_2 atmosphere to a solution of bromoaryl derivative (1 eq, 15 mmol) dissolved in dry THF (20 mL). The solution was stirred for 30 min at -60 °C, before addition to a solution of tetraethyl orthosilicate (8 eq, 120 mmol) in dry THF (5 mL) cooled at -30°C. After the addition was completed, the reaction mixture was allowed to warm to room temperature and stirred for 18 h. After that time, it was quenched by addition of water (10 mL) and diluted with AcOEt (20 mL). The organic layer was then separated, washed with a saturated aqueous solution of NH_4Cl (2 × 10 mL), and dried over Na_2SO_4. The solvent was removed by rotary evaporation. The pale yellow oil obtained after drying, was purified by fractional distillation at reduced pressure (81% yield).

^{1}H- and ^{13}C nuclear magnetic resonance (NMR) spectra of the laboratory-made compounds were used to confirm the assigned structure. Spectra were acquired on a Bruker Avance 500 spectrometer, operating at 500.130 MHz (^{1}H) and at 125.00 MHz (^{13}C). For the ^{13}C {^{1}H} spectra, a Waltz decoupling was employed and spectra were exponentially multiplied to give 0.8 Hz line broadening before Fourier transformation. The obtained peaks confirm the proposed structure: <u>^{1}H-NMR</u> (500 MHz, CDCl$_3$): δ 7.65 (m, 2H), 7.35 (m, 2H), 3.95 (q, 6H, *J* = 7.0 Hz), 2.38 (s, 3H), 1.31 (t, 9H, *J* = 7.0 Hz). <u>^{13}C-NMR</u> (125 MHz, CDCl$_3$): δ 18.4, 21.6, 58.7, 128.7, 134.9, 140.0.

Trimethoxy(diphenyl)silane (named **Si-biPh** in the following) was synthesized as reported in section 3.1.

Synthesis of TiO$_2$ nanoparticles. TiO$_2$ nanoparticels were prepared by the sol-gel technique according to the following procedure. A Ti(OC$_3$H$_7$)$_4$ (0.13 mol) solution in 2-propanol (48 mL) was stirred for 10 min at 65 °C. Then, water (225 ml) was added dropwise to the Ti(OC$_3$H$_7$)$_4$ solution. The final water/alkoxide and water/2-propanol molar ratios were 100 and 20, respectively. The slurry was stirred for 90 min at 65 °C, then it was dried overnight at 90 °C. The obtained xerogel was calcined at 300 °C for 5 h under O$_2$ stream (9 NL h^{-1}).

Functionalization of TiO$_2$ with siloxanes. The high degree of surface hydroxylation of the adopted TiO$_2$ nanoparticles, due to the adopted synthetic conditions and mild calcination temperatures, ensured a good reactivity of the oxide with the siloxane. Hence, no activation treatment was needed prior to the siloxane deposition. The functionalization was performed by adding the chosen amount of siloxane (varied in the range 0-33% w/w) to a titania dispersion in i-

propanol under vigorous stirring. Samples were then dried by means of a vacuum oven (40 °C, 400 mbar). Films of the functionalized particles were deposited by spin coating (2000 rpm, 20 s) a suspension of the silanized oxide in 2-propanol, onto previously cleaned glass slides.

Samples are named according to the following notation: T_siloxane acronym(%siloxane). Bare TiO_2 is referred to as T.

Samples characterization. X-ray powder diffraction (XRPD) patterns were collected at room-temperature between 10 and 80° with a Siemens D500 diffractometer, using the Cu Kα radiation. Rietveld refinement was performed using the GSAS software suite and its graphical interface EXPGUI. The average crystallite diameter, *d*, was estimated from the most intense reflection (101) of the anatase phase, using the Scherrer equation.

The particle size distributions of the sample powders in isopropanol were determined by Dynamic Light Scattering (DLS), using a Beckman Coulter N5 analyzer.

Specific surface area was determined by the BET method using a Coulter SA3100. Pore size distribution was determined from desorption isotherms using the Barrett-Joyner-Halenda (BJH) method.

The topography of titania films was investigated by Atomic Force Microscopy (AFM) using an NTMDT Solver PRO-M microscope operating in tapping mode. The average roughness factor of the samples (root mean square, rms) were determined on 5×5 μm^2 areas.

The distribution of carbon species at the film surface was evaluated by Scanning Electron Microscopy (SEM) using an HITACHI TM-1000 equipped with Energy-Dispersive X-ray spectroscopy (EDX, Hitachi ED3000).

The wetting features of the functionalized films were determined by static and dynamic contact angle (CA) measurements on a Krüss EasyDrop instrument, using several high purity solvents (water, toluene, glycerol, ethylene glycol). Measurements were performed by gently placing a 3 μL drop of solvent on the surface, then the drop size was changed at 15 μL min^{-1} while recording movies of 150 images. The drop profile was extrapolated using an appropriate fitting function. The reported CA values are the average of five independent determinations from different sample locations. The average contact angles θ_{avg} were calculated from θa and θr using the procedure reported by Tadmor [Tadmor2004]. Contact angle hysteresis $\Delta\theta$ were obtained as the difference between the advancing and receding contact angles.

The total surface free energy (SFE) values, with relative polar and disperse components, were obtained by the Owens-Wendt-Rabel- Kaelble method for the bare siloxane films (deposited as reported in Section 3.1) using the procedure reported by Lee et al. [Lee2003].

Fourier transform infrared spectroscopy (FTIR) was carried out to study the chemical structure of the adsorbed siloxanes at the TiO_2 surface. Spectra were recorded using a Jasco 4200 spectrometer equipped with an attenuated total reflectance (ATR) module.

The siloxane-TiO_2 interactions and the structure of the siloxane layer were investigated by ^{13}C and ^{29}Si solid state nuclear magnetic resonance (NMR) spectroscopy. Solid state cross-polarization magic angle spinning (CPMAS) NMR spectra were collected at 300 K on a Bruker Avance500 spectrometer, accessorized with a 4 mm MAS broadband probe. ^{13}C and ^{29}Si spectra were obtained at 125.62 and at 99.36 MHz, respectively, on solid samples (ca. 0.15 g) packed into a 4-mm MAS rotor (50 μL sample volume) spinning at 3 kHz. The resolution did not improve at higher spinning rate and/or temperature. The optimization of the pulse employed in the direct polarization (DP) and cross-polarization (CP) experiments, was carried out on the Si-Alk sample. ^{29}Si spectra were recorded with the variable amplitude method, with CP contact time of 1ms, a pulse delay of 20.0 s and 20000 scans. The ^{13}C spectra of aliphatic siloxanes were acquired in DP proton decoupled mode, with a pulse delay of 2.0 s and 15000 scans, whereas for aromatic molecules, a CP contact time of 3 ms, a pulse delay of 5.0 s, and 8000 scans were employed. Chemical shifts were externally referenced to TMS. ^{29}Si resonances were attributed according to literature studies on similar compounds [Chang2004; Huh2005], while the ^{13}C resonances were instead assigned on the grounds of the solution spectra of the corresponding unbound precursors.

The interaction between siloxanes and the oxide surface was also investigated by X-ray photoelectron spectroscopy (XPS) using an M-probe apparatus (Surface Science Instruments) working with monochromatic Al K_α radiation (1486.6 eV). The background was subtracted using the Shirley's method as reported by Ardizzone *et al.* [Ardizzone2009]. The binding energies (BE) were corrected for specimen charging by referencing the C 1s peak to 284.6 eV. The Ti 2p peak fitting was performed using Gaussian line shapes and fixing both BE and the full width at half maximum (FWHM) for the pristine Ti $2p_{3/2}$ component at 458.8 eV and 1.4 eV, respectively. The BE accuracy was $\pm$ 0.1 eV.

Computational set-up. The gas phase dipole moments of the adopted siloxanes were calculated at a semi-empirical level using a PM6 Hamiltonian (Gaussian09 package) in the vacuum for the most stable conformation, as located with Molecular Mechanics techniques and MMFFs force field with a stochastic Monte Carlo analysis of the potential energy surface. Vibrational analysis was used to characterize the PM6 minima.

Results and Discussion

At first, the role of the siloxane content (in the range 0-33% wt) will be presented with respect to a single siloxane molecule (Si-Alk). Then, the effects related to the siloxane structure will be discussed; in particular, the role of an alkyl vs. aryl side-chain will be first investigated, then the effect of side-chain length and fluorination will be presented.

3.2.1 Effect of siloxane content

Structural features. X-ray powder diffraction (XRPD) spectra show that the functionalization with siloxanes does not affect the bulk structure of TiO_2 particles (Figure 3.2.1).
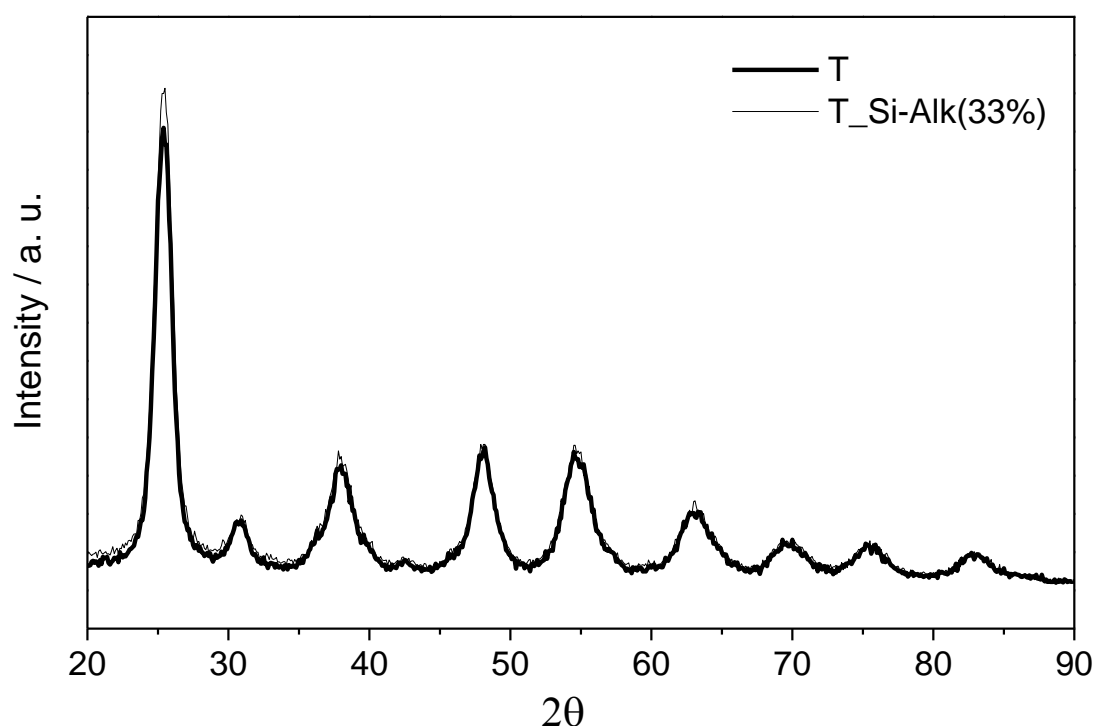
Figure 3.2.1 XRPD spectra of bare and siloxane-clad TiO$_2$.

The oxide phase composition (anatase : brookite 60 : 40) and crystallite size (6 nm) remain unchanged for all the tested siloxane contents. The observed lack of bulk structural effects related to siloxane addition can be rationalized on the grounds the surface nature of the siloxane-TiO_2 interactions and the absence of high temperature treatments following the siloxane deposition.

Morphological features of hybrid particles and films. The morphological features of the oxide particles are instead significantly altered by siloxane addition (Table 3.2.2). A marked decrease of both the specific surface area and the pore volume can be observed, even at low siloxane content. This is mainly related to a significant loss of pore accessibility, particularly for the smallest pores (d < 6 nm), as appreciable in Figure 3.2.2 inset. Figure 3.2.2 reports also the

adsorption-desorption isotherms of N_2 in subcritical conditions for the siloxane-clad titania samples, with their relative hysteresis loops.

Siloxane %	S_{BET} $m^2\,g^{-1}$	V_{pores} $mL\,g^{-1}$
0	204	0.317
5	171	0.279
9	151	0.224
20	83	0.157
33	44	0.107

Table 3.2.2 Specific surface area, S_{BET}, and total pore volume, V_{pores}, as a function of the siloxane content for T_Si-Alk samples.

Both bare and functionalized TiO_2 samples show E-type hysteresis loops, characteristic of "ink-bottle" pores. At increasing siloxane content, N_2 monolayer volumes decrease progressively, indicating a loss of specific surface area, and the hysteresis loops shift on the p/p_0 axis, as a result of a change in pore size distribution (notably the disappearance of the smallest mesopores).
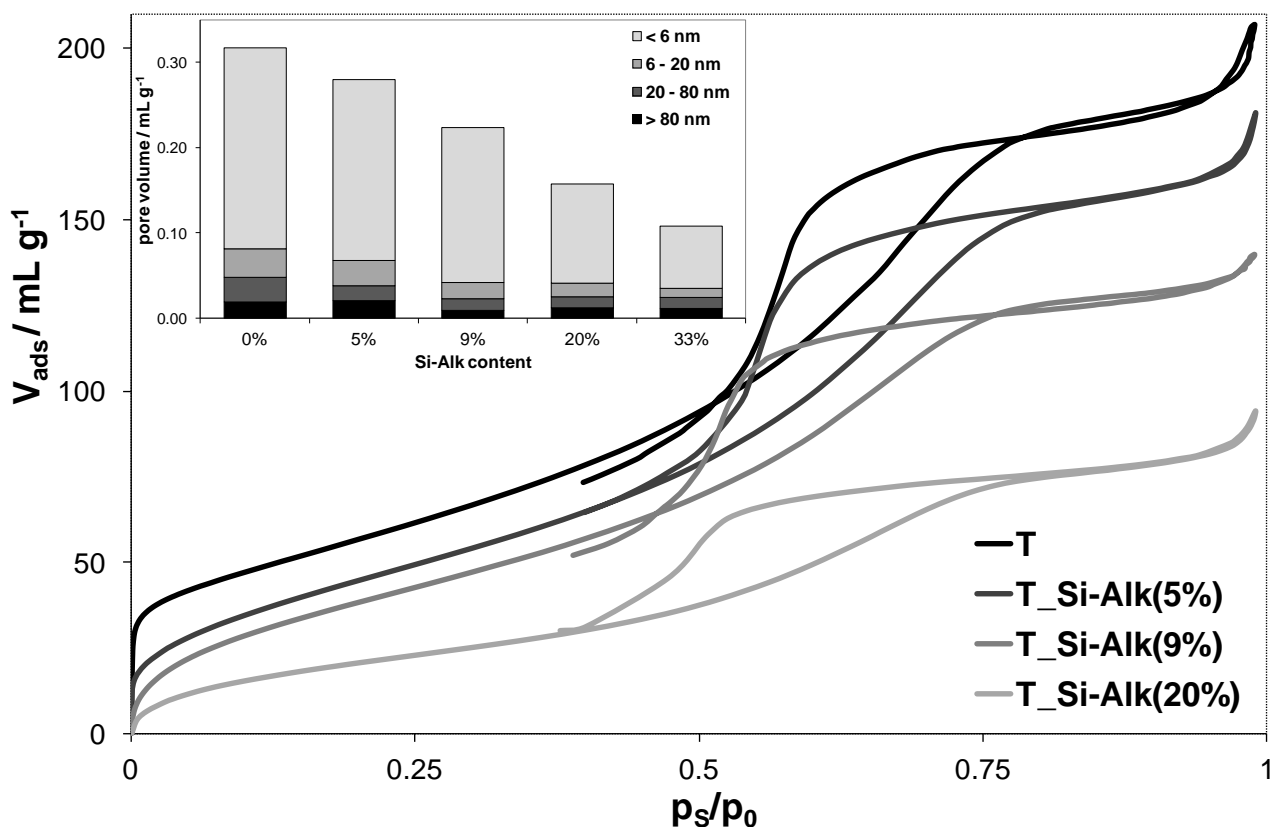
Figure 3.2.2 N_2 adosprion-desorption isotherms at subcritical conditions of T_Si-Alk samples with different siloxane amount. Inset: Pore size distribution as a function of siloxane content.

The observed effects, taking place even at very low siloxane content, may be traced back to a relevant hindrance of the siloxane alkyl chains in the oxide pores and to the occurrence of tail-tail interactions (e.g. Van der Waals forces) between the alkyl chains of neighboring siloxanes.

The morphology of the hybrid films was investigated by means of AFM (Figure 3.2.3). The AFM images show that the glass substrate is completely coated by the titania film, which exhibits a textured, hierarchical topography (root mean square, rms, of 150 nm), due to the presence of both nanometric particles and micrometric aggregates.
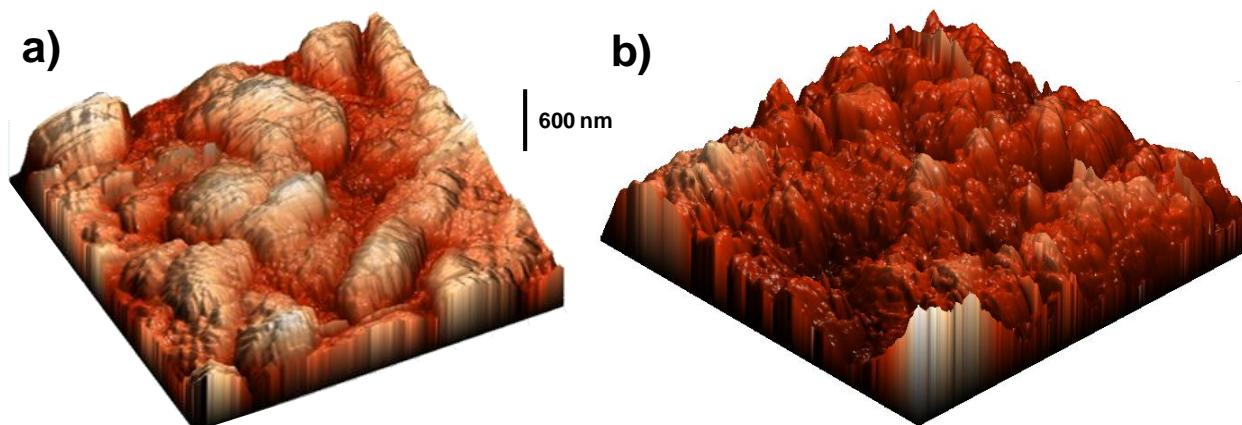
Figure 3.2.3 a) 2 x 2 μm^2 and b) 5 x 5 μm^2 AFM images of TiO$_2$ films deposited by the presented procedure.

The formation of micrometric aggregates of oxide nanoparticles presumably takes place during the drying step, since the DLS analysis of the TiO$_2$ particle dispersion in i-propanol showed a monomodal distribution of particle sizes in the nanometer range (300 nm). The particle size distribution and roughness features are not significantly altered by siloxane addition.

Wetting features. The siloxane addition determines a marked modification of the wettability of the film.
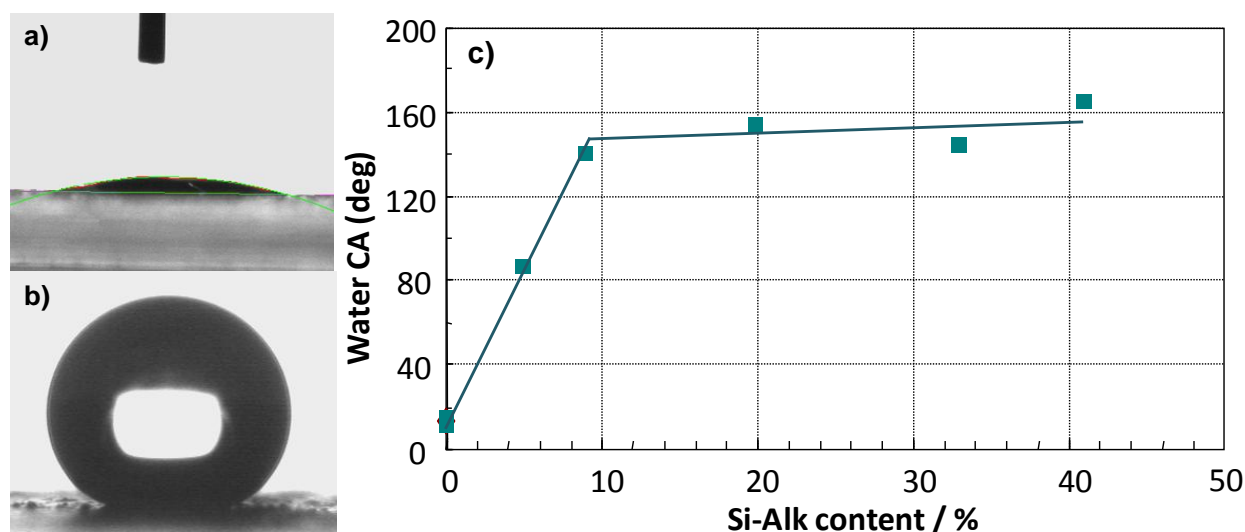
Figure 3.2.4 Wettability of siloxane-TiO$_2$ hybrid films: a) Water contact angle as a function of Si-Alk content, water drops on bare (b) and siloxane-clad TiO$_2$ films (c).

124

While pristine TiO_2 layers exhibit highly hydrophilic behavior (water contact angle $< 5°$, Figure 3.2.4a), siloxane-clad TiO_2 films show extremely large water contact angles (close to 150°, Figure 3.2.4b). In the latter case, the CA measurement was not straightforward since water drops tend to bounce and roll off the hybrid layer, because of its enhanced water repellency. Water CA values were thus determined by rising very slowly the support up to the contact with the pendant drop, till the drop stuck onto the TiO_2 film surface.

Figure 3.2.4c reports the observed water CA values as a function of siloxane content: An increased hydrophobicity is observed even at very low siloxane content and the CA values reach a quasi-plateau region close to 150° for siloxane percentages higher than 9%. The hybrid layers exhibit CA values much higher than the bare siloxane surface (see section 3.1), owing to their textured topography.

To explain such phenomenon, the wetting models for rough surfaces must be taken into account. In fact, Young's equation [Young1805], describing the wetting behavior of ideal surfaces, fails for real, rough surfaces. Two models depict the wettability of such in-homogeneous materials: The Wenzel model, which considers that the liquid spreads at the surface following the actual surface profile (Figure 3.2.5a), and the Cassie-Baxter model, in which air remains trapped inside the surface texture (Figure 3.2.5b).
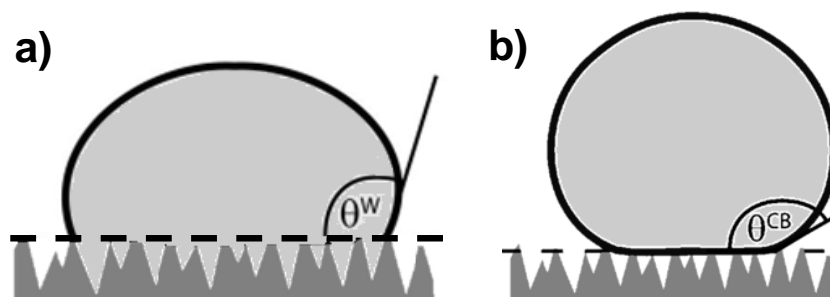
Figure 3.2.5 The Wenzel and Cassie-Baxter models describing the wettability of rough surfaces.

The Wenzel description (Figure 3.2.5a) predicts that the increase in surface area, arising from the material roughness, enhances the material natural wetting tendency [Wenzel1936]: Water will spread even more on a rough hydrophilic substrate in order to extend the energetically favorable solid/liquid contact, while it will reduce its CA on a rough hydrophobic surface to limit the solid/liquid (unfavorable) contact. The Wenzel equation relates the contact angle observed on a rough surface, θ_w, to the ideal Young contact angle, θ_Y, by the solid roughness r:

$$\cos \theta_w = r \cos \theta_Y$$

The solid roughness r is defined as the ratio between the true surface area over the apparent one, thus its value is always larger than unity. In the Wenzel model, the contact angle hysteresis, $\Delta\theta$, i.e., the difference between advancing, θ_a, and receding, θ_r, contact angles, can be very large.

Indeed, in advancing CA measurements, the drop contact line can pin on surface asperities During receding experiments, instead, the receding drop contact line may leave liquid in the cavities, causing a significant decrease of the contact angle (the drop contacts both the hydrophobic solid and itself).

The Wenzel model fails for highly rough, hydrophobic materials, where it is thermodynamically unfavorable that the liquid follows the surface asperities (a hydrophobic material has a higher surface energy wet than dry, $\gamma_{SL} > \gamma_{SV}$). In this state, the so called Cassie-Baxter state [Cassie1944], air remains trapped into the texture and the liquid drop sit on a composite surface consisting of both solid and air (Figure 3.2.5b). The resulting contact angle θ_{CB} is thus an average between the Young CA of the solid and the CA on the air pockets (180°, $\cos\theta = -1$), respectively weighted by the fractions f_s and $1-f_s$:

$$\cos\theta_{CB} = -1 + fs\ (\cos\theta_Y + 1)$$

Since the liquid has a very limited interaction with the solid surface, the contact angle hysteresis in the Cassie-Baxter state is very low since (generally, $\Delta\theta < 5°$).

In the present case, the titania particles impart to the film a multi-scale roughness in the nanometric/micrometric range. Such a textured, hierarchical topography is fundamental for the obtainment of a stable super-hydrophobic behavior [Nosonovsky2009]. Moreover, the occurrence of two polymorphs (anatase and brookite) in the TiO_2 particles may provide random exposure of facets further increasing the in-homogeneity of the texture.

The wetting properties of the functionalized TiO_2 films are the result of an interplay between the discussed substrate roughness and the presence of a layer of low surface energy material. The siloxane layer plays a pivotal role in modulating the interfacial features of the oxide, which would otherwise exhibit an extremely hydrophilic behavior.

The interaction between the TiO_2 surface and the siloxane molecules and the structure of the hydrophobic layer were investigated in detail using a combination of several spectroscopic techniques, that will be discussed in the following.

ATR-FTIR analysis. Figure 3.2.6 reports the FTIR spectra of TiO_2 layers coated with increasing amounts of Si-Alk (the spectrum of the bare TiO_2 was previously subtracted).

The functionalization with siloxane gives rise to strong bands in the region 800-1200 cm^{-1} and 2800-3000 cm^{-1}. Peak intensities increase with increasing siloxane content, suggesting that no saturation of the oxide surface takes place in the investigated range.
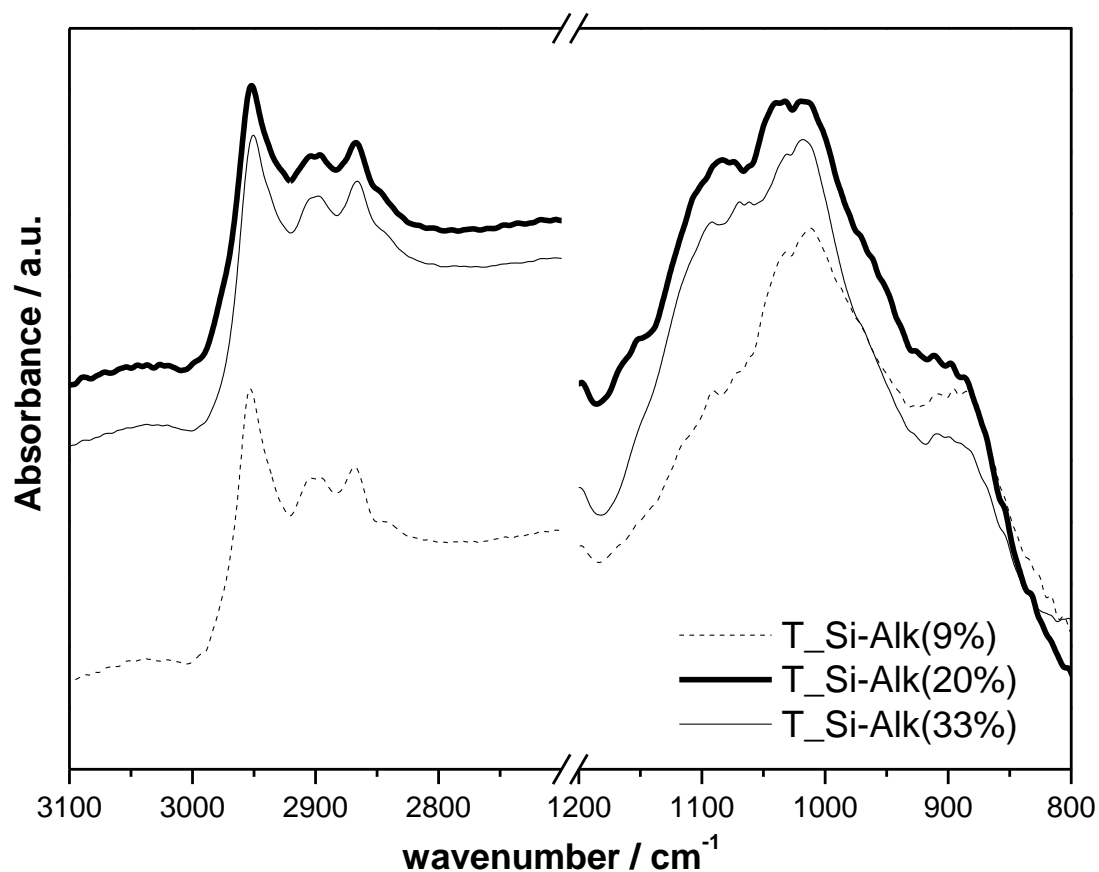
Figure 3.2.6 FTIR spectra of T_Si-Alk samples. The spectrum of T was previously subtracted.

The sharp bands in the 2900-2700 cm^{-1} region, can be assigned to ν_{C-H} stretching modes of the siloxane molecule, on the basis of their spectral position and of literature data [Bellamy1968]. The bands located at 919-926 cm^{-1} can be instead attributed to stretching vibrations of the Ti-O-Si bonds [Xu2006; Zeitler1957a; Young1948; Tripp1991]. On the other hand, a straightforward attribution of the components in the region 950-1150 cm^{-1} is not feasible because of the superimposition of Si-O-Si/Si-O-C bands. The Si-O-Si stretching vibrations are reported to occur in a wide region, from ca. 950 to 1150 cm^{-1} [Zeitler1957a; Young1948; Tripp1991], while Si-O-C bonds gives rise to peaks at ca. 1050 cm^{-1} [Xu2006; Zeitler1957a]. However, the peak at 1013 cm^{-1} may be attributed to Si-O-Si bonds at the TiO_2 surface.

Solid state NMR. [13]C and [29]Si cross-polarization magic angle spinning nuclear magnetic resonance (CPMAS NMR) analyses were performed to study the siloxane molecules chemisorbed at the TiO_2 surface and to obtain structural information about the hydrophobizing film.

Figure 3.2.7 reports the ^{29}Si CPMAS NMR spectra of the siloxanes-clad TiO_2 samples obtained from different starting amounts of Si-Alk. The [29]Si spectra show resonances in the region from -65 to -50 ppm, typical of Si groups, slightly shifted with respect to the resonance of the un-bound Si-Alk precursor (-46 ppm).
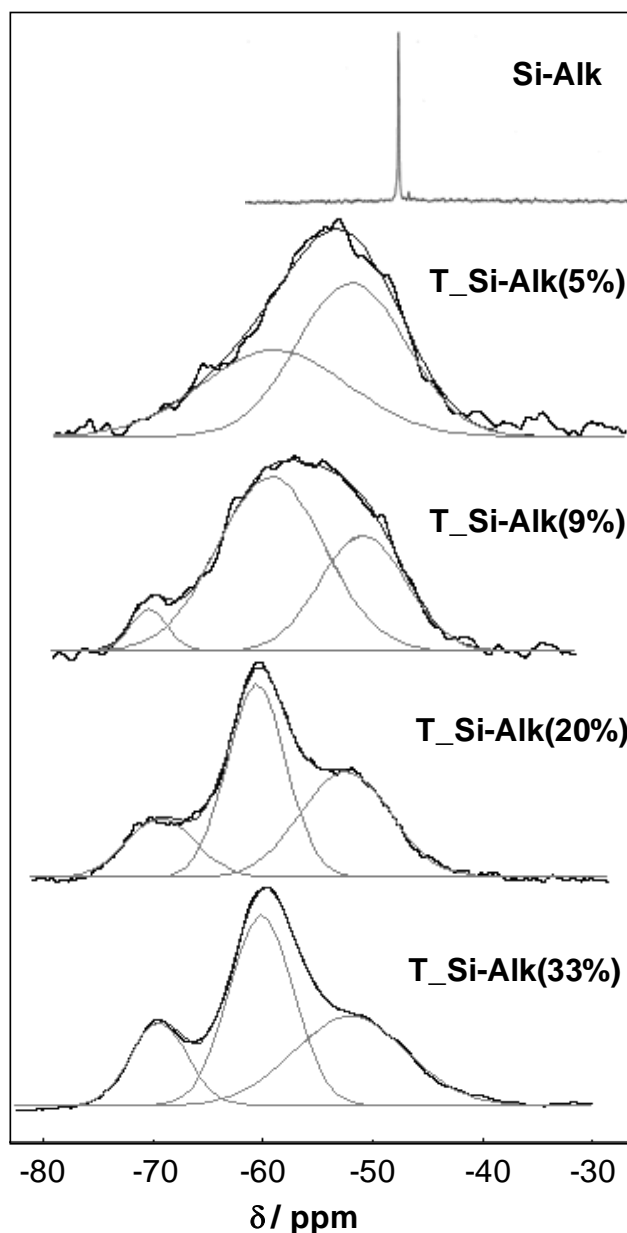
Figure 3.2.7 ^{29}Si NMR spectra of the Si-Alk molecule (in solution) and of the T_Si-Alk hybrids (CPMAS).

At increasing siloxane content, ^{29}Si signals become more and more structure, showing several well resolved resonances which are indicative of the co-presence of species with different chemical structures.

The three observed resonances were attributed to siloxane molecules in which the ethoxy groups have been substituted by one, two or three Si-O-Ti(Si) bonds, either with the oxide surface or with neighboring siloxane molecules, as shown in Figure 3.2.8.
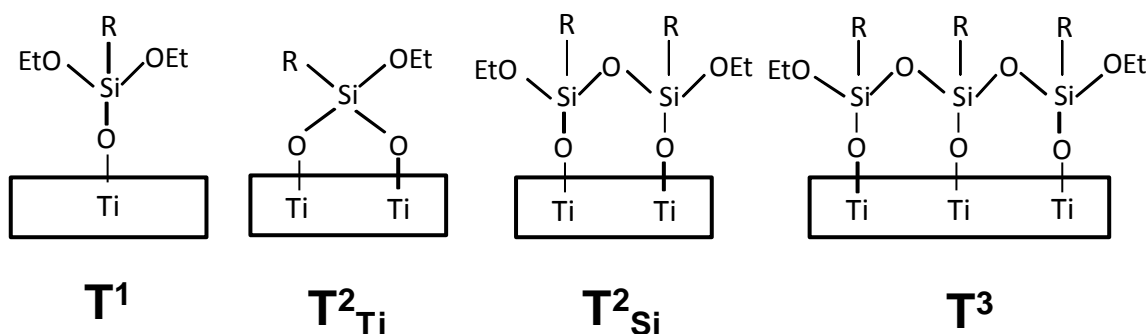
Figure 3.2.8 Sketch of the structures assigned to the different resonances of the ^{29}Si NMR peak (R represents the siloxane alkyl chain).

A fitting analysis of the ^{29}Si signals was carried out adopting Gaussian functions, in order to determine the chemical shift and relative abundance of the different structures (Table 3.2.3).

Sample	$\mathbf{T^1}$		$\mathbf{T^2_{Si}} / \mathbf{T^2_{Ti}}$		$\mathbf{T^3}$	
	δ ppm	%	δ ppm	%	δ ppm	%
T_Si-Alk(5%)	-51	57	-58	43	–	–
T_Si-Alk(9%)	-51	40	-58	56	-69	4
T_Si-Alk(20%)	-51	38	-59	46	-68	16
T_Si-Alk(33%)	-52	37	-60	45	-69	18

Table 3.2.3 ^{29}Si CPMAS NMR chemical shifts, δ, and relative percentage for the three observed Si resonances.

The obtained chemical shift values associated with the different species (named $\mathbf{T^1}$, $\mathbf{T^2}$ and $\mathbf{T^3}$) are in good agreement with the literature data for Si atoms coordination [Chang2004]. the resonance at about -51 ppm can be assigned to a species with only one Si-O-Ti bond to the oxide surface ($\mathbf{T^1}$ structure). Two different kinds of $\mathbf{T^2}$ structures, exhibiting one residual ethoxy group, can give rise to the signal at about -60 ppm: Either a siloxane molecule forming two Si-O-Ti bonds with the oxide surface ($\mathbf{T^2_{Ti}}$ structure), or a siloxane presenting only one bond with the TiO$_2$ surface and one Si-O-Si bond with a neighboring siloxane molecule ($\mathbf{T^2_{Si}}$ structure). The NMR technique does not allow to discriminate between these two structures. Further, the calculated bond strengths for Ti-O and Si-O bonds are quite similar (ca. 112 and 103 kcal mol^{-1} for Ti-O and Si-O, respectively) [Zeitler1957b]. Even ATR-FTIR analysis cannot clarify this point, since both Si-O-Ti and Si-O-Si stretching modes increase with increasing siloxane content. Therefore, the relative abundance of the two possible $\mathbf{T^2}$ structures ($\mathbf{T^2_{Ti}}$ and $\mathbf{T^2_{Si}}$) at this stage could not be conclusively assessed.

Finally, the resonance at ca. -69 ppm was attributed to a **T^3** structure, in which all three EtO-groups have been substituted by Si-O-Ti(Si) bonds. The formation of three Si-O-Ti bonds between the siloxane molecule and the oxide surface is discarded on the grounds of bond length/angle values in siloxanes and TiO$_2$ surface structure[3], and in agreement with Iguchi and coauthors [Iguchi2008]. The formation of two Si-O-Ti bonds and of one Si-O-Si bond with an adjacent siloxane can also be discarded on the same grounds. Thus, most feasible T^3 structure presents one bond with the oxide surface and two lateral bonds with neighboring siloxanes, giving rise to a cross-linked olygo/polymeric structure at the oxide surface.

As reported in Table 3.2.3, at low siloxane content, the T^1 component is prevalent, although there is also a significant amount of T^2 component. With increasing siloxane content, the T^2 structures become the prevailing ones. At siloxane amounts larger than 9%, the T^3 structure appears. Then, the relative enrichment in the siloxane-TiO$_2$ structural components remains almost unchanged at the two highest siloxane percentages.

On the grounds of these results, it can be proposed that siloxane molecules, at increasing siloxane content, are progressively involved in one, two and three bonds, as depicted in Figure 3.2.9. However, for all tested concentrations (except for lowest siloxane amount), the prevailing structure remains T^2.
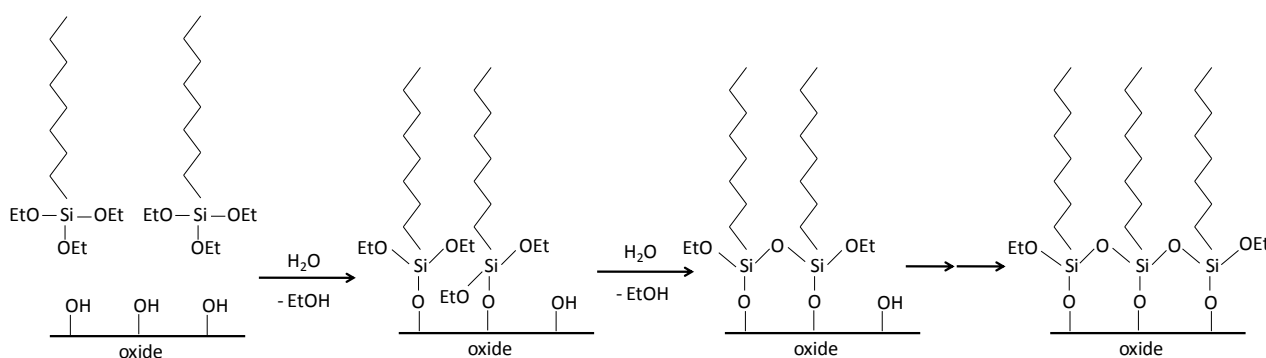
Figure 3.2.9 Sketch representing the mechanism of formation of siloxane-TiO$_2$ bonds.

XPS. X-ray photoelectron spectroscopy (XPS) analyses of the functionalized TiO$_2$ samples were carried out to deepen the insight into the siloxane-TiO$_2$ interactions. Survey XPS spectra showed no significant presence of impurities, except for the ubiquitous carbon contaminant.

The Si $2p_{3/2}$ peak, which in the case of the un-bound siloxane molecule occurs at 102.2 eV, in the functionalized TiO$_2$ samples exhibits a second component at higher BE (ca. 103.4 eV). The relative enrichment in the two Si components could not be quantitatively esteemed because of the high signal to noise ratio of this region, particularly for the samples with low siloxane content.

---

[3] http://webbook.nist.gov/chemistry.html.

Also the Ti 2p region (Figure 3.2.10) presents a second component in the case of functionalized samples. While pristine TiO_2 (Figure 3.2.10a) exhibits a Ti $2p_{3/2}$ peak at 458.8 eV, characteristic of Ti(IV) in the oxide [Crist2000], all siloxane-clad samples (Figure 3.2.10b) shows a complex pattern suggesting the co-presence of two components. The first peak, at lower BE, corresponds to the regular Ti 2p component of oxide materials, while the second one, Ti*, is shifted at higher BE by more than 1 eV. The Ti* component shows that some Ti species in the functionalized samples experience a more electron-attracting environment than Ti in the pristine oxide. The presence of a second component in both the Si and Ti XPS regions suggests the formation of a robust covalent bond between the siloxane molecule and the oxide surface.
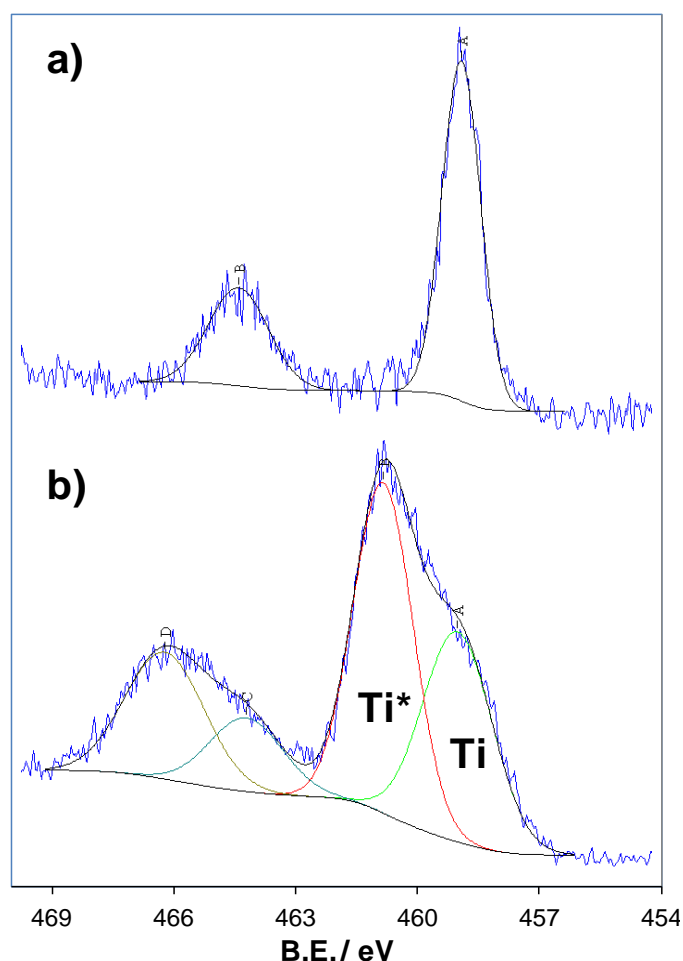
Figure 3.2.10 Ti 2p XPS spectra of a) T and b) T_Si-Alk(9%).

The oxygen 1s region exhibits as well a complex pattern in the case of siloxane-treated samples. In the pristine oxide, the oxygen signal can be fitted by two peaks: The component at 529.8 eV corresponds to oxygen in the TiO_2 lattice, while the second one (at 532.5 eV) can be attributed to surface OH groups [Ardizzone2009]. The spectrum of the un-bound siloxane precursor shows instead a single peak at 531.3 eV. In all the T_Si-Alk samples, the oxygen peaks can be fitted by several components, including those of bare oxide and of the siloxane molecules. The latter

component increase its weight at increasing siloxane content. No quantitative analysis of the different oxygen components was performed due to the large component of arbitrariness inherent in the fitting procedure in the presence of several components.

Table 3.2.4 reports the Si/Ti atomic ratios obtained by XPS for the various T_Si-Alk samples and compares them with the nominal Si/Ti ratio, calculated from the moles of siloxane and TiO_2 adopted in the synthesis (Si/Ti bulk). The XPS Si/Ti values increase linearly with the starting Si/Ti ratio. However, for all tested percentages, the measured ratios are larger than the nominal ones. This phenomenon can be attributed to the preferential location of the siloxane molecules at the oxide surface. This conclusion is also supported by the absence of bulk structural effects in functionalized TiO_2.

Sample	Si/Ti bulk	Si/Ti XPS	Ti*	
			B.E. / eV	FWHM / eV
T_Si-Alk(5%)	0.01	0.09	460.2	1.75
T_Si-Alk(9%)	0.03	0.13	460.3	1.55
T_Si-Alk(20%)	0.06	0.20	460.6	1.40
T_Si-Alk(33%)	0.10	0.30	460.1	1.20

Table 3.2.4 XPS Si/Ti atomic ratios and Ti* 2p binding energies, B.E., and FWHM values for the various T_Si-Alk samples.

The observed Si/Ti ratios are indicative of low density layers [Spori2007]. Such loosely packed structures possess an increased flexibility and permeability with respect to conventional densely packed layers, which may be exploited by several technological applications [Park2005].

Table 3.2.4 reports also the binding energy and width (FWHM) values of the Ti* component of the Ti 2p signal in siloxane functionalized TiO_2. Interestingly, the Ti* peak width decreases with increasing siloxane content. This may be related to a decrease in the conformational variety of the structures containing Si-O-Ti bonds. Indeed, at low siloxane content (T_Si-Alk) both T^1 and T^2_{Ti} structures may occur, resulting in a very broad Ti* (FWHM 1.7). At larger siloxane percentages, cross-linking between neighboring siloxane molecules takes place, so that structures like T^2_{Si} and T^3 may be prevalently formed. Such a progressive decrease in the possible configurations may result in the narrowing of the Ti* peak.

3.2.2 Effect of siloxane nature

The second crucial aspect to be investigated was the role played by the structure of the functionalizing molecule. In this respect, the effect of the molecule side-chain on the structure of the hydrophobing layer was studied. In addition, the chemical interactions between the siloxane molecule and several solvents were investigated to determine their consequence onto the wetting behavior of the hybrid films by non-aqueous solvents.

At first, siloxanes with an alkyl and aryl chain will be compared, then the role of the side-chain length and fluorination will be discussed.

3.2.2.1 Alkyl vs. aryl chain

In this section, Si-Alk, Si-Tol and Si-biPh will be compared for their ability to functionalize TiO_2, in the concentration range 0-29%.

Morphological features. The morphological properties of the oxides functionalized with the three tested siloxanes show interesting differences. For all the adopted molecules, the sample specific surface areas decrease progressively at increasing siloxane content (Figure 3.2.11).
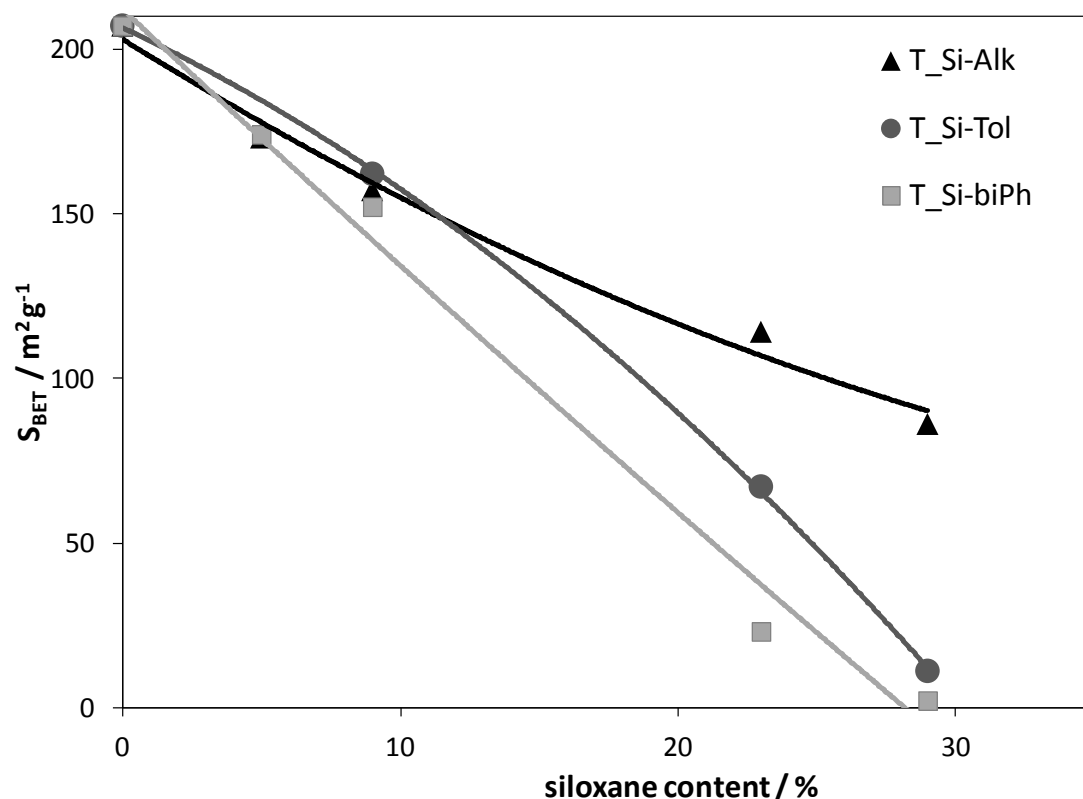
Figure 3.2.11 Specific surface area of the siloxane-TiO$_2$ samples *vs.* siloxane content.

However, such phenomenon is much larger in the case of the two aromatic molecules. For instance, at 29% coverage, the specific surface area of T_Si-Alk, T_Si-Tol and T_Si-biPh are

respectively ca. 80, 11 and 2 m^2 g^{-1}. Similarly, increasing the siloxane content causes a marked decrease of the pore volume, especially concerning the smallest mesopores, which is more significant in the case of the two aromatic molecules. At 29% coverage, the total pore volume of the T_Si-Alk, T_Si-Tol and T_Si-biPh samples are around 0.174, 0.056 and 0.016 mL g^{-1}, respectively. As previously discussed in the case of T_Si-Alk, the loss of surface area and pore volume can be traced back to the hindrance produced by the siloxane organic moieties into the pores of the oxide particles. Apparently, the aromatic moieties give rise to a more significant hindrance that could also be related to more relevant tail-tail interactions (see NMR discussion).

Furthermore, the different siloxanes exhibit striking differences, especially at low siloxane content, with respect to the distribution of carbon species, obtained by EDX mapping (Figure 3.2.12).
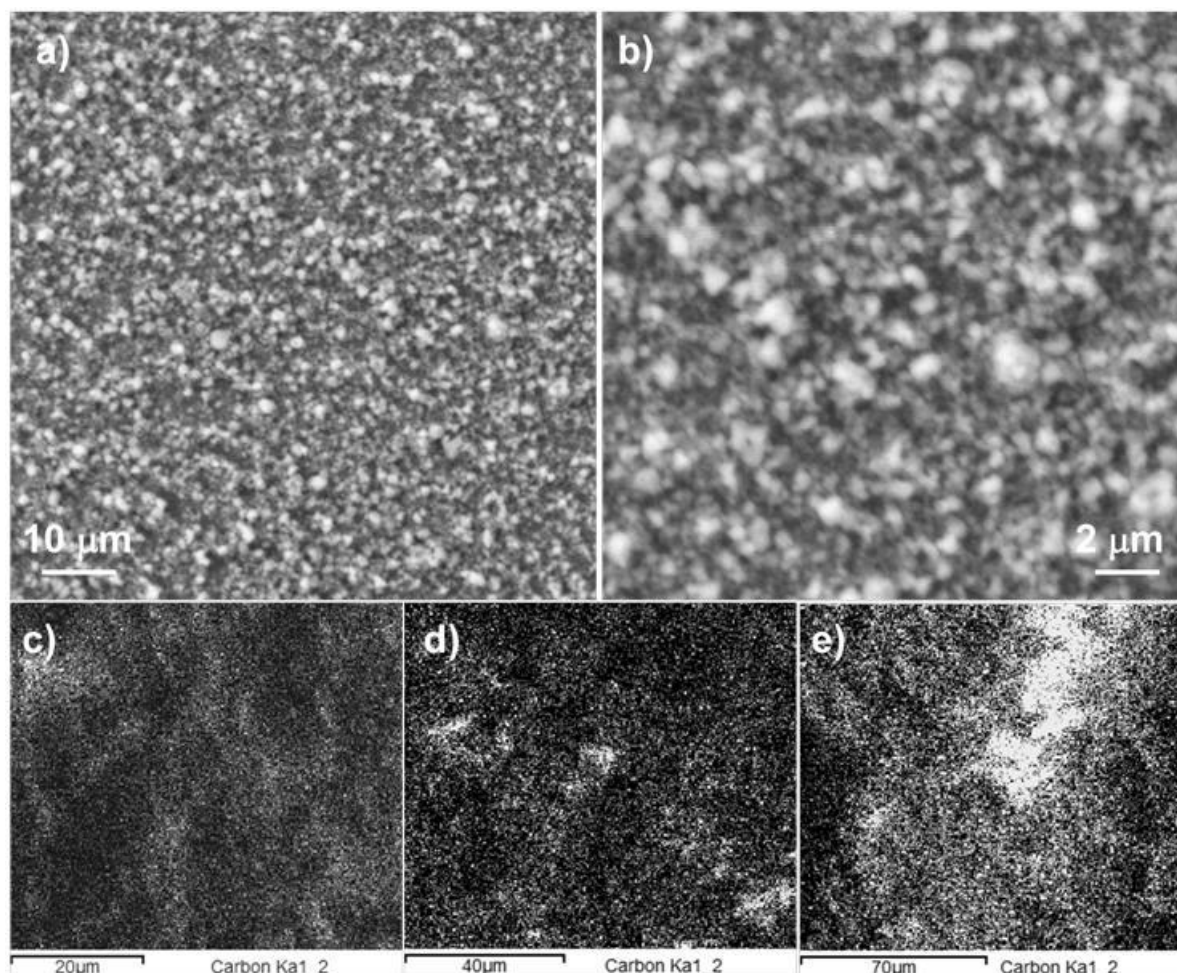
Figure 3.2.12 a,b) SEM images of TiO$_2$ films and carbon EDX mapping of c) T_Si-Alk(5%), d) T_Si-Ph(5%), e) T_Si-biPh(5%).

The distribution of carbon species (Figure 3.2.12c,d,e), thus the homogeneity of the siloxane layer, does not simply reflect the texture of the oxide film (Figure 3.2.12a,b) but is instead mainly affected by the molecule arrangement. The alkyl siloxane gives rise to a homogeneous distribution

of carbon species over all the layer (Figure 3.2.12c). The T_Si-Tol sample shows a rather homogeneous distribution, with only few small brighter spots corresponding to carbon enriched areas. Instead, the T_Si-biPh film presents large light spots, due to the localized presence of a high level of C-species, resulting from the inhomogeneous distribution of the siloxane over the TiO_2 layer.

Wetting features. Dynamic contact angle measurements were carried out to determine both the advancing θ_a and receding θ_r, contact angles as a function of the type of hydrophobizing molecule and of its content (Figure 3.2.13). The three tested siloxanes exhibit completely different wetting behaviors as a function of their amount in the hybrid film.
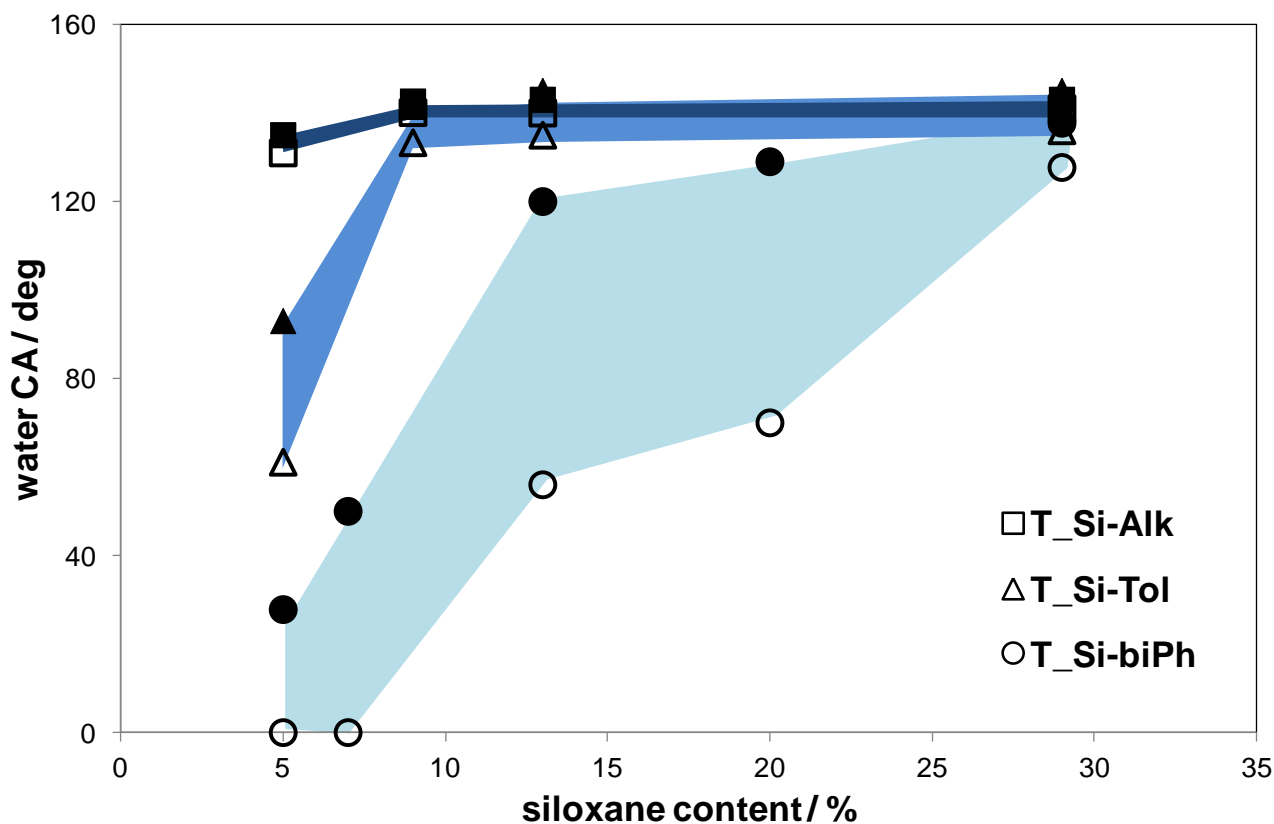
Figure 3.2.13 Water advancing (full markers) and receding angles (empty markers) contact angles as a function of siloxane content for siloxane-TiO$_2$ films.

The T_Si-Alk films present high contact angles and small hystereses between advancing and receding angles ($\Delta\theta < 5°$), starting from low siloxane content. Such a behavior is indicative of a Cassie-Baxter wetting regime.

On the other hand, T_Si-Tol wetting behavior shows a more marked dependence on the siloxane content. At low siloxane coverage, the water contact angle indicates a moderate hydrophobicity and the CA hysteresis is large. Increasing the siloxane amount results in an increase of the observed advancing contact angles, that become comparable to the T_Si-Alk ones, though the

CA hysteresis remains larger ($\Delta\theta < 10°$). Thus, in the case of T_Si-Tol, a Cassie-Baxter-like regime is appreciable only at high coverage.

T_Si-biPh shows instead a hydrophilic surface at the lowest siloxane coverage. At increasing siloxane content, water CAs increase while the hysteresis remains relevant ($\Delta\theta > 50°$). Only at the highest coverage, the contact angle hysteresis becomes comparable to those of T_Si-Tol samples ($\Delta\theta \sim 10°$). Thus, the wetting regime for T_Si-biPh samples varies from hydrophilic to hydrophobic, going through a broad Wenzel region, ending at the extreme of the investigated range of siloxane amounts with a Cassie-Baxter behavior.

The observed differences in the wetting properties of the hybrid films are rather unexpected, since transitions from Wenzel-like to Cassie-Baxter-like states are generally related to changes in the surface topography, such as an increase of surface roughness. In the present case, the oxide film topography remains unaltered and only the structure of the siloxane layer at the surface may change. Indeed, the actual length scale of surface features imparting a Cassie-Baxter behavior, is a debated topic in the literature [Kuna2009; Borras2010].

As previously discussed, the wetting properties of the siloxane-TiO_2 hybrid films are the result of an interplay between film roughness and siloxane chemistry and structure. Since the morphological features of the hybrid films remain almost unchanged and the three siloxane molecules present very similar surface free energy (SFE) values (31, 32 and 33 mN m^{-1} for Si-Alk, Si-Tol and Si-biPh, respectively), the different interfacial features of the hybrid films may derive from a different surface organization of the siloxane molecules.

Solid state NMR. Relevant differences in the organization of the siloxane layer at the oxide surface can be appreciated by solid state NMR. Figure 3.2.14 reports the ^{29}Si CPMAS NMR spectra of T_Si-Alk, T_Si-Tol and T_Si-biPh for 9% and 23% siloxane amounts.

The absence of physisorbed/excess siloxane molecules is confirmed by ^{29}Si CPMAS NMR spectra, since they would give rise to a separate sharp signal shifted in the direction of the unbound precursor.

^{29}Si resonances are in the spectral region typical of siloxane groups. The observed chemical shifts differ depending on the adopted siloxane: T_Si-Alk derivatives present peaks in the region from -51 to -69 ppm, while T_Si-Tol resonances are from -60 to -81 ppm and T_Si-biPh signals are from -39 to -48 ppm. The position of the observed peaks seems dependent on the type of organic side chain and on the number of ethoxy groups in the un-bound siloxane. The higher number of oxygens connected to the Si atom in Si-Alk and Si-Tol with respect to Si-biPh, determines the presence of a higher charge on the Si atom and consequently an up-field shift. A further up-field

shift of the ^{29}Si resonance (ca. 10 ppm) occurs by substituting the alkyl chain of T_Si-Alk with an aromatic ring (T_Si-Tol).
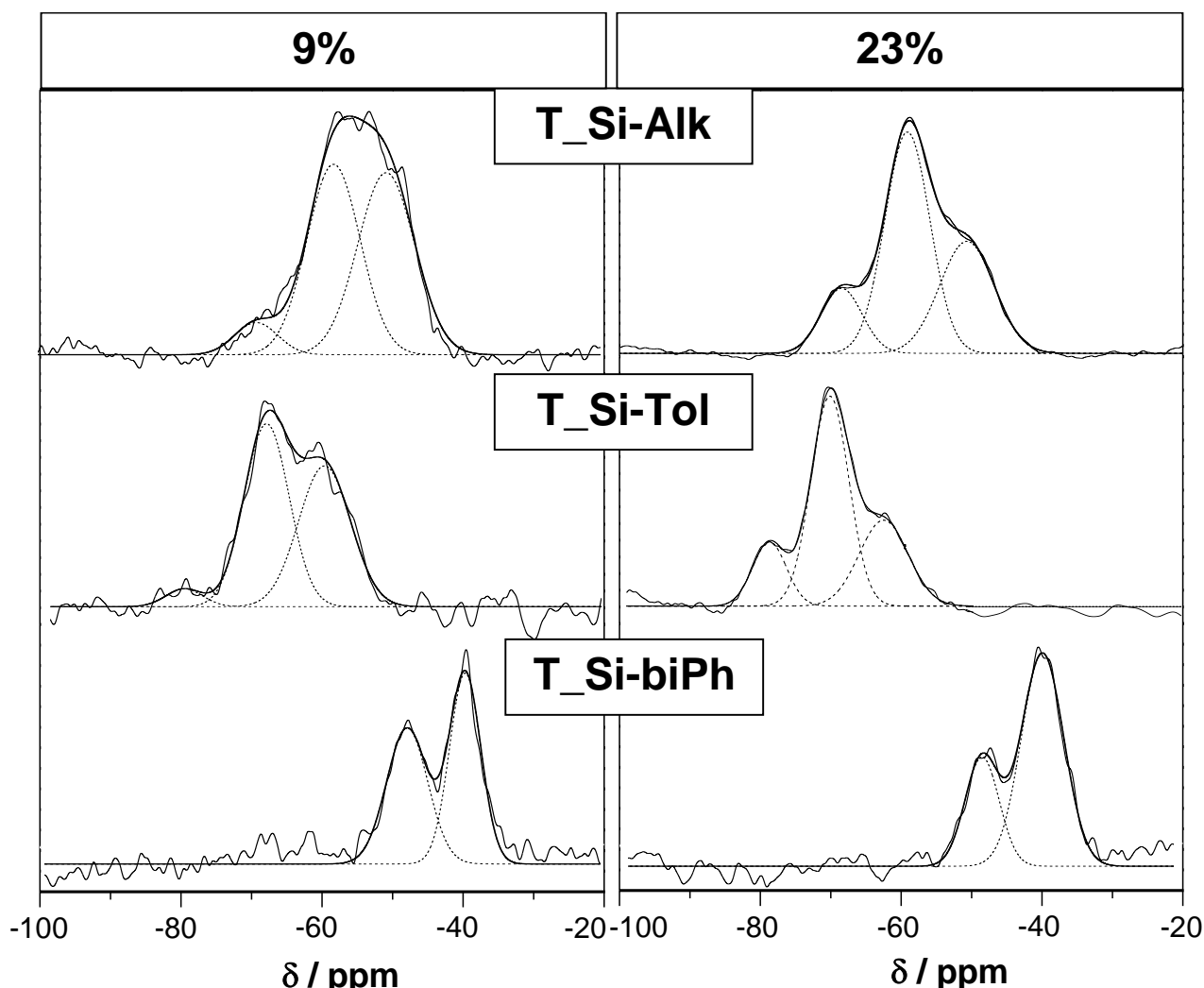
Figure 3.2.14 ^{29}Si CPMAS NMR spectra of T_Si-Alk, T_Si-Tol, and T_Si-biPh at 9% and 23% siloxane content.

The ^{29}Si spectra of the T_Si-Alk and T_Si-Tol samples show three well resolved resonances, indicative of the co-presence of several Si species with different chemical structures, as discussed in the section 3.2.1. Only two components are instead detected in the T_Si-biPh spectra.

Table 3.2.5 reports the chemical shift values, the line widths and the relative percentages of the observed resonances obtained by the fitting analysis of the ^{29}Si signals.

According to the considerations reported in section 3.2.1, resonances at -51, -60/-63 and -40/-39 ppm for the T_Si-Alk, T_Si-Tol and T_Si-biPh samples, respectively, can be attributed to the **T^1** structure. The signals at -58/-59, -69/-71 and -48 ppm for T_Si-Alk, T_Si-Tol and T_Si-biPh, respectively, can be assigned to the **T^2** structures. Finally, the ^{29}Si resonances at -69/-68 for T_Si-Alk and at -81/-80 ppm for T_Si-Tol, can be related to the **T^3** structure. The fact that T_Si-biPh samples do not show this latter resonance supports the adopted attributions, since Si-biPh has only two ethoxy groups and is consequently unable to form the T^3 structure.

137

		T_Si-Alk		T_Si-Tol		T_Si-biPh	
		9%	*23%*	*9%*	*23%*	*9%*	*23%*
T^1	δ *(ppm)*	-51	-51	-60	-63	-39	-39
	%	48	33	44	31	52	76
	$\Delta v_{1/2}$ *(Hz)*	755	775	715	695	447	616
T^2$_{Ti}$/T^2$_{Si}$	δ *(ppm)*	-58	-59	-69	-71	-48	-48
	%	47	53	56	58	48	31
	$\Delta v_{1/2}$ *(Hz)*	775	636	675	536	586	497
T^3	δ *(ppm)*	-69	-68	-	-80	-	-
	%	6	14	-	16	-	-
	$\Delta v_{1/2}$ *(Hz)*	576	576	-	477	-	-

Table 3.2.5 ^{29}Si CPMAS NMR chemical shifts, δ, relative percentage and line-width, $\Delta v_{1/2}$, for the proposed Si structures (T^1, T^2 and T^3) in the different siloxane-TiO$_2$ hybrids.

The relative enrichment in the different structures (Table 3.2.5) shows that the T^1 and T^2 components are prevalent in the case of T_Si-Alk and T_Si-Tol, at the lowest siloxane content. At higher siloxane coverage, the T^1 decreases and a significant percentage of T^3 structure arises. On the contrary, T_Si-biPh presents a marked decrease of the T^2 percentage with respect to the T^1 one, at increasing siloxane content. The T^1 structure may become favored in T_Si-biPh hybrids because it is less strained, owing to the presence of two phenyl groups in the siloxane molecule. Thus, at increasing surface content, the bi-substituted compound favors the T^1 structure, while the two tri-substituted siloxanes tend to form more and more polymeric T^3 structures.

The NMR spectra can also provide information about dynamic processes by analyzing the variations of the ^{29}Si signals line-widths. In fact, the peak widths are mainly affected by the dispersion of isotropic chemical shifts due to structural disorder. The line-widths ($\Delta v_{1/2}$) of the studied materials are reported in Table 3.2.5. T_Si-Tol and T_Si-biPh hybrids at all siloxane amounts present narrower line-widths with respect to the corresponding signals of the T_Si-Alk samples. Such change is caused by a reduction in molecular motion. Alkyl chains, being more flexible than aromatic rings, give access to more conformational freedom in the side-chain mobility, causing the observed broadening of the peak. Aromatic siloxanes instead show a narrower line-shape indicative of an increased homogeneity in the chemical environment surrounding the Si site. This can be possibly attributed to a more ordered packing of the aryl groups, due to the occurrence of π-π stacking interactions between the aromatic ring of neighboring siloxane molecules [Trebosc2005].

The π-π stacking interactions may promote the aggregation of siloxane molecules, markedly affecting the morphological properties of the resulting film. This conclusion is supported by both

EDX mapping, which exhibits notable differences in the siloxane distribution at the film surface, and BET analysis, which shows much lower surface area values in T_Si-Tol and Ti_Si-biPh samples, due to the occurrence of pore clogging by the more rigid and organized aryl chains. The occurrence of long range inhomogeneity in the film due to the inherent π-π interactions has significant effects on the wetting properties of the resulting material. Indeed, even at high coverage, the T_Si-Tol hybrids show higher CA hystereses than T_Si-Alk samples. Moreover, in the case of Si-biPh, the bi-functional molecule cannot form polymeric bonds between neighboring molecules at the TiO$_2$ surface, leading to a more patch-wise surface and consequently to very large contact angle hysteresis values. Conversely, the T_Si-Alk films are much more homogeneous, even at very low siloxane content, giving rise to large water contact angles and very low hysteresis values.

Chemical interactions. The structure of the siloxane molecules, beside determining the organization of the functionalizing layer, might also give rise to specific chemical interactions with the test solvents.

Table 3.2.6 reports the contact angles, with the relative hystereses, of the three siloxane hybrids with respect to several solvents.

Contact angle (deg)		T_Si-Alk			T_Si-Tol			T_Si-biPh		
		5%	*9%*	*29%*	*5%*	*9%*	*29%*	*5%*	*9%*	*29%*
water	θ_{avg}	133	141	142	77	137	141	14	35	133
	$\Delta\theta$	< 5	< 5	< 5	32	< 10	< 10	28	60	< 10
glycerol	θ_{avg}	138	137	139	51	132	136	< 10	18	80
	$\Delta\theta$	< 5	< 5	< 10	17	< 10	< 10	< 5	< 10	40
ethylene glycol	θ_{avg}	< 10	134	139	< 10	70	125	< 10	< 10	< 10
	$\Delta\theta$	< 5	< 5	< 5	< 5	16	< 5	< 5	< 5	< 5
toluene	θ_{avg}	< 10	< 10	< 10	< 10	< 10	< 10	< 10	< 10	< 10
	$\Delta\theta$	< 5	< 5	< 5	< 5	< 5	< 5	< 5	< 5	< 5

Table 3.2.6 Average contact angles, θavg, and hysteresis between advancing and receding angles, Δθ, of the tested siloxane-TiO$_2$ hybrid films with respect to different solvents.

The same wettability sequence is observed for all hybrids: water < glycerol < ethylene glycol < toluene. The latter solvent totally wets all the tested films. T_Si-Alk films are fully liophobic with respect to both water and glycerol, starting at very low siloxane content (5%). On the contrary T_Si-biPh films are liophilic for all the solvents, showing liophobic behavior only with respect to water at high siloxane amounts. T_Si-Tol samples exhibit an intermediate behavior, presenting a broad distribution of the wetting features.

Thus, the use of solvents other than water allow us to better appreciate the diverse wetting properties of the different siloxane composites. Indeed, water is a polar protic contact liquid, highly

self-associated through hydrogen bonding, which is highly sensitive to trace amounts of polar species, but largely insensitive to minor differences in non-polar species [Park2005]. It is clear from these considerations that the nature of the electrostatic interactions taking place at the interface between the solvent and the substrate should be considered.

To this respect, the dipole moments of the adopted siloxanes were esteemed by semiempirical calculations (Figure 3.2.15b). These calculations do not consider the siloxanes-surface interactions. However, this is a minor approximation in this context, since electrostatic interactions between substrate and solvent are mainly local. The calculated modules of the siloxane dipole moment are compared with the polar and disperse components of the surface tensions of the adopted solvents (Figure 3.2.15a).
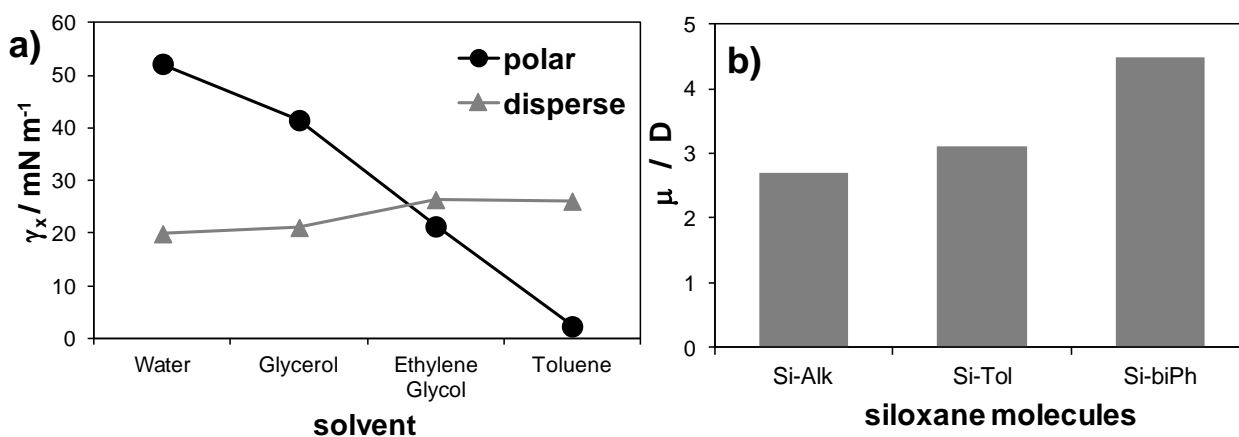
Figure 3.2.15 a) Polar and disperse components of surface tension for the different adopted solvents. b) Modules of the calculated dipole moments for the three siloxane molecules.

By comparing data in Figure 3.2.15 and those in Table 3.2.6, it appears that solvents with a large polar component of the surface tension, exhibit high contact angle values on hybrid films where the adopted siloxane has a low dipole moment. Hence, the comparison of siloxane dipole moments with solvent polar components can be used in a predictive way to determine the lyophilic/lyophobic behavior of a hybrid surface.

3.2.2.2 Length of the alkyl chain and fluorination

In this section, Si-8C, Si-18C and Si-8C(F) will be compared for their ability to functionalize TiO_2. The amount of siloxane was maintained constant (33% w/w). This content was selected on the grounds of the previously shown results relative to other siloxane molecules, indicating an invariance of the hybrid features (CA, NMR, and FTIR) for siloxane amounts larger than 30%.

Morphological features. The morphological properties of the oxides functionalized with the three tested siloxanes present significant differences. For all the adopted molecules, the sample specific surface areas decrease progressively at increasing siloxane content (Table 3.2.7), mainly as

a result of the loss in pore volume. However, such phenomenon is much larger in the case of the case of T_Si-18C. On the grounds of previous results about different siloxanes and in agreement with NMR data (reported below), the present morphological data support the formation of a very compact and ordered siloxane layer in the T_Si-18C functionalized samples, due to presence of relevant tail-tail networks.

sample	S_{BET} m^2 g^{-1}	V_{pores} mL g^{-1}
T	214	0.35
T_Si-8C(33%)	33	0.10
T_Si-8C(F)(33%)	42	0.11
T_Si-18C(33%)	2	0.01

Table 3.2.7 Specific surface area, S$_{BET}$, and total pore volume, V$_{pores}$, for the different siloxane-TiO$_2$ samples.

Wettability features. Before considering the wetting behavior of the siloxane-TiO$_2$ hybrids, the surface properties of the bare siloxane films will be discussed.

The total SFE and relative polar and disperse components obtained for the present siloxanes are reported in Figure 3.2.16. The unfluorinated siloxanes, Si-8C and Si-18C, exhibit similar SFE values but a different polar/disperse component ratio: The disperse component is higher in the case of the longer alkyl chain. On the other hand, the fluorinated compound, Si-8C(F), presents a much lower total SFE. In particular, the disperse component is almost halved with respect to the un-fluorinated analogue, as expected from the weak dispersive interactions of fluorocarbons related to the high ionization potential of fluorine and its low polarizability.
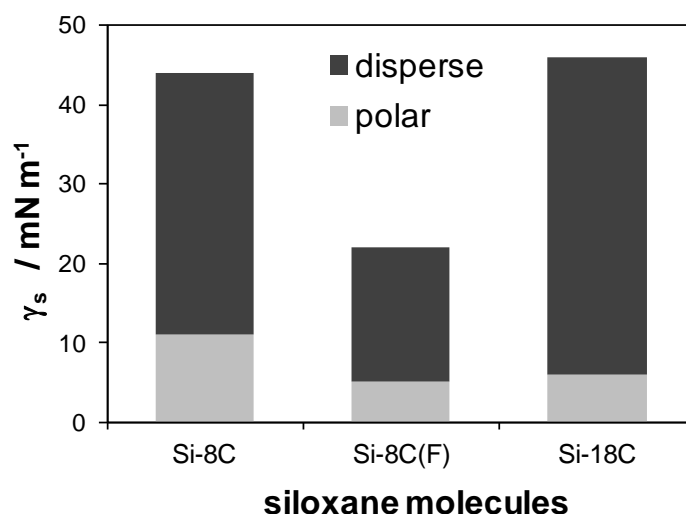

Figure 3.2.16 Surface free energy,γ$_s$, with relative disperse and polar components (determined by OWRK model) for bare siloxane films.

Table 3.2.8 reports the CA values measured for the different siloxane-TiO_2 hybrid films. For all adopted siloxanes, the water contact angles are larger than 150°, with very low measured hystereses (< 5°), characteristics of superhydrophobic surfaces. Water CA determinations were complicated by the enhanced water repellency of the surface: The simple detachment of the drop from the tip produced, almost invariably, rolling off of the drop. Toluene gives rise instead to complete wetting for all the tested substrates, apart from T_Si-8C(F). The fluorinated compound was the only siloxane presenting a good degree of oleophobicity (toluene CAs ~53°). In the case of T_Si-8C(F), the CA measurement of CH_2I_2 drops presented the same difficulties as for water CA determination: Diiodomethane drops tend to roll off the surface, making the direct measurement difficult, so CA determinations were performed by keeping the syringe needle inside the drop. However, such a procedure, together with the high density of the liquid, resulted in an increased flattening of the drop profile.

Solvent		samples		
		T_Si-8C	T_Si-8C(F)	T_Si-18C
Water	θ_{avg}	>150	>150	>150
	$\Delta\theta$	< 5	< 5	< 5
Glycerol	θ_s	150	142	139
EtGly	θ_s	110	108	114
CH_2I_2	θ_s	97	>133	75
Toluene	θ_s	0	53	0

Table 3.2.8 Wetting features of the tested siloxane-TiO_2 hybrid films: Average contact angles, θavg, and hysteresis between advancing and receding angles, Δθ, of water; static contact angle, θs, of non-aqueous solvents.

The wetting properties of the siloxane-TiO_2 hybrids can be rationalized to some extent on the grounds of the surface energy components of the bare siloxanes films (Figure 3.2.16). The fact that the wettability towards polar solvents (water, glycerol, ethylene glycol) does not vary significantly between T_Si-8C(F) and the unfluorinated hybrids, can be explained by the similar polar SFE component of Si-8C(F) and Si-8C (and Si-18C). It is only the disperse component that changes markedly between fluorinated and unfluorinated molecules. Thus, the ability of Si-8C(F) to interact with polar solvents remains unaltered. Conversely, apolar solvents, like toluene and CH_2I_2, give much larger CAs on T_Si-8C(F) because of the lower ability of the fluorinated siloxane to give disperse interactions.

Solid state NMR. ^{13}C and ^{29}Si solid state NMR were employed to investigate the specificity of the attachment modes of the presently adopted siloxanes to the TiO_2 surface.

Figure 3.2.17 reports the ^{29}Si CPMAS NMR spectra of the siloxane-TiO_2 hybrids.
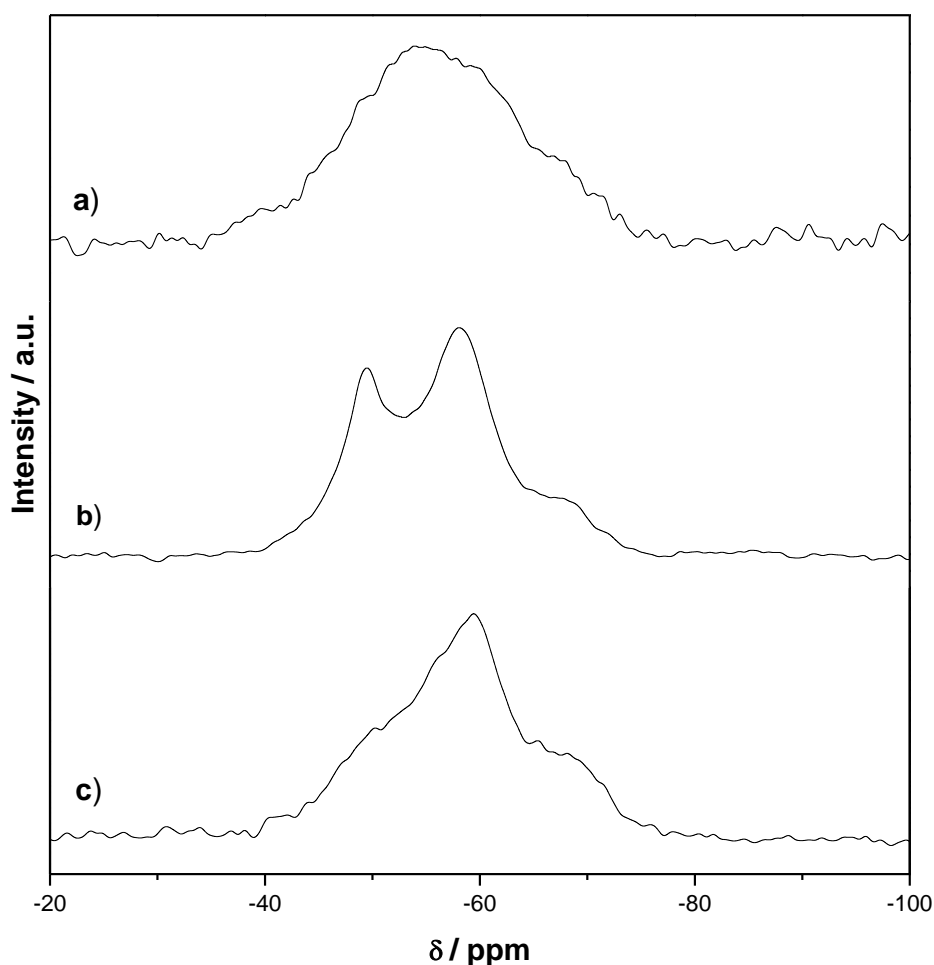
Figure 3.2.17 ^{29}Si CPMAS NMR spectra of a) T_Si-8C(F), b) T_Si-18C, and c) T_Si-8C.

While all spectra exhibit ^{29}Si resonances in the chemical shift region of siloxane groups (from -40 to -80 ppm), the signal shapes of the three compounds are remarkably different. The ^{29}Si spectra of T_Si-18C and T_Si-8C show three well resolved resonances, though in the latter sample with a minor signal resolution. Conversely, T_Si-8C(F) presents a very broad and featureless peak. The partial substitution of hydrogen atoms by fluorine on the silicon chain leads to an increase of the relaxation rate, broadening the NMR signal.

The different resonances appreciable in the ^{29}Si NMR signals were fitted with Gaussian curves to esteem the relative percentages of the coexisting structures (Table 3.2.9).

In agreement with the results obtained for other siloxanes (see section 3.2.1), the lower field resonances of T_Si-8C and T_Si-18C samples (at -51.0 and -50.0 ppm, respectively), can be attributed to **T^1** structures, while the resonances at -59.0 and -58.0 ppm for respectively T_Si-8C and T_Si-18C, can be attributed to **T^2** structures (either **T$^2_{Ti}$** or **T$^2_{Si}$**). Finally, the ^{29}Si resonances at -69.0 for octyl and -68.0 ppm for octadecyl derivatives can be related to the **T^3** structure.

A small chemical shift differences is appreciable in the T^2 (-52.0 ppm) and T^3 (-60.0 ppm) resonances of sample T_Si-8C(F), with respect to the unfluorinated siloxanes. Such down-field shift

of ^{29}Si NMR signal can be attributed to the presence of the fluorine atoms on the silicon chain, due to the larger local electron density of the fluorine atom with respect to the hydrogen one. Fluorine electronegativity is clearly related to observed induced shift [Mirau2005], fluorine being the most electronegative substituent.

	T_Si-8C			T_Si-8C(F)			T_Si-18C		
	T^1	T^2	T^3	T^1	T^2	T^3	T^1	T^2	T^3
δ (ppm)	-51	-59	-69	-	-52	-60	-50	-58	-68
%	25	65	10	-	64	36	30	66	5
$\Delta v_{1/2}$ (Hz)	895	839	532	-	1334	1157	497	767	397

Table 3.2.9 ^{29}Si CPMAS NMR chemical shifts, δ, relative percentage and line-width, $\Delta v_{1/2}$, for the proposed Si structures (T^1, T^2 and T^3) in the different siloxane-TiO$_2$ hybrids.

The relative enrichment in the T^x structures is reported in Table 3.2.9. For all siloxanes, the T^2 component is the prevailing one (64-66%), although unfluorinated samples present also a relevant presence of T^1 structure (25-30%). Notably, the T_Si-8C(F) lacks the T^1 structure and has a larger content of the T^3 structure. Such phenomena may be related to a different reactivity of Si-8C(F) with respect to the unfluorinated analogues. The withdrawing effects of F and O may induce a higher pre-polymerization of the siloxane in solution, before the bonding to the oxide surface.

^{13}C MAS NMR spectra of all the studied hybrids, present very low intensity signals of the CH$_2$- and CH$_3$- carbons ascribable to the ethoxy groups on the siloxane molecules. This confirms the high substitution degree of ethoxy groups during oxide functionalization, and consequently the prevalence of the T^2 and T^3 structures with respect to the T^1 one.

The line widths of the ^{29}Si resonances relative to the T^1, T^2 and T^3 structures (Table 3.2.9) can provide information about the dynamic processes in the materials. The T^3 structure, being the more strained and more ordered structure, exhibits in all samples the narrowest line-width with respect to the corresponding T^1 and T^2 resonances.

The T_Si-18C sample presents the sharpest peaks, which can be attributed to a lack of mobility of the siloxane chains. The long alkyl chains of Si-18C tend to align because of Van der Waals lateral forces, causing for steric hindrance a minor number of possible conformations and consequently, a decrease in line width. These conclusions are supported by the BET data about the sample specific surface area.

The fluorinated T_Si-8C(F) sample presents instead an opposite behavior. The observed large $\Delta v_{1/2}$ values may be related to the presence of the fluorine atoms in the alkyl chain, which may

alter the relaxation rate of the material. Indeed, the F atoms could support a larger conformational freedom by increasing the mobility for electrostatic repulsion between the chains. These latter data are consistent with the surface free energy data presented in Figure 3.2.16, which showed for Si-8C(F) the lowest disperse component.

Conclusions

Films of functionalized TiO_2 nanoparticles were synthesized by a simple and inexpensive preparation procedure involving the oxide surface derivatization by different kinds of siloxanes using a mild impregnation method. This procedure was successfully applied to the tailoring of the surface properties of TiO_2 films. In particular the wetting features with respect to water and other solvents were investigated. The resulting materials were extensively characterized to rationalize the observed wetting properties on the grounds of the morphological features of the film and of the characteristics of the siloxane layer.

^{29}Si solid state NMR demonstrated that the attachment modes of the siloxane molecules at the oxide surface, besides changing with the siloxane content, are significantly affected by the siloxane structure. Such differences in the siloxane-oxide interaction were shown to play a pivotal role in determining the wetting properties of the surface.

In the case of alkyl trifunctional siloxanes, a homogeneous functionalizing layer was observed, in which siloxane molecules form progressively one, two or three Si–O-Ti(Si) bonds. On the grounds of a combination of spectroscopic techniques (NMR, XPS, FTIR), the prevailing structure was determined to be T^2_{Si}, in which the siloxane molecule has one bond with the oxide surface and one with a neighboring siloxane. The resulting films show an enhanced water repellency, starting at low siloxane content. The observed lotus effect was attributed, on the grounds of the classical Cassie-Baxter model, to the multiscale roughness of the functionalized surface, due to the presence of both nanoparticles and micrometric aggregates (as shown by AFM images).

Increasing the length of the alkyl chain (from C8 to C18) results in more ordered siloxane layers, characterized by a lower degree of conformational freedom. The excellent superhydrophobic properties of the resulting materials, can be traced back to the ordered and homogeneous siloxane layer.

The substitution of the alkyl chain with aromatic end groups significantly alters the situation. The presence of π-π stacking interactions between the aryl tails, favors the formation of locally ordered monolayer, which are instead more heterogeneous and patch-wise at a macroscopic level. The resulting wetting properties are much more dependent on the siloxane content. For instance, in the case of a bi-functional bi-aryl siloxane, films are hydrophilic at low coverage. They

become hydrophobic only at high siloxane content, exhibiting however a Wenzel-type wetting behavior.

The wettability of the hybrid films towards solvents other than water was also investigated. In agreement with the results obtained for bare siloxane films (section 3.1), the siloxane dipole moment, determined by semiempirical calculations, imposes the sequence of wettability by solvents. Solvents with a large polar component of the surface tension, exhibit high contact angle values on hybrid films where the adopted siloxane has a low dipole moment.

Finally, the role of the partial fluorination of the siloxane alkyl chain was considered. The presence of the partially fluorinated chain favors a polymeric organization of the siloxane molecules at the TiO_2 surface. Solid state NMR shows a prevailing T^3 attachment mode and no T^1 strucutre. Further, fluorinated siloxanes exhibit lower polar and disperse SFE components with respect to the un-fluorinated analogues. The combination of the lower SFE and of the ordered structure of the hydrophobing layer further improves the wetting feature with respect to un-fluorinated alkyl siloxanes, adding to the superhydrophobicity also oleophobic features.

In conclusion, the combination of the morphology and of the structural polymorphism of the TiO_2 nanoparticles gives rise to films with hierarchical topography, that show superhydrophobic behavior when functionalized with a homogeneous hydrophobizing layer, such as in the case of alkyl siloxanes. The siloxane chemical and structural features impose the mode of attachment of the molecules at the oxide surface, altering the structure of the hydrophobing layer. Therefore, the wetting properties of the TiO_2 film with respect to any solvent can be tuned by modulating the structure of the functionalizing molecule.

3.3 Advanced applications of siloxane-TiO$_2$ composites

The tailoring of the wetting properties of surfaces has been the focus of extensive experimental and theoretical research, mainly devoted to the production of surfaces with enhanced water repellency [Callies2005]. Such materials have indeed an enormous applicative interest for applications like self-cleaning materials, protective coatings for outdoor cultural heritage, anti-corrosion and anti-biofouling films, anti-freezing and anti-snow surfaces [Xue2010;Yao2011]. Recently, interest in omniphobic surfaces has arisen because of their numerous and economically relevant, potential applications in fields such as crude oil transfer, fluid power systems, antifouling and anticrawling materials.

The possibility to obtain materials with patterned wetting features, *i.e.* the site-selective localization of hydrophobic/hydrophilic patches on a surface, represents another fundamental aim of research in the field of surface modification. Indeed, materials with patterned wettability can bear relevance to countless applications, *e.g.* condensation of water from the gas phase, liquid transportation, microfluidic devices, offset printing, transport of electrolytes and gas bubbles in electrolyte fuel cells and supercapacitors [Yao2011; Nakata2012].

The innovative siloxane-TiO$_2$ hybrid films developed in the present thesis work (see section 3.2) were applied as self-cleaning surfaces with respect to both aqueous solutions and apolar solvents. Moreover, they were employed for the fabrication of surfaces with patterned wettability by photocatalytic lithography. Finally, another lithographic approach, probe-based electro-oxidative lithography, was applied to the surface modification at the nanometer scale of siloxane films deposited onto oxide substrates (both TiO$_2$ and ITO).

3.3.1 Self-cleaning surfaces

Surfaces tend to become contaminated in a natural environment. Cleaning them is cumbersome and expensive, and requires the use of surfactants, which have become important environmental pollutants. The development of substrates that can clean themselves may play a pivotal role in several technological applications, ranging from the protection of outdoor cultural heritage to self-cleaning textiles. For instance, the production of self-cleaning glass materials bears relevance to automotive, architecture (*e.g.* the cleaning of skyscraper windows), optical sensors and other applications. Further, the creation of sprays and paints with self-cleaning properties would have an enormous commercial interest (*e.g.* graffiti-resistant walls).

Self-cleaning property can be obtained by exploiting the so-called lotus effect. When a water droplet rolls off the surface of a lotus leaf, it removes the dust and dirt accumulated over it. Such effect is based on the enhanced water repellency of lotus leaves (extremely high water contact angles and low contact angle hysteresis).

In the present thesis work, the siloxane-TiO_2 hybrid films developed via a simple and inexpensive preparation procedure (section 3.2) were used to impart self-cleaning properties to glass substrates. Both aqueous and apolar solvents were considered to develop omniphobic self-cleaning surfaces.

Experimental section

The studied materials were hybrid films prepared using TiO_2 nanoparticles functionalized with various siloxanes (Table 3.3.1), according to the procedure reported in section 3.2.

Name	Acronym	Formula
Isooctyltriethoxysilane	**Si-Alk**	
Triethoxy(p-tolyl)silane	**Si-Tol**	
Trimethoxy(diphenyl)silane	**Si-biPh**	
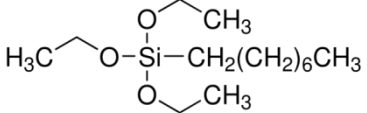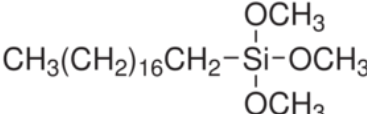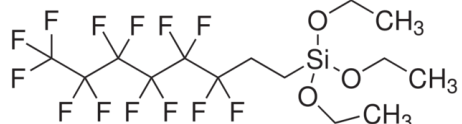
Triethoxy(octyl)silane	**Si-8C**	
Trimethoxy(octadecyl)silane	**Si-18C**	
1H,1H,2H,2H- perfluorooctyl- triethoxysilane	**Si-8C(F)**	

Table 3.3.1 Studied siloxanes.

The wetting features of the functionalized films were determined by static and dynamic contact angle (CA) measurements on a Krüss EasyDrop using several high purity solvents (water, toluene, glycerol, ethylene glycol). Measurements were performed by gently placing a 3 μL drop of solvent on the surface, then the drop size was changed at 15 μL min^{-1} while recording movies of 150 images. The drop profile was extrapolated using an appropriate fitting function. The reported CA values are the average of five independent determinations from different sample locations. Contact angle hysteresis $\Delta\theta$ were obtained as the difference between the advancing and receding contact angles.

Self-cleaning tests were performed as follows. The hybrid layers were stained by a 0.02 M aqueous solution of a dye (methylene blue, methyl orange, or alizarin red), then washed with water to evaluate the stain removal. The dye interaction with the film surface was evaluated by Fourier transform infrared spectroscopy (FTIR), using a Jasco 4200 spectrometer, accessorized by an attenuated total reflectance (ATR) module.

In order to evaluate the self-cleaning properties with respect to solvents other than water, self-cleaning tests were also performed staining functionalized titania films with a methylene blue solution in CH_2I_2.

Results and Discussion

The diverse hydrophilic/hydrophobic behavior of the bare and siloxane-clad TiO_2 films can be appreciated in Figure 3.3.1.

The marked hydrophilic properties of the pristine TiO_2 layer (Figure 3.3.1a) gives rise to a good dispersibility in water of its powders (Figure 3.3.1c) and causes the staining of its films by an aqueous dye solution (Figure 3.3.1e). The drops of dye solution spread out on the film surface, leaving a stain that cannot be significantly removed by washing the layer with water.

Instead, after coating with siloxanes (T_Si-Alk(9%)), the surface exhibits a highly

hydrophobic/superhydrophobic behavior (contact angle around 150°, Figure 3.3.1b), resulting in complete buoyancy of the coated powders over water (Figure 3.3.1d) and self-cleaning properties (Figure 3.3.1f). The hybrid film is not wetted by the dye solution and the drops roll off the surface without leaving any trace.
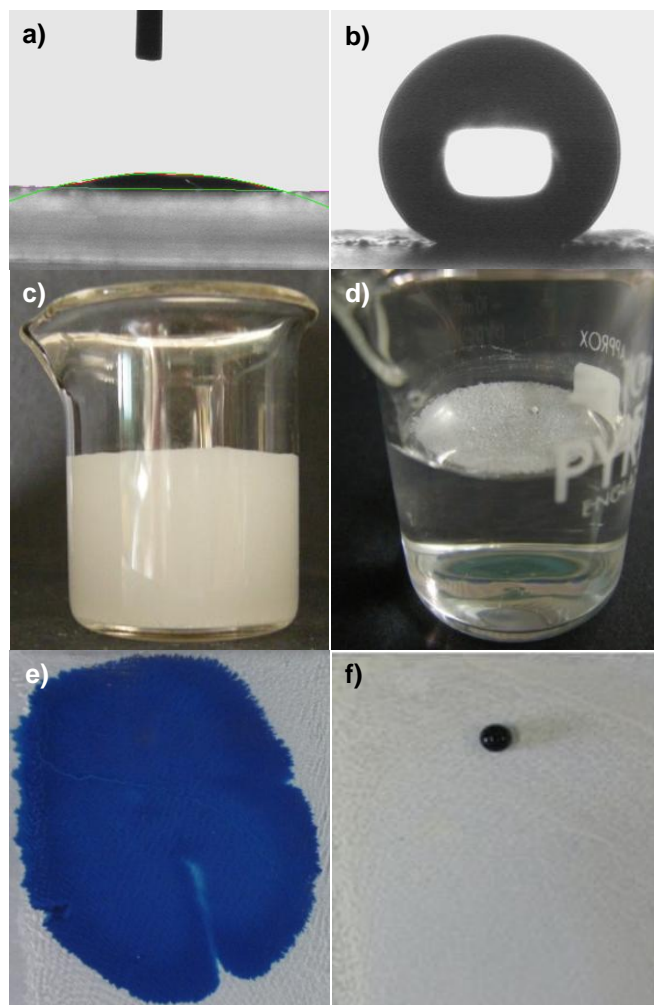

Figure 3.3.1 Water contact angles, powder dispersibility in water and film self-cleaning properties with respect to a methylene blue aqueous solution, of bare TiO$_2$ (a,c,e) and siloxane-clade TiO$_2$, T_Si-Alk(9%) (b,d,f).

The self-cleaning properties can be modulated by changing the structure and content of the adopted functionalizing molecule. Figure 3.3.2 shows the widely different self-cleaning abilities of hybrid films prepared using the same content of siloxane (13%), but different siloxane molecules (Si-Alk and Si-biPh). An alizarin dye aqueous solution was dropped over the films and then the eventual stain was washed with water. The T_Si-Alk(13%) layer shows excellent self-cleaning properties, while the T_Si-biPh(13%) film exhibits a behavior which is intermediate between those of T_Si-Alk and of bare TiO$_2$. On the T_Si-biPh layer, the aqueous drop spreads partially onto the film surface. When the substrate is tilted, the drop slides along the surface, leaving a trail that can be only partially removed by washing with water. The T_Si-Tol layers, not shown for reasons of space, exhibit a behavior similar to T_Si-biPh.

Drop of dye solution   **After washing with water**
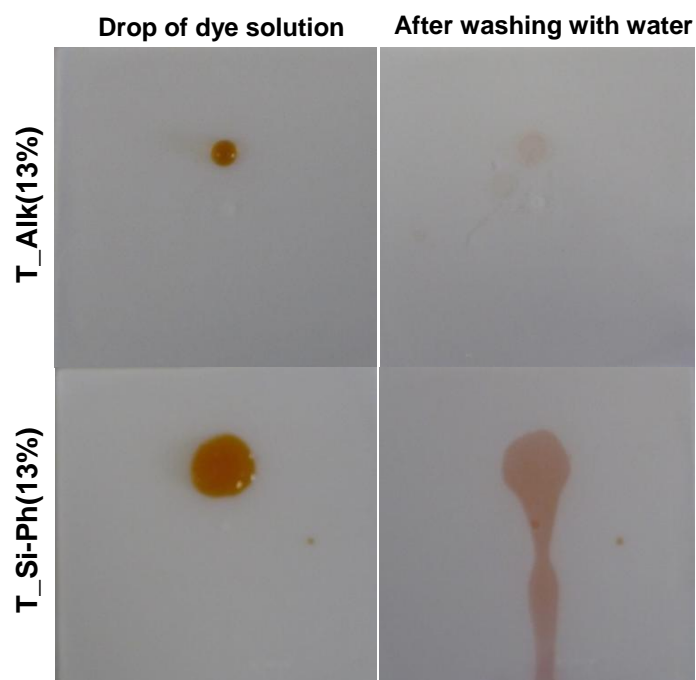
Figure 3.3.2 Self-cleaning tests with alizarin red dye aqueous solution on T_Si-Alk(13%) and T_Si-Ph(13%).

        The differences in the self-cleaning behavior of these two films (T_Si-Tol and T_Si-biPh) can be better appreciated by ATR-FTIR spectra (Figure 3.3.3). The dye adsorption results in peaks at 1445 and 1590 cm^{-1}, corresponding to ν(Ar C=C), at 1332 cm^{-1}, attributable to δ(OH), at 1262 and 1289 cm^{-1}, due to ν(CO), and at 1068 and 1160 cm^{-1}, which are assigned to ν(SO$_3$) [Moriguchi2003]. T_Si-biPh presents far more intense peaks corresponding to the adsorbed dye; thus, the self-cleaning properties of the films vary in the order: T_Si-biPh < T_Si-Tol < T_Si-Alk.

Figure 3.3.3 ATR-FTIR spectra of adsorbed alizarin dye onto the T_Si-Tol(13%) and T_Si-biPh(13%) films. The curves of the as-prepared samples were subtracted.

The widely different self-cleaning of the tested hybrids can be rationalized on the grounds of their different wetting behavior. In particular, the self-cleaning ability seems to be mainly related to the contact angle hysteresis. In fact, while both T_Si-Alk and T_Si-Tol present similar water con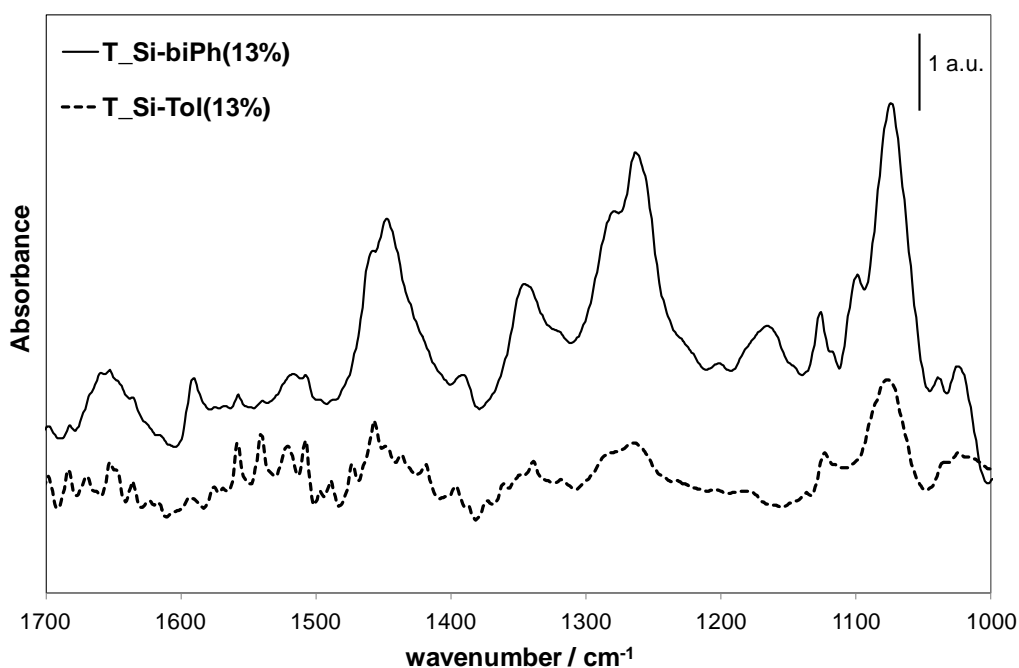tact angle values (close to 150°), their contact angle hystereses are different ($\Delta\theta < 5°$ for T_Si-Alk, $\Delta\theta < 10°$ for T_Si-Tol). The higher CA hysteresis of T_Si-Tol results in worse self-cleaning properties with respect to T_Si-Alk. The worst sample, T_Si-biPh shows the highest hysteresis ($\Delta\theta \sim 50°$).

By changing the type of adopted siloxane, it is possible to modulate the self-cleaning properties also with respect to non-aqueous solvents. Figure 3.3.4 compares the self-cleaning properties of pristine TiO_2, T_S-18C and T_S-8C(F) layers (prepared using a 33% siloxane) with respect to dye solutions either in water (methyl orange) or in CH_2I_2 (methylene blue).
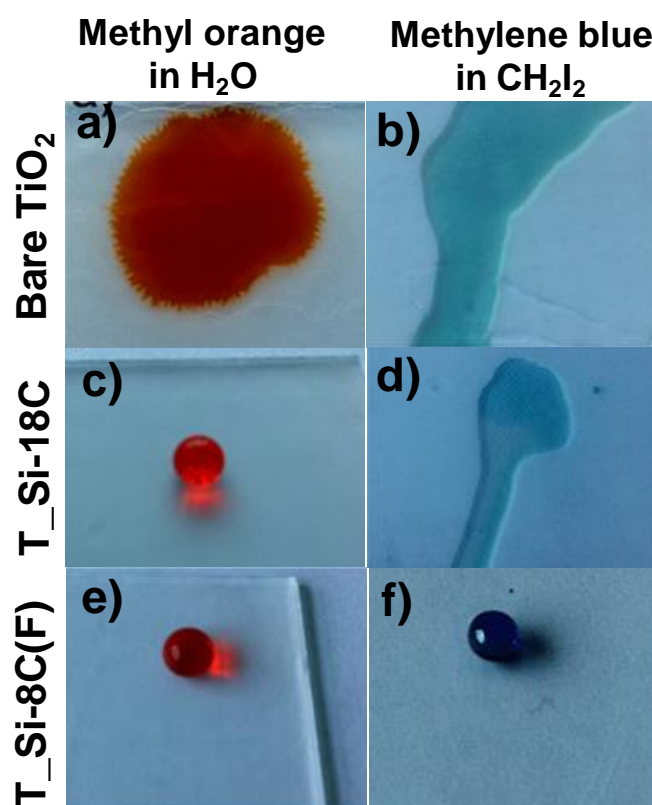
Figure 3.3.4 Self-cleaning tests performed with dye solutions in both aqueous and non-aqueous solutions (CH_2I_2) for films of a,b) bare TiO_2, c,d) T_Si-18C and e,f) T_Si-8C(F).

The pristine TiO_2 layer (Figure 3.3.4a,b) is stained by both the aqueous solution and the apolar solvent. The T_S-18C (Figure 3.3.4c,d) shows instead self-cleaning properties with respect to the aqueous dye solution, while it is stained by the dye solution in CH_2I_2. The behavior of the T_S-18C layer is fully comparable to that of T_S-8C films (not shown for reasons of space). The only film showing self-cleaning properties with respect to both tested solvents is the T_S-8C(F) layer (Fig. 5e,f). The different behavior of the tested siloxanes can be rationalized on the grounds of

their wettability with respect to both aqueous and non-aqueous solvents. The unfluorinated siloxanes give rise to hybrid films (T_S-18C, T_S-8C) which are superhydrophobic (water CA > 150°, $\Delta\theta$ < 5°), but not oleophobic (toluene CA ~ 0°, CH_2I_2 CA close to 90°). As a result, such films show self-cleaning properties only with respect to the dye aqueous solution. The fluorinated molecule T_S-8C(F), instead, shows an omnipohobic behavior: Both water and CH_2I_2 droplets roll off the surface, as a consequence of the low surface free energy imparted by the fluorinated alkyl chain and of the ordered structure of the hydrophobing layer.

Conclusions

A simple and inexpensive procedure was adopted to induce self-cleaning properties in glass substrates. The adopted procedure, based on the deposition of siloxane-TiO_2 hybrid coatings, can be applied to almost every kind of substrates.

The final self-cleaning properties with respect to both water and non-aqueous solvents were efficiently modulated by changing the structure of the siloxane molecule, finding a strict correlation between the self-cleaning ability and contact angle hysteresis values.

By the present procedure, omniphobic surfaces showing excellent self-cleaning properties with respect to highly apolar solvents, such as CH_2I_2, were obtained by use of fluorinated siloxanes.

3.3.2 Photocatalytic lithography

The obtainment of patterned surfaces with localized hydrophobic/hydrophilic patches plays a pivotal role in countless applications, including cell growth, spotting of biomolecules, fluid microchips, microreactors, and ink-jet printing [Yao2011; Nakata2012].

Siloxane monolayers can be exploited to obtain hydrophobic/hydrophilic contrast upon patterning with techniques, such as photolithography, that provoke the site-selective degradation of the organic monolayer. Photolithography can be use to pattern a siloxane monolayer, without the use of expensive photoresists, by irradiation with UV-C light ($\lambda < 185$ nm). However, this approach is limited to specific functional groups and under constrained environments [Paz2011].

An alternative approach involves the use of siloxane-functionalized films of photoactive semiconductors, such as TiO_2. This approach, called photocatalytic lithography, allows the direct patterning of a siloxane monolayer adsorbed at the photocatalyst surface, by photocatalytic oxidation, in the presence of an inexpensive patterning mask.

With respect to traditional photolithography, photocatalytic lithography involves the use of longer wavelengths (in the present study, in the range 365-400 nm) and the highly oxidizing power of TiO_2 degrades the organic chain of the siloxane to harmless H_2O and CO_2 [Nakata2012]. Further, the photocatalytic activity of TiO_2, which is limited to UV irradiation, does not affect the durability of the hybrid films under environmental lighting.

The patterning of siloxane-TiO_2 films by photocatalytic lithography represents a very promising approach that, besides the straightforward applications in offset printing and printed-circuit boards, may open the door to the site-selective localization of several functionalities (*e.g.*, polymers, nanoparticles, biological molecules) at the oxide surface.

In the present thesis work, patterned structures with tunable hydrophobic and oleophobic patches were obtained by photocatalytic lithography. The resulting wetting contrast was exploited to obtain the site-selective adsorption of a dye molecule, by a procedure that could be extended to obtain the site-selective localization of a large variety materials.

Experimental section

TiO_2 nanoparticle films were functionalized with various siloxanes by adopting the procedure reported in section 3.2. The tested siloxanes were commercial products by Sigma Aldrich, both unfluorinated (triethoxy(octyl)silane, **Si-8C**), and fluorinated (1H,1H,2H,2H-perfluorooctyl-triethoxysilane, **Si-8C(F)**).

The siloxane-TiO$_2$ composite films were photocatalytically litographed by irradiating with UV-A rays in the presence of a paper mask onto the TiO$_2$ film. The irradiation source was a 500 W iron halogenide lamp (Jelosil HG500), emitting in the 315-400 nm wavelength range.

The kinetics of the siloxane photodegradation was investigated by monitoring the contact angle of water and diiodomethane as a function of the irradiation time. In addition, the functionalized TiO$_2$ before and after UV irradiation was analyzed by Fourier transform infrared spectroscopy (FTIR) using a Jasco 4200 spectrometer, accessorized by an attenuated total reflectance (ATR) module.

The site-selective adsorption of dyes onto the patterned surface was obtained by simply wetting the surface with the a solution of the chosen dye dissolved in water or CH$_2$I$_2$.

Results and Discussion

Although light can be used to pattern the present hybrid films, they were not altered by room-light. Their wetting properties proved to be stable for several months of storage in a well lighted laboratory. This is not surprising since TiO$_2$ photocatalytic activity is activated by UV irradiation and room-light lamps emit only a very small amount of UV light.

The siloxane-TiO$_2$ hybrids, covered by a paper mask, were irradiated with UV light for 1h. While the film areas protected by the photomask remain unmodified, the siloxane molecules in the areas exposed to UV light are photocatalytically oxidized and completely degraded (Figure 3.3.5). As a result, areas covered by the mask remain superhydrophobic, whereas the irradiated area become superhydrophilic (water CA ~ 0°). The exposure time was optimize by studying the kinetics of the siloxane photodegradation (reported below), to in order to obtain a high wettability contrast.
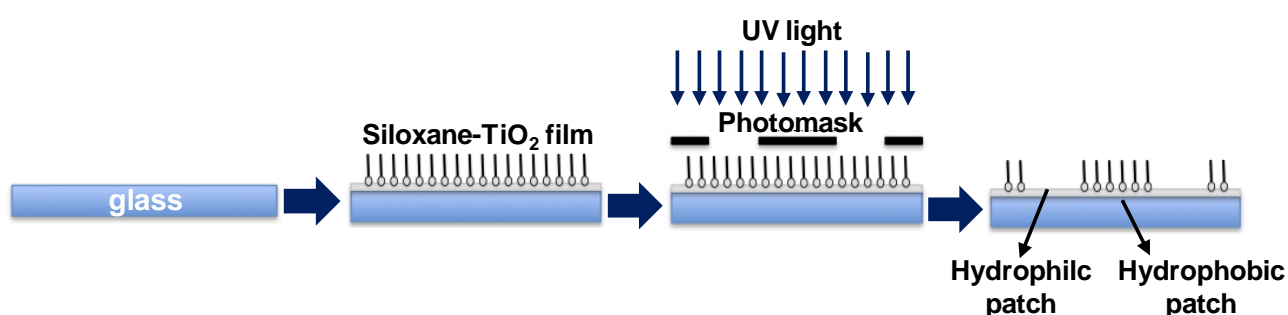
Figure 3.3.5 Sketch representing the photocatalytic lithography process.

The boundary between the superhydrophobic and superhydrophilic regions was highlighted by wetting the surface with an aqueous solution of methyl orange. Only the hydrophilic areas were wetted and consequently adsorbed the dye (Figure 3.3.6).
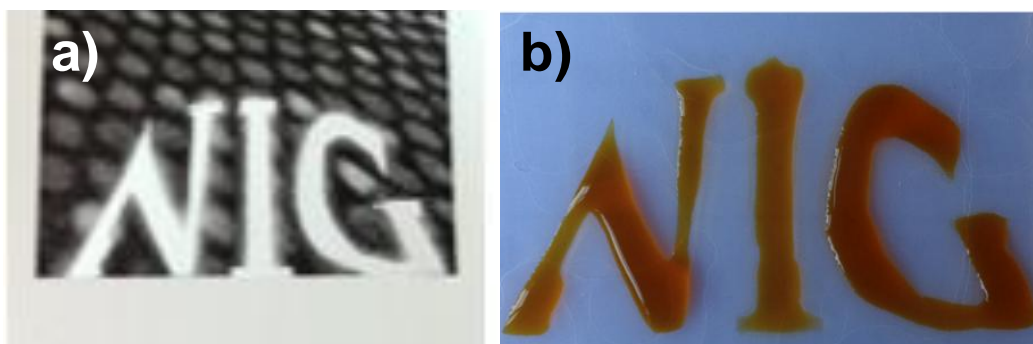
Figure 3.3.6 a) The photomask representing the logo of the research group I belong to (Nanomaterials and Interfaces group, NIG), which was adopted in the present photocatalytic lithography experiments. b) The resulting pattern lithographed on a T_Si-8C(33%) film, highlighted by adsorption of methyl orange dye.

The kinetics of photodegradation of the siloxane layer was investigated by monitoring the variation of water and CH_2I_2 static contact angles over irradiation time (Figure 3.3.7).
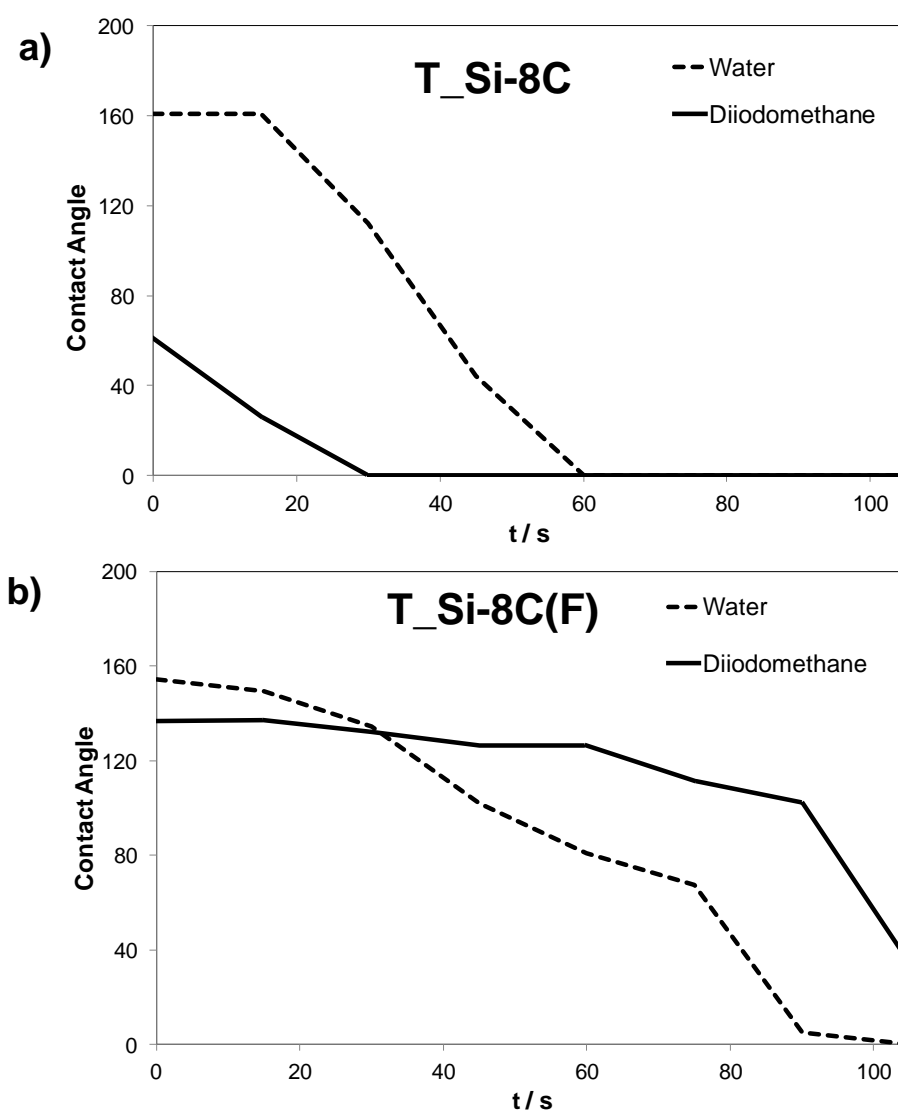
Figure 3.3.7 Variation of water and CH₂I₂ contact angles as a function of the time of UV irradiation for a) T-Si 8C and b) T-Si 8C(F) layers.

Both T-Si-8C and T-Si-8C(F) layers were investigated, showing marked differences in the

evolution of the film wetting features. In particular, the fluorinated siloxane appears to be more stable under UV light, giving measurable water and CH_2I_2 CAs after more than 1 h of irradiation (Figure 3.3.7b). Interestingly, while the T_Si-8C film shows a steep fall of the CH_2I_2 CA values, the T_S-8C(F) layer exhibits a CH_2I_2 repellency more permanent than hydrophobicity (after ~ 30 min of irradiation, the CH_2I_2 CA becomes higher than the water CA). This phenomenon may be related to different degradation pathways occurring in the two layers.

FTIR measurements were performed to enlighten the presence of surface functionalizing groups before and after UV irradiation (Figure 3.3.8).
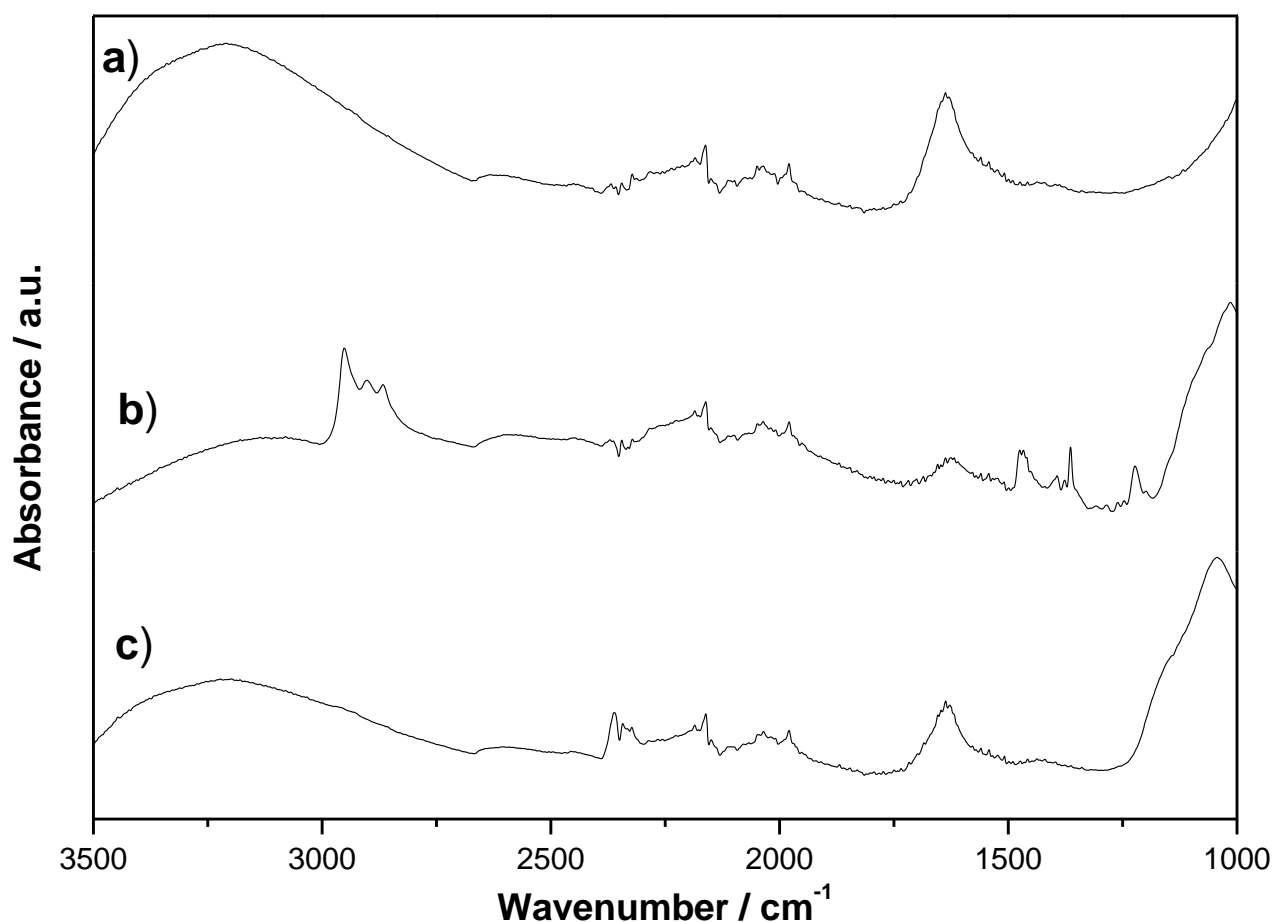
**Figure 3.2.8 ATR-FTIR spectra of the bare TiO$_2$ (a), and of siloxane-clad TiO$_2$ before (b) and after (c) UV irradiation.**

The functionalization with siloxanes gives rise to strong bands in the 800-1400 and 2800-3000 cm^{-1} regions (Figure 3.2.8b). Absorption peaks in the region 2800-3000 cm^{-1} correspond to the stretching modes of CH groups, while those at 919-926 cm^{-1} are generally attributed to stretching vibrations of the Ti-O-Si bond [Xu2006]. The stretching vibrations of Si-O-Si linkages may instead occur from 950 to 1150 cm^{-1}, overlapping the region of Si-O-C bonds (1090-1050 cm^{-1}).

After irradiation (Figure 3.2.8c) all bands relative to the siloxane molecule become less intense and the spectrum becomes more similar to that of pristine TiO$_2$ (Figure 3.2.8a). Conversely,

the peaks associated with adsorbed water increase, as a consequence of the degradation of the hydrophobic siloxane layer. Absorption peaks attributable to Si-C and C-H bonds (1126-1372 cm^{-1} and 2800-3000 cm^{-1}) are almost absent after irradiation. However, the bands relative to the Ti-O-Si and Si-O-Si stretching and bending are still evident. These observations may suggest that the oxidation process attacks the more external alkyl chains, while the Si-O-Ti and Si-O-Si bonds are less modified.

An indirect oxidation mechanism involving OH radicals has been proposed as the dominant one for the degradation of monolayers attached at titanium dioxide [Paz2011].This mechanism is consistent with the inverse correlation, observed by Tizazu and coworkers [Tizazu2009], between the rate of degradation of alkylphosphonic acid monolayers and the ability of oxygen-containing species to reach the surface by penetrating in between the chains of the monolayer. An indirect mechanism may in our case support the larger stability of the T_Si-C8(F) molecule during the photocatalytic lithography. In fact, the penetration of oxygen-containing species to the TiO$_2$ surface may be efficiently hindered by the higher degree of polymerization of the Si-8C(F) monolayer (higher content of T^3 structure, see section 3.2), slowing down the oxidation kinetics. Moreover, the strength of the C-F bonds, which imparts chemical stability, could contribute to the higher resistance towards oxidation.

Conclusions

The semiconductor nature of the presently employed TiO$_2$ nanostructured films can be exploited to obtain patterned surfaces with superhydrophobic/superhydrophilic and oleophobic/oleophilic contrast. The adopted procedure based on photocatalytic lithography, represents a simple and inexpensive alternative to the available patterning techniques.

A tunable degree of hydro- and oleo-philicity could be obtained by tailoring the irradiation time and the type of siloxane employed. The analysis of the kinetics of contact angle decrease and of the adsorbed surface species by FTIR provided a deeper insight in the mechanism of photocatalytic oxidation.

The patterned surfaces were adopted to obtain the site-selective adsorption of a dye molecule. Such very simple approach could be exploited to produce complex, hierarchical structures, in which polymers, metal nanoparticles, or biological molecules could be site-selectively attached to a surface.

3.3.3 Probe-based electro-oxidative lithography

The main disadvantage of photocatalytic lithography is its poor lateral resolution. Indeed, the occurrence of remote photo-oxidation (*i.e.*, the diffusion of holes in TiO_2 and the surface diffusion of active oxygen species) limits the resolution of the lithographic process to the micrometer scale [Fujishima2008].

Other patterning techniques, such as electro-oxidative scanning probe lithography and dip-pen lithography, possess a much higher lateral resolution [Wouters2009]. Scanning-probe oxidative lithography can be used to achieve the site-selective oxidation of siloxane monolayers on the nanometer scale.

So far, this technique has been applied almost exclusively to Si wafers and, to the author's best knowledge, there are no previous reports of its application on TiO_2 or other technologically relevant oxides, such as ITO.

In the present thesis, electro-oxidative probe lithography was applied for the first time to two transparent semiconductor oxides with very large applicative interest, ITO and TiO_2.

3.3.3.1 Probe-based electro-oxidative lithography of siloxane-ITO films

Indium tin oxide (ITO) currently represents the most frequently employed transparent conductive oxide, because of its high electrical conductivity, good optical transparency, and its ease of film deposition [Ginley2010]. Nowadays, ITO represents an essential component in a wide range of technological applications, from flat panel displays to OLEDs, from solar cells to LCDs. The fast evolution of such technologies requires the ability to site-selectively modulate crucial surface features of ITO films, like their wettability, friction and adhesion properties.

In this respect, the application of electro-oxidative probe lithography to siloxane-modified ITO layers is here reported for the first time. The surface modification induced by the electro-oxidation of the siloxane layer was exploited to achieve the site-selective growth of metal nanoparticles.

Moreover, the oxidation process taking place in siloxane-ITO samples was investigated by Scanning Kelvin Probe Microscopy (SKPM). SKPM, which determines the variation of the surface potential on the nanometer scale, has so far been scarcely exploited in the field of monolayers. In the present thesis, SKPM is used to investigate the lithographic process in a systematic way and to compare the oxidation mechanisms taking place in siloxane-ITO samples and in the reference siloxane-Si substrates.

Experimental Section

Materials. Reagents were purchased from different suppliers. Biscyclohexane (BCH) was distilled over sodium before use, while all other reagents were used without further purification. ITO float glass slides (CEC100S) were purchased from PG&O (surface resistivity: 80 Ω/sq). Double side polished p-type silicon wafers (100) were obtained from University Wafer (resistivity 10-20 Ω cm). The ITO slides and Si wafers were cleaned with Ar plasma for 2 minutes before use.

Self-assembly of siloxane monolayers. *n*-Octadecyltrichlorosilane (OTS) monolayers were deposited on the oxide surface by immersing the ITO slide (or Si wafer) in a 14 mM OTS solution in BCH for 1 minute. Then, it was dried and sonicated in toluene. The deposition procedure was repeated twice. The resulting monolayers were characterized by their water contact angles, using a Krüss DSA10 apparatus. Moreover, they were analyzed by Fourier transform infrared (FTIR) spectroscopy in the grazing angle reflectance mode using a Bruker Hyperion spectrometer. Finally, the topography of the monolayers was investigated by atomic force microscopy (AFM) using an NT-MDT Solver LS working in tapping mode with Ultrasharp tips (μMash).

Probe-based electro-oxidative lithography. Lithography experiments were carried out using an Ntegra Aura AFM (NT-MDT), using a Pt coated AFM tip (μMash). The oxidation tests were carried at room temperature and at controlled humidity (RH) in a home-built AFM chamber. Lithography experiments were carried out in "vector mode", *i.e.*, moving the tip along the trajectories where voltages are to be applied. The bias voltage, pulse duration, and relative humidity (RH) were varied, while contact force, and temperature were kept constant. The obtained oxidized patterns were imaged afterwards using the same tip, working in contact and in tapping mode.

Site-selective growth of metal nanoparticles. The oxidized patterns were adopted as templates for the site-selective deposition of Ag nanoparticles, adopting the following procedure. The lithographed substrates were immersed in an aqueous solution of Ag(II) acetate for 10 min. Then, they were copiously rinsed with deionized water and dried in a stream of Ar. The adsorbed Ag ions were reduced in the vapor phase by hydrogen peroxide. Several cycles of a developing step using a commercial Ag enhancer (Aldrich) were performed to increase the particle size. Finally, the residues from the preparation process were removed by application of adhesion tape, leaving the Ag particles unaffected. The adopted cleaning process does not affect the non-oxidized OTS monolayer, owing to its hydrophobic properties.

Scanning Kelvin probe measurements. Scanning Kelvin probe microscopy (SKPM) was employed to characterize the surface potential distribution in the lithographed samples. Measurement were performed at ambient humidity (RH 30-50%) using an NTegra Aura

AFM/SKPM instrument (NT-MDT), operated in tapping mode. Pt-coated cantilever (µMasch) were used (force constant, and nominal resonant frequency values of 1.75 N/m, and 135 kHz, respectively). The sample was scanned at 1.0 Hz frequency, by maintaining a 2.5 V peak-to-peak AC voltage at the resonance frequency of the cantilever between the probe tip and the sample.

Results and Discussion

OTS monolayers on ITO. OTS monolayers were deposited on both silicon wafers and ITO layers by adopting a similar procedure. Water contact angle measurement were carried out to evaluate the monolayer formation and the quality of the resulting monolayer was investigated by AFM and FTIR analyses.

The obtained water contact angles were 105° and 109° for OTS-coated Si and ITO, respectively. The AFM images show the presence of homogeneous OTS layers on both Si wafers and ITO layers. The latter exhibit a rougher surface with respect to Si, owing to the inherent roughness of the ITO layer on float glass substrates (Figure 3.3.9a,b).
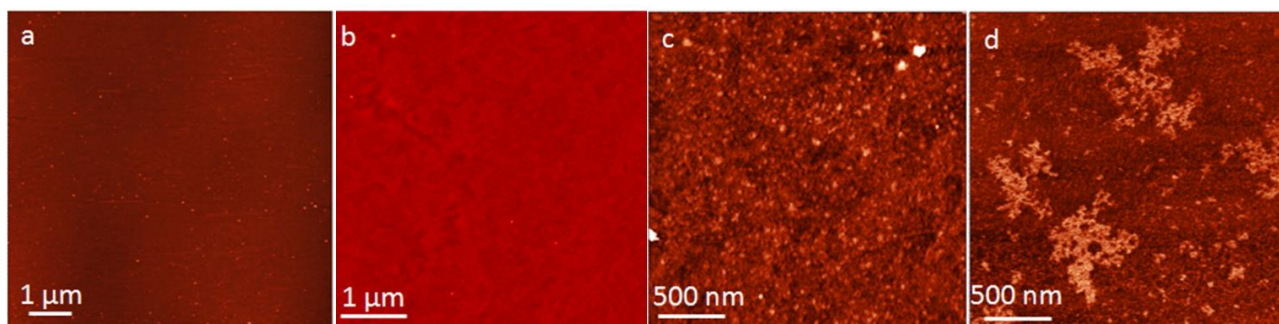
Figure 3.3.9 AFM height images recorded in tapping mode of a) OTS-Si and b) OTS-ITO. OTS-ITO samples showing dendritic islands: c) height and d) phase image recorded in tapping mode.

The successful formation of the monolayer was additionally confirmed by FTIR measurements performed in the grazing incident reflectance mode (Figure 3.3.10).
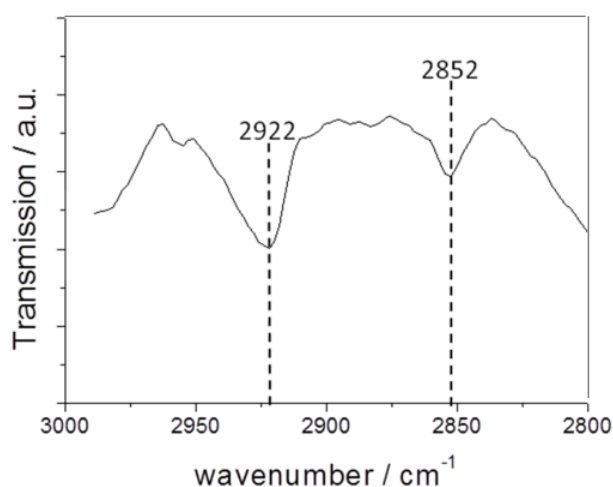

Figure 3.3.10 FTIR spectrum, measured in the grazing incident reflectance mode, of an OTS-ITO sample.

The peak positions of the CH$_2$ stretching vibrations of OTS-ITO (2922 and 2852 cm^{-1}), although indicative of a less well arranged monolayer than in OTS-Si samples, are still an indication for a reliably packed monolayer on ITO.

Depending on the temperature and humidity conditions adopted during the monolayer deposition, the OTS monolayers may present dendritic structures observable in AFM phase images recorded in tapping mode (Figure 3.3.9d). Indeed, the monolayer formation is markedly affected by the deposition parameters, in particular by the environmental humidity and by the water content of the OTS solution [Bush2007; Haensch2010]. In the present study, the dendritic structures were clearly appreciable on phase images but no effect on the corresponding height images was observed (Figure 3.3.9c). This observation, in combination with the measured water contact angle of 108°, allow us to exclude the formation of an incomplete monolayer on these samples. This hypothesis is in agreement with results by Maoz et al. [Maoz1995], reporting the presence of dendritic structures on Si wafer samples whose FTIR spectra revealed the formation of a densely packed monolayer. Further, the later described electro-oxidation lithography and site-selective deposition of Ag could be carried out both on the dendritic structures and on the background monolayer. Thus, the dendritic islands may represent regions where the monolayer is more compact, while the rest of the film is coated by a less ordered and compact monolayer.

Electro-oxidative lithography on Si and ITO substrates. The process of electro-oxidative lithography is based on the application of a negative bias voltage between a conductive SFM tip and the substrate, which gives rise to the local oxidation of the substrate surface. The lateral resolution, *i.e.* line-width of the generated patterns, critically depends on the dimension of the tip and on the applied voltage, pulse duration and relative humidity [Wouters2005]. The electro-oxidative lithography of OTS-Si substrates is a well established technique. The process involves the local conversion of the exposed OTS methyl groups into carboxyl functionalities. The formation of hydrophilic groups in the electro-oxidized regions causes an increase in friction forces with respect to the unmodified, hydrophobic OTS monolayer. Such difference in friction forces is appreciable in lateral force images recorded in contact mode. The use of prolonged pulse duration or higher bias may also result in the oxidation of the underlying Si layer, leading to the growth of SiO$_2$. The substrate oxidation gives rise to an increase in height appreciable in height images both in contact and tapping mode [Wouters2005].
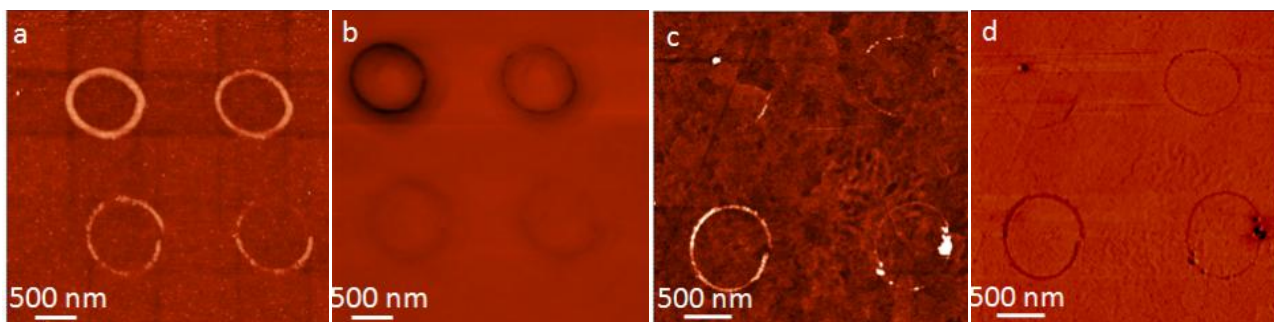
Figure 3.3.11 Height images recorded in tapping mode and lateral force images recorded in contact mode for electro-oxidized samples of: a,b) OTS-Si; c,d) OTS-ITO.

In the present thesis work, OTS-Si was electro-oxidized using a bias voltage of -10 V, RH of 65% and pulse duration in the range 3-10 ms (Figure 3.3.11a-b). By adopting even more severe oxidation conditions (bias voltage: -12 V, RH: 75%, pulse duration: 10 - 25 ms), only incomplete lithography was achieved in the case of OTS-ITO. The occurrence of incomplete lithography may result from the disruption of the water meniscus between the SFM tip and the substrate during the electro-oxidation process. A stable water meniscus between tip and substrate is widely recognized as a fundamental requirement in electro-oxidative lithography. In fact, the oxidizing species responsible for the local oxidation, are generated by the decomposition of water molecules in the meniscus by electrical current [Wouters2009; Maoz1999]. A too fast electron exchange between the tip and the OTS-ITO substrate may be the cause of the disruption of the water meniscus. While the ITO surface resistivity is higher than the bulk resistivity of Si, the presence of a SiO_2 native layer may reduce the efficiency of charge injection in the case of silicon substrates. The hypothesis of a too fast electron transfer is confirmed by the fact that complex patterns could be inscribed (Figure 3.3.11c-d) by slowing down the electron transfer. Such an effect could be obtained by using a Si spacer between the ITO substrate and the electrical circuit, acting as a resistor in series with the tip/sample resistance. As an alternative, cantilevers with higher resistivity could be employed (*e.g.*, Phosphorous n-doped Si cantilever, Veeco, force constant 20 to 80 N/m, resonant frequency 229 to 287 kHz, resistivity: 1 to 10 Ω cm).

With respect to lithography on OTS-Si, longer pulse duration, higher bias voltage, and relative humidity are required in the electro-oxidation of OTS-ITO in the presence of a Si spacer. The lithographed patterns exhibit very narrow line (< 100 nm). The modulation of the line width is however more complex than in the case of OTS-Si, since increasing the pulse duration over a certain threshold causes the disruption of the water meniscus and consequently, incomplete lithography. The final contrast of the lithographed patterns is poorer than in the case of OTS-Si, due to the higher roughness of ITO layers with respect to Si wafers.

Electro-oxidized areas on OTS-ITO samples exhibit an increase in height. Such an effect is often observed also in the electro-oxidation of OTS-Si, where it is attributed to the growth of SiO_2 [Wouters2005]. To understand the origin of the phenomenon in OTS-ITO, electro-oxidative lithography experiments were carried out on pristine ITO layers. The lithography of pristine ITO was successfully achieved using even less severe oxidation conditions (bias voltage: -10 V, RH: 70%, pulse duration: 2 - 7 ms) and inserting a Si spacer (Figure 3.3.12). An increase in height is clearly appreciable from height images, which can be tentatively attributed to the occurrence of overoxidation of the ITO layer, resulting in crystal growth or phase change [Park2011].
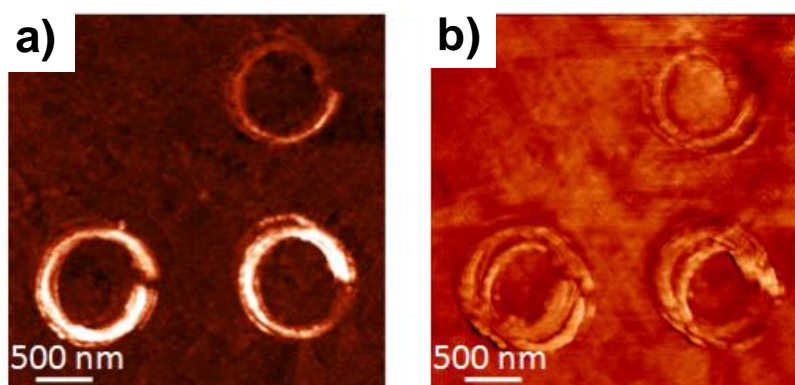
Figure 3.3.12 a) Height image recorded in tapping mode and b) lateral force image recorded in contact mode for electro-oxidized samples of an ITO film.

Site-selective growth of metal nanoparticles on chemical templates. The electro-oxidative lithography in OTS-ITO involves the overoxidation of the underlying oxide substrate. In the case of Si, this effect takes place after the local conversion of the exposed OTS methyl groups into carboxyl moieties. In order to verify if any monolayer oxidation was taking place in the case of OTS-ITO, a site-selective particle growth was tested. The site-selective synthesis of nanoparticles can in fact be used as an indirect verification of the presence of such oxidized groups [Wouters2009; Maoz2000]. While the non-electrooxidized areas are chemically inert, patterned areas represent chemically active surface sites where the site-selective generation of nanoparticles can take place. Metal ions are selectively adsorbed by the oxidized functionalities in the lithographed areas and can be subsequently reduced to generate metal nanoparticles (Figure 3.3.13). During my thesis work, the electro-oxidized areas were used as templates for the site-selective generation of Ag nanoparticles by reduction of Ag(II) ions.
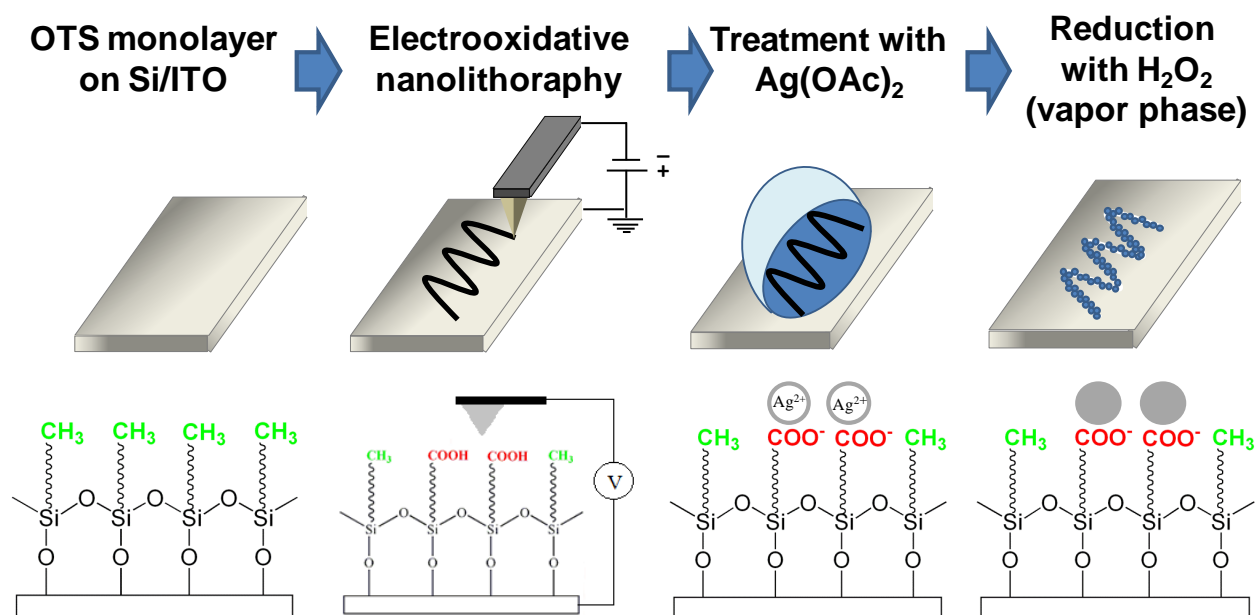
Figure 3.3.13 Schematic representation of the process of the selective-growth of Ag nanoparticle on the electro-oxidized areas.

Figure 3.3.14 shows that the oxidized areas in the treated OTS-ITO samples are selectively covered with Ag particles, with a quite homogeneous height (6 - 7 nm). The Ag nanoparticles present a remarkable stability, since they are not removed by the cleaning process performed using an adhesion tape.
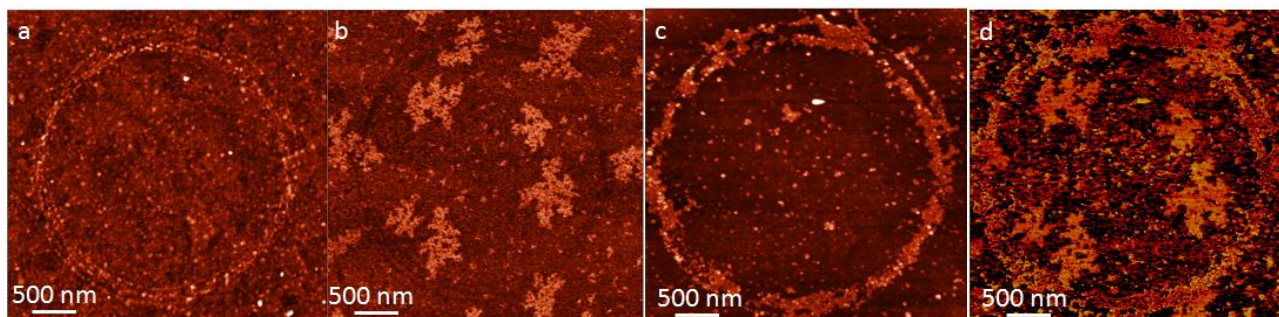
Figure 3.3.14 Height and phase images recorded in tapping mode for the electro-oxidized OTS-ITO showing dendritic islands before (a,b) and after (c,d) the site-selctive growth of Ag nanoparticles.

The formation of polar functional groups, which can be exploited to bind metal ions and nanoparticles, seems to occur along with the overoxidation of the ITO substrate. This represents a significant difference with respect to the electro-oxidative lithography of OTS-Si.

The test of selective-growth of metal nanoparticles was carried out also on OTS-ITO samples presenting dendritic islands. Figure 3.3.14c-d shows that the electro-oxidized areas on both the dendritic islands and the rest of the monolayer are selectively covered by particles. This represents an additional proof of the occurrence of a complete monolayer on these ITO samples.

Scanning Kelvin Probe Microscopy. A systematic investigation of the oxidation mechanism in both bare and OTS-coated Si and ITO samples was carried out by Scanning Kelvin Probe

165

Microscopy. Patterns composed of four circles were electro-oxidized on each substrate by varying the pulse duration, while keeping the bias voltage and the RH constant. Several patterns were investigated for each substrate. In order to allow a more reliable comparison of the SKPM values, all patterns were electro-oxidized and analyzed adopting the same tip (one for oxidation, one for SKPM), so that tip geometry and material properties remained unmodified.

SKPM images were recorded using both an AC bias voltage of 1 and 2.5 V. The former value resulted in a lower noise level in the case of the un-coated Si and ITO samples.

Figure 3.3.15 Height images recorded in tapping mode and surface potential images recorded using SPKM for the electro-oxidized samples of: a,b) bare Si and c,d) OTS-Si.

In the case of pristine Si (Figure 3.3.15a-b), the surface potential shows only a slight difference between electro-oxidized and non-oxidized areas (0 ± 10 mV). The presence of native oxide on the non-oxidized areas may reduce the obtainable contrast with the oxidized structures, which also consists of SiO_x.

On the other hand, the electro-oxidized patterns in OTS-Si (Figure 3.3.15c-d) show a much stronger increase in potential. While the average surface potential in the non-electro-oxidized areas is -10 ± 10 mV, the oxidized areas show values varying from +10 to +80 mV, depending on the pulse duration applied during the oxidation process (Fig. 3.3.16b,c). In particular, the surface potential increases with the oxidation time.
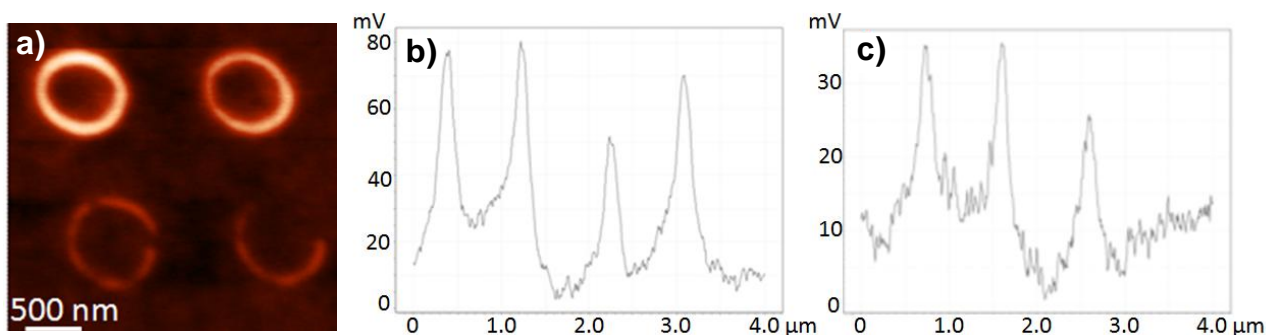
Figure 3.3.16 Surface potential image (a) and profiles (top circles, b, and bottom circles, c) for the electro-oxidized OTS-Si.

These data are in agreement with literature results [Sugimura2002a; Sugimura2002b]. In those studies, the authors attributed the bright areas to non-coated SiO_2, but no other

characterization method was used to confirm this attribution. Moreover, different studies report conflicting attributions of the observed surface potential areas to specific chemical species [Sugimura2002a; Sugimura2002b; Bush2007; Lee2008].

Pristine ITO presents an entirely different behavior (Figure 3.3.17a-b). A decrease in surface potential is observed in electro-oxidized areas and the surface potential exhibits a non-linear relationship with the oxidation time. Further, a decreased lateral resolution is appreciable, probably related to the higher surface conductivity of the pristine ITO layer with respect to the previously investigated samples.
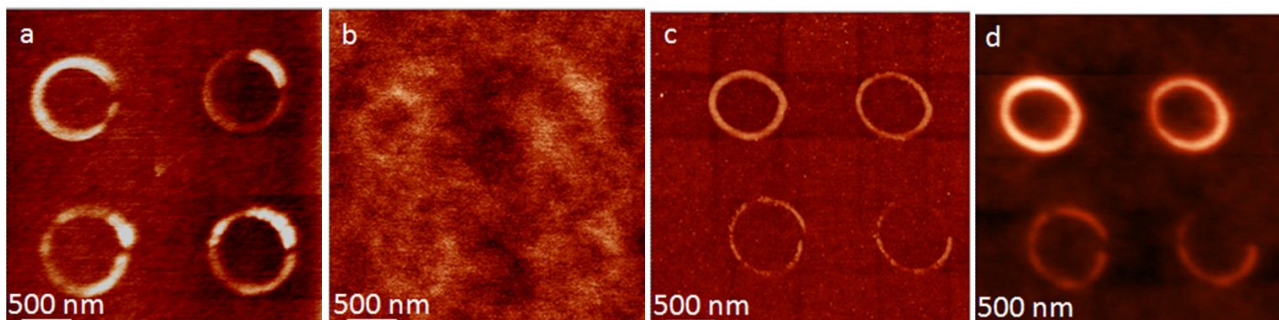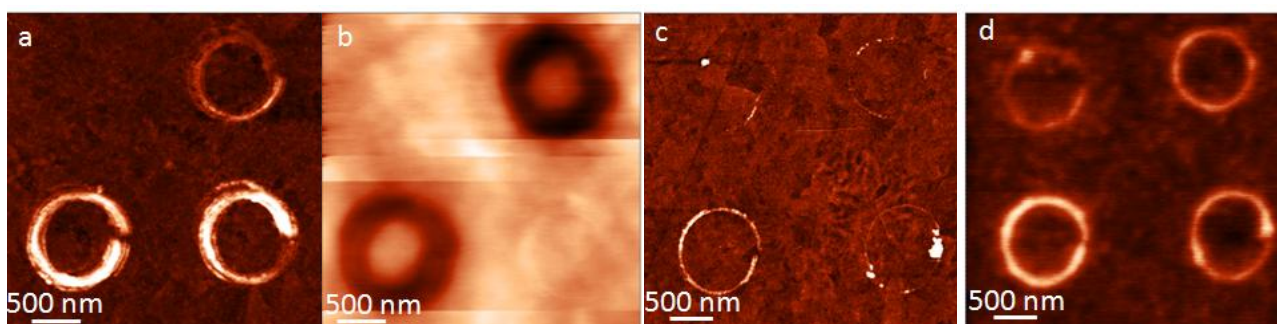

Figure 3.3.17 Height images recorded in tapping mode and surface potential images recorded using SPKM for the electro-oxidized samples of: a,b) bare ITO and c,d) OTS-ITO.

Conversely, SKPM images of electro-oxidized OTS-ITO are very similar to those of OTS-Si (Figure 3.3.17c-d). Non-oxidized areas present an average surface potential of 5 ± 8 mV, whereas electro-oxidized areas exhibit an increase in surface potential (from +10 to +60 mV), depending on the pulse duration (Figure 3.3.18b,c). Similarly to what observed for OTS-Si, the measured surface potential increases with the oxidation time.
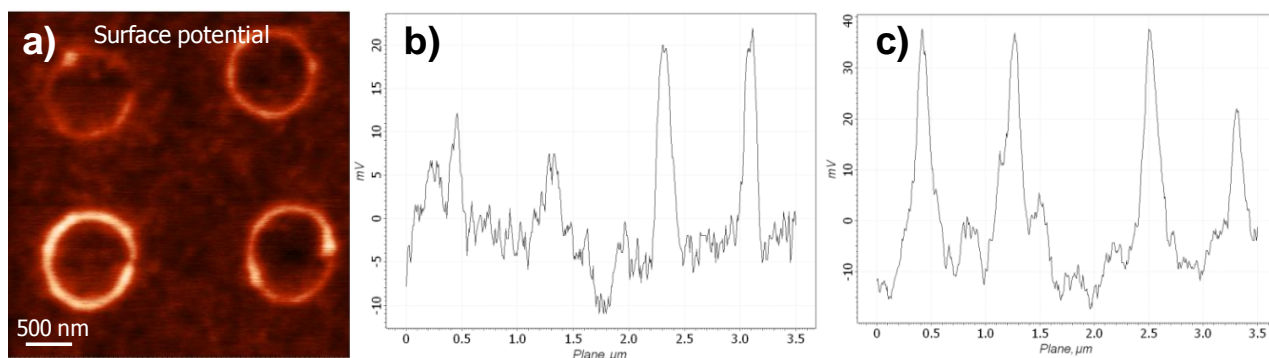
Figure 3.3.18 Surface potential image (a) and profiles (top circles, b, and bottom circles, c) for the electro-oxidized OTS-ITO.

The similar behaviors of OTS-Si and OTS-ITO may suggest that the silane monolayer completely shields the surface potential of the substrate, regardless of their distinctive workfunctions and electron affinities. The different properties of the substrate materials are instead evident in the surface potential images of the pristine substrates, which are completely different from the images of the relative OTS-coated films.

167
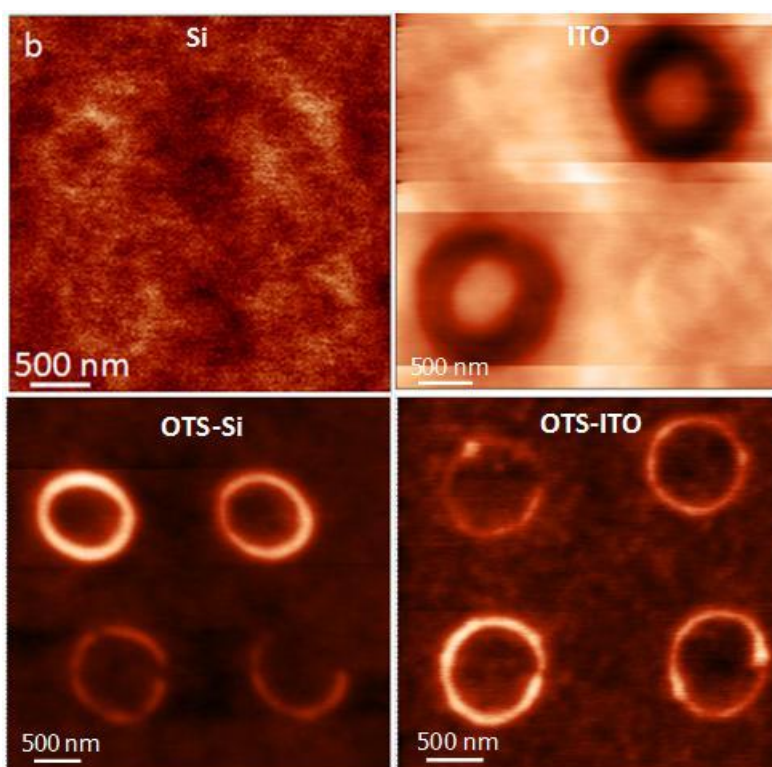
Figure 3.3.19 Comparison of the surface potential images of the electro-oxidized patterns on bare and OTS-coated Si and ITO.

SKPM images indicate that the surface potential is mainly affected by the chemical reactions taking place in the lithographed areas, whereas the contribution to the surface potential of the un-oxidized monolayer is only minor. However, the silane monolayer completely shields the inherent substrate properties of the underlying oxide, so that the effect of the substrate can be neglected. This consideration has a significant impact on the tailoring of the workfunctions of surfaces.

Conclusions

Electro-oxidative lithography is a powerful patterning technique that has been so far almost exclusively applied to the surface patterning of Si substrates. Here, the electro-oxidative lithography process was for the first time applied to the surface modification of OTS monolayers deposited onto an ITO film. Such transparent and conductive oxide was chosen because of its tremendous applicative interest. The current applications, ranging from displays to solar cells, could benefit from the tailoring of critical surface properties, like wettability, adhesion, and conductivity, at the nanometer scale.

The electro-oxidative lithography of OTS-ITO presented significant differences with respect to the "reference" OTS-Si samples. The higher surface conductivity of ITO leads to the instability of the water meniscus between the SFM tip and substrate and, consequently, to incomplete lithography. Successful and complete lithography was obtained by reducing the rate of electron

transfer either by increasing the resistivity of the AFM cantilever or by inserting a Si spacer between the ITO layer and the electrical contact.

The lithographyc process gives rise to both the overoxidation of the substrate, as determined by tests onto pristine ITO layers, and to the oxidation of the OTS monolayer. The formation of hydrophilic functionalities, as a consequence of the monolayer oxidation, was exploited to obtain the site-selective deposition of silver nanoparticles onto the electro-oxidized areas. The presented procedure can be adopted to obtain the self-assembly of other materials (*e.g*., semiconductor quantum dots, dyes, polymers, biological molecules), leading to the fabrication of complex, hierarchical nanostructures and opening the door to the fine tailoring of the surface properties of the material at the nanometer scale.

Finally, Scanning Kelvin Probe Microscopy analyses of the lithographed substrates were carried out to gain insight into the mechanism of electro-oxidative lithography. While the surface potential images of OTS-Si and OTS-ITO exhbited marked similarities, the bare substrates showed a totally different behavior. It is noteworthy that the topography or lateral force images were completely blind to such marked differences in the behavior of the different substrates. Scanning Kelvin Probe Microscopy thus represents a powerful and unique tool to investigate the oxidation mechanism of self-assembled monolayers.

3.3.3.2 Probe-based electro-oxidative lithography of siloxane-TiO₂ films

The electro-oxidative lithography procedure successfully developed for the surface patterning of ITO layers, was extended to siloxane functionalized TiO₂ layers.

In this respect, suitable TiO₂ substrates had to be developed. AFM-based electro-oxidative lithography requires in fact conductive and smooth substrates. In this thesis, TiO₂ layers with the required characteristics were produced by coating ITO commercial glass slides with a thin TiO₂ layer. The resulting transparent films were used as substrate for the siloxane functionalization and surface modification by electro-oxidative lithography.

Experimental section

Materials. Reagents were purchased from different suppliers. Biscyclohexane (BCH) was distilled over sodium before use, while all other reagents were used without further purification. ITO float glass slides were purchased from PG&O (surface resistivity: 80 Ω/sq) and from Sigma-Aldrich (surface resistivity: 15-25 and 70-100 Ω/sq).

Deposition of TiO₂ transparent films. TiO₂ transparent, smooth and conductive films were used as substrates for the probe-based electrooxidative lithography. They were prepared starting from a titania stable and homogeneous sol, synthesized as follows. N-butanol (5.3 mL) and acetylacetone (0.4 mL) were mixed in a test tube. Then, 4.2 mL titanium(IV) butoxide was added to the solution, which was subsequently stirred for 30 min at room temperature. Glacial acetic acid (0.3 mL) was added dropwise to the solution under stirring. The resulting sol (yellowish and transparent) was stable for several weeks. The titania films were deposited by spin coating (2000 rpm, 20 s) the obtained sol on ITO layers (Aldrich, PG&O). The resulting film were immediately calcined at 400°C under O_2 flux (1 L h^{-1}) for 1.5 h.

TiO₂ film characterization. The precursor sol was characterized by thermogravimetric (TG) analysis using a Perkin Elmer TGA7, to determine the temperature of complete decomposition of the organic species in the sol.

The occurrence of organic residues in the TiO₂ films was investigated by Fourier transform infrared (FTIR) spectroscopy in the grazing angle reflectance mode using a Bruker Hyperion spectrometer.

The morphology of the TiO₂ layers was analyzed by scanning electron microscopy (SEM) using a HITACHI TM-1000, and by atomic force microscopy (AFM) using an NT-MDT Solver LS working in tapping mode.

The surface resistivity of the obtained films was measured by an impedance method on a 1 x 1 cm^2 square geometry using Scanning Electrochemical Microscopy (SECM).

Static water contact angles were determined using a Krüss DSA10 apparatus, before and after UV irradiation by a Benda NU6KL LW lamp, emitting at 366 nm (surface power density: 0.6 mW cm^{-2}).

Self-assembly of siloxane monolayers. The TiO$_2$ films were cleaned with Ar plasma for 2 minutes before use. *n*-Octadecyltrichlorosilane (OTS) monolayers were deposited on the oxide surface by immersing the TiO$_2$ films in a 14 mM OTS solution in BCH. The ITO was immersed for 1 minute, then was dried and sonicated in toluene. The deposition procedure was repeated twice. The resulting monolayers were characterized by their water contact angles, using a Krüss DSA10 apparatus. Moreover, they were analyzed by Fourier transform infrared (FTIR) spectroscopy in the grazing angle reflectance mode using a Bruker Hyperion spectrometer. Finally, the topography of the monolayers was investigated by atomic force microscopy (AFM) using an NT-MDT Solver LS working in tapping mode with Ultrasharp tips (μMash).

Probe-based electro-oxidative lithography. Lithography experiments were carried out using an Ntegra Aura AFM (NT-MDT), using a Pt coated AFM tip (μMash). The oxidation tests were carried at room temperature and at controlled humidity (RH) in a home-built AFM chamber with controllable humidity. Lithography experiments were carried out in "vector mode", *i.e.*, moving the tip along the trajectories where voltages are to be applied. The bias voltage, pulse duration, and relative humidity (RH) were varied, while contact force, and temperature were kept constant. The obtained oxidized patterns were imaged afterwards using the same tip, working in contact and in tapping mode.

Results and discussion

TiO$_2$ film characterization. The synthesis of the TiO$_2$ layers is based onto the calcination of thin, spin coated films, obtained from a stable titania sol. The complete removal of the organic species present in the non-aqueous sol was verified by TG analysis (Figure 3.3.21a). Although the main mass loss takes place between 80 and 300 °C, a much smaller weight loss is appreciable around 450 °C. However, after plasma treatment, the TiO$_2$ layer presents no trace of organic contaminants, as shown by FTIR analysis (Figure 3.3.20b). The FTIR spectrum exhibits instead a very large amount of surface OH species, as appreciable from the very intense and broad band in the 3700-3000 cm^{-1} spectral range, generally attributed to the OH stretching vibration of hydroxyl groups interacting by hydrogen bonding.

Figure 3.3.20 a) TG analysis of the stable titania sol. b) FTIR spectrum measured in the grazing incident reflectance mode of the TiO$_2$ film after plasma treatment.

The resulting films show a moderate mechanical robustness and are stable towards sonication in various solvents. Moreover, they exhibit an excellent transparency, which is testified by the easy readability of written text underneath the coated glass substrate (Figure 3.3.21).

Figure 3.3.21 Transparency of the obtained TiO$_2$ films.

The morphology of the films was investigated by SEM and AFM analyses. SEM images (Figure 3.3.22) show the presence of numerous small cracks in the films. The occurrence of such cracks could be limited by modulating the calcination conditions (slower heating, less intense oxygen flux).

Figure 3.3.22 SEM images of the TiO$_2$ film.

AFM images instead show really homogeneous surfaces (Figure 3.3.23). However, the average roughness of the surface, evaluated on 5 x 5 μm^2 areas, was critically dependant on the type of ITO substrate adopted. Comparing two samples with the same surface resistivity (70-100 Ω/sq), it was found that Aldrich samples presented a much lower average roughness with respect to PG&O slides. (rms < 1 nm for Aldrich; rms >> 1 nm for PGO). Such a marked difference could arise from the different surface structure of the ITO layer. Since electro-oxidative lithography requires very smooth surface (rms $\leq$ 1 are preferentially employed), the Aldrich ITO slides were adopted as substrates for the deposition of TiO$_2$ film.
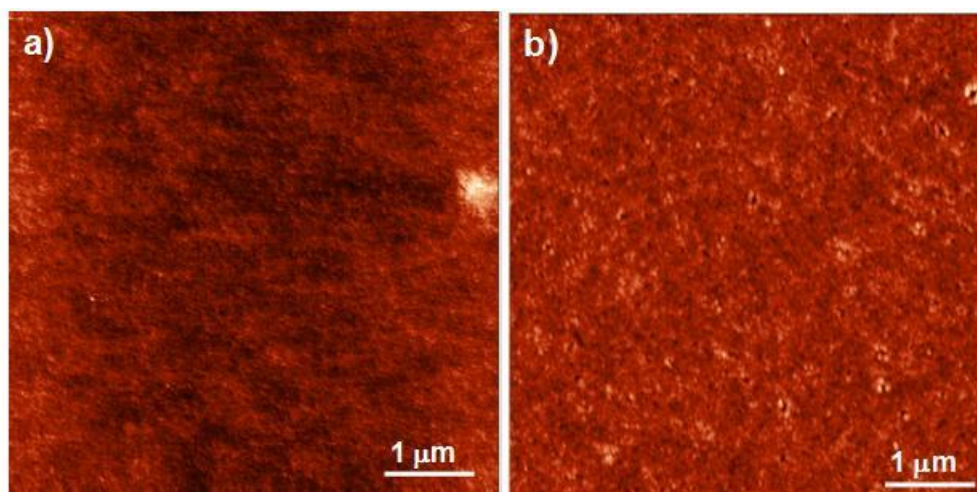
Figure 3.3.23 AFM height images measured in tapping mode of the TiO$_2$ film deposited onto different ITO substrates: a) ITO Aldrich 70-100 Ω/□, and b) ITO PG&O 70-100 Ω/□.

AFM analysis was also employed to measure the thickness of the TiO$_2$ films, which was determined to be of about 170 nm.

The TiO$_2$ films were also conductive as determined by surface resistivity measured by an impedance method using Scanning Electrochemical Microscopy (SECM). Table 3.3.2 reports the

surface resistivity values determined for bare and calcined ITO films and for the relative TiO_2 layers.

$R_{nominal}$ ITO Ω/sq	R_{meas} calcined ITO Ω/sq	R_{meas} TiO_2 - ITO Ω/sq
15 – 25	25.6	41.5
70 – 100	105	135

Table 3.3.2 Surface resistivity values, R, for bare ITO layers before and after the calcination treatment, and for TiO_2 films obtained using the relative ITO film.

The surface resistivity of the TiO_2 films is larger than the resistivity of the relative ITO layer adopted for its preparation. This can be attributed to the presence of the TiO_2 layer which possess a much lower conductivity than ITO. Moreover, the thermal treatment adopted during the synthesis is known to reduce the conductivity of ITO films, due to thermally activated processes taking place in the oxide layer. Indeed, an increase of surface resistivity of the bare ITO films after calcination was observed also in the present case.

The prepared TiO_2 films are also photoactive, as proved by the measurement of their water contact angle before and after UV irradiation (Figure 3.3.24). The water contact angle of the as-prepared substrate is close to 40°. However, upon irradiation with UV, the contact angle progressively decrease until a superhydrophilic surface is obtained (water CA $\sim$ 0°). The CA values of the TiO_2 film before irradiation could be obtained again after storage in the dark for several days.
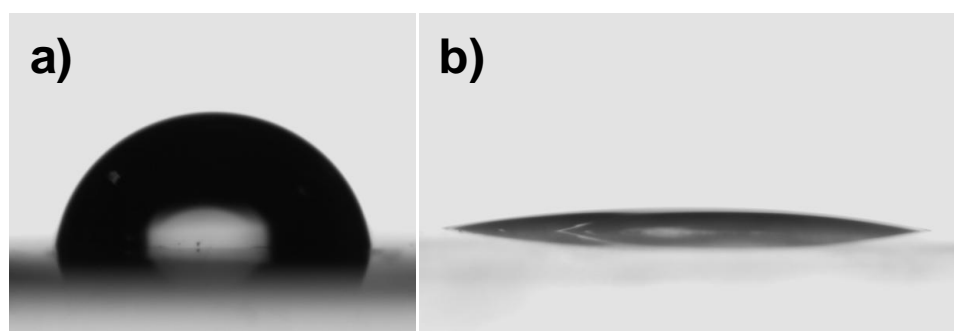
Figure 3.3.24 Water contact angles of a) the as-prepared TiO films and b) after UV irradiation for 2 h.

OTS monolayer formation. Siloxane monolayers were deposited onto the cleaned TiO_2 samples using the same procedure adopted for ITO and Si substrates. Relevant parameters such as immersion time and duration of the cleaning step, were optimized for the specific substrate. The formation of the OTS monolayer was assessed by water contact angle measurements and the quality of the monolayer was determined by FTIR and AFM analyses.

TiO$_2$ layers were plasma treated before the OTS deposition. The plasma cleaning step serves the double purpose of removing the possible organic contaminants and of promoting the surface hydroxylation of the surface, needed for the formation of a good monolayer. As a result, samples showed a complete wettability by water at the end of the plasma treatment. After OTS deposition, water contact angle were of ~ 109°.
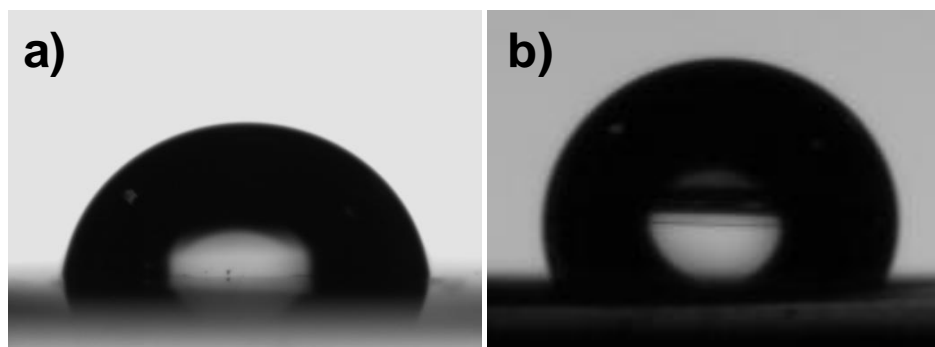
Figure 3.3.25 Water contact angles of a) the as-prepared TiO films and b) after OTS monolayer deposition.

Both in the case of ITO and of TiO$_2$, a much longer immersion time in the OTS/BCH solution was required with respect to OTS deposition on Si. In particular, Si wafers require only a few seconds, while ITO needs an immersion time of a few minutes and TiO$_2$ requires the longest immersion time (more than 1 h).

The humidity conditions during the OTS SAM deposition appear to be more crucial than in the case of Si. Often imperfect monolayers were formed, as assessed by the position of the stretching vibration of CH$_2$- groups in FTIR spectra (3.3.27) of the film surface, measured in the grazing incident reflectance mode.
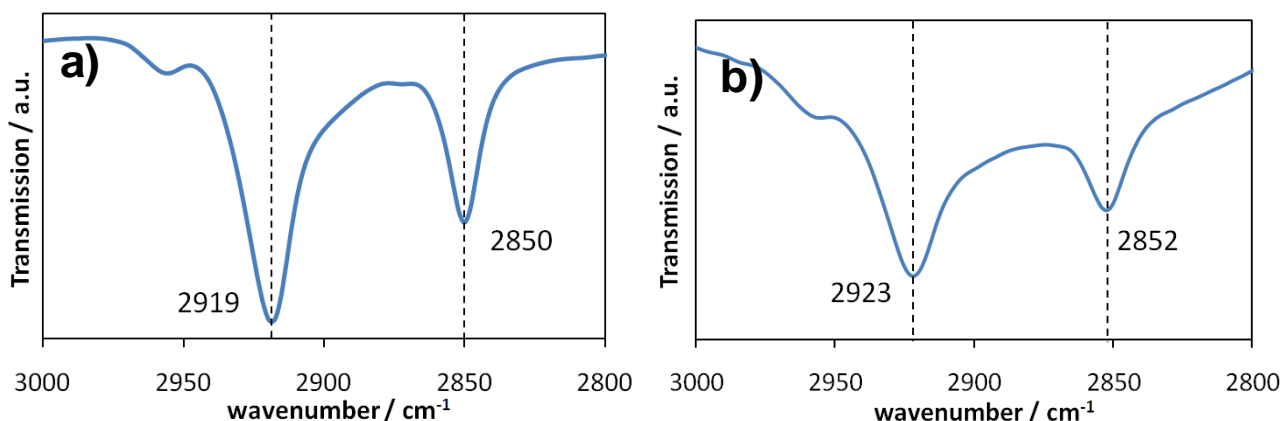
Figure 3.3.26 FTIR spectra, measured in the grazing incident reflectance mode for OTS-TiO$_2$ samples, in the case of a) a densely packed OTS monolayer and b) an OTS monolayer presenting dendritic structures.

The positions of the CH$_2$- stretching vibrations in Figure 3.3.26a (2919 and 2850 cm^{-1}) are indicative of the formation of a densely packed monolayer [Maoz1995], while Figure 3.3.26b shows a much less ordered self-assembled monolayer. This latter sample exhibited the presence of

dendritic structures in AFM images (Figure 3.3.27b), that in agreement with previous results on ITO, were attributed to areas of less dense and ordered monolayer. The formation of such structures occurred when extremely dry conditions were adopted (freshly distilled BCH and toluene solvents). Moreover, in this case the water contact angle determinations showed an unusual wetting behavior. A change in the shape (and contact angle) of the drop was observed after a few seconds from its deposition on the surface, indicative of an unstable surface state. Conversely, the use of aged solvents resulted in the formation of aggregates of polymerized silane molecules at the film surface (Figure 3.3.27c).
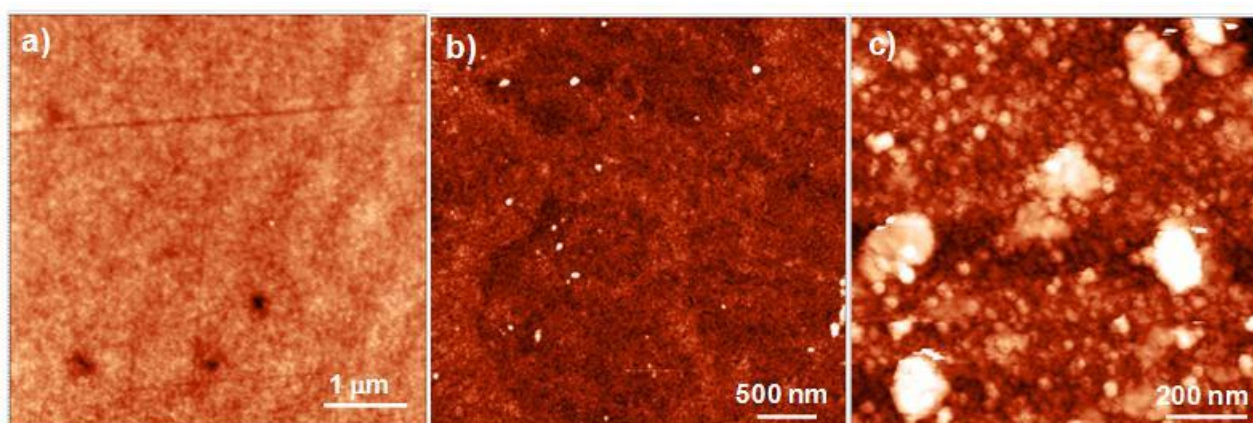
Figure 3.3.27 AFM height images measured in tapping mode on OTS-TiO$_2$ samples: a) a densely packed monolayer; b) dendritic structures of less organized monolayer; c) occurrence of silane polymerization.

Electro-oxidative lithography. The electro-oxidative lithography of OTS-TiO2 samples was successfully carried out (Figure 3.3.28) by adopting quite different conditions with respect to both Si and ITO layers. In the case of ITO the conduction was too high and a Si between the ITO substrate and the electrical circuit was employed to act as a resistor in series with the tip/sample resistance. The conduction of the layer represents a critical parameter also in the case of OTS-TiO$_2$ samples. However, in the latter case, the conduction needs to be promoted. Thus, no spacers were needed and the TiO$_2$ films with higher conductivity were employed (40 Ω/sq). Moreover, higher bias voltage and longer pulse duration were required (-15 V and 70-90 ms, respectively). On the contrary, the relative humidity is a less crucial parameter, an electro-oxidative lithography could be carried out at relative mild air humidity conditions (55%). Such observation is in agreement with previous results about ITO. In fact, in the case of ITO, the high conductivity of the ITO layer was thought to cause a too fast electron exchange between the tip and the substrate, with consequent disruption of the water meniscus. Therefore, lithography could be successfully carried out by slowing down the electron exchange and by working at high relative humidity conditions. The situation is reversed in the case of OTS-TiO$_2$ samples, which present a much lower surface

conductivity and therefore need to enhance the electron transfer taking place between tip and substrate.

The occurrence of electro-oxidative lithography is clear by both height and lateral force images (Figure 3.3.28).
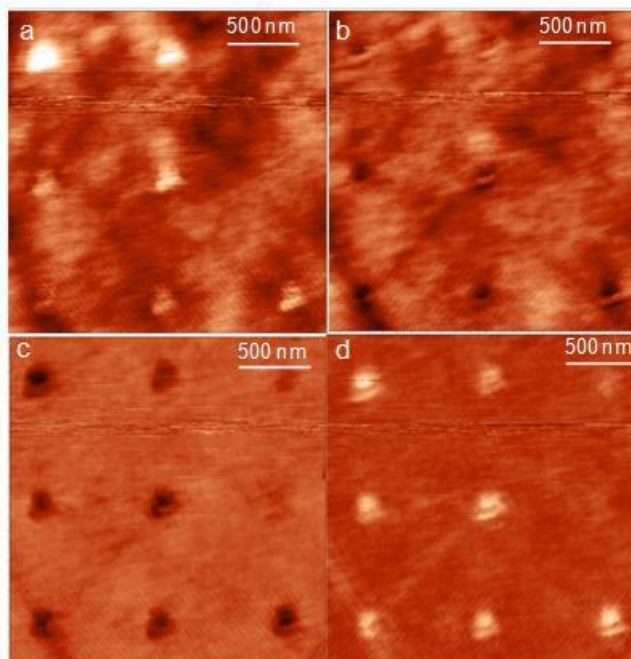
Figure 3.3.28 Height (a,b) and lateral force (c,d) images obtained in contact mode for electro-oxidized OTS-TiO$_2$ samples. Images on the left (a,c) were collected by setting the direction scan direction from left to right, while those on the right (b,d) were collected by reversing the scan direction.

Figure 3.3.28 presents AFM images recorded by varying the scan direction: images a and c were measured by setting the direction scan direction from left to right, while images b and d were recorded by reversing the scan direction. In this way, it is possible to recognize artifacts in the height contrast deriving from cross-talk effects [Wouters2005].
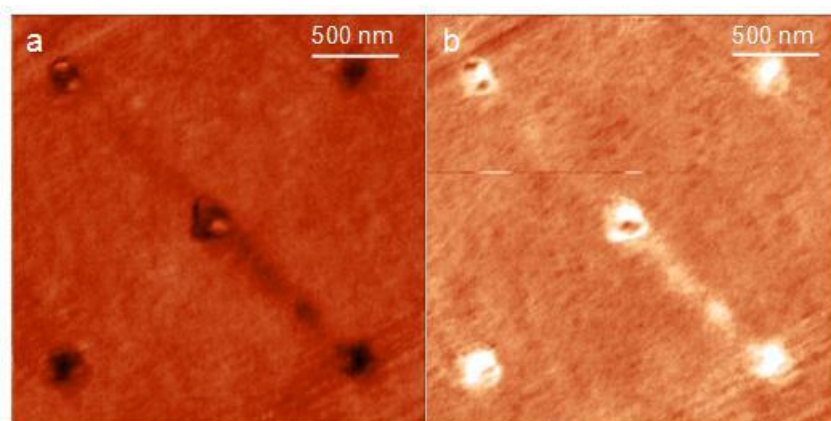

Figure 3.3.29 Height images obtained in contact mode for electro-oxidized OTS-TiO$_2$ samples. Image a was recorded by setting the direction scan direction from left to right, while image b was recorded by reversing the scan direction.

The cross-talk effect causes the appearance of a positive height contrast in areas of high friction (like the oxidized areas of a monolayer), but without any real corrugation. These artifacts can be recognized since, by reversing the scan direction, the height contrast becomes negative, as in Figure 3.3.29a,b.

Thus, it appears that using the adopted conditions, the overoxidation of the underlying oxide rarely takes place for OTS-TiO_2 samples, whereas the OTS oxidation is clearly visible from LF images. This represents a significant difference with respect to the electro-oxidative lithography of OTS-ITO, in which the two processes (oxidation of the monolayer and of the oxide substrate) were much more difficult to separate. Such difference allows us to conclude that no overoxidation of the underlying ITO layer is taking place.

With respect to OTS-ITO, the lateral resolution of the lithographed pattern is lower. This could result from a different pathway of the charges into the TiO_2 layer, but it may also be improved by optimizing the oxidation conditions.

Conclusions

TiO_2 transparent layers were synthesized by a multi-step synthetic procedure. The resulting materials combine the optical transparency and photoactivity of TiO_2 to a good mechanical robustness, very low surface roughness (rms < 1), and electrical conductivity. They thus represent promising candidates for several applications, from sensors to optically transparent electrodes.

Such innovative layers were functionalized with a silane molecule. In this respect, the behavior of TiO_2 showed interesting similarity with ITO, such as the occurrence of dendritic structures in the silane monolayer and a slower kinetics of monolayer adsorption with respect of Si.

The electro-oxidative lithography of the OTS-TiO_2 layers was successfully carried out for the first time. Relevant differences with respect to the mechanism of electro-oxidative lithography in OTS-Si and OTS-ITO were determined. In particular, no overoxidation of the oxide layer was observed. Further, the difference in the adopted oxidation parameters can be traced back to the lower surface conductivity of TiO_2 layer with respect to ITO.

The presented procedure of electro-oxidative lithography of TiO_2 films proved to be effective in tailoring the surface features of TiO_2 at the nanoscale and could be exploited to achieve further surface modifications by site-selective adsorption of relevant functionalities, such as dyes, metal nanoparticles or semiconductor quantum dots.

4. Conclusions and outlook

During my PhD, my research activity has focused onto the synthesis and the study of the physicochemical properties of nanometric TiO_2. In particular, two main subjects were investigated, one more applicative and the other more fundamental.

The first part of my PhD was devoted to the study of photocatalytic applications of TiO_2, in particular towards the improvement of the photocatalytic activity of TiO_2 to obtain more efficient photocatalysts for the degradation of environmental pollutants. Several synthetic procedures, the use of dopants and mixed oxides were tested to obtain TiO_2 powders and films able to overcome the main current limitations of TiO_2 photocatalysts, namely their low activity under solar irradiation, low quantum efficiency and the occurrence of poisoning effects.

In order to improve the photocatalytic activity of TiO_2 under solar irradiation, the introduction of non-metal ions (nitrogen) in the TiO_2 lattice was explored. N-doped TiO_2 samples were obtained from different titania precursors ($Ti(Oi-Pr)_4$, $TiCl_3$) and adopting different N-sources (ammonia, triethylamine, tea). All obtained samples were exhaustively characterized, in order to obtain a complete picture of the modifications induced in the titania structure and surface features by the modifications of the synthetic pathway. Samples were characterized from the structural, morphological, electrochemical, optical and compositional point of view. Moreover, other features, such as magnetic properties, were determined and ab initio calculations of the electronic properties of the doped samples were performed. All N-doped samples showed a broad absorption in the visible region which was traced back, on the grounds of first principles calculations, to the formation of localized intragap electronic levels. Sample thin films were tested for their photocatalytic activity, under UV, visible and simulated solar irradiation, towards the degradation of gas phase ethanol and acetaldehyde. The most active N-doped sample, both under UV and solar irradiation, was the oxide showing the largest amount of paramagnetic $N_b^{\bullet}$ species. Under visible irradiation instead, the sample with the largest activity was the one showing the narrowest apparent band gap and the concomitant presence of anatase and brookite polymorphs, which might hinder charge recombination processes.

The structure of N-doped samples was elucidated not only by ordinary powder diffraction, but also by means of synchrotron radiation, using Extended X-ray Absorption Fine Structure (EXAFS) to understand the position of dopant ions inside the TiO_2 crystal lattice. These data were obtained during a short research stay at the European Synchrotron Radiation Facility (ESRF) in Grenoble. Average Ti nearest neighbors distances were obtained from EXAFS experiments and

compared with Density Functional Theory (DFT) calculations, showing that N substitutes oxygen at low levels of doping, whereas oxygen vacancy creation is observed at higher dopant concentrations.

TiO_2 photocatalytic activity was improved also by controlling the TiO_2 morphology through template synthesis in order to enhance the diffusion and adsorption of pollutants at the TiO_2 surface. The morphologic features of titania particles were tailored by using soft templates, in order to obtain materials with a high degree of porosity in the mesoporosity range. Two classes of soft templates were investigated: alkylpyridinium surfactants and block copolymers of the Pluronic family. As for the first class, both monomeric (dodecylpyridinium chloride, DPC) and dimeric gemini-like surfactants (gemini spacer 3, GS3) were employed. Mesoporous TiO_2 samples were synthesized by a classical sol-gel route followed by an hydrothermal growth in the presence of one of the structure directed agents. The surfactant/oxide interactions at the solid/liquid interface were evaluated by adsorption isotherms, showing marked differences between the two surfactants. While DPC exhibited weak adsorbate/adsorbent interactions and weak self-aggregation tendency, resulting in the formation of very small, globular micelles, GS3 instead showed strong interactions with the TiO_2 surface and the formation of elongated rods and further hexagonal arrangements could be proposed. Such different behaviors lead to significant diversities in the porous structure of the TiO_2 samples. The small pores generated by the DPC micelle tend to collapse because of the heat of combustion generated during the surfactant removal step at 600 °C. On the contrary, GS3 leads to a significant fraction of pores in the mesoporosity range.

However, the use of cationic surfactants has an intrinsic limitation: high calcination temperatures are required to remove entirely the template. Such harsh conditions markedly reduce the surface area of the oxide due to particle sintering and crystal growth. Non-ionic structure directing agents, such as amphiphilic block copolymers, can be instead completely removed at much lower temperatures. Three block copolymers of the Pluronic family, characterized by different micelle size in water as determined by light scattering analysis, were employed to induce mesoporosity in nano-TiO_2. The surfactants were removed by combining UV and thermal treatments in order to avoid pore collapse while obtaining a good oxide crystallinity. Obtained samples presented a high surface area and significant fraction of pores in the mesoporosity range. A good correlation was observed between the sequence of average pore size in mesoporous TiO_2 and the micelle size of the used copolymer. A fine modulation of pore size and total volume was obtained by changing polymer type and concentration, effectively enhancing the photocatalytic properties of the oxide towards the degradation of methylene blue. The mesoporous oxides were also used as scaffolds to obtain Bi-promoted TiO_2, resulting in a further increase of the photocatalytic performance (see below).

In order to improve the quantum yield of photocatalytic reactions, mixed oxides were investigated to slow down the recombination process. In particular, Bi_2O_3 was proposed as a cheaper alternative to noble metals to enhance the separation of photogenerated charges. Bi_2O_3 was also allowed to form into the mesoporous network of TiO_2 samples obtained by surfactant template synthesis. The obtained materials were characterized by X-ray diffraction (XRD), N_2 adsorption at subcritical temperatures (BET), high resolution transmission microscopy (HRTEM), Fourier transform infrared (FTIR) spectroscopy, and zeta potential determinations, providing an insight into the composite structure and into the specificity of the Bi_2O_3-TiO_2 composites with respect to traditional sol-gel TiO_2 nanomaterials. All samples were tested for the photocatalytic degradation of methylene blue stains and of formic acid under dry and wet conditions, respectively. The presence of Bi promotes the photocatalytic activity of the final samples in both tested reactions. Photocurrent measurements of Bi_2O_3-TiO_2 composites were performed in order to assess any effect of the Bi addition on the fate of the photogenerated electron-hole pair. The obtained results agree with the observed marked enhancement in photocatalytic activity of the Bi_2O_3-TiO_2 samples, showing an increased recombination time of photogenerated charges in Bi_2O_3-TiO_2 composites. This effect may be related to the finely dispersed nature of Bi_2O_3 within the mesoporous network of the TiO_2 scaffold.

In order to address poisoning issues in TiO_2 thin films, the combination of photocatalysis with another advanced oxidation technique, ozonation, was proposed. Photocatalytic ozonation by TiO_2 films was tested towards the mineralization of highly recalcitrant pollutants such as bisphenol A and cumylphenol. A specific deposition procedure of the TiO_2 film onto a rough Al support was developed in order to obtain photocatalytic films with high surface area and good mechanical robustness. Photocatalytic ozonation was compared to the separate photolytic, photocatalytic, and ozonation techniques to investigate the synergistic processes taking place in the combined process. The combination of the two treatments leads to synergistic effects that dramatically enhance the final mineralization of the pollutants. Moreover, the degradation pathway taking place during the photocatalytic ozonation of bisphenol A and 4-cumylphenol was studied by combining HPLC–MS determinations and FTIR analyses of the used catalyst.

The second part of my PhD thesis was devoted to the development of oxide-based materials with tailored surface properties by means of surface functionalization with siloxanes.

Firstly, the role played by the structure of the siloxane molecule onto the wetting features of a smooth surface was investigated. The surface energy of different hydrophobing molecules, both fluorinated and unfluorinated, deposited in smooth layers over an inert substrate, was determined by analyzing contact angle values with literature models. The obtained values were compared with

dipole moments determined by theoretical calculations employing semiempirical Hamiltonians, finding a close correlation between the calculated dipole moments and the polar components of the surface energy.

Siloxanes were then employed to functionalize TiO_2 nanoparticles, in order to obtain rough composite films. The TiO_2 surfaces functionalized by different siloxanes were tested in self-cleaning experiments. Further, patterned structures with tunable hydrophobic and oleophobic patches were obtained by exploiting the photocatalytic activity of TiO_2 films. The resulting wetting contrast was exploited to obtain a site selective adsorption of a dye molecule, with a procedure that can be adapted to the site selective deposition or growth of a large variety materials, such as semiconductor quantum dots, polymers or biological molecules.

Another patterning technique was exploited to obtain the site-specific modification of the siloxane monolayer. Probe-based electro-oxidative lithography was chosen among the available patterning techniques, because of its high lateral resolution and limited application to oxide surfaces such as TiO_2. In the present thesis, probe-based electrooxidative lithography of octadecyltrichlorosilane (OTS) monolayers adsorbed on TiO_2 and indium tin oxide (ITO) are reported for the first time. The conductivity of the layer and the environmental humidity are critical parameters, affecting the stability of the water meniscus between the probe and the substrate and thus the electro-oxidation process. The resulting surface functionalization was exploited to obtain the site selective growth of metal nanoparticles. The electro-oxidation mechanism was studied by advanced characterization techniques such as Scanning Kelvin Probe Microscopy (SKPM), and the oxidation processes taking place on Si, ITO and TiO_2 were compared. For instance, in the case of OTS-ITO, a local overoxidation of the ITO substrate occurs simultaneously to the monolayer oxidation, whereas in OTS-TiO_2, no overoxidation of the oxide substrate takes place.

This thesis goes beyond the mere application of siloxane-TiO_2 composite materials, because it investigated more fundamental aspects related to the bonding and structure of the siloxane layers onto TiO_2 nanoparticle films by combining contact angle measurements with CP/MAS NMR, ATR-FTIR and XPS analyses. The influence of the siloxane amounts on the wettability and self-cleaning properties of TiO_2 was studied, together with the role played by the hydrophobing molecule structure (aliphatic vs. aromatic side-chain, linear vs. branched, length of the side-chain, fluorinated vs. un-fluorinated molecules). It appears that the attachment modes of silicon, besides changing with the siloxane content of the surface, are markedly affected by the siloxane structure. For instance, alkyl trifunctional siloxanes give rise, starting for low oxide coverage (9 % w/w), to continuous functionalized layers in which silicon atoms are progressively bound by one, two, or three groups, these being either – O–Ti or –O–Si. These films are uniform and highly hydrophobic

showing excellent self-cleaning properties at low contents; they present a Cassie-Baxter wetting behavior in which water drops float over a composite solid-gas carpet. The substitution of the alkyl chain with aromatic end groups favors localization versus spreading for the siloxanes, due to π-π stacking interactions. In these cases, the films, which are locally ordered, are less uniform on the whole. For instance, the bifunctional biaryl compound gives rise to layers which are initially, i.e., at low coverage, hydrophilic and end up to be hydrophobic at higher coverage. These are characterized by patch-wise localizations producing a wettability in which the water drops spread following the surface rough profile. Therefore, the structure of the siloxane appears to be a key parameter tuning the features of wettability of the surface by water.

However, at the end of this comprehensive and multi-faceted study, several questions are still left unanswered. Some of the most intriguing open problems are presented here as suggestions for further research.

Solar light activated photocatalysis: Although N-doping provides TiO_2 photocatalysts with a visible absorption and a certain degree of photocatalytic activity under solar light irradiation, it also creates some problems such as low UV light photoactivity, unstable N species after photocatalysis and low oxidation power of the photogenerated holes [Zhang2010]. In order to overcome such limitations intrinsic to N-doping, the modification of N-doped TiO_2 with metal ions, metal oxides and other non-metal elements could be investigated.

Mesoporous photocatalysts with mixed oxides for quantum efficiency improvement: The role of pore size in photocatalysis is still a debated topic [Sanchez2008]. It is still not clear whether mesoposous materials exhibit improved photocatalytic performance because of their higher surface area or because of the presence of mesopores. Further research is needed to clarify this aspect.

The use of a mesoporous structure as scaffold for the creation of metal/mixed oxide composites has instead proven to be a winning strategy. However, an exhaustive characterization of the finely dispersed oxide in the TiO_2 matrix is challenging. In our study, indirect evidence were used to prove the presence of a second segregated oxide. Other techniques, such as EXAFS or XPS, may shed new light on the structure of the Bi_2O_3 clusters. Moreover, other oxides, such as WO_3, can be investigated to improve the TiO_2 quantum efficiency.

Photocatalytic ozonation by TiO_2 films: This combined process proved to be highly effective for the removal of highly recalcitrant compounds. Its main limitation towards plant scale application is the high cost of ultraviolet light irradiation. The energy demand of this combined method could be considerably decreased by using solar-irradiation. Thus, tests employing solar-light activated photocatalysts should be carried out.

Applicability of siloxane-TiO$_2$ composites as self-cleaning coatings: These composite materials, although promising, suffer from manifold limitations that could hinder their commercial application. Oxide-based protective films have currently limited durability, and other issues concern the fabrication costs and large-area production [Yao2011]. New deposition procedure suited to plant-scale application need to be developed to obtain uniform and adherent coatings onto numerous types of substrates (glass, ceramics, metals, stone, polymers).

Lithography techniques: Probe-based electro-oxidative lithography currently represents one of the patterning techniques with the highest lateral resolution, however its main limitations concern the reproducibility, which is critically linked to the tip quality, and the time and expense associated with patterning [Wouters2009]. Photocatalytic lithography represents a low cost alternative that does not require any expensive equipment. However, photocatalytic lithography has a quite poor lateral resolution (in the micrometer range) due to remote photocatalytic oxidation [Fujishima2008]. New strategies need to be devised in order to improve its resolution. A promising approach combining AFM-based lithography and UV irradiation was proposed by Kobayashi et al. [Kobayashi2002].

Investigation of the structure of the hydrophibing layer in siloxane-oxide composites: The investigation of the interaction between oxide surface and siloxane molecule by solid state NMR could be extended to other systems, such as SiO$_2$ or Al$_2$O$_3$. In the these systems, it would be possible to investigate at the same time the Si atom of the siloxane molecule and the Si/Al atoms at the oxide surface (by either ^{29}Si and ^{27}Al NMR), thus clarifying debated aspects such as the nature of the T^2 attachment mode and the monolayer formation mechanism onto different oxides.

5. References

Adamo C., Barone V. (1999) Toward Reliable Density Functionals Without Adjustable Parameters: the PBE0 Model. Journal of Chemical Physics 110:6158–6170.

Addamo M., Augugliaro V., Lopez E.G., Loddo V., Marci G., Palmisano L. (2005) Oxidation of oxalate ion in aqueous suspensions of TiO_2 by photocatalysis and ozonation. Catalysis Today 107–108:612–618.

Agustina T.E., Ang H.M., Vareek V.K. (2005) A review of synergistic effect of photocatalysis and ozonation on wastewater treatment. Journal of Photochemistry and Photobiology C: Photochemistry Reviews 6:264–273.

Alexandridis P., Nivaggioli T., Hatton T.A. (1995) Temperature effects on structural-properties of pluronic P104 and F108 PEO-PPO-PEO block-copolymer solutions. Langmuir 11:2847-2847.

Alum A., Yoon Y., Westerhoff P., Abbaszadegan M. (2004) Oxidation of bisphenol A, 17β-estradiol, and 17α-ethynyl estradiol and byproduct estrogenicity. Environmental Toxicology 19:257-264.

Antonietti M., Berton B., Göltner C., Hentze H.-P. (1998) Synthesis of Mesoporous Silica with Large Pores and Bimodal Pore Size Distribution by Templating of Polymer Latices. Advanced Materials 10:154-159.

Ardizzone S., Bianchi C.L., Cappelletti G. (2006) Growth of TiO_2 nanocrystals in the presence of alkylpyridinium salts: the interplay between hydrophobic and hydrophilic interactions. Surface and Interface Analysis 38:452–457.

Ardizzone S., Bianchi C.L., Cappelletti G., Annunziata R., Cerrato G., Morterra C., Scardi P. (2009) Liquid phase reactions catalyzed by Fe- and Mn-sulphated ZrO_2. Applied Catalysis A: General 360:137–144.

Ardizzone S., Bianchi C.L., Cappelletti G., Gialanella S., Pirola C., Ragaini V. (2007) Tailored Anatase/Brookite Nanocrystalline TiO_2. The Optimal Particle Features for Liquid and Gas-Phase Photocatalytic Reactions. Journal of Physical Chemistry C 111:13222-13231.

Ardizzone S., Bianchi C.L., Quagliotto P., Viscardi G. (2002) Adsorption of cationic 'gemini' surfactants at the TiO_2/solution interface. Surface and Interface Analysis 34:652–656.

Asahi R., Morikawa T., Ohwaki T., Aoki K., Taga Y. (2001) Visible-Light Photocatalysis in Nitrogen-Doped Titanium Oxides. Science 293:269-271.

Attard G.S., Bartlett P.N., Coleman N.R.B., Elliott J.M., Owen J.R., Wang J.H. (1997) Mesoporous platinum films from lyotropic liquid crystalline phases. Science 278:838-840.

Attard G.S., Glyde J.C., Göltner C.G. (1995) Liquid-crystalline phases as templates for the synthesis of mesoporous silica. Nature 378:366-368.

Augugliaro V., Litter M., Palmisano L., Soria J. (2006) The combination of heterogeneous photocatalysis with chemical and physical operations: A tool for improving the photoprocess performance. Journal of Photochemistry and Photobiology C: Photochemistry Reviews 7:127-144.

Bai H., Liu Z., Sun D.D. (2010) Hierarchically multifunctional TiO_2 nano-thorn membrane for water purification. Chemical Communications 46:6542-6544.

Barrett E.P., Joyner L.G., Halenda P.H. (1951) The determination of pore volume and area distributions in porous substances. I. Computations from nitrogen isotherms. Journal of the American Chemical Society 73:373–380.

Bellamy L. et al., Advances in Infra-red Group Frequencies, Methuen, London, 1968.

Bhat M.A., Dar A.A., Amin A., Rashid P.I., Rather G.M. (2007) Temperature dependence of transport and equilibrium properties of alkylpyridinium surfactants in aqueous solutions. Journal of Chemical Thermodynamics 39:1500–1507.

Bian Z.F., Zhu J., Wang S.H., Cao Y., Qian X.F., Li H.X. (2008) Self-assembly of active Bi_2O_3/TiO_2 visible photocatalyst with ordered mesoporous structure and highly crystallized anatase. Journal of Physical Chemistry C 112:6285-6262.

Bianchi C.L., Cappelletti G., Ardizzone S., Gialanella S., Naldoni A., Oliva C., Pirola C. (2009) N-doped TiO_2 from $TiCl_3$ for photodegradation of air pollutants. Catalysis Today 144:31–36.

Bickley R.I., Gonzales-Carreno T., Lees J.L., Palmisano L., Tilley R.J.D. (1991) A structural investigation of titanium dioxide photocatalysts. Journal of Solid State Chemistry 92:178-190.

Biggers W.J., Laufer H. (2004) Identification of juvenile hormone-active alkylphenols in the lobster Homarus americanus and in marine sediments. The Biological Bulletin 206:13.

Bleta R., Alphonse P., Lorenzato L. (2010) Nanoparticle Route for the Preparation in Aqueous Medium of Mesoporous TiO_2 with Controlled Porosity and Crystalline Framework. Journal of Physical Chemistry C 114:2039-2048.

Boiadjieva T., Bianchi C.L., Cappelletti G., Ardizzone S., Rondinini S., Vertova A. (2004) The role of surface electrification on the growth and structural features of titania. nanoparticles. Physical Chemistry Chemical Physics 6:3535-3539.

Borras A., Gonzales-Elipe A.R. (2010) Wetting Properties of Polycrystalline TiO_2 Surfaces: A Scaling Approach to the Roughness Factor. Langmuir 26:15875–15882.

Bosc F., Ayral A., Albouy P.A., Guizard C. (2003) A simple route for low-temperature synthesis of mesoporous and nanocrystalline anatase thin films. Chemistry of Materials 15:2463-2468.

Bosc F., Edwards D., Keller N., Keller V., Ayral A. (2006) Mesoporous TiO_2-based photocatalysts for UV and visible light gas-phase toluene degradation. Thin Solid Films 495:272-279.

Bremner D.H., Di Carlo S., Chakinala A.G., Cravotto G. (2008) Mineralisation of 2,4-dichlorophenoxyacetic acid by acoustic or hydrodynamic cavitation in conjunction with the advanced Fenton process. Ultrasonics Sonochemiztry 15:416–419.

Bremner D.H., Molina R., Martinez F., Melero J.A., Segura Y. (2009) Degradation of phenolic aqueous solutions by high frequency sono-Fenton systems. Applied Catalysis B: Environmental 90:380–388.

Brinker C.J., Lu Y., Sellinger A., Fan H. (1999) Evaporation-induced self-assembly: Nanostructures made easy. Advanced Materials 11:579-585.

Bush B.G., DelRio F.W., Opatkiewicz J., Maboudian R., Carraro C. (2007) Effect of Formation Temperature and Roughness on Surface Potential of Octadecyltrichlorosilane Self-Assembled Monolayer on Silicon Surfaces. The Journal of Physical Chemistry A 111:12339–12343.

Butt H.-J., Raiteri R. (1999) in: A.J. Milling (Ed.), Surface Characterization Methods: Principles, Techniques, and Applications, Dekker, New York.

Callies M., Quéré D. (2005) On water repellency. Soft Matter 1:55–61.

Cao M., Song X., Wang J., Wang Y. (2006) Adsorption of hexyl-α,ω-bis(dodecyldimethyl ammonium bromide) Gemini Surfactant on Silica and Its Effect on Wettability. Journal of Colloid and Interface Science 300:519-525.

Cappelletti G., Bianchi C.L., Ardizzone S. (2008) Nano-titania assisted photoreduction of Cr(VI). The role of the different TiO_2 polymorphs. Applied Catalysis B: Environmental 78:193–201.

Carp O., Huisman C.L., Reller A. (2004) Photoinduced reactivity of titanium dioxide. Progress in Solid State Chemistry 32:33-177.

Cassie A.B.D., Baxter S. (1944) Wettability of porous surfaces. Transactions of the Faraday Society 40:546-551.

Chang H.Y., Thangamuthu R., Lin C.W. (2004) Structure-property relationships in PEG/SiO_2 based proton conducting hybrid membranes—A ^{29}Si CP/MAS solid-state NMR study. Journal of Membrane Science 228:217-226.

Chen X., Mao S.S. (2007) Titanium Dioxide Nanomaterials: Synthesis, Properties, Modifications, and Applications. Chemical Reviews 107:2891-2959.

Choi S.Y., Mamak M., Coombs N., Chopra N., Ozin G.A. (2004) Thermally stable two-dimensional hexagonal mesoporous nanocrystalline anatase, meso-nc-TiO_2: Bulk and crack-free thin film morphologies. Advanced Functional Materials 14:335-344.

Crist B.V. (2000) Handbook of Monochromatic XPS Spectra: The Elements and Native Oxides. Wiley: Chichester, UK.

de Boer J.H., Lippens B.C., Linsen B.G., Broekhof J.C.P., van den Heuvel A., Osinga T.J. (1966) Thet-curve of multimolecular N_2-adsorption. Journal of Colloid and Interface Science 21:405–414.

Deborde M., Rabouan S., Mazellier P., Duguet J.P., Legube B. (2008) Oxidation of bisphenol A by ozone in aqueous solution. Water Research 42:4299–4308.

Dholam R, Patel N, Santini A, Miotello A (2010) Efficient indium tin oxide/Cr-doped-TiO_2 multilayer thin films for H_2 production by photocatalytic water-splitting. International Journal of Hydrogen Energy 35:9581-9590.

Di Paola A., Marcì G., Palmisano L., Schiavello M., Uosaki K., Ikeda S., Ohtani B. (2002) Preparation of polycrystalline TiO_2 photocatalysts impregnated with various transition metal ions: Characterization and photocatalytic activity for the degradation of 4-nitrophenol. Journal of Physical Chemistry B 106:637-645.

Di Valentin C., Finazzi E., Pacchioni G., Selloni A., Livraghi S., Paganini M.C., Giamello E. (2007) N-doped TiO_2: theory and experiment. Chemical Physics 339:44–56.

Di Valentin C., Pacchioni G.-F., Selloni A., Livraghi S., Giamello E. (2005) Characterization of Paramagnetic Species in N-Doped TiO_2 Powders by EPR Spectroscopy and DFT Calculations. Journal of Physical Chemistry B 109:11414–11419.

Dovesi R., Saunders V.R., Roetti C., Orlando R., Zicovich-Wilson C.M., Pascale F., Civalleri B., Doll K., Harrison N.M., Bush I.J., D'Arco P., Llunell M. (2006) CRYSTAL06 User's Manual. University of Torino, Torino, Italy.

Dudarev S.L., Botton C.A., Savrasov S.Y., Humphreys C.J., Sutton A.P. (1998) Electron-energy-loss spectra and the structural stability of nickel oxide: An LSDA+U study. Physical Review B 57:1505–1509.

Emeline A.V., Kuznetsov V.N., Rybchuk V.K., Serpone N. (2008) Visible-Light-Active Titania Photocatalysts: The Case of N-Doped TiO_2s—Properties and Some Fundamental Issues. International Journal of Photoenergy 1-19.

Fan A., Somasundaran P., Turro N.J. (1997) Adsorption of alkyltrimethylammonium bromides on negatively charged alumina. Langmuir 13:506–510.

Fernandez-Garcıa M., Martınez-Arias A., Hanson J.C., Rodriguez J.A. (2004) Nanostructured Oxides in Chemistry: Characterization and Properties. Chemical Reviews 104:4063–4104.

Fierro S., Comninellis C. (2010) Kinetic study of formic acid oxidation on Ti/IrO2 electrodes prepared using the spin coating deposition technique. Electrochimica Acta 55:7067–7073.

Firouzi A., Kumar D., Bull L.M., Besier T., Sieger P., Huo Q., Walker S.A., Zasadzinski J.A., Glinka C., Nicol J., Margolese D., Stucky G.D., Chmelka B.F. (1995) Cooperative Organization of Inorganic-Surfactant and Biomimetic Assemblies. Science 267:1138-1143.

Foulkes W.M.C., Haydock T. (1989) Tight-binding models and density-functional theory. Physical Review B 39:12520–12536.

Fowkes F.M. (1964) Attractive forces at interfaces, Industrial and Engineering Chemistry. 56:40-52.

Fowkes F.M. (1968) Calculation of work of adhesion by pair potential summation. Journal of Colloid and Interface Science 28:493-505.

Fowkes F.M. (1972) Donor-acceptor interactions at interfaces. Journal of Adhesion 4:155-159.

Fowler R.H.,. Guggenheim E.A (1965) Statistical Thermodynamics, Cambridge University Press, London, UK.

Fox H.W., Zisman W.A. (1952a) The spreading of liquids on low-energy surfaces. II. Modified tetrafluoroethylene polymers. Journal of Colloid Science 7:109-121.

Fox H.W., Zisman W.A. (1952b) The spreading of liquids on low-energy surfaces. II. Modified tetrafluoroethylene polymers. Journal of Colloid Science 7:428-442.

Fox M.A., Dulay M.T. (1993) Heterogeneous photocatalysis. Chemical Reviews 93:341-357.

Fuerstenau D.W., Jang H.M. (1991) On the nature of alkylsulfonate adsorption at the rutile/water interface. Langmuir 7:3138–3143.

Fujishima A., Honda K. (1972) Electrochemical Photolysis of Water at a Semiconductor Electrode. Nature 238:37-38.

Fujishima A., Zhang X., Tryk D.A. (2008) TiO_2 photocatalysis and related surface phenomena. Surface Science Reports 63:515-582.

Fujo K., Ikeda S. (1992) Size of Micelles of 1-Dodecylpyridinium Chloride in Aqueous NaCl Solutions. Bulletin of the Chemical Society of Japan 65:1406–1410.

Galan J.J., Gonzalez-Perez A., Del Castillo J.L., Rodrıguez J.R. (2002) Thermal parameters associated to micellization of dodecylpyridinium bromide and chloride in aqueous solution. Journal of Thermal Analysis and Calorimetry 70:229–234.

Garoma T., Matsumoto S. (2009) Ozonation of aqueous solution containing bisphenol A: effect of operational parameters. Journal of Hazardous Materials 167:1185–1191.

Gerischer H., Heller A. (1992) Photocatalytic Oxidation of Organic Molecules at TiO_2 Particles by Sunlight in Aerated Water. Journal of the Electrochemical Society 139:113-118.

Ginley D.S., Perkins J.D. (2010) in: Handbook of Transparent Conductors. (Eds: D. S. Ginley , H. Hosono , D. C. Paine), Springer-Verlag , Berlin, Germany, Ch. 1.

Gultekin I., Ince N.H. (2007) Synthetic endocrine disruptors in the environment and water remediation by advanced oxidation processes. Journal of Environmental Management 85:816-832.

Guo Z.B., Feng R. (2009) Ultrasonic irradiation-induced degradation of low-concentration bisphenol A in aqueous solution. Journal of Hazardous Materials 163:855–860.

Haensch C., Hoeppener S., Schubert U.S. (2010) Chemical modification of self-assembled silane based monolayers by surface reactions. Chemical Society Reviews 39:2323–2334.

Hagfeldt A., Lindström H., Södergren S., Linquist S.-E. (1995) Photoelectrochemical studies of colloidal TiO$_2$ films - the effect of oxygen studied by photocurrent transients. Journal of Elecroanalitical Chemistry 381:39-46.

Hait S.K., Moulik S.P. (2002) Gemini surfactants: a distinct class of self-assembling molecules. Current Science 82:1101–1111.

Herzer N., Hoeppener S., Schubert U.S. (2010) Fabrication of patterned silane based self-assembled monolayers by photolithography and surface reactions on silicon-oxide substrates. Chemical Communications 46:5634–5652.

Huh S., Chen H.-T., Wiench J.W., Pruski M., Lin V.S.-Y. (2005) Cooperative Catalysis by General Acid and Base Bifunctionalized Mesoporous Silica Nanospheres. Angewandte Chemie International Edition 44:1826-1830.

Iguchi N., Cady C., Snoeberger R.C., Hunter B.M., Sproviero E.M., Schmuttenmaer C.A., Crabtree R.H., Brudvig G.W., Batista V.S. (2008) Characterization of Siloxane adsorbates covalently attached to TiO$_2$. Proceedings of SPIE 7034:70340C 1-8.

Ihara T., Miyoshi M., Iriyama Y., Matsumoto O., Sugihara S. (2003) Visible-light-active titanium oxide photocatalyst realized by an oxygen-deficient structure and by nitrogen doping. Applied Catalysis B: Environmental 42:403-409.

Irie H., Watanabe Y., Hashimoto K. (2003) Nitrogen-Concentration Dependence on Photocatalytic Activity of TiO$_{2-x}$N$_x$ Powders. Journal of Physical Chemistry B 107:5483-5486;

Jing L., Wang J., Qu Y., Luan Y. (2009) Effects of surface-modification with Bi$_2$O$_3$ on the thermal stability and photoinduced charge property of nanocrystalline anatase TiO$_2$ and its enhanced photocatalytic activity. Applied Surface Science 256:657-663.

Kaelble D.H. (1970) Dispersion-Polar Surface Tension Properties of Organic Solids. Journal of Adhesion 2:66-81.

Kaune G., Memesa M., Meier R., Ruderer M.A., Diethert A., Roth S.V., D'Acunzi M., Gutmann J.S., Mueller-Buschbaum P. (2009) Hierarchically structured titania films prepared by polymer/colloidal templating. ACS Applied Materials and Interfaces 1:2862–2869.

Kim H., Noh K., Choi C., Khamwannah J., Villwock D., Jin S. (2011) Extreme superomniphobicity of multiwalled 8 nm TiO_2 nanotubes. Langmuir 27:10191–10196.

Kitamura T., Ikeda M., Shigaki K., Inoue T., Anderson N.A., Ai X., Lian T.Q., Yanagida S. (2004) henyl-Conjugated Oligoene Sensitizers for TiO_2 Solar Cells. Chemistry of Materials 16:1806-1812.

Kobayashi K., Tomita Y., Yoshida S. (2002) Nanometer-Scale Patterning of Oxygen Molecules Adsorbed on TiO_2 Surface by an Atomic Force Microscope with a Conductive Cantilever. Nano Letters 2:925-927.

Koopal L.K., Lee E.M., Boehmer M.R. (1995) Adsorption of cationic and anionic surfactants on charged metal oxide surfaces. Journal of Colloid and Interface Science 170:85–97.

Kosmulski M. (2009) Compilation of PZC and IEP of sparingly soluble metal oxides and hydroxides from literature. Advances in Colloid and Interface Science 152:14-25.

Kresge C.T., Leonowicz M.E., Roth W.J., Vartuli, J.C., Beck J.S. (1992) Ordered mesoporous molecular sieves synthesized by a liquid-crystal template mechanism. Nature 359:710-712.

Kresse G., Hafner J. (1993) Ab initio molecular dynamics for liquid metals. Physical Review B 47:558–561.

Kresse G., Joubert D. (1999) From ultrasoft pseudopotentials to the projector augmented-wave method. Physical Review B 59:1758–1775.

Kuna J.J., Voitchovsky K., Singh C., Jiang H., Mwenifumbo S., Ghorai P.K., Stevens M.M., Glotzer S.C., Stellacci F. (2009) The effect of nanometre-scale structure on interfacial energy. Nature Materials 8:837–842.

Kuznetsov V.N., Serpone N. (2009) On the Origin of the Spectral Bands in the Visible Absorption Spectra of Visible-Light-Active TiO_2 Specimens. Journal of Physical Chemistry C 113:15110-15123.

Lee E.S., Oh Y.T., Youn Y.S., Nam M., Park B., Yun J., Kim J.H., Song H.-T., Oh K.T. (2011) Binary mixing of micelles using Pluronics for a nano-sized drug delivery system. Colloids and Surfaces B 82:190-195.

Lee J., Jang Y., Sung M. (2003) Atomic Layer Deposition of TiO_2 Thin Films on Mixed Self-Assembled Monolayers Studied as a Function of Surface Free Energy. Advanced Functional Materials 13:873−876.

Lee S.H., Ishizaki T., Saito N., Takai O. (2008) Surface Characterization on Binary Nano/Micro Domain Composed of Alkyl and Amino-terminated Self-assembled Monolayer. Applied Surface Science 254:7453 – 7458.

Li D., Neumann A.W. (1990) A reformulation of the equation of state for interfacial tensions. Journal of Colloid and Interface Science 137:304-307.

Liang Q., Chen Y., Fan Y., Hu Y., Wu Y., Zhao Z., Meng Q. (2012) Applied Surface Science 258:2266 –2269.

Liaw W.-C., Chen K.-P. (2007) Preparation and characterization of poly(imide siloxane) (PIS)/titania(TiO$_2$) hybrid nanocomposites by sol–gel processes. European Polymer Journal 43: 2265-2278.

Lin C.-L., Yeh M.-Y., Chen C.-H., Sudhakar S., Luo S.-J., Hsu Y.-C., Huang C.-Y., Ho K.-C., Luh T.-Y. (2006) Silica-Titania-Based Organic-Inorganic Hybrid Materials for Photovoltaic Applications. Chemistry of Materials 18:4157-4162.

Lindgren T., Mwabora J.M., Avendano E., Jonsson J., Hoel A., Granquist C.-G., Lindquist S.-E. (2003) Photoelectrochemical and Optical Properties of Nitrogen Doped Titanium Dioxide Films Prepared by Reactive DC Magnetron Sputtering. Journal of Physical Chemistry B 107:5709-5716.

Linsebigler A L., Lu G., Yates Jr. J.T. (1995) Photocatalysis on TiO$_2$ surfaces: principles, mechanisms, and selected results. Chemical Reviews 95:735-758.

Little L.H. (1966) Infrared Spectra of Adsorbed Species. Academic Press, London.

Loddo V., Addamo M., Augugliaro V., Palmisano L., Schiavello M., Garrone E. (2006) Optical Properties and Quantum Yield Determination in Photocatalytic Suspensions. American Institute of Chemical Engineers Journal 52: 2565-2574.

Long R., English N.J. (2009) Synergistic Effects of Bi/S Codoping on Visible Light-Activated Anatase TiO$_2$ Photocatalysts from First Principles. Journal of Physical Chemistry C 113:8373–8377.

Magnacca G., Cerrato G., Morterra C., Signoretto M., Somma F., Pinna F. (2003) Structural and surface characterization of pure and sulfated iron oxides. Chemistry of Materials 15:675–687.

Manne S., Schäffer T.E., Huo Q., Hansma P.K., Morse D.E., Stucky G.D., Aksay I.A. (1997) Gemini Surfactants at Solid-Liquid Interfaces: Control of Interfacial Aggregate Geometry. Langmuir 13:6382- 6387.

Manoudis P.N., Karapanagiotis I., Tsakalof A., Zuburtikudis I., Kolinkeovà B., Panayiotou C. (2009) Superhydrophobic films for the protection of outdoor cultural heritage assets. Applied Physics A 97:351-360.

Manoudis P.N., Karapanagiotis I., Tsakalof A., Zuburtikudis I., Panayiotou C. (2008) Superhydrophobic Composite Films Produced on Various Substrates. Langmuir 24:11225-11232.

Maoz R., Cohen S.R., Sagiv J. (1999) Nanoelectrochemical Patterning of Monolayer Surfaces: Toward Spatially Defined Self-Assembly of Nanostructures. Advanced Materials 11:55 – 61.

Maoz R., Frydman E., Cohen S.R., Sagiv S. (2000) Constructive Nanolithography: Site-Defined Silver Self-Assembly on Nanoelectrochemically Patterned Monolayer Templates. Advanced Materials 12:424 – 429.

Maoz R., Sagiv J., Degenhardt D., Möhwald H., Quint P. (1995) Hydrogen-bonded multilayers of self-assembling silanes: structure elucidation by combined Fourier transform infra-red spectroscopy and X-ray scattering techniques. Supramolecular Science 2:9–24.

Martinez-Ferrero E., Sakatani Y., Boissière C., Grosso D., Fuertes A., Fraxedas J., Sanchez C. (2007) Nanostructured Titanium Oxynitride Porous Thin Films as Efficient Visible-Active Photocatalysts. Advanced Functional Materials 17:3348-3354.

Mehrian T., de Keizer A., Korteweg A.J., Lyklema J. (1993) Thermodynamics of adsorption of dodecylpyridinium chloride on Na-kaolinite. Colloids and Surfaces A 73:133–143.

Menger F.M., Keiper J.S. (2000) Gemini surfactants. Angewandte Chemie 39:1906–1920.

Mirau P. (2005) A Practical Guide to Understanding NMR of Polymers. Wiley-Interscience: New York,; Vol. 67, p 2.

Mohamed M.M., Bayoumy W.A., Khairy M., Mousa M.A. (2007) Synthesis of micro-mesoporous TiO_2 materials assembled via cationic surfactants: morphology, thermal stability and surface acidity characteristics. Microporous and Mesoporous Materials 103:174–183.

Monkhorst H.J., Pack J.D. (1976) On Special Points for Brillouin Zone Integrations. Physical Review B 13:5188–5192.

Moriguchi T., Yano K., Nakagawa S., Kaji F. (2003) Elucidation of adsorption mechanism of bone-staining agent alizarin red S on hydroxyapatite by FT-IR microspectroscopy. Journal of Colloid and Interface Science 260:19–25.

Morris A. J., Meyer G. J. (2008) TiO_2 Surface Functionalization to Control the Density of States. Journal of Physical Chemistry C 112:18224-18231.

Morterra C., Bolis V., Fisicaro E. (1989) The hydrated layer and the adsorption of co at the surface of TiO_2 (anatase). Colloids and Surfaces 41:177–188.

Nakata K., Fujishima A. (2012) TiO_2 photocatalysis: Design and applications. Journal of Photochemistry and Photobiology C: Photochemistry Reviews 13:169–189.

Neumann A.W., Good R.J., Hope C.J., Sejpol M. (1974) An equation-of-state approach to determine surface tensions of low-energy solids from contact angles. Journal of Colloid and Interface Science 49:291-304.

Newville M. (2001) IFEFFIT : interactive XAFS analysis and FEFF fitting. Journal of Synchrotron Radiation 8:322–324.

Nosonovsky M., Bhushan B. (2009) Superhydrophobic Surfaces and Emerging Applications: Non-Adhesion, Energy, Green Engineering. Current Opinion in Colloid & Interface Science14:270–280.

Ohtani B. (2008) Preparing Articles on Photocatalysis—Beyond the Illusions, Misconceptions, and Speculation. Chemistry Letters 37:217-229.

Ohtani B. (2010) Photocatalysis A to Z—What we know and what we do not know in a scientific sense. Journal of Photochemistry and Photobiology C: Photochemistry Reviews 11:157–178.

Oropeza F.E., Harmer J., Egdell R.G., Palgrave R.G. (2010) A critical evaluation of the mode of incorporation of nitrogen in doped anatase photocatalysts. Physical Chemistry Chemical Physics 12:960–969.

Ottewill R.H., Rastogi M.C. (1960) The stability of hydrophobic sols in the presence of surface-active agents—part 3. An examination by microelectrophoresis of the behaviour of silver iodide sols in the presence of cationic surface-active agents. Transactions of the Faraday Society, 56:880–892.

Owens D.K., Wendt R.C. (1969) Estimation of the surface free energy of polymers. Journal of Applied Polymer Science 13:1741-1747.

Oyama T., Yanagisawa I., Takeuchi M., Koike T., Serpone N., Hidaka H. (2009) Remediation of simulated aquatic sites contaminated with recalcitrant substrates by TiO_2/ozonation under natural sunlight. Applied Catalysis B: Environmental 91:242–246.

Ozin G.A. (2000) Panoscopic materials: synthesis over 'all' length scales. Chemical Communications 6:419-432.

Paoli E., Cappelletti G., Falciola L. (2010) Electrochemistry as a tool for nano-TiO_2 deposition and for photoremediation pollutant monitoring. Electrochemical Communications 12:1013–1016.

Park J.-S., Vo A.N., Barriet D., Shon Y.-S., Lee T.R. (2005) Systematic Control of the Packing Density of Self-Assembled Monolayers Using Bidentate and Tridentate Chelating Alkanethiols. Langmuir 21:2902–2911.

Park K.-S., Choi Y.-J., Kang J.-G., Sung Y.-M., Park J.-G. (2011) The effect of the concentration and oxidation state of Sn on the structural and electrical properties of indium tin oxide nanowires. Nanotechnology, 22:285712.

Paz Y. (2011) Self-assembled monolayers and titanium dioxide: From surface patterning to potential applications. Beilstein Journal of Nanotechnology 2:845–861.

Perdew J.P., Burke K., Ernzerhof M. (1996) Generalized gradient approximation made simple. Physical Review Letters 77:3865-3868.

Perdew J.P., Wang Y. (1992) Accurate and simple analytic representation of the electron gas correlation energy. Physical Review B 45:13244–13249.

Piera E., Ayllón J.A., Doménech X., Peral J. (2002) TiO_2 deactivation during gas-phase photocatalytic oxidation of ethanol. Catalysis Today 76:259–270.

Quagliotto P., Viscardi G., Barolo C., Barni E., Bellinvia S., Fisicaro E., Compari C. (2003) Gemini pyridinium surfactants: synthesis and conductometric study of a novel class of amphiphiles. Journal of Organic Chemistry 68:7651–7660.

Ravel B., Newville M. (2005) ATHENA, ARTEMIS, HEPHAESTUS: data analysis for X-ray absorption spectroscopy using IFEFFIT. Journal of Synchrotron Radiation 12:537–541.

Rivas F.J., Encinas A., Acedo B., Beltran F.J. (2009) Mineralization of bisphenol A by advanced oxidation processes. Journal of Chemical Technology & Biotechnology 54:589–594.

Rouquerol J., Rouquerol F., Sing K.S.W. (1999) Adsorption by powders and porous solids. Academic Press, London.

Saadoun L., Ayllon J.A., Jimenez-Becerril J., Peral J., Domenech X. (2000) Synthesis and photocatalytic activity of mesoporous anatase prepared from tetrabutylammonium-titania composites. Materials Research Bulletin 35:193-202.

Sakthivel S., Shankar M.V., Palanichamy M., Arabindoo B., Bahnemann D.W., Murugesan V. (2004) Enhancement of photocatalytic activity by metal deposition: characterisation and photonic efficiency of Pt, Au and Pd deposited on TiO_2 catalyst. Water Research 38:3001-3008.

Sanchez C., Boissere C., Grosso D., Laberty C., Nicole L. (2008) Design, synthesis and properties of inorganic and hybrid thin films having periodically organized nanoporosity. Chemistry of Materials 20:682-737.

Sawada E., Kakehi H., Chounan Y., Miura M., Sato Y., Isu N., Sawada H. (2010) UV-induced Switching Behavior of Novel Fluoroalkyl End-capped Vinyltrimethoxysilane Oligomer/Titanium Oxide Nanocomposite between Superhydrophobicity and Superhydrophilicity with Good Oleophobicity. Composites Part B 41:498 –502.

Serpone N. (2006) Is the Band Gap of Pristine TiO2 Narrowed by Anion- and Cation-Doping of Titanium Dioxide in Second-Generation Photocatalysts?. Journal of Physical Chemistry B 110:24287-24293.

Shamaila S., Sajjad A.K.L., Chen F., Zhang J. (2010) Bismuth-Doped Ordered Mesoporous TiO_2: Visible-Light Catalyst for Simultaneous Degradation of Phenol and Chromium. Chemistry A European Journal 16:13795-13804.

Simoncic B., Span J. (1998) Thermodynamics of micellization of n-alkylpyridinium chlorides: a potentiometric study. Acta Chimica Slovenica 45:143–152.

Somasundaran P., Fuerstenau D.W. (1966) Mechanisms of alkyl sulfonate adsorption at the alumina-water interface. Journal of Physical Chemistry 70:90–96,.

Spori, D.M., Venkataraman N.V., Tosatti S.G.P., Durmaz F., Spencer N.D., Zuercher S. (2007) Influence of Alkyl Chain Length on Phosphate Self-Assembled Monolayers. Langmuir 23:8053–8060.

Stausholm-Moeller J., Kristoffersen H.H., Hinnemann B., Madsen G.K.H., Hammer B. (2010) DFT+U study of defects in bulk rutile TiO$_2$. Journal of Chemical Physics 133:144708/1–144708/8.

Sugimura H., Hanji T., Hayashi K., Takai O. (2002a) Surface Potential Nanopatterning Combining Alkyl and Fluoroalkylsilane Self-Assembled Monolayers Fabricated via Scanning Probe Lithography. Advanced Materials 14:524 – 526.

Sugimura H., Hayashi K., Saito N., Nakagiri N., Takai O. (2002b) Surface potential microscopy for organized molecular systems. Applied Surface Science 188:403 – 410.

Tadmor R. (2004) Line Energy and the Relation between Advancing, Receding, and Young Contact Angles. Langmuir 20:7659-7664.

Tadros T. (2009) Polymeric surfactants in disperse systems. Advances in Colloid and Interface Science 147-148:281-299.

Tafalla D., Salvador P., Benito R.M. (1990) Kinetic approach to the photocurrent transients in water photoelectrolysis at n-TiO$_2$ electrodes. Analysis of the photocurrent-time dependence. Journal of the Electrochemical Society 137:1810-1815.

Taylor D.J.F., Thomas R.K., Penfold J. (2007) Polymer/surfactant interactions at the air/water interface. Advances in Colloid and Interface Science 132:69-110.

Teter M.P., Payne M.C., Allan D.C. (1989) Solution of Schrödinger's equation for large systems. Physical Review B 40:12255–12263.

Tizazu G., Adawi A.M., Leggett G.J., Lidzey D.G. (2009) Photopatterning, Etching and Derivatization of Self-Assembled Monolayers of Phosphonic Acids on Titania. Langmuir 25:10746−10753.

Torres R.A., Nieto J.I., Combet E., Petrier C., Pulgarin C. (2008) Influence of TiO$_2$ concentration on the synergistic effect between photocatalysis and high-frequency ultrasound for organic pollutant mineralization in water. Applied Catalysis B: Environmental 80:168−175.

Torres-Palma R.A., Nieto J.I., Combet E., Petrier C., Pulgarin C. (2010) An innovative ultrasound, Fe^{2+} and TiO$_2$ photoassisted process for bisphenol A mineralization. Water Research 44:2245–2252.

Trebosc J., Wiench J.W., Huh S., Lin V.S.-Y., Pruski M. (2005) Solid state NMR study of MCM-41-type mesoporous silica nanospheres. Journal of the American Chemical Society 127:3057–306.

Tripp C.P., Hair M.L. (1991) The reaction of chloromethylsilanes with silica: a low frequency infrared study. Langmuir 7:923-927.

van Oss C.J., Chaudhury M.K., Good R.J. (1988) Interfacial Lifshitz-van der Waals and polar interactions in macroscopic systems. Chemical Review 88:927-940.

van Oss C.J., Good R.J., Chaudhury M.K. (1986) The role of van der Waals forces and hydrogen bonds in "hydrophobic interactions" between biopolymers and low energy surfaces. Journal of Colloid and Interface Science 111:378-390.

Wang C.C., Ying J.Y. (1999) Sol-Gel Synthesis and Hydrothermal Processing of Anatase and Rutile Titania Nanocrystals. Chemistry of Materials 11:3113-3120.

Wang D., Wang X., Liu X., Zhou F. (2010a) Engineering a Titanium Surface with Controllable Oleophobicity and Switchable Oil Adhesion. Journal of Physical Chemistry C 114:9938–9944.

Wang J.S., Li H., Li H.Y., Zou C. (2010b) Mesoporous $TiO_{2-x}A_y$ (A = N, S) as a visible-light-response photocatalyst. Solid State Science 12:490-497.

Wang S., Shiraishi F., Nakano K. (2002) A synergistic effect of photocatalysis and ozonation on decomposition of formic acid in an aqueous solution. Chemical Engineering Journal 87:261–271.

Wang X.C., Yu J.C., Yip H.Y., Wu L., Wong P.K., Lai S.Y. (2005) A Mesoporous Pt/TiO_2 Nanoarchitecture with Catalytic and Photocatalytic Functions. Chemistry: A European Journal 11:2997-3004.

Watanabe N., Horikoshi S., Kawabe H., Sugie Y., Zhao J., Hidaka H. (2003) Photodegradation mechanism for BPA at the TiO_2/H_2O surfaces. Chemosphere 52:851–859.

Wenzel R.N. (1936) Resistance Of Solid Surfaces To Wetting By Water. Industrial & Engineering Chemistry 28:988-994.

Wouters D., Hoeppener S., Schubert U.S. (2009) Local Probe Oxidation of Self-Assembled Monolayers: Templates for the Assembly of Functional Nanostructures. Angewandte Chemie International Edition 48:1732-1739.

Wouters D., Willems R., Hoeppener S., Flipse C.F.J., Schubert U.S. (2005) Inside Front Cover: Oxidation Conditions for Octadecyl Trichlorosilane Monolayers on Silicon: A Detailed Atomic Force Microscopy Study of the Effects of Pulse Height and Duration on the Oxidation of the Monolayer and the Underlying Si Substrate. Advanced Functional Materials 15:938-944.

Wu Q.L., Rankin S.E. (2011) Tuning the Mesopore Size of Titania Thin Films Using a Polymeric Swelling Agent. Journal of Physical Chemistry C 115:11925-11933.

Wu S. (1971) Calculation of interfacial tension in polymer system. Journal of Polymer Science C 34:19-30.

Wu S. (1973) Polar and nonpolar interactions in adhesion. Journal of Adhesion 5:39-55.

Xu P., Wang H., Tong R., Iv R., Shen Y., Du Q., Zhong W. (2006) A two-dimensional infrared correlation spectroscopic study on the thermal degradation of poly (2-hydroxyethyl acrylate)-co-methyl methacrylate/SiO$_2$ nanohybrids. Polymer Degradation and Stability 91:1522-1529.

Xu Q.F., Wang J.N., Sanderson K.D. (2010) Organic-Inorganic Composite Nanocoatings with Superhydrophobicity, Good Transparency, and Thermal Stability. ACS Nano 4: 2201–2209.

Xue C.-H., Jia S.-T., Zhang J., Ma J.-Z. (2010) Large-area fabrication of superhydrophobic surfaces for practical applications: an overview. Science and Technology of Advanced Materials 11: 033002 (15pp).

Yanagisawa K., Ovenstone J. (1999) Crystallization of Anatase from Amorphous Titania Using the Hydrothermal Technique: Effects of Starting Material and Temperature. Journal of Physical Chemistry B 103:7781–7787.

Yang J., Zhang Z., Men X., Xu X. (2011) Superoleophobicity of a Material Made from Fluorinated Titania Nanoparticles. Journal of Dispersion Science and Technology 32:485–489.

Yang K., Dai Y., Huang B., Feng Y.P. (2010) Density functional characterization of the antiferromagnetism in oxygen-deficient anatase and rutile TiO$_2$. Physical Review B 81:033202/1-033202/4.

Yao X., Song Y., Jiang L. (2011) Applications of the Bio-inspired Special Wettable Surfaces. Advanced Materials 23:719-734.

Yogi C., Kojima K., Takai T., Wada N. (2009) Photocatalytic degradation of methylene blue by Au-deposited TiO$_2$ film under UV irradiation. Journal of Materials Science 44:821–827.

Young C.W., Servais P.C., Currie C.C., Hunter M.J. (1948) Organosilicon Polymers. IV. Infrared Studies on Cyclic Disubstituted Siloxanes. Journal of the American Chemical Society 70:3758-3764.

Young T. (1805) An essay on the cohesion of fluids. Philosophical Transactions of the Royal Society of London 95:65-87.

Yu J.C., Yu J.G., Ho W.K., Zhao J.C. (2002) Light-induced super-hydrophilicity and photocatalytic activity of mesoporous TiO_2 thin films. Journal of Photochemistry and Photobiology A 148:331-339.

Zeitler V.A., Brown C.A. (1957a) The infrared spectra of some Ti-O-Si, Ti-O-Ti and Si-O-Si compounds. Journal of Physical Chemistry 61:1174-1177.

Zeitler V.A., Brown C.A. (1957b) Tetrakistriphenylsiloxytitanium and Some Related Compounds. Journal of the American Chemical Society 79:4616–4618.

Żenkiewicz M. (2007) Comparative study on the surface free energy of a solid calculated by different methods. Polymer Testing 26:14-19.

Zhang J., Wu Y., Xing M., Leghari S.A.K., Sajjad S. (2010) Development of modified N doped TiO_2 photocatalyst with metals, nonmetals and metal oxides. Energy & Environmental Science, 3:715–726.

Zhang M., Zhang T., Cui T. (2011) Wettability conversion from superoleophobic to superhydrophilic on titania/single-walled carbon nanotube composite coatings. Langmuir 27:9295–9301.

Zhang X., Jin M., Liu Z., Nishimoto S., Murakami T., Fujishima A. (2007) Superhydrophobic TiO_2 Surfaces. Preparation, Photocatalytic Wettablility Conversion and Superhydrophobic-Superhydrophilic Patterning. Journal of Physical Chemistry C 111:14521-14529.

Appendix:
Publications and congress presentations

Scientific publications

Research papers (published)

1. F. Milanesi, G. Cappelletti, R. Annunziata, C. L. Bianchi, D. Meroni, S. Ardizzone, Siloxane-TiO_2 Hybrid Nanocomposites. The Structure of the Hydrophobic Layer, *Journal of Physical Chemistry C*, **2010**, *114*, 8287–8293.

2. D. Meroni, S. Ardizzone, G. Cappelletti, C. Oliva, M. Ceotto, D. Poelman, H. Poelman, Photocatalytic removal of ethanol and acetaldehyde by N-promoted TiO_2 films. The role of the different nitrogen sources, *Catalysis Today*, **2011**, 161, 169-174.

3. G. Cappelletti, S. Ardizzone, F. Spadavecchia, D. Meroni, I. Biraghi, Mesoporous Titania Nanocrystals by Hydrothermal Template Growth, *Journal of Nanomaterials*, **2011**, 597954.

4. S. Ardizzone, G. Cappelletti, D. Meroni, F. Spadavecchia, Tailored TiO_2 layers for the photocatalytic ozonation of cumylphenol, a refractory pollutant exerting hormonal activity, *Chemical Communications*, **2011**, *47*, 2640-2642.

5. D. Meroni, S. Ardizzone, G. Cappelletti, M. Ceotto, M. Ratti, R. Annunziata, M. Benaglia, L. Raimondi, Interplay between Chemistry and Texture in Hydrophobic TiO_2 Hybrids, *Journal of Physical Chemistry C*, **2011**, *115*, 18649–18658.

6. A. Colombo, G. Cappelletti, S. Ardizzone, I. Biraghi, C. L. Bianchi, D. Meroni, C. Pirola, F. Spadavecchia, Bisphenol A endocrine disruptor complete degradation using TiO_2 photocatalysis with ozone, *Environmental Chemistry Letters*, **2012**, *10*, 55–60.

7. M. Ceotto, L. Lo Presti, G. Cappelletti, D. Meroni, F. Spadavecchia, R. Zecca, M. Leoni, P. Scardi, C. L. Bianchi, S. Ardizzone, About the nitrogen location in nanocrystalline N-doped TiO_2: Combined DFT and EXAFS approach, *Journal of Physical Chemistry C,* **2012**, *116*, 1764–1771.

8. D. Meroni, S. Hoeppener, S. Ardizzone, Stephanie Höppener, U.S. Schubert, Probe-based Electrooxidative Lithography of OTS SAMs Deposited onto Transparent ITO Substrates: A

Scanning Kelvin Probe Microscopy Study, *Advanced Functional Materials*, **2012**, *22*, 4376–4382.

9. D. Meroni, V. Pifferi, B. Sironi, G. Cappelletti, L. Falciola, G. Cerrato and S. Ardizzone, Block copolymers for the synthesis of pure and Bi-promoted nano-TiO_2 as active photocatalysts, *Journal of Nanoparticle Research*, **2012**, 14:1086, DOI 10.1007/s11051-012-1086-z

10. G. Cappelletti, S. Ardizzone, D. Meroni, G. Soliveri, M. Ceotto, C. Biaggi, M. Benaglia, L. Raimondi, Wettability of Bare and Fluorinated Silanes: A Combined Approach Based on Surface Free Energy Evaluations and Dipole Moment Calculations, *Journal of Colloid and Interface Science*, **2013**, *389*, 284-291.

11. G. Soliveri, R. Annunziata, S. Ardizzone, G. Cappelletti, D. Meroni, Multiscale rough TiO_2 films with patterned hydrophobic/oleophobic features, *Journal of Physical Chemistry C*, in press. DOI: dx.doi.org/10.1021/jp309397c

Book chapter (Invited)

S. Ardizzone, I. Biraghi, G. Cappelletti, D. Meroni, F. Spadavecchia, Physico-chemical tailoring of material surface properties, in: L. Rimondini (Ed.), Surface tailoring of inorganic materials for biomedical applications, Bentham, London, **2012**, pp. 3-42.

Research papers (submitted)

G. Maino, D. Meroni, V. Pifferi, L. Falciola, G. Cappelletti, S. Ardizzone, Electrochemically assisted deposition of transparent, mechanically robust TiO_2 films for advanced applications. *ACS Applied Materials and Interfaces*, submitted

G. Soliveri, D. Meroni, G. Cappelletti, R. Annunziata, V. Aina, G. Cerrato, S. Ardizzone, Role of functionalization procedure and of oxide nature on the wettability of organic/inorganic hybrids. *Colloids and Surfaces A: Physicochemical and Engineering Aspects*, submitted

Congress presentations

Invited presentations

D. Meroni, S. Hoeppener, S. Ardizzone, U.S. Schubert, "Surface modification of ITO layers by AFM-based electrooxidative lithography", 4th Congress of the European Association for Chemical and Molecular Sciences (4th EuCheMS) – Praga, Repubblica Ceca – 26 – 30 agosto 2012

Oral presentations

D. Meroni, S. Ardizzone, C.L. Bianchi, G. Cappelletti, D. Poelman, Nanostructured TiO_2 films by spin coating for air remediation, XXIII Congresso della Società Chimica Italiana – Sorrento, Italy – July 5-10, 2009

D. Meroni, G. Cappelletti, S. Ardizzone, I. Biraghi, Complete mineralization of bisphenol A by the combination of ozonation and photocatalysis, Giornate dell'Elettrochimica Italiana Elettrochimica per il Recupero Ambientale (GEIERA2010) – Modena, Italy – September 5-10, 2010

D. Meroni, S. Ardizzone, M. Ceotto, R. Annunziata, L. Raimondi, M. Benaglia, G. Cappelletti, Organic-inorganic hybrids: the role played by surface energy and structure of the hydrophobizing molecole, 25th European Colloid and Interface Society Congress (ECIS2011) – Berlin, Germany – September 4-9, 2011

D. Meroni, S. Hoeppener, S. Ardizzone, U.S. Schubert, "Scanning probe electro-oxidative lithography of OTS monolayers on ITO films: A Scanning Kelvin Probe Microscopy investigation" - 26th Conference of the European Colloid and Interface Society (ECIS2012) – Malmö, Sweden – September 2-7, 2012

G. Soliveri, D. Meroni, G. Cappelletti, R. Annunziata, S. Ardizzone, G. Cerrato, "Wettability features of nano-oxides: the tailoring of the attachment modes of siloxane", V Workshop on Oxide Based Materials (OXIDE2012) – Turin, Italy – September 24-26, 2012

Poster presentations

D. Meroni, S. Ardizzone, G. Cappelletti, C. Oliva, C. Pirola, D. Poelman, H. Poelman, N-doped TiO_2 Nanoparticles. Photocatalytic Degradation of Ethanol and Acetaldehyde in the Gas Phase, 6th European meeting on Solar Chemistry and Photocatalysis: Environmental Applications (SPEA6) – Prague, Czech Republic – June 13-16, 2010

D. Meroni, G. Cappelletti, R. Annunziata, M. Benaglia, S. Rossi, M. Ratti, S. Ardizzone, The nature of the hydrophobic layer in hybrid nanomaterials, XXXIX Congresso Nazionale di Chimica Fisica (CF2010) – Stresa, Italy – September 20-24, 2010

C. Oliva, F. Spadavecchia, D. Meroni, G. Cappelletti, S. Ardizzone, S. Cappelli, EPR features of second generation photocatalysts, XXXIX Congresso Nazionale di Chimica Fisica (CF2010) – Stresa, Italy – September 20-24, 2010

D. Meroni, V. Pifferi, F. Spadavecchia, M. Vescovi, I. Biraghi, Tailored TiO2 nanoparticles by means of template and microemulsion routes, XXXIX Congresso Nazionale di Chimica Fisica (CF2010) – Stresa, Italy – September 20-24, 2010.

B. Sironi, V. Pifferi, S. Ardizzone, C. Cappelletti, I. Biraghi, D. Meroni, Modulation of the interfacial features of nanometric TiO2 by template-mediated synthesis, 25th European Colloid and Interface Society Congress (ECIS2011) – Berlin, Germany – September 4-9, 2011

F. Spadavecchia, C. Oliva, G. Cappelletti, S. Ardizzone, I. Biraghi, S. Cappelli, D. Meroni, The role of the nitrogen source in affecting the features of second generation photocatalysts, 25th European Colloid and Interface Society Congress (ECIS2011) – Berlin, Germany – September 4-9, 2011

G. Soliveri, D. Meroni, B. Sironi, G. Cappelletti, S. Ardizzone, "Nanometric TiO_2-based materials for environmental remediation and self-cleaning", Giornate dell'Elettrochimica Italiana Elettrochimica per il Recupero Ambientale (GEIERA2012) – Santa Marina Salina, Messina, Italy – June 17 – 22, 2012

F. Spadavecchia, D. Meroni, G. Cappelletti, S. Ardizzone, S. Regazzoni, "N, Ag codoped nano-TiO_2: the effect of synthetic parameters on gas phase photocatalytic activity" – 7th European meeting on Solar Chemistry and Photocatalysis: Environmental Applications (SPEA7) – Oporto, Portugal –June 17 – 20, 2012

G. Cappelletti, S. Ardizzone, D. Meroni, M. Ceotto, Cinzia Biaggi, M. Benaglia, L. Raimondi, "Surface Free Energy of Bare and Fluorinated Siloxanes: Comparing Experimental Evaluation and Dipole Moments Calculations" - 26th Conference of the European Colloid and Interface Society (ECIS2012) – Malmö, Sweden –September 2-7, 2012

G. Soliveri, D. Meroni, G. Cappelletti, R. Annunziata, S. Ardizzone, "Roughness influence on the attachment modes of siloxanes on TiO$_2$ surfaces" - 26th Conference of the European Colloid and Interface Society (ECIS2012) – Malmö, Sweden –September 2-7, 2012

D. Meroni, V. Pifferi, B. Sironi, G. Cappelletti, L. Falciola, S. Ardizzone, G. Cerrato, "Mesoporous TiO$_2$ as scaffold for Bi-promoted photocatalysts", V Workshop on Oxide Based Materials (OXIDE2012) – Turin, Italy – September 24-26, 2012